DIRECT INJECTION OF NATURAL GAS FOR DIESEL ENGINE FUELING

by

PATRIC OUELLETTE

B.Ing., Ecole Polytechnique de Montreal, 1989
M.A.Sc., The University of British Columbia, 1992

A THESIS SUBMITTED IN PARTIAL FULFILLMENT OF

THE REQUIREMENTS FOR THE DEGREE OF

DOCTOR OF PHILOSOPHY

in

THE FACULTY OF GRADUATE STUDIES

Department of Mechanical Engineering

We accept this thesis as conforming
to the required standard

THE UNIVERSITY OF BRITISH COLUMBIA

February 1996

In presenting this thesis in partial fulfilment of the requirements for an advanced degree at the University of British Columbia, I agree that the Library shall make it freely available for reference and study. I further agree that permission for extensive copying of this thesis for scholarly purposes may be granted by the head of my department or by his or her representatives. It is understood that copying or publication of this thesis for financial gain shall not be allowed without my written permission.

Department of MECHANICAL ENGINEERING

The University of British Columbia
Vancouver, Canada

Date April 26 1996

ABSTRACT

Transient turbulent underexpanded jets are formed when natural gas is directly injected, late in the compression stroke, in the combustion chamber of diesel engines. An analysis of gaseous jets, entering a large chamber at high Reynolds number and at sonic nozzle conditions, defines the similarity conditions pertaining to the jet penetration and mixing with the surrounding air. It is shown that the jet penetration varies with $(\dot{M}_n/\rho_{ch})^{1/4}\ t^{1/2}$, where $\dot{M}_n$ is the momentum injection rate at the nozzle, ρ_{ch} the chamber gas density and t the time from beginning of injection. This dependency is supported by jet theory and by experimental data. The experimental data, which are also used to confirm the validity of multidimensional simulations, were obtained by schlieren visualization of underexpanded transient methane jets.

Autoignition or ignition through pilot fuel combustion of the gaseous jets leads to transient flames whose configuration is affected by the length of the ignition delay. The ignition and combustion of the gaseous jets were studied using a multidimensional model which includes a new ignition scheme reproducing well the temperature dependency of methane autoignition data, a two-step high-temperature kinetic, and an eddy-dissipation turbulent combustion model. The simulations indicate that transient flames penetrate at much the same rate as cold jets, which can be formally shown for autoigniting flames with little or no premixed combustion (early-ignition). The simulations demonstrate that the ignition delay and the nozzle injection rate of the gaseous jets affectsthe proportion of premixed and mixing-limited burning. In the case of pilot-ignited gaseous jets, it is shown that increasing the interaction between the pilot fuel sprays and the gaseous jets promotes early ignition of the gaseous jets. Results also indicate that injecting the natural gas later than the pilot fuel spray promotes early ignition and complete combustion of the gaseous fuel jet.

The simulations, of both cold and igniting jets, permitted to highlight consequences and practical considerations regarding the choice of injection pressure, nozzle diameter, number of holes, and regarding the ignition of methane jets through pilot fuel combustion.

RÉSUMÉ

Lorsque du gaz naturel est injecté à haute pression dans la chambre de combustion d'un moteur diesel, des jets transitoires, turbulents et sous-détendus sont formés. Une analyse de ces jets, débouchant à la vitesse du son et avec un nombre de Reynolds élevé dans une large chambre, permet de définir les conditions de similitude s'appliquant au taux de changement de la pénétration et du mélange avec l'air des ces jets. L'analyse révèle que la pénétration des jets issu d'orifices circulaires varie selon $(\dot{M}_n/\rho_{ch})^{1/4}\ t^{1/2}$, où $\dot{M}_n$ est le taux d'injection de la quantité du movement du gaz à l'orifice, ρ_{ch} la densité du gas dans la chambre de combustion, et t le temps écoulé depuis le début de l'injection. Cette dépendance est supportée par la théorie des jets et par des données expérimentales. La technique de strioscopie a été utilisée pour déterminer expérimentalement le taux de changement de la pénétration des jets transitoires pour différents rapports de pression. Les données obtenues ont aussi servi à confirmer la validité des simulations numériques effectuées dans ce travail.

Lorsque les jets de méthane s'enflamment, suivant auto-allumage où un allumage causé par la combustion d'une petite quantité d'essence diesel, une flamme de diffusion est formée et pénètre dans la chambre de combustion. La configuration de la flamme formée dépend du délai d'allumage. Des flammes de diffusion transitoires typique de celles évoluant dans un moteur diesel ont été étudiées à l'aide de simulations numériques incluant un modèle simplifié du mécanisme chimique d'auto-allumage du méthane, un modèle cinétique de la combustion à haute température et un modèle de combustion turbulente du genre proposé par Magnussen *et al.* Les simulations révèlent que les flammes pénétrent dans la chambre de combustion pratiquement au même taux que les jets qui ne s'allume pas, ce qui peut être démontré de façon claire pour les flammes qui s'enflamme rapidement suivant le début de l'injection. Les simulations indiquent aussi que le délai d'allumage et le taux d'injection du méthane changent les charactéristiques de

la combustion en affectant la proportion de l'oxidation du méthane se produisant sous un régime de réactants prémélangés et de combustion limitée par le mélange d'essence et d'air.

Quand la combustion d'une petite quantité d'essence diesel est utilisée pour allumer les jets de gaz naturel, les simulations indiquent qu'une augmentation de l'interaction entre les jets de gaz naturel et les brouillards de diesel permet un allumage plus rapide et augmente le taux de combustion initial des jets gazeux. Les résultats indiquent aussi que l'incoporation d'un délai entre l'injection de l'essence diesel et celle du gaz naturel favorise la combustion complète des jets gazeux.

Les simulations numériques ont aussi permis d'identifier les conséquences et les aspects pratiques des choix de pression d'injection, et du nombre et diamètre des orifices.

TABLE OF CONTENTS

LIST OF SYMBOLS

The specified units are intented as typical units. Equivalent units with appropriate conversion factors may have been used in the thesis.

a	distance between nozzle and virtual origin	[mm]
a, b	stoichiometric coefficients	
a', b'	empirical species coefficients	
A	pre-exponential constant	
A_{mag}, B_{mag}	constants in Magnussen model	
A_{ps}, A_n	area of the pseudo-diameter and of the nozzle exit plane	[mm^2]
$\overline{C}$	mean concentration of the species specified by the subscript	[mol/cm^3]
C_c	constant in penetration rate equation	
C_d	discharge coefficient	
C_m	concentration on jet axis	[mol/cm^3]
C_t	proportionality constant in penetration rate equation	
C_p	specific heat at constant pressure	[kJ/kg/K]
C_v	specific heat at a constant volume	[kJ/kg/K]
d_{eq}	equivalent diameter	[mm]
d_n	nozzle diameter	[mm]
d_{ps}	pseudo-diameter	[mm]
d_s	diameter of N small holes	[mm]
D	diffusion coefficient	
e/D	relative surface roughness	
E_a	activation energy	[kJ/mol]
h_m	enthalpy of species m	[kJ/kg]

I	internal energy	[J], [ergs]
k	specific turbulent kinetic energy	[m^2/s^2]
K	heat conductivity	[W/m/K]
l	turbulent length scale	[mm]
L/d	length to diameter ratio of nozzles	
m_l, m_f, m_r	mass of methane within lean, flammable and rich zones within the chamber	[g]
m_{ch}	mass entrained within the gas jet	[g]
$\dot{m}$, $\dot{m}_{ch}$	mass entrainment rate of chamber air within the gas jet	[g/s]
m_i, m_{inj}	mass of fluid injected	[g]
$\dot{m}_{inj}$, $\dot{m}_n$	mass injection rate of fluid at nozzle	[g/s]
$\dot{M}_n$	momentum injection rate at the nozzle	[kg m/s^2]
M_n	Mach number at nozzle	
M_o	total momentum injected (puff jets)	[kg m/s]
M_{ps}	Mach number at pseudo-diameter	
N	number of nozzles	
N_{inj}	number of cells within the nozzle	
P_{ch}	chamber gas pressure	[MPa]
P_e	nozzle exit gas pressure	[MPa]
P_o	upstream gas stagnation pressure	[MPa]
Pr	Prandtl number	
ΔP	pressure drop across nozzle	[MPa]
Q	heat release per unit volume	[J/m^3]
$r_{½}$	jet half-radius (radial location where velocity is half of centerline velocity)	[mm]
R	average radius of the vortex head	[mm]

R	gas constant	[kJ/kg/K]
RR	reaction rate	[mol/cm^3/s]
Re_t	turbulent Reynolds number	
s	stoichiometric oxygen requirement	
S	spray tip penetration	[mm]
Sc	Schmidt number	
t	time elapsed from the beginning of injection	[ms]
t^*	non-dimensional time	
t_{eq}	time scale based on equivalent diameter	[ms]
t_{inj}	injection duration	[ms]
t_{inj}^*	non-dimensional injection duration = $t_{inj}U_n/d_{eq}$	
T_c	chamber core temperature	[K]
T_{lb}	transition temperature between ignition and high-temperature kinetic scheme	[K]
T_o	upstream gas stagnation temperature	[K]
T_{ps}	gas temperature at pseudo-diameter plane	[K]
u'	gas fluctuating velocity	[m/s]
U_{df}	diesel fuel nozzle velocity	[m/s]
U_n	nozzle gas velocity	[m/s]
U_{ps}	pseudo-diameter gas velocity	[m/s]
$U_{CL}(z)$	centerline velocity at distance z from nozzle	[m/s]
$U(r,z)$	velocity at distance z from the nozzle & at a normal dist. r from jet axis	[m/s]
V	average velocity of the vortex head	[m/s]
W	molecular weight	[g/mol]
X_{cp}	combustion products mass fraction above which eddy-dissipation combustion	

	model is active	
Y	molar fraction	
z	distance from the nozzle	[mm]
z_f	flame tip penetration (based on maximum axial reaction rate location)	[mm]
z_t	jet penetration (nozzle to jet tip distance)	[mm]
z_t'	jet penetration from virtual origin of the jet	[mm]
z_t^*	non-dimensional jet penetration	
Z	compressibility factor	

GREEK SYMBOLS

γ	ratio of specific heat	
ε	dissipation of specific turbulent kinetic energy	[m^2/s^3]
θ_{df2}	injection angle of the diesel fuel spray relative to gaseous jet axis	
μ_{air}	kinematic viscosity of air	[kg/m/s]
ν_t	turbulent viscosity	[m^2/s]
ρ	density of the substance specified by the subscript	[kg/m^3]
ρ_{ch}	air density in the chamber	[kg/m^3]
ρ_g	injected gas density at chamber pressure	[kg/m^3]
ρ_n	gas density at nozzle exit	[kg/m^3]
ρ_o	upstream gas stagnation density	[kg/m^3]
τ	time scale specified by the subscript (c - conversion, l - laminar, k - chemical kinetics or t - turbulent)	
τ_i	autoignition delay	
Φ	equivalence ratio (ratio of local fuel/air fraction to soichiometric fuel/air fraction)	

χ_m	mass fraction of injected fluid on jet axis

SUBSCRIPTS AND SUPERSCRIPTS

b	burned
ch	chamber air
CL	centerline
CP	combustion products
df	diesel fuel
f	fuel, flame
g	injected gaseous fuel
hts	high temperature scheme
ign	ignition
j	jet
k	kinetic
l	liquid diesel fuel
m	species m
mix	of mixture
n	at nozzle exit
o	oxidizer
P	combustion products
ps	at pseudo diameter exit plane
PS	combustion products at spark time
r	reaction r
t	turbulent

*	dimensionless

ABBREVIATIONS

BOI	beginning of injection
BTDC	before top-dead-center
CA	crank-angle degrees
CI	compression ignition
CNG	compressed natural gas
CO	carbon monoxide
DDC	Detroit Diesel Corporation
DDEC	Detroit Diesel electronic control
df2	diesel fuel #2
EOI	end of injection
LHV	lower heating value
NO_x	oxides of nitrogen
pdf	probability density function
PR	pressure ratio
PW	pulse width - duration of injection in crank angle degrees
RPM	revolutions per minute
RR	reaction rate
SI	spark ignition
TDC	top-dead-center
SMR, smr	Sauter mean radius

LIST OF TABLES

LIST OF FIGURES

ACKNOWLEDGEMENT

I wish to express my gratitude to Dr. P.G. Hill for his invaluable help, judicious advice and encouragements during the realisation of this project and the writing of this thesis. I also wish to thank Bruce Hodgins who designed the prototype injector and for his technical help. This thesis would not have been possible without the help of numerous people in the department of mechanical engineering at U.B.C.. I would like to thank Alan Steeves and Gerry Rohling for their constant availability and help with computer related problems. I would also like to thank all the office personel.

I address very special thanks to the one person who during these two years offered incessant moral support and encouragements and who actively participated to the realisation of this thesis, my wife, Patty. I also thank Miguel and Stéphane for the spice they brought to the realisation of this thesis.

I acknowledge the financial support of NSERC, of U.B.C. Awards and Financial Aid Office and of my supervisor, P.G.Hill. I am also grateful for the support from Housing and Conferences.

Finalement je tiens à remercier spécialement toute ma famille qui malgré leur éloignement m'ont soutenus par leur constant soutien et leurs prières.

CHAPTER 1

INTRODUCTION

1.1 DIRECT INJECTION OF NATURAL GAS IN DIESEL ENGINES

The direct injection of natural gas in a diesel engine offers an efficient method of reducing emissions while retaining the fuel economy associated with compression-ignition engines. Under the regulatory pressure of the U.S. Environmental Protection Agency, manufacturers of medium-size heavy-duty diesel engines, such as those found in many buses, have refined injection control and combustion chamber design as to minimize nitrogen oxides and particulate emissions. Yet, manufacturers must now resort to other techniques to meet increasingly stringent emissions regulations. By virtue of its lower flame temperature, natural gas offers a potential for reduced NO_x (nitrogen oxides). Also, owing to the simpler chemical structure of methane, which constitutes 90 to 98% of natural gas, the potential to form particulate matter and unburned hydrocarbons during combustion is reduced.

Figure 1.1 illustrates schematically the direct injection concept. The injector allows natural gas to be injected directly into the chamber near

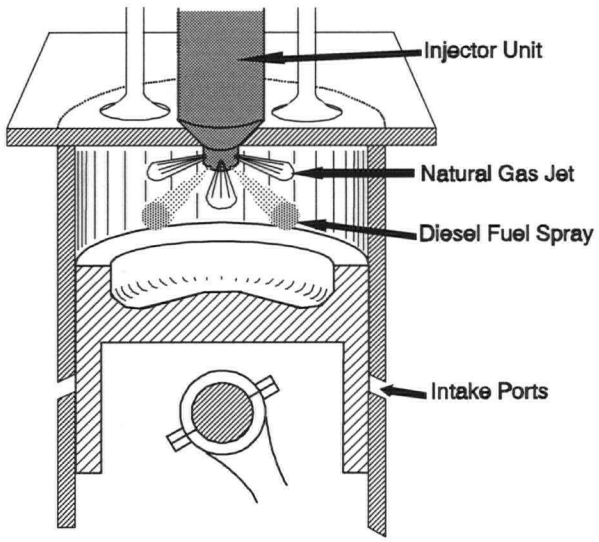

Figure 1.1 Late cycle, direct injection of natural gas with pilot diesel fuel.

the end of the compression stroke. A high natural gas injection pressure must be used to overcome the end-of-combustion chamber pressure. At typical end-of-compression temperatures and pressures, natural gas has a prohibitively long ignition delay. A small amount of pilot diesel fuel is consequently injected in the chamber to provide the ignition.

In diesel engines, the liquid fuel is injected a few crank angle degrees before TDC (top-dead-center). The liquid breaks up into droplets that vaporize on contact with the hot air in the chamber. The mixture of evaporated diesel fuel and air autoignites and, following a premixed combustion phase, a mixing-limited combustion proceeds. Although natural gas can be liquefied, it is gaseous at the temperature and pressure required for the injection. While diesel fuel has a constant density of approximately 750 kg/m^3, that of natural gas varies with pressure, and under the conditions that will be considered in this thesis, may be between 55 and 110 kg/m^3. Natural gas is compressible with the consequence that it responds differently than diesel fuel to the difference between the pressure within the injector and that in the chamber. Also, as a gas, it need not atomize and evaporate as it enters the combustion chamber. Natural gas differs chemically from diesel fuel. Its autoignition delay tends to be significantly longer, and its laminar burning speed is also lower at engine pressures.

As the natural gas enters the chamber, it forms a transient jet that travels away from the nozzle. The natural gas mixes with the air in the chamber, ignites and burns. The properties of the transient jet formed by the gas injection are discussed in the next section, and it is shown that the transient jets are turbulent compressible jets. The nozzle velocity is approximately 450 m/s, and the nozzle flow is likely to be underexpanded, that is the nozzle exit pressure will be greater than the chamber pressure.

Very little fundamental work has been done on the problem of transient reactive compressible jets for compression-ignition engine application. This is not surprising, as there has

been only a handful of attempts in utilizing the concept in the past 10 to 15 years, with most of the early work done on large marine diesels. Fundamental work is needed to establish the effect of injector design (number and diameter of nozzles), of operation conditions (injection pressure and temperature) and of combustion chamber conditions (pressure and temperature) on the mixing, ignition and combustion of the natural gas as directly injected in a combustion chamber. This need can be appreciated in view of the outlined physical and chemical differences between diesel fuel and natural gas, of the added complexities of compressible flow effects in the nozzle area, and of interactions between the pilot fuel spray and the gaseous jet leading to ignition.

This thesis is about the fundamentals, leading to practical design considerations, of the gas mixing, ignition and combustion when directly injected at high pressure in a diesel engine combustion chamber. The work reported in this thesis constitutes a part of a wider research and development effort, which includes the design, testing and development of an injector for direct injection of natural gas in a diesel engine. The engine targeted in the project is a medium size heavy-duty two-stroke engine, which is typically used in buses. Figure 1.1 illustrates schematically the concept of the conversion technique. A gas/diesel injector unit replaces the conventional liquid fuel injector unit. Figure 1.2 shows a schematic injector and the natural gas fueling system. The conversion requires the replacement of the injector unit, the installation of an intensifier and of storage tanks. The intensifier compresses the natural gas from its decreasing tank pressure to the required injection pressure. Some discussion about the engine performance and testing can be found in Hodgins, Gunawan and Hill [1992] and Tao, Hodgins and Hill [1994].

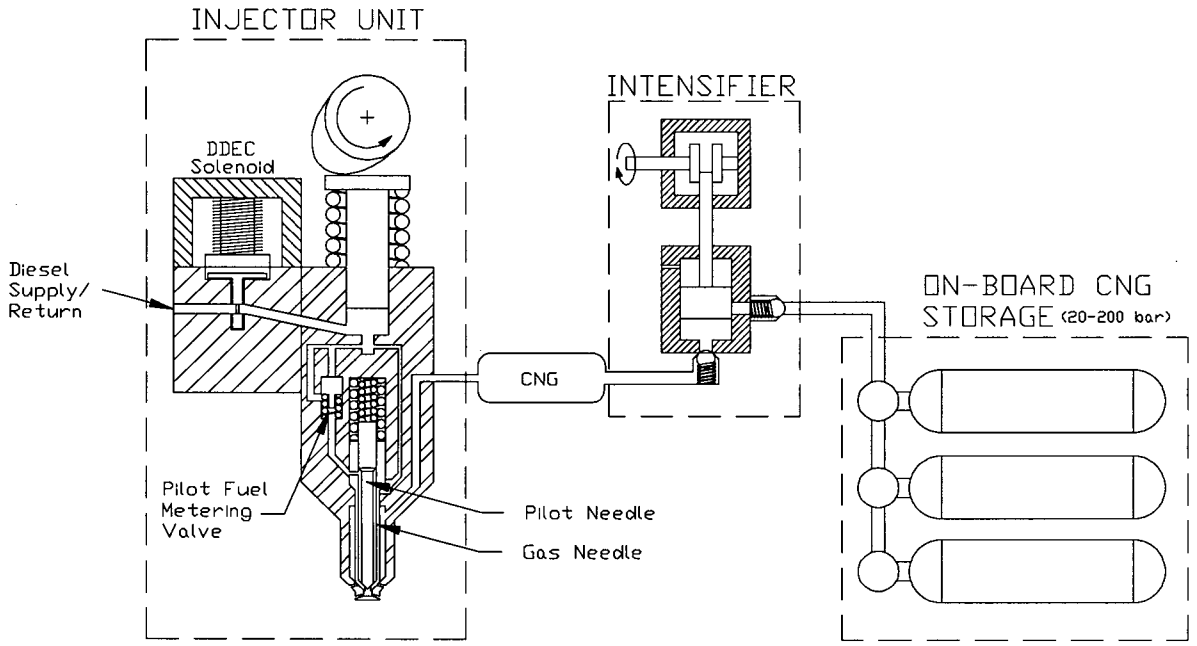

Figure 1.2 - Schematic of natural gas fueling system (DDEC: Detroit Diesel Electronic Control, CNG: compressed natural gas).

1.2 TRANSIENT GASEOUS JETS FOR DIESEL ENGINE FUELING

The main features of the gaseous jets that need to be considered are presented in this section. Typical diesel engine conditions, and the associated time and length scales, are first reviewed.

The conditions and scales are somewhat engine dependent. Here a Detroit Diesel Corporation 6V-92 turbocharged, after-cooled, two-stroke diesel engine is considered. The specifications of the engine are given in Appendix A. The scales and conditions should resemble those of other heavy-duty medium-size diesel engines. The bore of the engine is 123 mm, and the compression ratio is 17. The gross rated power output is 224 kW (300 HP) at 2100 RPM.

The conditions in the chamber vary with load and speed, but as an indication, the medium

load pre-combustion pressure is approximately 4 MPa, while the peak pressure is 5.5 Mpa. The corresponding pre-combustion temperature may be 850 K. At 1200 RPM, a compression and expansion cycle lasts 50 ms. The injection duration and the ignition delay, the time elapsed between the beginning of the injection (BOI) and the sudden change in pressure increase rate, are of the order of 1 ms. The combustion duration is between 5 and 10 ms. Important length scales are the chamber radius (61 mm), the distance between the piston crown and the top wall at TDC (1.5 mm), the bowl-in-piston depth (12.5 mm), and the nozzle diameter, which is around 0.15 mm for diesel fuel and 0.5 mm for natural gas injection.

In diesel fuel operation, injected fuel mass per cylinder per cycle is of the order of 15 mg at low load (1200 RPM), 30 mg at medium load, 50 mg at high load. Natural gas has a slightly higher LHV than diesel fuel by 5% to 10% depending on the quality of the diesel fuel and of the local natural gas. Consequently, fuel mass requirements are essentially the same.

The knowledge of typical conditions in diesel engines, along with the experience gained through experimental engine testing, permits a characterization of the transient gaseous jets that need to be investigated. First, it is advantageous for control purposes to operate the nozzles at choked conditions for the injection of the gaseous fuel. The injection velocity is then constant and therefore the mass flow rate is constant once an injection pressure has been selected. The injection pressure is defined in this thesis as the stagnation pressure of the natural gas upstream of the nozzle. Choked conditions provide sonic velocity at the nozzle exit. For methane, the main constituent of natural gas, the speed of sound is approximately 450 m/s (at 350 K). To meet the choking conditions despite the variation of chamber pressure (P_{ch}) with time (compression, combustion and expansion) and with load, the injection pressure (P_o) must be set such that the critical pressure ratio ($PR_{crit} = P_o/P_{ch} = 1.86$, for methane assuming perfect gas law) is attained for the typical pressure levels encountered (about 7.5 MPa at high load, up to 9 MPa).

This condition means that most of the time, the nozzles will be operated at underexpansion conditions, that is the nozzle pressure will be higher than the chamber pressure, and expansion will take place outside the nozzle.

To provide a natural gas mass injection rate similar to that of diesel fuel in the original engine, nozzles of the order of 0.5 mm in diameter are required, with the value depending on the choice of the injection pressure and on the number of nozzles. The injection pressure must be greater than about 12 MPa to satisfy choking conditions under most operating conditions, but injection pressures up to 20 MPa have been suggested. Under these conditions, the density at the nozzle may be between 40 and 70 kg/m^3. The nozzle Reynolds number is between 8.25×10^5 and 1.5×10^6; thus the jets are fully turbulent.

A consequence of the high injection pressure is that real-gas behavior is significant. For example, the compressibility coefficient for an injection pressure of 15 MPa and a temperature of 350 K is 0.92. Furthermore, the nozzles have a length-to-diameter ratio of about 6, and frictional effects must be considered.

As the gaseous fuel enters the chamber, a vortex head is formed. If the injection finishes before or as the vortex head leaves the nozzle, then a puff jet is formed. Experimental knowledge has shown that the jets under consideration here are not of the puff jet type (discussed in Section 2.1).

The characteristic travel distance of the jet, before it impinges on walls, is of 120 diameters, based on a typical bore radius of 60 mm and on a nozzle diameter of 0.5 mm. This is significant because the region of interest is well beyond the 10-to-20-diameter region, in which nozzle effects render the establishment of general rules difficult.

As the natural gas is injected, it comes into contact with hot air and with hot combustion products from the pilot diesel fuel combustion. The methane jet ignites, and subsequently, there

is a rapid combustion of the natural gas which has mixed with the air during the ignition delay. A mixing-limited combustion usually follows, during which the rate of combustion is controlled by the rate of mixing between fuel and oxidizer. The mixing-limited part of the combustion depends on the injection process. The ignition depends on the chemical kinetic properties of the fuel, and on the interaction between the igniting pilot diesel fuel sprays and the gaseous jets. The nature of this interaction is the entrainment of hot combustion products within the gas jet, and is controlled by the flow field generated by the jets and pilot fuel sprays.

In summary, the injection and combustion of natural gas in a diesel engine involves transient turbulent underexpanded jets of natural gas injected into air. The jets are issued from round nozzles at near-sonic or sonic velocity. The nozzle flow may involve significant real gas behavior, and is subject to frictional losses. The transient jets ignite due to contact with hot gas pockets resulting from the interaction with igniting pilot fuel sprays. Following ignition, the natural gas may burn in a premixed fashion, or may burn directly in a mixing-limited combustion if the ignition delay is short.

The jet drives the mixing of the natural gas and air, and therefore the combustion. The complex problem described above is most easily treated by considering first the problem of the cold jet[1]. This view is reflected in the organization of the thesis and in the statement of objectives.

1.3 OBJECTIVES

The work presented in this thesis has four main objectives. Each of these objectives is presented below with a brief statement of the methods of analysis employed. The first objective

[1] In this thesis, the term "cold jet" is used to designate non-igniting jets, and may be applied to jets propagating in high-temperature chambers.

concerns the penetration and mixing of cold jets, while the three last objectives pertain to igniting and burning transient jets.

I) The first objective is to establish the dependency of transient underexpanded jet penetration and mixing rate on the choice of injection pressure, on the nozzle diameter and on the pressure and temperature in the chamber. The effects of injection duration and turbulence levels are also sought.

The first step in meeting this objective was to review the similarity and scaling laws of steady-state and transient jets, including in particular compressible underexpanded turbulent jets of different molecular weights. This review is presented in Chapter 2. The penetration of underexpanded methane jets is measured experimentally in Chapter 3, using flow visualization. Multidimensional modelling is applied to extend the scope of the experimental work to the study of mixing rate, of injection duration and of turbulence levels (Chapter 5). The KIVA-II code, which was used as a base code for the modelling, is described and tested for transient underexpanded jets in Chapter 4.

II) The second objective is to establish the effect of ignition and combustion on the cold jet dependencies.

This objective aims at verifying the hypothesis that the characterization of cold jets ensuing from the first objective remains valid when ignition and combustion take place. Multidimensional modelling of igniting and burning transient jets is used to verify the veracity and the limits of that hypothesis. A methane autoignition model and a turbulent-limited combustion model were implemented in KIVA-II. The combustion model is presented in Chapter 6, along with an examination of its performance, while the modelling of transient igniting jets

is presented in Chapter 7.

III) A third objective is to establish the effects of injection pressure, of nozzle diameter, and of chamber conditions on the ignition and combustion of transient methane jets.

IV) A fourth objective is to investigate the effect of interaction between the pilot fuel sprays and the gaseous jets, and the effects of injection delay and injection rate on the ignition and combustion of methane jets ignited through pilot fuel combustion.

The injection delay is the delay between the injection of pilot diesel fuel and that of the natural gas. Both these objectives are investigated in Chapter 7 using the multidimensional model. When considering objectives **II)** and **III)**, autoigniting jets are considered. In the fueling system presented in Figs. 1.1 and 1.2, pilot diesel fuel jets are used to provide the ignition of the natural gas jets. The mechanisms by which the pilot fuel combustion promotes the ignition of the methane jets are discussed in Chapter 7, along with an investigation of the effects of injection conditions on that ignition.

All the objectives stem from the practical need to understand the effects of design choices and of operation conditions on the penetration, mixing, ignition and combustion of natural gas directly injected in diesel engines.

Multidimensional modelling of the gas injection, ignition and combustion is performed in this thesis and is used as an analytical tool permitting the study of various hypotheses. The advantages of multidimensional models are their capacity of conserving mass and momentum, of handling many complex processes, and their controllability. These attributes are well suited to the exploration of the relationships between gas injection parameters and the jet mixing and combustion within the changing environment of a diesel engine. The limitations of multi-

dimensional models are nevertheless recognized and are discussed at various points in the thesis.

1.4 SCOPE AND LIMITATIONS

The main scope of the work has been to relate the injection parameters to the combustion of the gaseous fuel in a typical diesel environment. Simplification of the diesel environment is often used in this thesis to permit unequivocal interpretation of simulation results. In particular most of the computational results are obtained by considering the injection of a gaseous fuel in a constant-volume cylindrical chamber through a single centrally located hole. In this constant-volume simplification, pressures, temperatures and turbulence levels typical of diesel engines can be reproduced. Characteristic length scales, such as the nozzle-to-wall distance may also be reproduced. The geometry permits one to perform axisymmetric computations which allow greater mesh refinement while keeping reasonable computational times. Three-dimensional computations were performed to compare with the experimentally determined penetration data.

Since natural gas is composed of 90-98% methane gas, the experimental work and the numerical work were based on methane. This simplification removes some of the uncertainties regarding thermodynamic and chemical properties of natural gas which vary in composition with time of year and location.

The model was developed with the intent of eventually performing three-dimensional simulations of natural gas and pilot fuel combustion in a variable-volume chamber. However, in the work reported in this thesis, wall effects, swirl, and piston motion are not considered. Furthermore, simple methane oxidation models are used. Intermediate species, equilibrium species, NO_x and residual gases are not considered.

1.5 SUMMARY OF RESULTS

In Chapter 2, it is shown that the analysis of available information on steady and transient turbulent gas jets leads to a simple general description of compressible turbulent transient jets of various molecular weights. The scaling laws of steady jets, the relationship between steady and transient jets, and experimental knowledge leads to the following relationship for the jet tip penetration of such jets:

$$z_t' = C_t \left(\frac{4}{\pi}\right)^{1/4} \left(\frac{\dot{M}_n}{\rho_{ch}}\right)^{1/4} t^{1/2} \qquad \textbf{(1.1)}$$

where z_t' is the distance between the jet tip and a virtual origin, thereafter called the jet penetration, $\dot{M}_n$ the momentum rate at the nozzle, ρ_{ch} the chamber or surrounding air density, t the time elapsed from the beginning of injection, and C_t a constant. The conditions and range of validity of Eq. 1.1 are discussed in Chapters 2 and 3. It is also demonstrated that Eq. 1.1 is equivalent to the following equation, which shows the appropriate length and time scales for transient jets:

$$\frac{z_t'}{d_{eq}} = C_t \left(\frac{tU_n}{d_{eq}}\right)^{1/2} , \quad d_{eq} = d_n \left(\frac{\rho_n}{\rho_{ch}}\right)^{1/2} \qquad \textbf{(1.2)}$$

where d_n, ρ_n and U_n are the nozzle diameter, density and velocity.

In Chapter 3, the experimental penetration rates obtained in this work are found to support Eqs. 1.1 and 1.2. Numerical modelling is shown in Chapter 4 to reproduce well the experimentally observed penetration rates, although the cases studied are under-predicted by some 10%. The numerical results will also be shown to be consistent with the proposed scaling. In Chapter 5, it is demonstrated, using numerical modelling, that the length and time scales of Eq. 1.2 are also appropriate when considering the mixing rate of transient jets. In the same chapter,

it is also shown that gaseous jets and sprays injected with the same nozzle momentum injection rate mix at much the same rate.

When considering igniting transient jets in Chapter 7, the reaction zone penetration of jets that ignite almost instantaneously as they enter the chamber is found to match the penetration of the unity equivalence ratio in a cold jet. This indicates that the scaling of transient jet identified above remains valid for igniting jets, and that the injection process controls the combustion. The width of the igniting jets is found to be larger, as a results of hot gas expansion. In Chapter 7, the validity of this finding in the case of late-ignition and when the gas jets are ignited by pilot fuel sprays is discussed. Support for the validity of the ignition and combustion model is presented in Chapter 6.

Practical design considerations that arise from the findings are discussed in Chapters 5 and 7, and summarized in the conclusions.

CHAPTER 2

TURBULENT GAS JETS

2.1 INTRODUCTION

As the injector is actuated, natural gas is injected through the nozzles and forms jets which propagate across the combustion chamber. Photographic evidence of impulsively started jets, such as those of Batchelor [1967] (see also Van Dyke [1988]), shows that a vortex head is formed and propagates away from the nozzle, as depicted schematically in Fig. 2.1. In a so-called puff jet, the vortex head contains all of the injected fluid. In a transient jet, a quasi-steady

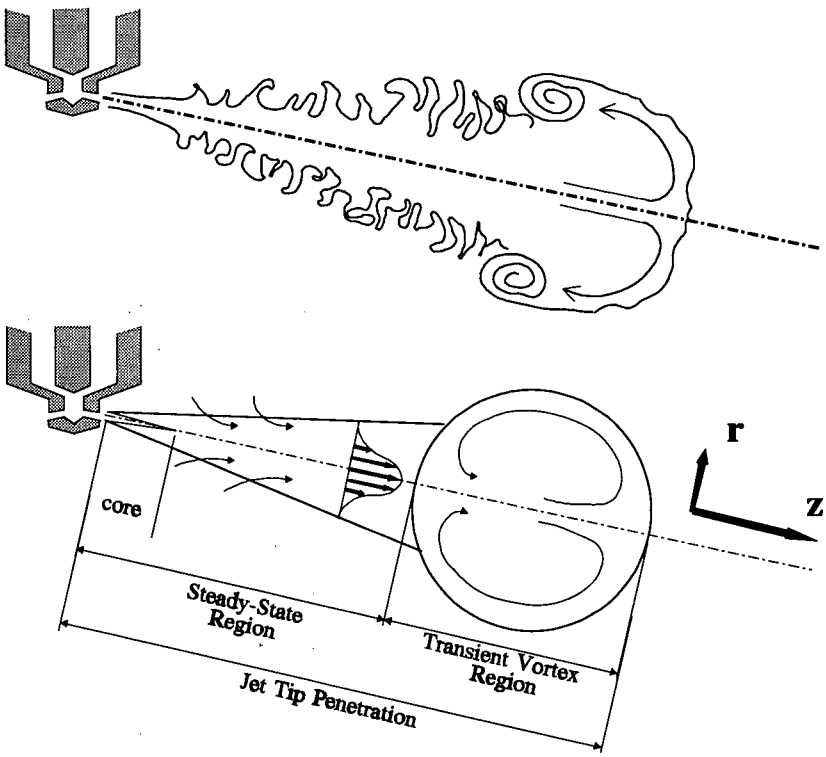

Figure 2.1 - Turbulent transient jet structure and model.

jet is formed behind the vortex head. Flow visualization of transient methane jets reported in Chepakovich [1993] indicates that, for engine application, the jets are of the latter type. The time dependency of the jet tip penetration (see Fig. 2.1 for definition) can be used to determine the type of jet. In the case of transient jets issued from round nozzles, the total momentum of the vortex head can be taken as a fraction of the total momentum injected:

$$\dot{M}_n t = k_1 \rho \pi R^3 V \tag{2.1}$$

where $\dot{M}_n$ is the momentum rate at the nozzle, k_1 a proportionality constant, and ρ, R and V the average density, radius and velocity of the vortex head. The vortex head concept can be seen in Fig. 2.1. From the transient jet visualization performed in Miyake *et al* [1983], it can be seen that the radius R of the vortex head is a constant fraction of the distance from the nozzle z_t:

$$R = k_2 z_t \tag{2.2}$$

where k_2 is approximately 0.28. The velocity of the vortex head can be written as:

$$V = k_3 \frac{dz_t}{dt} \tag{2.3}$$

where k_3 is a proportionality constant of the order of 1, and z_t is the distance of the vortex head front from the nozzle. Substituting these into Eq. 2.1 and integrating:

$$z_t \propto t^{1/2} \tag{2.4}$$

For puff-type jets, all the injected momentum M_o is contained in the vortex head, such that instead of Eq. 2.1 we have:

$$M_o \propto \rho \pi R^3 V \tag{2.5}$$

and upon integration, one obtains that

$$z_t \propto t^{1/4} \tag{2.6}$$

Figure 2.2 shows the penetration rate of gaseous jets as a function of the square-root of time. The graph is taken from the flow visualization studies of injected methane in a pressurized

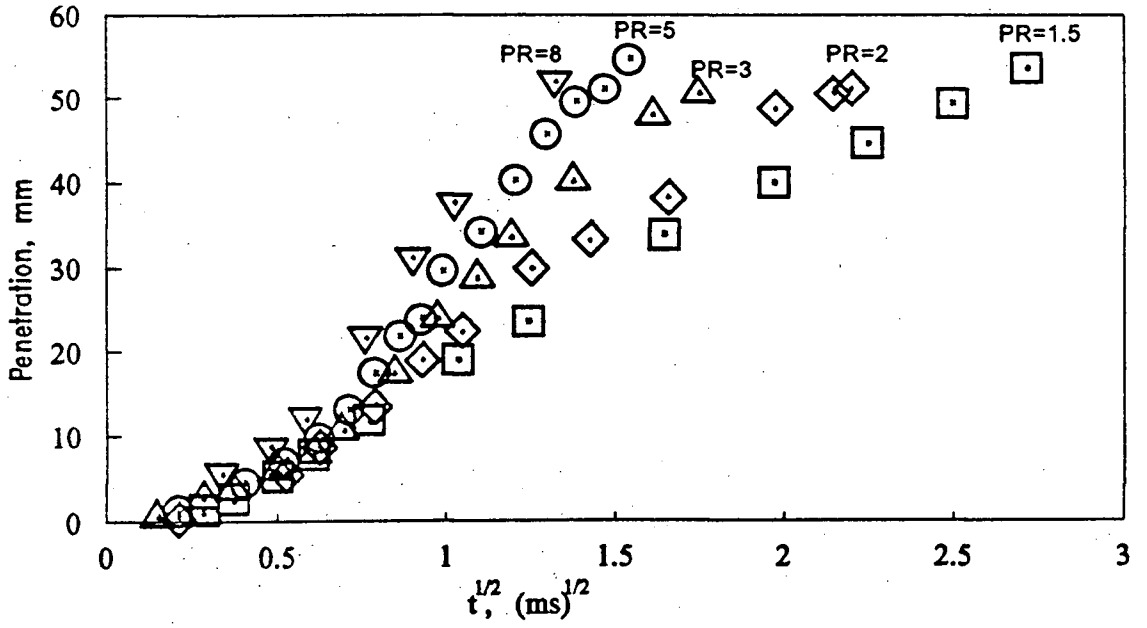

Figure 2.2 - Square-root of time dependency of gaseous jets for engine application. From Chepakovich [1993]. *PR* is the pressure ratio.

chamber in Chepakovich [1993]. The square-root-of-time dependency is present after a short development period. This confirms that jets under consideration here are of the transient type and not of the puff type. Transient sprays of diesel engines have also been found to respect largely the square-root-of-time dependency [Heywood 1988]. Puff jets have been reported for example by Solomon [1988] who investigated experimentally the penetration of plasma jets for ignition applications. The penetration of these jets was observed to follow the $t^{1/4}$ dependency.

Figure 2.1 shows a schematic representation of a transient turbulent jet and an integral model of the transient jet. The model was proposed by Turner [1962] for plumes, extended to

impulsively started laminar jets by Abramovich and Solan [1973] and to incompressible turbulent transient jets by Witze [1980]. The penetration rate predicted by the model compared favorably with experimental data, and is discussed in Section 2.3.1, as it contributes to an understanding of transient jets. Behind the vortex head, the jet can be considered steady. The steady part of the jet feeds mass and momentum to the vortex head, such that its mass, momentum and size increase. The vortex head travels according to its own momentum, being slowed down by frictional forces and by the need to accelerate the surrounding fluid. The presence of the steady-state jet behind the vortex head is significant because there is considerable knowledge of steady-state jets, which is useful in our understanding of transient jets. Steady-state jet knowledge is accordingly reviewed in the next section.

In the introduction chapter, the natural gas jets for diesel engine fueling were found to be turbulent transient underexpanded jets, with a molecular weight difference between injected fluid and chamber air. The objective of this chapter is to provide a general description of such jets. Steady-state jets are first reviewed (Section 2.2) as their understanding is directly relevant to transient jets. Current knowledge of transient jets is examined in Section 2.3, with an identification of the dependencies of the penetration rate on injection and chamber conditions. Since multidimensional modelling has been used in this work, previous modelling efforts of transient jets are discussed in Section 2.4. The emphasis of this work was on gaseous jets; however, in view of the large amount of studies performed on sprays, it is of interest to review briefly the differences and similitude between gaseous jets and sprays. Such a review is presented in the last section of this chapter.

2.2 STEADY-STATE JETS

2.2.1 Incompressible Jets of Uniform Density

When the maximum Mach number found in the jet is below approximately 0.3, compressibility effects are negligible. Incompressible steady-state jets have been studied extensively (Ricou and Spalding [1961], Abramovich [1963], Witze [1980]). As one fluid is injected at a certain velocity in another fluid whose pressure field is uniform, a mixing layer develops between the injected fluid and the surrounding gas. Mass from the surrounding fluid is entrained in the injected fluid. For incompressible air jets issued from round nozzles into stagnant air, the rate of entrainment is found to be proportional to the distance from the nozzle and to the mass injection rate (Ricou and Spalding). The mass flow rate $\dot{m}$ at a cross-section of the jet is found to be

$$\frac{\dot{m}}{\dot{m}_n} = 0.32\frac{z}{d_n} \tag{2.7}$$

where $\dot{m}_n$ is the mass flow rate at the nozzle, z the distance from the nozzle and d_n the nozzle diameter. The relationship was verified experimentally by direct measurement of the mass entrainment rate, from which the constant of 0.32 was obtained. The mass entrainment rate was found to be independent of the nozzle Reynolds number for Reynolds number greater than $3x10^4$.

The turbulent steady-state jet can be divided into three regions: a central core, a transition region and a fully-developed region. In the central core, there is a region where the velocity is uniform because the mixing has not yet taken place. In the fully-developed region, the velocity profile is said to be self-similar. Similarity is a well-observed feature of turbulent jets, and denotes that non-dimensional velocity profiles are independent of the distance from the nozzle: where $U(r,z)$ is the velocity at a distance z from the nozzle and at a normal distance r from the jet axis, U_{CL} is the centerline velocity at z, and R is the radial extent of the jet at z. Typically,

$$\frac{U(r,z)}{U_{CL}(z)} = f(\eta) \qquad \eta = \frac{r}{R} \tag{2.8}$$

the fully-developed region starts at a distance of 10 to 20 diameters from the nozzle.

From momentum conservation considerations, and from experimental knowledge, the center-line velocity decay in the jet can be obtained as a function of the distance from the nozzle. For round jets, the velocity on the axis of the jet is found to be proportional to *1/z*. The centerline velocity can be scaled by using the nozzle velocity. For example the centerline velocity decay of a round jet can be expressed by

$$\frac{U_{CL}}{U_n} = \frac{k_d}{(z/d_n)} \tag{2.9}$$

where k_d from a variety of studies is approximately 5. (Witze [1980]- 5.56 for 0<z/d<100, Wignanski and Fiedler [1969] - 5.05 for 15<z/d<100). Equations 2.8 and 2.9 provide a complete description of the velocity in the fully-developed part of turbulent jets. Similar equations can be formulated for other types of jets and for other profiles (temperature, concentration). To account for the region where the velocity profile is still influenced by the nozzle velocity profile, one must replace z by a distance from a virtual origin located behind the real nozzle location.

2.2.2 Incompressible Jets of Different Densities

When gases of different densities are injected into air, the entrainment rate of the chamber air is different than when air is injected. The difference in density may be a result of different molecular weights or of different temperature, or both. The axial velocity decay in this case is different. The similarity of profiles in the jet is still preserved at some distance from the nozzle. It is confirmed experimentally (see for example Ricou and Spalding) that jets of different densities can be scaled when an equivalent diameter is used:

$$d_{eq}=d_n\left(\frac{\rho_g}{\rho_{ch}}\right)^{1/2} \tag{2.10}$$

where ρ_g and ρ_{ch} are the injected fluid and chamber or surrounding fluid densities, taken at the same pressure. This modification is directly obtainable from momentum conservation and similarity arguments. This new length scale is also readily applicable to scale injected fluids which differ in temperature from the chamber fluid. For example, hot air jets can be scaled with Eq. 2.10 with ρ_g being the density of air at the injection temperature and at the chamber pressure. Ricou and Spalding confirmed experimentally the equivalent diameter concept by showing that the mass entrainment $\dot{m}$ rate in the jet could be given by

$$\frac{\dot{m}}{\dot{m}_n} = 0.32\frac{z}{d_n(\rho_g/\rho_{ch})^{1/2}} \tag{2.11}$$

Similarly, the velocity decay of Eq. 2.9 can be expressed in terms of the equivalent diameter of Eq. 2.10. Birch *et al* [1978] reports a decay constant k_d of 5.01 for the velocity decay of a methane jet in air, which compares favorably with the constant obtained by Wignanski and Fiedler for uniform density jets.

2.2.3 Correctly Expanded Jets

As the pressure ratio across the nozzle is increased above one, the velocity at the nozzle increases. As the Mach number increases above 0.3, compressibility effects occur in the nozzle region and must be considered in establishing nozzle exit conditions. The similarity of jets still exists in the fully developed region where the local Mach numbers are low, but the effect of compressibility on the nozzle density and velocity must be incorporated in the scaling. A logical modification to the equivalent diameter proposed in the previous section can be written as

$$d_{eq} = d_n\left(\frac{\rho_n}{\rho_{ch}}\right)^{1/2} \qquad (2.12)$$

where ρ_n is the nozzle exit density.

The nozzle density ρ_n includes the density change encountered when injecting a gas of different density. Consequently, the equivalent diameter of Eq. 2.12 replaces that of Eq. 2.10 when compressible jets are considered.

2.2.4 Underexpanded Jets

When the upstream to chamber pressure ratio is greater than approximately 1.85 (for methane, assuming perfect gas behavior), the exit plane pressure of a constant area duct with friction or of a converging nozzle becomes higher than the chamber pressure, and underexpansion occurs outside the nozzle. Underexpansion is a complex adjustment process involving expansion waves and compression waves which form a barrel-shaped shock pattern. Figure 2.3 shows a schematic of the expansion process outside the nozzle. Ewan and Moodie [1986] and Birch, Brown, Dodson and Swaffield [1984] proposed a pseudo-diameter model which permits retention of classical jet analysis for underexpanded jets. The pseudo-diameter correction was found to scale well the experimental data of these authors for steady-state jets with pressure ratios as high as 30.

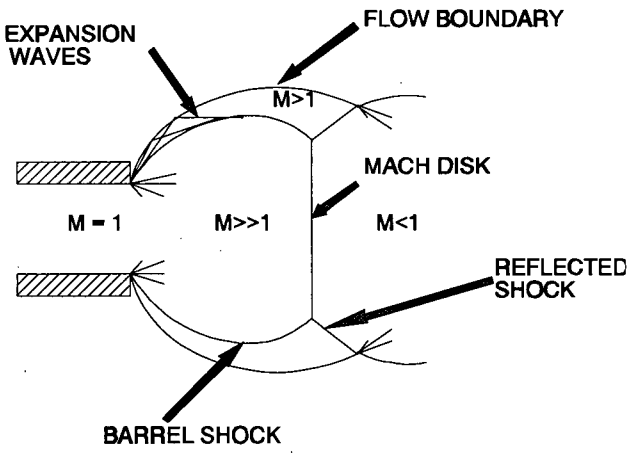

Figure 2.3 Schematic of underexpansion process.

Figure 2.4 shows the pseudo-diameter concept used in the following analysis. Based on

the assumption that no mixing takes place in the underexpansion adjustment region, mass conservation is used to provide an equivalent diameter:

$$\frac{A_{ps}}{A_n} = \frac{C_d \rho_n U_n}{\rho_{ps} U_{ps}} \qquad (2.13)$$

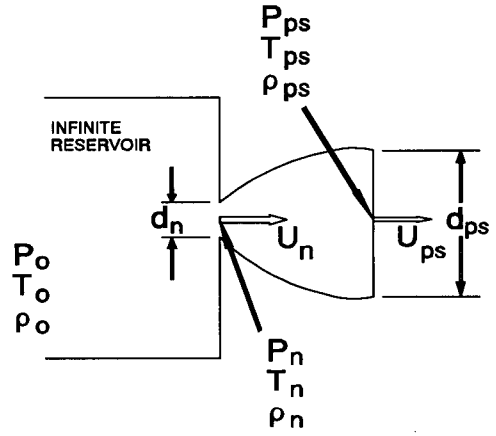

Figure 2.4 Pseudo-diameter concept for underexpansion model.

where the subscript *ps* and *n* refer respectively to conditions at the pseudo-diameter exit plane and at the nozzle, and where C_d is a discharge coefficient. The nozzle conditions can be calculated from one-dimensional flow, which can include frictional effects and real gas behavior. As the nozzle is choked, the nozzle Mach number M_n is unity. Pseudo-diameter conditions were obtained by Ewan and Moodie and Birch *et al* by assuming that M_{ps} is unity at the pseudo-diameter. Ewan and Moodie further assumed that the post-shock temperature was the same as the nozzle exit temperature. The same result is obtained by assuming instead that the stagnation temperature is constant over the expansion region. This assumption appears more warranted since mass is already conserved under the no-mixing assumption. Both assumptions lead to the same result since the Mach number is unity at both real and pseudo-diameters. The density at the equivalent exit plane is given at the temperature prescribed from the unity Mach number and from the exit plane pressure which must be the chamber pressure. If perfect gas law is assumed, and based on the above assumptions, the velocities U_n and U_{ps} are the same, and the pseudo-diameter becomes

$$\frac{d_{ps}}{d_n} = \sqrt{C_d \left(\frac{\rho_n}{\rho_{ps}}\right)} \qquad (2.14)$$

In Ewan and Moodie, and Birch *et al*, the nozzle density is obtained from the upstream conditions assuming perfect gas law and isentropic one-dimensional flow through a choked nozzle:

$$\rho_n = \frac{\rho_o}{\left[1+\frac{\gamma-1}{2}\right]^{1/(\gamma-1)}} = \frac{P_o}{RT_o}\left[\frac{2}{\gamma+1}\right]^{1/(\gamma-1)} \tag{2.15}$$

The pseudo-diameter density is

$$\rho_{ps} = \frac{P_{ch}}{RT_{ps}} = \frac{P_{ch}}{RT_o}\left(\frac{\gamma+1}{2}\right) \tag{2.16}$$

where the assumption of constant stagnation temperature has been used. Substituting Eqs. 2.15 and 2.16 into Eq. 2.14:

$$\frac{d_{ps}}{d_n} = \sqrt{C_d \left(\frac{2}{\gamma+1}\right)^{\gamma/(\gamma-1)} \left(\frac{P_o}{P_{ch}}\right)} \tag{2.17}$$

With a ratio of specific heat of 1.3, Eq. 2.17 reduces to

$$\frac{d_{ps}}{d_n} = \sqrt{0.546\ C_d \left(\frac{P_o}{P_{ch}}\right)} \tag{2.18}$$

which is valid under the assumption of perfect gas law and isentropic expansion between upstream conditions and nozzle conditions. Assuming a ratio of specific heat of 1.35, a constant of 0.537 was obtained by Ewan and Moodie. Birch *et al* [1984] obtained a constant of 0.582 by assuming that the post-shock temperature was the same as the upstream temperature.

Both Ewan and Moodie and Birch *et al* confirmed that the experimental data could be scaled well using the pseudo-diameter instead of the nozzle diameter.

Ewan and Moodie included the correction of Eq. 2.12 for compressibility effects in the

length scale, replacing ρ_n by ρ_{ps}. The equivalent diameter used was then of the form:

$$d_{eq} = d_n\left(\frac{\rho_{ps}}{\rho_{ch}}\right)^{1/2}\left(0.537 C_d \frac{P_o}{P_{ch}}\right)^{1/2} \tag{2.19}$$

where the first nozzle diameter modifier takes into consideration effects of compressibility and of gas injected with different densities, and the second modifier takes into account the underexpansion.

Although the analysis is valid, a simplification that relates these results directly to the ones stated in Sections 2.2.1 to 2.2.3 appears possible here. If, instead of using the pseudo-diameter derived for perfect gas law, the equivalent area of Eq. 2.13 is used, which derives directly from the pseudo-diameter assumptions, then Eq. 2.19 can be written as:

$$d_{eq} = C_d^{1/2} d_n\left(\frac{\rho_{ps}}{\rho_{ch}}\right)^{1/2}\left(\frac{\rho_n}{\rho_{ps}}\right)^{1/2}\left(\frac{U_n}{U_{ps}}\right)^{1/2} \tag{2.20}$$

which, incorporating the discharge coefficient in the nozzle diameter, further simplifies to

$$d_{eq} = d_n\left(\frac{\rho_n}{\rho_{ch}}\right)^{1/2}\left(\frac{U_n}{U_{ps}}\right)^{1/2} \tag{2.21}$$

When perfect gas law behavior is considered at the nozzle, the velocities U_n and U_{ps} are equal, which permits one to write for underexpanded jets:

$$d_{eq} = d_n\left(\frac{\rho_n}{\rho_{ch}}\right)^{1/2} \tag{2.22}$$

which is the same as the equivalent diameter proposed in Eq. 2.12 for compressible jets. Equation 2.22 is interesting since it suggests that whether correctly expanded jets or underexpanded jets are considered, the equivalent diameter $d_{eq}=d_n(\rho_n/\rho_{ch})^{1/2}$ is the appropriate length scale. Furthermore, as ρ_n/ρ_{ch} is equal to ρ_g/ρ_{ch} when considering incompressible jets of different densities, the equivalent diameter of Eq. 2.22 should be applicable to all turbulent jets

issued from converging round nozzles.

If the equivalent diameter is truly a universal length scale, it should correlate jets with different nozzle conditions. For example, a single constant should correlate the centerline velocity decay when the equivalent diameter is used. Alternatively, as done in Birch *et al* [1978] and Birch *et al* [1984], the axial concentration delay should be universally expressed as

$$\frac{C_m}{C_n} = \frac{k_d}{(z+a)/d_{eq}} \tag{2.23}$$

where C_m is the axial concentration, C_n the nozzle concentration, and a a correction for the virtual origin of the jet. In Birch *et al* [1984], a constant k_d of 4.9 was found to correlate well both underexpanded jets and subsonic jets. In Birch *et al* [1978], where incompressible methane jets are considered, the proposed constant was to be 4.7 for 10<d<30, but was closer to 4 in the far field. The 1984 paper also reports the scatter of universal constant values in the literature. This is not surprising, particularly for high-pressure jets, where the scaling requires the knowledge of the nozzle density, velocity and of the discharge coefficient, for near-sonic jets with potentially significant deviation from perfect gas law behavior. Moreover, the experimental measurements are complicated by the need to measure velocity or concentration over a very wide range because of the asymptotic decay. The important conclusion is that the physical significance of the equivalent diameter is supported within experimental errors by various investigations.

It should be noted that when real gas behavior is considered in the nozzle area, as is done in this thesis, Eq. 2.21 can be used directly to determine the equivalent diameter. Also, when replacing the real nozzle by an equivalent one, the length of the expansion region (barrel) may need to be considered in establishing distances from the nozzle. Ewan and Moodie report the barrel length as a function of pressure ratio. According to those data, the barrel length over a

pressure ratio range between 2 and 5 is approximately one diameter, and will be consequently neglected in this thesis.

2.3 TRANSIENT JETS

The modelling of a transient jet as a travelling vortex head fed by a quasi-steady state jet (such as presented in Fig. 2.1) provides a simple physical understanding of transient jets and also shows the connection existing between steady and transient jets. For that reason, such models are briefly reviewed. Experimental knowledge of transient jets and discussion about their similarity is then discussed.

2.3.1 Integral Models

Following observation of starting buoyant plumes, Turner [1962] suggested that they could be modelled by a quasi-steady plume feeding a moving cap. Using a mass and momentum balance, he showed that the proposed model was consistent with experimental observations. Abramovich and Solan [1973] studied the initial development of impulsively started laminar round jets. Experimental measurements showed a dependency of the tip penetration on the square-root of time after an initial development period. The vortex head was found to travel at about half the velocity of the corresponding location steady-state velocity. Following the model proposed by Turner, the starting laminar jet was modelled as a quasi-steady jet feeding mass and momentum to a vortex head. The vortex head momentum is reduced by a drag force and by the need to accelerate the surrounding fluid. It was also assumed that no mixing with the surrounding air takes place on the vortex head, and the internal structure was neglected. The model prediction of tip penetration and velocity compared favorably with experimental data.

Witze [1980] performed some hot-wire measurements of the center-line velocity in an

impulsively started turbulent air jet. The nozzle velocities were 53 and 103.5 m/s, such that the jet was considered incompressible. The Reynolds numbers were 6360 and 12420. Results showed that steady-state values of the jet center-line velocity are reached very shortly after the arrival of the vortex head. The steady-state values reached were also found to be in agreement with steady-state jet theory for the center-line velocity decay with distance from the nozzle.

With the assumption of quasi-steady state validated by experimental measurements, at least at the jet center-line, Witze extended the analysis of Abramovich and Solan [1973] to transient incompressible turbulent jets issued from round nozzles. Again, the transient jet was modelled as a quasi-steady jet feeding a vortex head moving away from the nozzle. The same assumptions of uniform properties within the vortex head and of entrainment at the surface of the head vortex were applied. Despite these assumptions, Witze obtained very good agreement between experimental data and model prediction.

The work of Abramovitch and Solan, and that of Witze, are significant in that they bring a physical description of transient jets consistent with experimental observations. The model can be readily used to understand the effects of nozzle and chamber conditions on the jet propagation. The momentum of the head vortex is increased by influx from the quasi-steady jet and slowed down by the surrounding fluid. The momentum influx depends on the density and velocity at the plane between the quasi-steady jet and the head vortex. As momentum is conserved throughout the quasi-steady jet, a larger momentum at the nozzle will also provide a higher momentum to the head vortex. This means that higher nozzle exit density, higher velocity and larger nozzle diameter each favor higher penetration rate. On the other hand, higher density of the surrounding air will tend to slow down the jet, as a result of increased drag.

The presence of steady-state conditions behind the vortex head is of particular interest since all knowledge of steady-state jets then becomes directly relevant to transient jets. For

example the treatment of the underexpansion model discussed in Section 2.2.4 is relevant now to transient jets and provides some understanding of the consequence of underexpansion on jet penetration. As the injection pressure is increased such that the pressure ratio is greater than critical, the nozzle remains choked, with sonic velocity at the nozzle, but the density of the fluid at the nozzle increases. The net effect is still to increase the nozzle momentum. If the injection pressure is maintained constant but the chamber pressure decreases with an associated density decrease, then there is less resistance to the jet propagation and the penetration also increases.

The presence of the quasi-steady jet behind the vortex head is even more significant because it invites consideration of the similarity of transient jets. Since steady-state jets are self-similar, and since steady jets drive transient jets, it appears a reasonable hypothesis that transient jets are themselves similar. The equivalent diameter of Eq. 2.22 was identified as a general length scale for turbulent compressible jets, and could presumably scale transient jet characteristic dimensions. For transient jets a time scale is also needed, and can be constructed by using the ratio of equivalent diameter to nozzle velocity d_{eq}/U_n.

The similarity of transient jets and their scaling is now discussed in light of experimental data available in the literature.

2.3.2 Jet Penetration Measurements and Scaling

Witze measured the penetration of transient air jets issued from a 1.2 mm diameter nozzle, with velocities of 53 and 103 m/s, such that the jets can be classified as incompressible. The Reynolds number are respectively 6360 and 12420, which is above the transition to turbulent flow but below the $3x10^4$ level at which Reynolds number dependency becomes negligible. The measurements were performed with hot wire anenometry, such that the penetration time was obtained, somewhat arbitrarily, by measuring the time at which 70% of the steady-state velocity

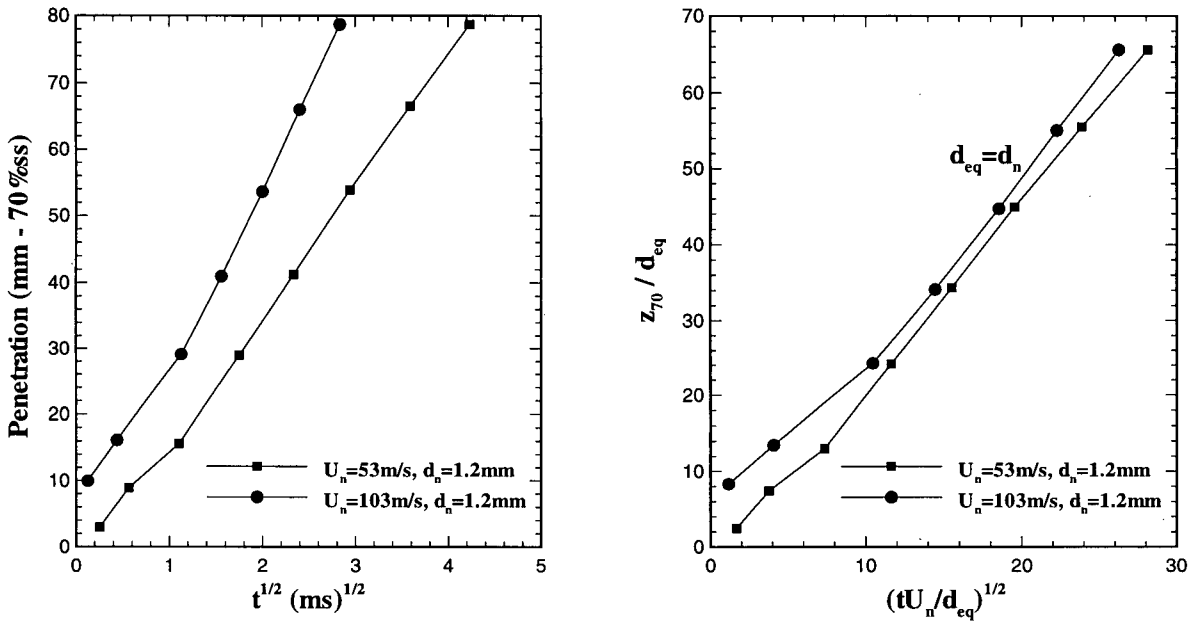

Figure 2.5 - Incompressible turbulent air jet penetration (70% of steady-state velocity) as a function of the square-root of time, Witze [1980]. Left:raw data, right:scaled data.

was reached at a given location. The data are presented in Fig. 2.5, with the raw data plotted as a function of the square-root of time on the left graph. The quadratic nature of the jet penetration is found to be valid away from the near-field area (at a distance of 15 to 20 diameters), where there is a transition between the velocity profile of the nozzle flow and the velocity profile characteristic of turbulent jets. For incompressible jets of air in air, the equivalent diameter becomes $d_{eq}=d_n$, and this length scale is used to non-dimensionalize the penetration on the right graph of Fig. 2.5. The scaling shows that the slopes are much the same, but the curves do not collapse perfectly. Kuo and Bracco [1982] suggested that the discrepancy is due to the Reynolds number dependency[1].

Miyake *et al* [1983] measured optically the penetration rate of sonic methane jets issued

[1] They proposed that a length scale of the form $d_{eq}=d_n Re^{0.053}$ be used. This Reynolds number dependency was obtained from their numerical simulation results and scales Witze data somewhat better, but it is not a general dependency as it does not disappear at high Reynolds number.

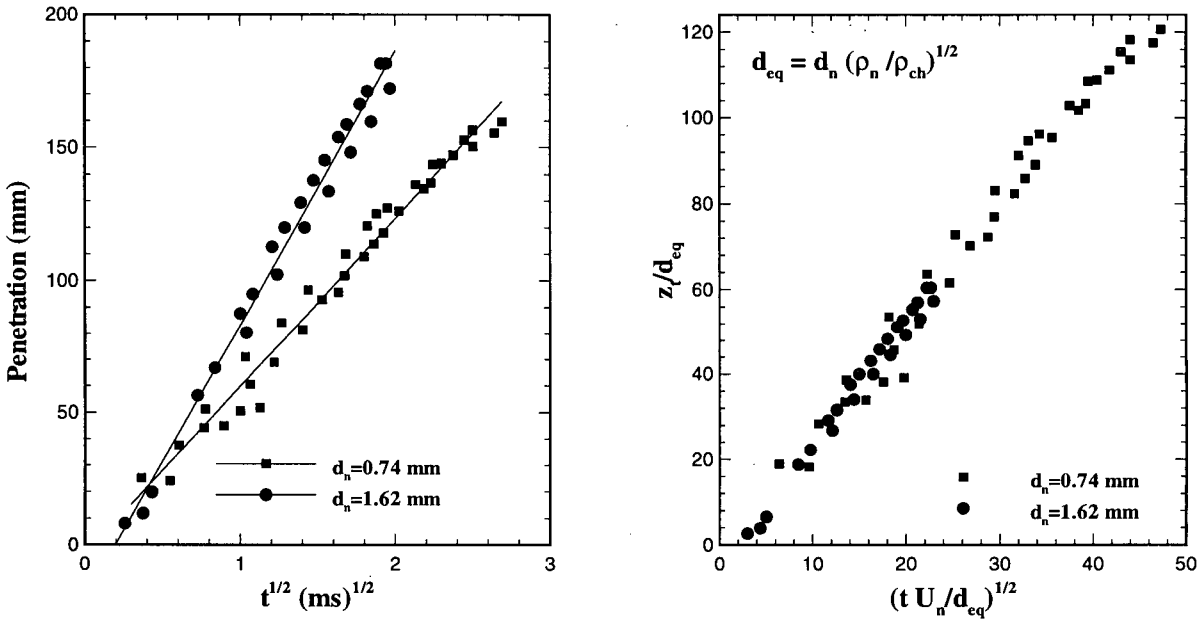

Figure 2.6 - Penetration rate and non-dimensional penetration rate of methane jets issued from different nozzle diameters (Miyake [1983]). U_n = 409 m/s, ρ_n/ρ_{ch}=3.2.

from nozzles of different diameters. The scaled data are presented in Fig. 2.6. It is seen that the scaling is very good.

Chepakovich [1993] measured visually the penetration rate of underexpanded methane jets. He varied the pressure ratio, such that the nozzle density increased. His data are scaled with the equivalent diameter of Eq. 2.22 in Fig. 2.7. The data collapse near a single curve in the region of $20<z_t/d_{eq}<100$, with however more scattering. The jets observed by Chepakovich propagated near a wall, which explains the visible change of slope at z_t/d_{eq} equal to 100. Furthermore it should be emphasized that the nozzle conditions were evaluated assuming ideal gas conditions in the nozzle, which may also account for some of the scatter considering that real gas behavior may be significant at the pressure levels used by Chepakovich (upstream pressures

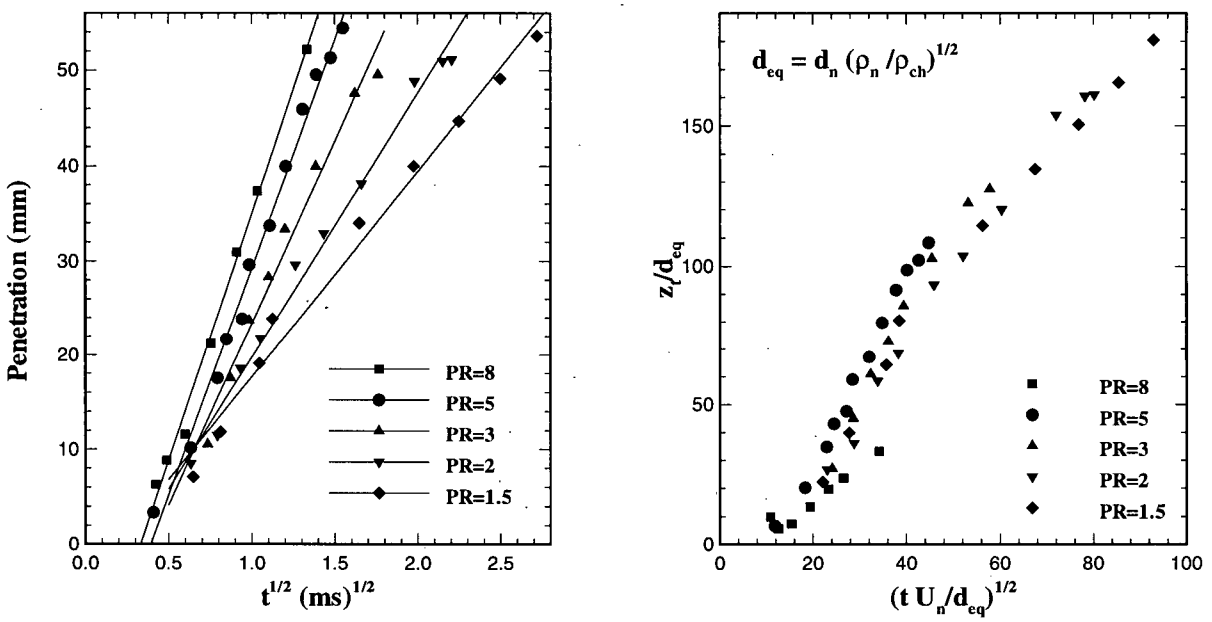

Figure 2.7 - Penetration and non-dimensional penetration of underexpanded and correctly expanded methane jets (Chepakovich [1993]). *PR* is the pressure ratio.

were up to 11 MPa at room temperature)[2].

Each experimental study reported supports the validity of the equivalent diameter as a similarity length scale for transient jets. Further confidence and insight is gained by verifying that the slope of the z_t^* (z_t / d_{eq}) vs $t^{*1/2}$ ($[tU_n / d_{eq}]^{1/2}$) curves are the same for the three reported studies. The non-dimensional data of Miyake have a slope of 2.77. The data of Chepakovich have a slope of 3.0 over $30<z/d_{eq}<100$. In the case of Witze, the penetration is defined differently and may have a Reynolds number dependency, such that it is difficult to compare with the two other cases. According to the computations of Kuo and Bracco [1982], the penetration z_{70}, based on the achievement of 70% of the steady-state velocity, corresponds roughly to the

[2] It is appropriate to state that the scaling problem is not trivial, as it requires reasonably accurate knowledge of the nozzle conditions. However, measurements of the velocity and of its profile in the region of the nozzle are not practical for sonic jets of small dimensions. To further complicate the matter, the time scales are short and there is a transient injector response which may be dependent on the pressure ratio. Furthermore, deviation from perfect gas law may be significant, and some estimate of friction or of a discharge coefficient is needed.

penetration of the vortex center. The vortex diameter D is a constant fraction of the jet penetration z_t, and based on the photographs in Miyake *et al*, the ratio of D/z_t is approximately 0.28. Since z_t is equal to $z_{70} + D/2$, it is found that z_t/z_{70} is approximately 1.16. The slope in Fig. 2.5 is 2.6, which translates into a slope of 3.0 for the actual tip penetration.

In summary, the length scale $d_{eq}=d_n(\rho_n/\rho_{ch})^{1/2}$ and the time scale d_{eq}/U_n are valid similarity scales for transient turbulent jets, and the penetration can be expressed as:

$$z_t^* = C_c + C_t(t^*)^{1/2} \tag{2.24}$$

where C_t has a value of approximately 2.9. The constant C_c is not universal as it depends on the injector transient characteristics (i.e. opening time) and on the velocity profile at the nozzle. It may be removed by defining a virtual origin a such that $z_t'=z_t + a$. Equation 2.24 is typically valid for z_t/d_{eq} greater than 20.

Although Eq. 2.24 is simple, a more fundamental expression for the jet tip penetration emerges as the equivalent diameter and the length scale are replaced in Eq. 2.24:

$$z_t' = C_t \left(d_n\left(\frac{\rho_n}{\rho_{ch}}\right)^{1/2} U_n\right)^{1/2} t^{1/2} \tag{2.25}$$

$$z_t' = C_t\left(\frac{4}{\pi}\right)^{1/4} \left(\frac{\dot{M}_n}{\rho_{ch}}\right)^{1/4} t^{1/2} \tag{2.26}$$

where $\dot{M}_n$ is the momentum injection rate at the nozzle. When incorporating the small modification to the constant C_t=2.9 obtained above, the tip penetration of transient turbulent jets is expressed as

$$z_t' = 3.08 \left(\frac{\dot{M}_n}{\rho_{ch}}\right)^{1/4} t^{1/2} \tag{2.27}$$

which is valid for incompressible jets, compressible jets (underexpanded or not), jets of different densities (because of molecular weights difference and/or temperature difference), for Reynolds number above $3x10^4$ and for distances greater than approximately 20 d_{eq}. It is also significant that other classes of jets can be expressed in the same way. The penetration of a turbulent conical sheet jet reported in Ouellette and Hill [1992] can be written as in Eq. 2.27, but with a different constant ($C_t \approx 1.14$). Puff jets travelling have been reported as $z_t = C(M_o t/\rho_{ch})^{1/4}$, where M_o is the total injected momentum (Richards [1965]). Furthermore, even some correlations for the tip penetration of liquid sprays can be expressed in the same form as Eq. 2.27, as will be discussed in Section 2.5.

The results of Eqs. 2.24 and 2.27 are further substantiated by a formal dimensional analysis which, for free transient turbulent jets issued from round nozzles in a large chamber, leads to (see appendix B):

$$\frac{z_t}{d_n(\frac{\rho_n}{\rho_{ch}})^{1/2}} = f[\frac{tU_n}{d_n(\frac{\rho_n}{\rho_{ch}})^{1/2}}, \frac{t}{t_{inj}}, \frac{\sqrt{k}}{U_n}] \qquad \textbf{(2.28)}$$

where t_{inj} is the injection duration, and k the turbulent kinetic energy per unit mass in the chamber. For times t less than t_{inj}, and for turbulence free chamber conditions, Eq. 2.28 indicates that the penetration rate is solely dependent on the nozzle velocity and on the equivalent diameter $d_n(\rho_n/\rho_{ch})^{1/2}$, supporting Eq. 2.24. The dimensional analysis highlights the fact that when the injection is of finite duration, as it is in engines, the penetration rate should change. Similarly if high turbulence levels are present in the chamber, the mixing and penetration may change, as discussed in Chapter 5.

2.3.3 Mixing Rate

So far the tip penetration has been discussed as a main characteristic of transient jets. In engines, the mixing rate of the injected fuel with the air is also important as it affects the combustion rate. Presumably, the mixing rate is directly related to the penetration rate. This relationship is briefly discussed here with further comments in Chapter 5.

Mixing rates of transient jets do not appear to have been experimentally studied. However, the already quoted measurements of Ricou and Spalding [1961] provide an excellent measure of mixing rate for steady-state jets. Their main result can be expressed as:

$$\frac{d\dot{m}_{ch}}{dz} = 0.282\ (\dot{M}_n \rho_{ch})^{1/2} \qquad \textbf{(2.29)}$$

which states that the rate of change of entrainment rate $\dot{m}_{ch}$ in the jet is proportional to the square-root of nozzle momentum injection rate and of the chamber air density. Now for a transient jet, the mass of chamber air contained in the jet at any time can be obtained by integrating over the jet extent and over time. As an approximation, the extent of the jet at time t is taken as z_t. One obtains for the mass of chamber air m_{ch} in the penetrating jet:

$$m_{ch} \approx \frac{1}{2}\dot{M}_n^{3/4}\rho_{ch}^{1/4}\ t^{3/2} \qquad \textbf{(2.30)}$$

which incorporates Eq. 2.27. Equation 2.30 states that the mixing, represented by the quantity of air entrained in the transient jet, is increased by an increase in momentum injection rate but also by an increase in chamber density. This is significant because it shows that for a fixed momentum injection rate, increasing the chamber density decreases the penetration, but increases the mixing. By extracting the mass injected from Eq. 2.30, the following result can be obtained: which indicates that the length and time scale identified for the penetration rate of jets should apply directly to the mixing rate. Equation 2.31 can also be written as:

$$\frac{m_{ch}}{m_{inj}} \approx \frac{1}{2}\frac{z_t}{d_{eq}} = \frac{1}{2}\left(\frac{tU_n}{d_{eq}}\right)^{1/2} \tag{2.31}$$

$$m_{ch} \propto z_t^3 \, \rho_{ch} \tag{2.32}$$

which simply states that the mass of entrained air in the jet can be perceived as the volume occupied by the transient jet times the density, which is, far enough from the nozzle, essentially that of the chamber air.

2.4 NUMERICAL SIMULATION OF TURBULENT FREE JETS

The capability of multidimensional models to reproduce the transient jet tip penetration dependency identified above is now discussed. Steady-state numerical modelling is first discussed.

2.4.1 Steady-State Jets

Malin [1989] and Hanjalic and Laundner [1980], among others, report that the k-ε turbulent model leads to an over-estimation of the spreading rate (jet half-width / distance from nozzle) of steady-state turbulent jets. For round free jets of air into air, the turbulence model is reported to predict a spreading rate of 0.11, while the accepted experimental value is 0.085-0.09. The k-ε model used in this thesis is the standard one corrected only for compression effects, and a low velocity injection test reaching steady-state values confirmed that the spreading rate was over-predicted at 0.1. The reason for the inaccuracy is related to the assumption of isotropy in modelling the turbulence. The assumption apparently does not stand for jets, in which normal strains differ from aligned strain.

Algebraic corrections have been proposed (Hanjalic and Laundner, Malin) for steady-state

turbulent jet modelling, but they require knowledge of the jet centerline location and conditions. This may be difficult to obtain in complex, varying volume geometries such as engine combustion chambers.

For transient jets, the travelling of the vortex head is dependent on the influx of momentum to the head vortex and to its own inertia (as highlighted by the quasi-steady/head vortex model discussed in Section 2.3.1). The inertial effects are not dependent on diffusion such that the solution inaccuracy for steady-state jets may not affect the transient jet to the same extent. The momentum influx to the vortex head is however affected by diffusion, and numerical modelling may result in penetration rates lower than those observed experimentally.

The sensitivity of the penetration rate to the quasi-steady jet spreading rate was investigated by Chepakovich [1993] using an integral model similar to that of Witze. Chepakovich considered the effect of a 50% increase or decrease in the turbulent Reynolds number ($Re_t = r_{1/2}U_{CL}/\nu_t$). The turbulent Reynolds number is a constant in jets and is directly related to the spreading rate ($r_{1/2} = C\ z/Re_t$). The 50% change in Re_t leads to a 30% change in penetration rate, a higher Re_t leading to a higher penetration. The inaccuracy in spreading rate reported for k-ε is approximately 20%, and corresponds to a 15% change in turbulent Reynolds number. If the change observed by Chepakovich is linear, this 15% change in Re_t would cause a 9% error in penetration rate.

Gaillard [1984], knowing the deficiency of the k-ε turbulence model, adjusted the model constants to reproduce better mass entrainment rate in steady-state jets. Using the optimized constants ($C_{\varepsilon 1}$=1.52 instead of 1.44, and $C_{\varepsilon 2}$=1.89 instead of 1.92 in the turbulent dissipation equation (F.14), the spreading rate of the simulated steady-state jet $r_{1/2}/z$ was found to be 0.08. Similarly, the mass entrainment rate of the simulated jet was found to follow the correlation of Eq. 2.7 (from exp. of Ricou and Spalding, with equivalent diameter), but with a constant of 0.27

instead of 0.32. It appears that the model uniformly caused an under-prediction of mass entrainment rate and spreading rate. The inaccuracy could be due to grid size or to the effect of confinement. There is insufficient literature support at the moment to change the original values of k-ε, and those values are kept in this thesis. The performance of k-ε in predicting transient jet penetration will be verified in this thesis by comparing computational results with existing data in the literature and with the flow visualization results of this thesis.

2.4.2 Transient Jets

Numerical solution of the Navier-Stokes equations have also been used to study the characteristics of transient jets. Kuo and Bracco [1982] modelled incompressible transient turbulent jets using k-ε. Their numerical results display the $t^{1/2}$ dependency of the jet penetration and also support similarity of transient jets by scaling their numerical results with an equivalent diameter and a time scale constructed from that equivalent diameter (as mentioned earlier, they included a Reynolds number dependency in their equivalent diameter formulation). They found that the tip penetration, defined as the time required to reach 70% of the center-line steady-state velocity at a given point, could be predicted as

$$z_t^* = 2.06\ t^{*0.5} \quad for\ z_t^* > 7 \tag{2.33}$$

where $z_t^* = z_t/(d_n\, Re^{0.053})$ and $t^* = tU_n/(d_n\, Re^{0.053})$. Because of the inclusion of the Reynolds number in their scaling, it is difficult to compare the value of the constant with that obtained in Section 2.3.2. Assuming a Reynolds number of 3×10^4, the constant corresponding to C_t of Eq. 2.24 would be 2.7 x 1.16 = 3.1, where the correction for the different definition of penetration is applied. This compares with a value of 2.9 obtained from the experimental investigations. This result at least confirms that multidimensional simulation using the k-ε turbulent model reproduces

the proper inertial travel of the head vortex, and a quite close agreement of the penetration distance. The good agreement may well indicate that the inertial momentum of the head vortex is dominant over viscous effects, such that the inaccuracy of k-ε is not as serious in considering the tip penetration of the vortex head as it is for the entrainment rate of steady jets.

It is also of interest that their numerical simulations indicated that a large fraction of steadiness was present at the back of the head vortex. According to numerical results, 99.9% of the steady-state center-line velocity and 85% of the steady-state momentum was reached behind the vortex head. This observation further substantiates the quasi-steady state assumption made in the above integral treatment of jets.

2.5 COMPARISONS OF GASEOUS JETS AND SPRAYS

There is much interest in knowing whether gaseous jets penetrate and mix with the same dependencies as sprays. Sprays have been the object of continuous research, as efforts were made to reduce emissions from diesel engines. Consequently, diesel engines operate on optimized injection conditions, and it may be that these conditions can be transposed with success to gaseous jets.

A first point of comparison is the penetration rate of sprays. Diesel engine researchers have used analogy to gas jets to establish the main dependency of spray penetration. In particular the following correlation has been proposed (from Hiroyasu in Heywood [1988]) to represent the tip penetration S of non-evaporating liquid sprays:

$$S = 2.95 \left(\frac{\Delta P}{\rho_{ch}}\right)^{1/4} (d_n t)^{1/2} \qquad \textbf{(2.34)}$$

which is valid after the spray break-up length, and where ΔP is the pressure drop across the

nozzle. Replacing the velocity at the nozzle, which is given by

$$U_n = (2\Delta P/\rho_l)^{1/2} \tag{2.35}$$

where ρ_l is the liquid density, Equation 2.34 leads to

$$S = 2.64 \left(\frac{\dot{M}_n}{\rho_{ch}}\right)^{1/4} t^{1/2} \tag{2.36}$$

which is identical to Eq. 2.27 for gaseous jets, except for a slightly different constant. Another correlation, that of Dent [1980] (also in Heywood) is also amenable to this form. These results indicate that under some conditions, sprays can behave much like gas jets, and that given equivalent momentum and chamber conditions, the penetration of gaseous jets and that of sprays may be quite similar.

Flow visualization of both sprays and gaseous jets performed by Miyake [1984] illustrates this point. His photographs show that when injected with the same momentum rate, gaseous jets and non-evaporating sprays have visually a similar spreading angle and very similar penetration rate.

Kuo and Bracco [1982] reviewed the difference between turbulent jets and sprays. They note from observation of flow visualization that both transient sprays and jets have a stem and a vortex head that scale in time in similar fashion. However they also point to a major difference between sprays and jets; whereas jets have little dependency on the geometry of the nozzle, sprays are very dependent on the nozzle geometry, as evidenced by a wealth of experimental observations (Heywood [1988]). In particular, the angle of spread of sprays is found to be dependent on the density ratio between the liquid and the chamber, and on the length-to-diameter (*L/d*) ratio of the nozzles. Typically, the spray cone angle is reduced by an increasing liquid-to-

air density ratio and by an increasing *L/d* ratio. The reason for the nozzle influence is that the initial spreading of the liquid spray is an aerodynamic phenomenon, at least near the nozzle, whereas the spreading angle of jets is a shear-induced mass transfer.

The nozzle geometry dependency of sprays is not included in the correlation proposed in Eq. 2.34, and it is unlikely that the spray penetration *S* remains the same despite a change in cone angle. Consequently, Eq. 2.34 is probably not general, which is supported by the work of Kuo and Bracco, who proposed an equivalent diameter to scale sprays that contains such effects as those above mentioned. However the similarity between Eq. 2.34 and 2.27 indicates that under some conditions, presumably that the angle of spreads are similar, the penetration of sprays and jets with equivalent nozzle momentum and in a chamber at the same gas density is very similar.

Abraham, Magi, MacInnes and Bracco [1994] used numerical modelling to compare evaporating sprays and gaseous jets for engine application, specifically to determine which would mix faster. Computations showed that for equivalent mass and momentum injection rate, sprays mix faster. This was demonstrated by observing the amount of fuel in rich, flammable and lean fractions. However, the mixing rate of natural gas with air reported in that paper is much different than the one obtained in this work for similar conditions. The comparison between the mixing rate of sprays and that of gaseous jets is re-examined in Chapter 5.

2.6 SUMMARY

For a transient turbulent jet issued from a round nozzle, of sufficiently high Reynolds number (greater than $3x10^4$), for constant injection rate and for times before the end of injection, the tip penetration rate can be expressed as

where z_t' is the distance of the jet tip from the virtual origin of the jet, $\dot{M}_n$ is the momentum injection rate at the nozzle, and ρ_{ch} the chamber density. Equation 2.27 is valid only at a certain

$$z_t' = 3.08 \left(\frac{\dot{M}_n}{\rho_{ch}}\right)^{1/4} t^{1/2} \quad \textbf{(2.27)}$$

distance from the nozzle, of typically z_t / d_{eq} greater than 20 diameters. Equation 2.27 is equivalent and derived from the following equation which shows the scaling employed

$$\frac{z_t'}{d_{eq}} = 2.9 \left(\frac{tU_n}{d_{eq}}\right)^{1/2}, \quad d_{eq} = d_n \left(\frac{\rho_n}{\rho_{ch}}\right)^{1/2} \quad \textbf{(2.37)}$$

Equations 2.27 and 2.37 are valid for many classes of turbulent jets, including incompressible jets, heated jets, compressible jets and jets of different densities. Equations 2.27 and 2.37 provide the relationship between injection and chamber conditions and the penetration of gaseous jets. It should however be highlighted that to calculate the nozzle velocity and gas density, the knowledge of the pressure ratio across the nozzle is required.

It was suggested that the mixing of the injected fluid with the surrounding air, expressed by the total amount of air entrained in the jet, could be given by:

$$m_{ch} \propto \dot{M}_n^{3/4} \rho_{ch}^{1/4} t^{3/2} \quad \textbf{(2.30)}$$

which indicates, for example, that given a fixed nozzle momentum, increasing the chamber gas density will increase mixing according to $\rho_{ch}^{1/4}$ while decreasing the penetration according to $1/\rho_{ch}^{1/4}$.

Reviewed studies revealed that multidimensional models could reproduce the main features of transient jets, in particular the square-root of time dependency and the scaling using the diameter and the nozzle velocity, at least for incompressible jets. It is also reviewed that the turbulent model k-ε is known to over-predict the mass entrainment rate of steady-state jets. It is suggested however that the inaccurate modelling of the steady-state jets does not necessarily

imply an accordingly inaccurate tip penetration prediction.

Reviewed material also showed that gaseous jets and sprays share common attributes. They scale in time in much the same way, and some correlations for the penetration of sprays resemble Eq. 2.27. However it is also found that the cone angle of sprays is dependent on the nozzle and on the density ratio between the injected liquid and the chamber air. This dependency renders a general comparison of sprays and jets difficult.

CHAPTER 3

FLOW VISUALIZATION OF TRANSIENT UNDEREXPANDED METHANE JETS

3.1 INTRODUCTION

There are two main objectives to the experimental investigation presented in this chapter. First, the experiments are to substantiate further the proposed scaling for transient turbulent underexpanded jets. Second, the experiments are to validate the multidimensional simulations of transient underexpanded jets. In both these objectives, an accurate description of the nozzle conditions is required, since both require the nozzle gas density and the nozzle gas velocity. The underexpanded methane jets are experimentally characterized by measuring the tip penetration as a function of time. The experimental data are obtained in the same flow visualization system as used in Ouellette and Hill [1992] and in Chepakovich [1993]. The data presented in this chapter differ from those presented in Chepakovich principally in the description of the nozzle conditions. In particular, the transient needle lift information and more accurate pressure measurements were required and obtained for the establishment of more accurate boundary conditions for the numerical modelling. The nozzle diameter of the injector used in this thesis is also larger than the one used by Chepakovich. The experimental apparatus and method are presented in Section 3.2. The results are discussed in Section 3.3.

3.2 DESCRIPTION OF APPARATUS

3.2.1 Injector and Actuation

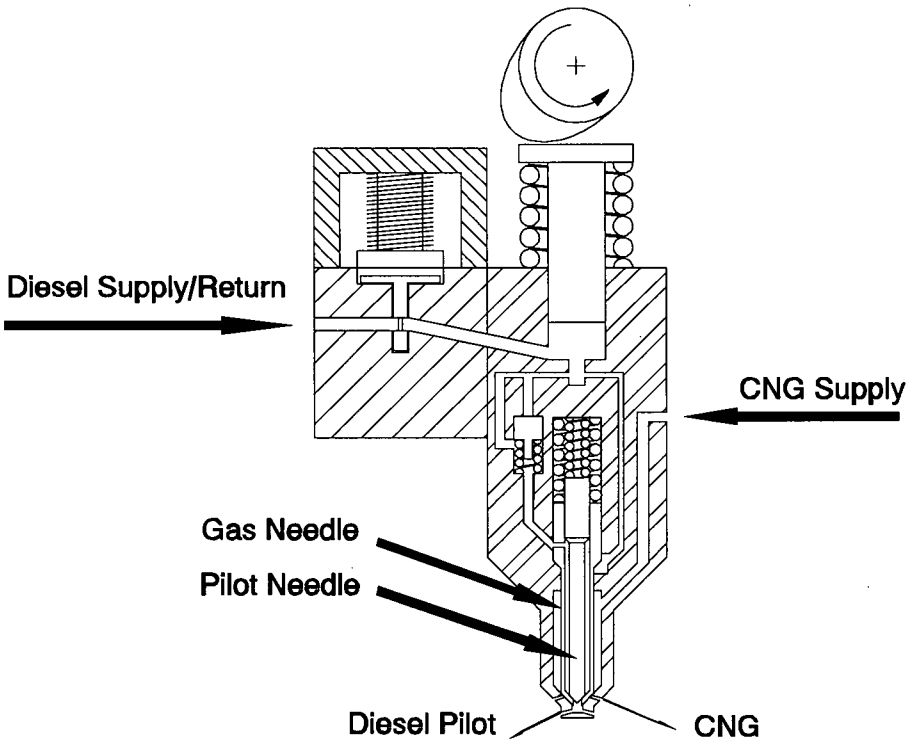

Figure 3.1 - Schematic representation of injector.

A prototype dual fuel injector designed for retrofit of Detroit Diesel engines was used in these flow visualization tests. The prototype has been used in engine research, is the object of a patent, and has been designed by P.G. Hill and K.B. Hodgins at the University of British Columbia. The protoype injector schematic can be seen in Fig. 3.1. A concentric needle system is used to allow both pilot diesel fuel and natural gas through the injector tip. For the purpose of these experiments, only gas injection was required. Consequently, the diesel port providing the hydraulic actuation to the diesel pilot needle was plugged, such that only the gaseous fuel was injected. A camshaft and flywheel turning at 715 RPM and powered by an electric motor provided actuation of the injector. As the solenoid is energized, the

supply/return line of diesel is closed. The cam then pressurizes the diesel fuel within the injector by forcing the plunger downward. The diesel pressure rises until the gas needle lifts up, allowing natural gas to flow in the chamber. The diameter of the six natural gas holes on the tip is 0.5 mm.

The prototype injector used has a built-in hydraulic port permitting measurement of the actuation pressure. This actuation pressure yields information about the needle lift timing.

The injector sits in the actual head of a diesel engine, modified to accommodate the camshaft mounted directly above it, and the chamber bolted below it. A schematic view of the arrangement can be seen in Fig. 3.2.

3.2.2 Chamber

The chamber height is 70 mm, and its cross-section in the plane normal to the injector is 123 x 123 mm. The chamber is fitted with two quartz windows 25 mm in thickness, and can be pressurized up to 5.5 MPa. Although the engine combustion chamber is cylindrical, the square chamber remains a realistic environment since the jets are little affected by the presence of the wall prior to impingement on them. When the injector sits in the head, the tip protrudes below the top wall, or fire deck. The holes in the nozzle are

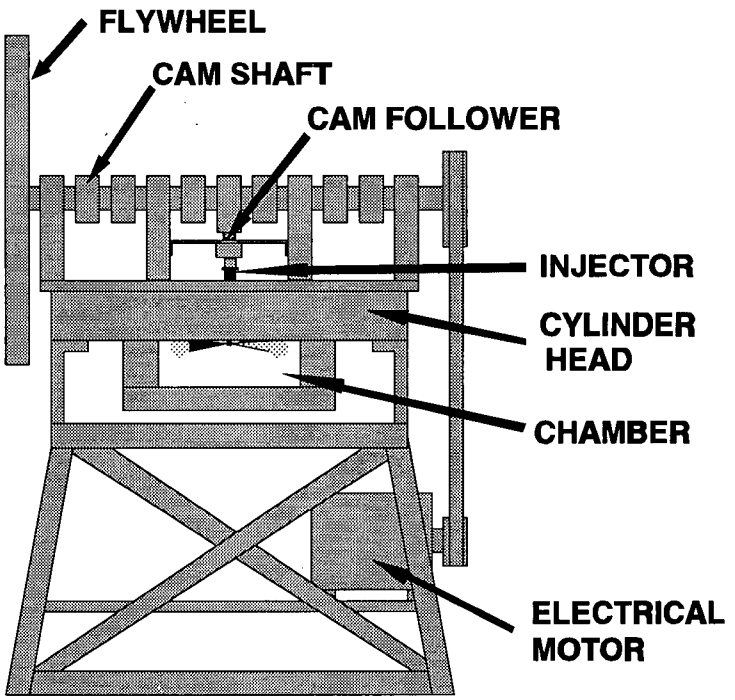

Figure 3.2 - Schematic view of experimental apparatus.

drilled such that there is an angle of 10 degrees between the jet axis and the fire deck.

3.2.3 Flow Visualization System

Schlieren photography is used to render visible the gas injection. A continuous wave mercury arc lamp is placed at the focal point of a concave mirror, such that a collimated beam of light is produced. The chamber is placed between that mirror and a second identical one which focusses the beam back to a knife edge and camera. The arrangement is seen in Fig. 3.3 in an overhead view.

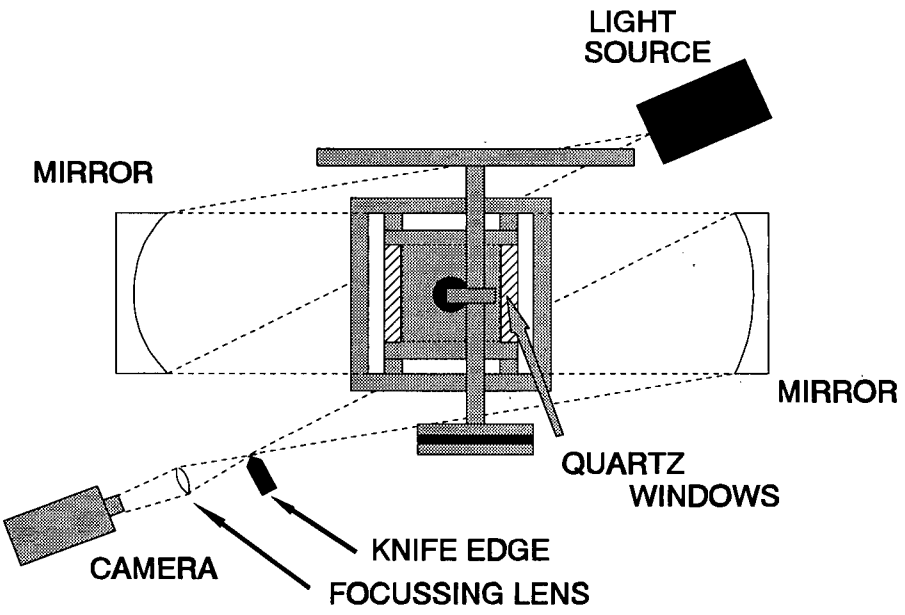

Figure 3.3 - Overhead schematic of flow visualization arrangement.

3.2.4 Image Acquisition System

A black-and-white video CCD (charge-coupled devices) camera was used to record the injection event. The camera was used in single-shot mode, capturing one frame per

injection at a controllable time after the BOI (beginning of injection). The camera is electronically shuttered at 1/10,000th of a second, and the video output was sent to a frame-grabber board housed in a 386 computer. The digitized images were saved and jet penetration rates were later measured using an in-house software.

3.2.5 Control System and Error Evaluation

An 80C196 micro-controller evaluation board provides the control required for injection and image acquisition timing. The controller receives digital input from an angular position sensor connected to the end of the camshaft. The sensor has a resolution of 0.25 crank angle (CA) degrees, and also provides an index pulse at the beginning of each rotation. The sensor output signal is used to determine rotational speed and to provide timing to the injector controller. The desired BOI, PW (pulse width = duration of injection) and picture acquisition time are manually dialed and are analog inputs to the controller's input channels. The controller sends the signal required to actuate the injector, to place the frame grabber board in a ready mode and to reset the camera such that the picture is taken at the specified crank angle degree. Once the picture is acquired, it can be saved. Pictures at various times after the BOI were taken to reconstruct the injection event. An overview of the control system can be seen in Fig. 3.4.

Because of delays inherent to the injector design, the BOI signal sent by the controller does not correspond to the actual BOI of the gas. The gas BOI can be either observed visually by determining the first crank angle at which the gaseous jet is visible, or by monitoring the pressure signal from the injector's hydraulic line. Both methods correlate well, but in either case an uncertainty exists, because there is a slight random variation of the actual BOI, which appears to be at most 0.25 CA° (0.05 ms). Fig. 3.5 is a typical pressure

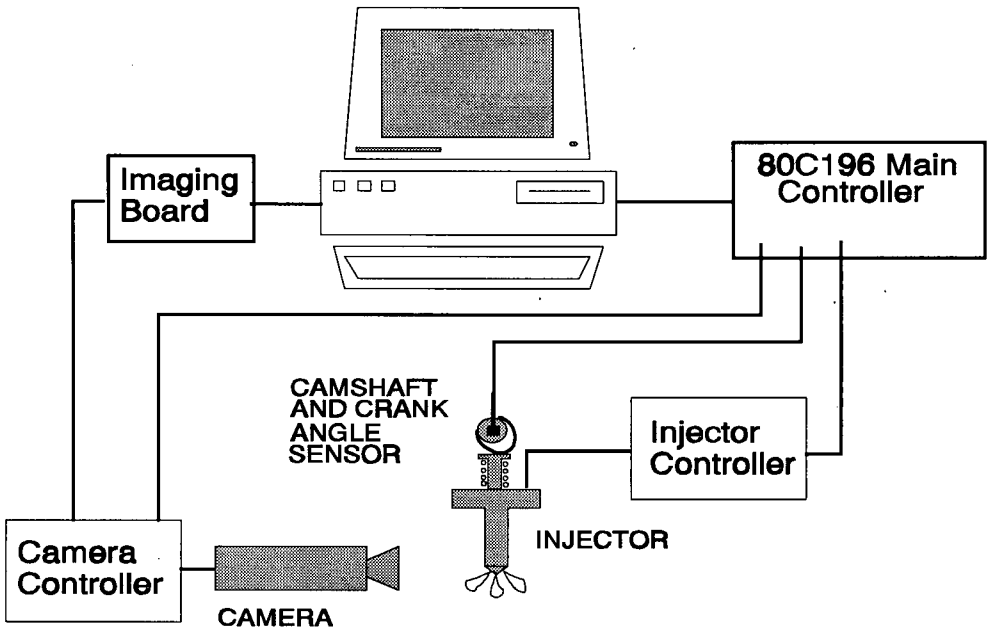

Figure 3.4 - Control system for the acquisition of a picture at specific times after BOI.

signal from the hydraulic line, and indicates the major events. The time required for the gas needle to fully open was obtained from this hydraulic pressure monitoring, and was found to be approximately 0.1 ms, or 0.5°.

There is an uncertainty of .1 ms (.43 CA) in the time at which the pictures are acquired due to the shutter speed of the camera. Repeatability tests were conducted and it was found that jet penetration measurements had a standard

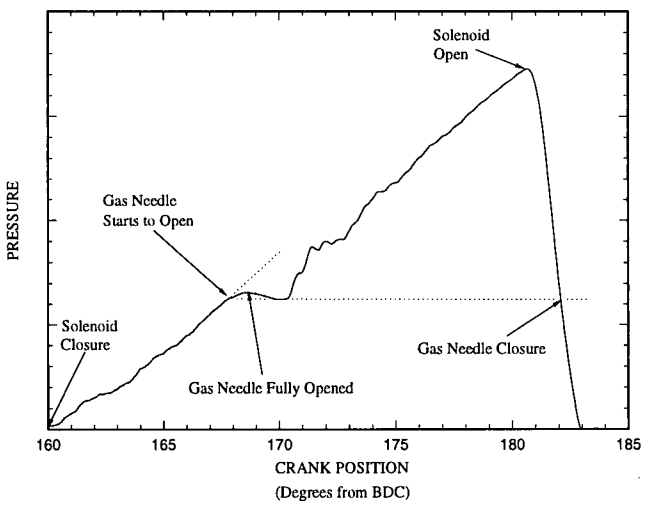

Figure 3.5 - Injector hydraulic pressure trace used to estimate needle transient openning time and actual BOI.

deviation from the average of approximately 1 mm, with maximum observed deviation from the average around 2 mm. A randomness of the turbulent jet overall shape was observed during all tests, accounting for the largest departure from mean penetration.

3.2.6 Experimental Method

The chamber was pressurized to 1.5 MPa with regulated compressed air. A pressure transducer was used to accurately determine and reproduce the actual pressure in the chamber. At 298 K, this pressure corresponds to a density of 17.5 kg/m^3. In the engine near top dead center, the pressure maybe 4.5 MPa and the temperature 800 K, which yield a density of 19.5 kg/m^3. As the compressed air filled the chamber, it generated turbulence that was allowed to decay. The bottled pressurized methane was regulated to the desired pressure. Again a small pressure transducer ensured a repeatable and known pressure level.

The mercury arc lamp was allowed to warm up for a few minutes after it was turned on. The appropriate software was loaded and the fuel pump and camshaft were powered. The BOI was arbitrarily set at 20° BTDC. The crank angle at which to capture the jet was set on the controller. The pulse width, the duration of the injection signal, was set to be greater than the delay between the BOI and the capture crank angle. Typically, pictures were acquired at 0.5, 1, 2, 3, 5, 7 and 10 crank angle degrees after the visible BOI. Each picture was saved for analysis.

As methane is injected in the chamber, which occurs only when requested by the user, the density in the chamber may change. Although it takes many injections to cause a significant density change, methane may stratify at the top of the chamber, changing the density in the nozzle area. To avoid this situation, the chamber was purged and refilled with fresh air after the acquisition of 5 pictures.

The saved pictures were later retrieved to measure the features of the transient jet. A scaling of the picture was first obtained by pointing with the computer mouse to a characteristic dimension of the chamber (on a frame without the jet). The location of the nozzle was also identified. The location of any points on the frame can subsequently be given relatively to the nozzle location. This method is used to obtain the radial penetration, the normal spread and the total penetration. These distances are identified in Fig. 3.6. As the illuminated frame encompasses a width of roughly 60 mm and that it occupies roughly 80% of the frame width, or 400 pixels, each pixel corresponds to .15 mm. As one can point within one pixel of the desired location, this method introduces little error. There is more uncertainty associated with the choice of the boundary between the turbulent jet and the surrounding air.

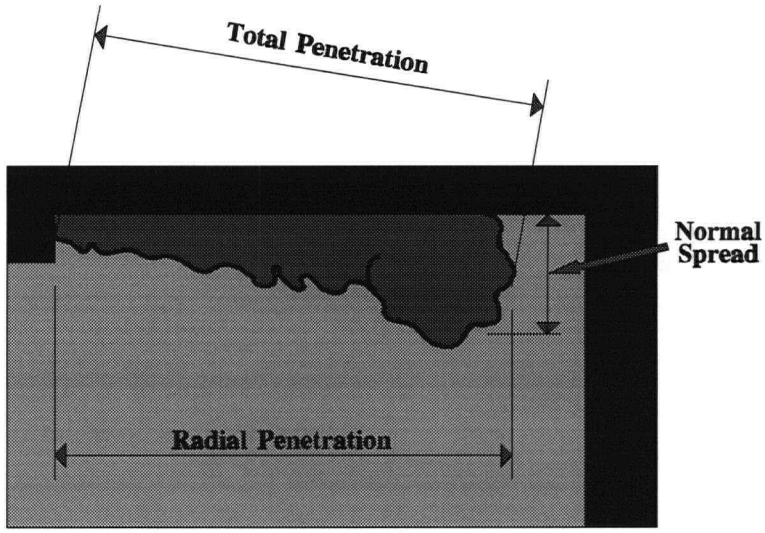

Figure 3.6 - Definition of penetration mesurements.

3.3 RESULTS

3.3.1 Penetration Rate

Figure 3.7 is an assembly of 4 individual frames reconstructing the injection event. The pressure ratio for the presented case is 2.5 and the nozzle diameter is 0.5 mm. The nozzle is located near the upper left-hand corner of each frame. It should be noted that other

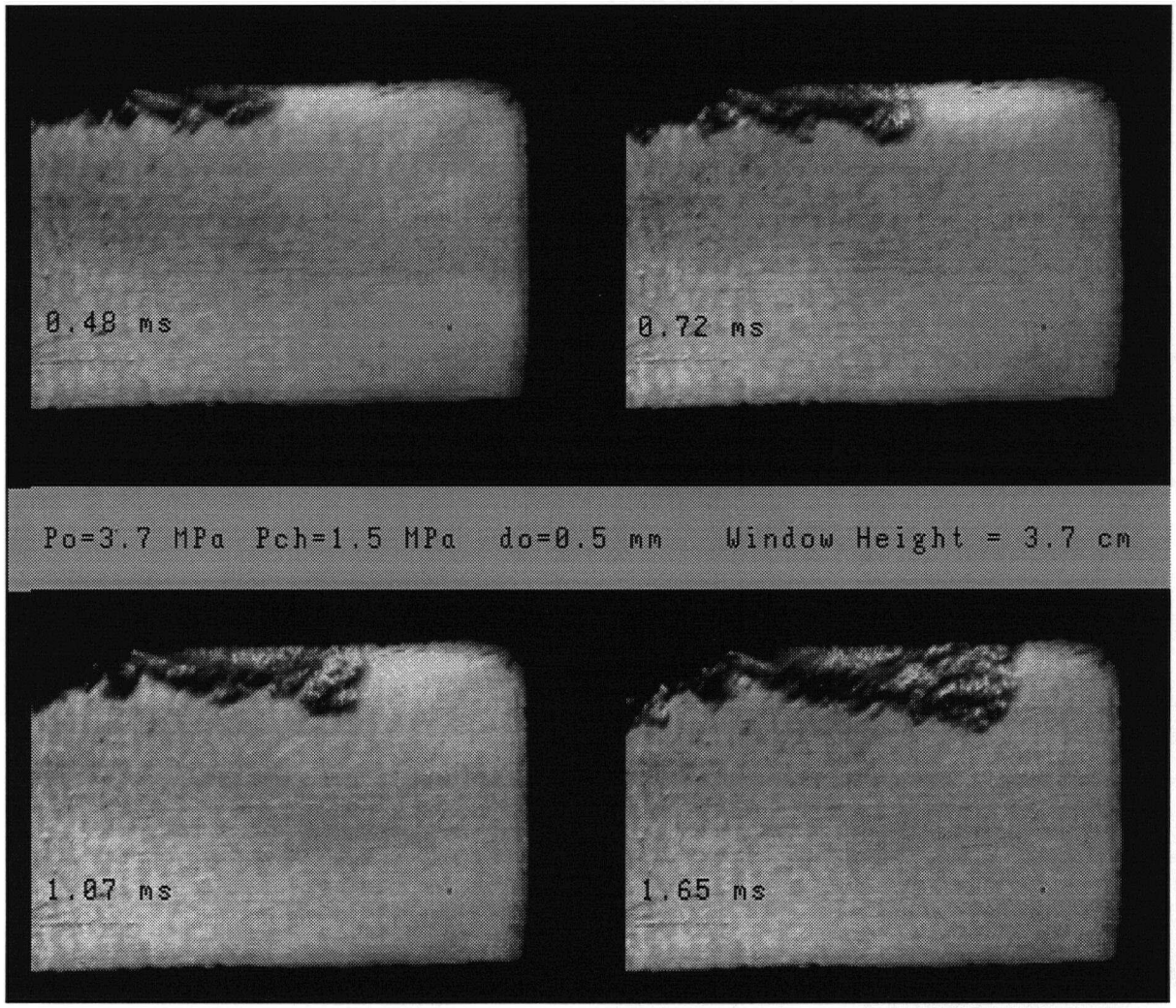

Figure 3.7 - Assembly of four schlieren photographs at various times after BOI.

jets are visible, but are not propagating in the plane normal to the field of view. One such jet is seen to propagate with an apparent rate roughly half of that of the main jet, and another one is seen under the nozzle. The jet is seen to propagate rapidly across the chamber, being more than half-way across the chamber width at 1 ms after BOI. In the first three frames, the presence of a head vortex is visible, while it is lost in turbulent structures in the fourth frame. The jet is seen to be in contact with the top wall to some extent. Since the jet half-angle of spread is more than 10°, it is not surprising that there is some contact with the top wall. In the last frame, the center of the head vortex forms an angle of approximately 7° with the fire deck, while the injection angle is 10°. This difference indicates that there is

some further attraction of the jet towards the top wall. The injection angle is a design choice, and the 10° of the prototype injector corresponds to the angle of the original diesel injector sprays. The experiments with this prototype permitted to investigate wall effects to some extent.

Figure 3.8 shows the penetration rate measured for the four pressure ratios studied. As observed in prior studies, there is a definite dependency on pressure ratio. As indicated

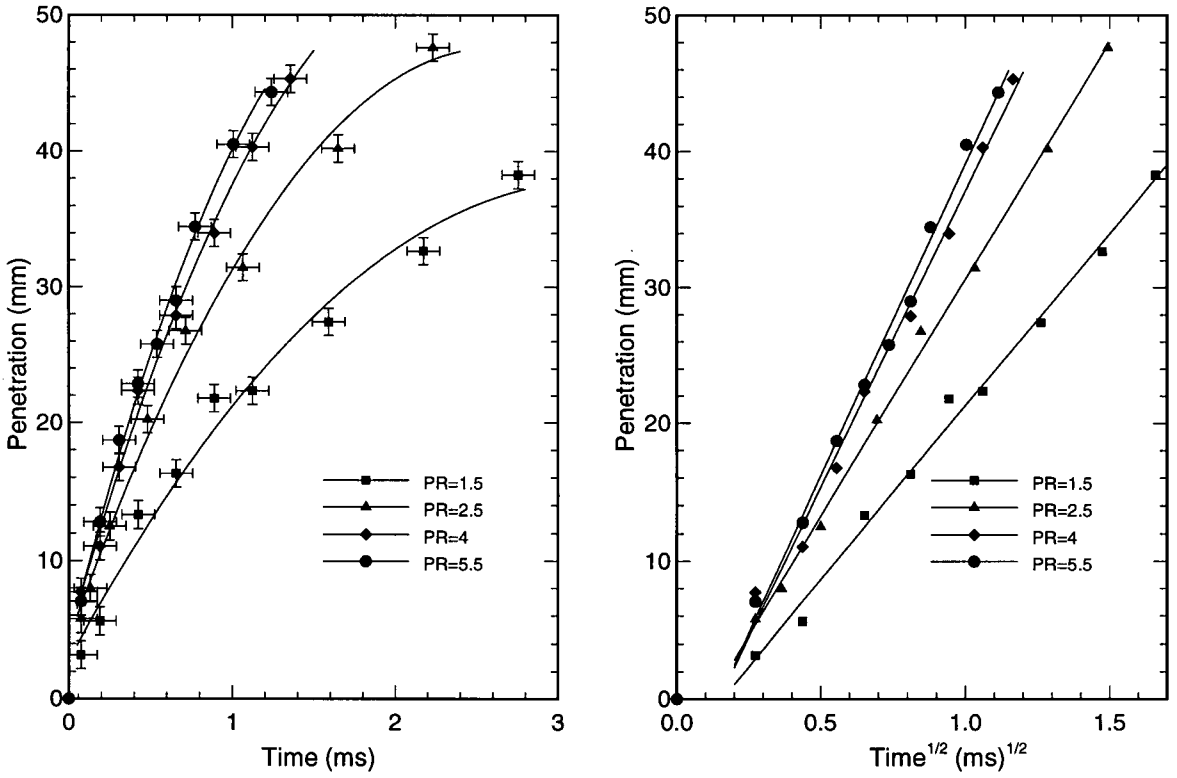

Figure 3.8 - Experimental Penetration Rate. The nozzle diameter is 0.5 mm, and the chamber pressure is 1.5 MPa. The injection is continous (t_{inj}>3ms).

in Chapter 2, the penetration is dependent on the density ratio, which is increased by the pressure ratio. In the flow visualization experiments, the injection density may be between 15 to 50 kg/m^3. In the engine, the injection pressure may be between 10 and 20 MPa, with injection densities between 55 and 110 kg/m^3 (assuming a gas temperature of 350 K). This

indicates that penetration rates are even faster in engines than the one observed here. The penetration of the case with a pressure ratio of 5.5 would correspond approximately to penetration rates in engines with injection pressure of 8 MPa. For a pressure ratio of 5.5, a penetration of 45 mm is observed for the first millisecond. This is significant since in engines the distance from the nozzle to the bowl is about 45 mm, and the ignition delay is in the order of 1 ms. This indicates that too high injection pressure may well cause over-penetration of the gaseous jet, with undesirable wall contact.

The graph on the right hand-side of Fig. 3.8 shows the data plotted as a function of the square-root of time. As previous studies have indicated, the transient gaseous jets for injection in diesel engines have a direct proportionality to the square-root of time. In the above results the injection duration is continuous, but the order of the injection duration in engine is 1 ms, such that the results are representative. As the graph also illustrates, the relationship does not exists for the first 15 diameters. The data points may be found in Appendix E.

3.3.2 Estimate of Conditions at the Nozzle

Scaling of the results using the equivalent diameter proposed in Chapter 2 would further substantiate its validity. In order to do this, the nozzle conditions must first be established. Figure 3.9 illustrates a schematic cross-section of the injector tip. The holes, typically numbering 6, have a typical diameter of 0.5 mm and a length-to-diameter ratio of 5.6. These holes represent the minimum area of the injector gas feeding port, such that choking is occurring at the exit plane of the nozzle if a critical pressure ratio is maintained. The minimum cross-sectional area between the needle and the inside wall of the tip is over 4 times the combined nozzle area (for nozzle diameter of 0.5 mm). With at most a unity

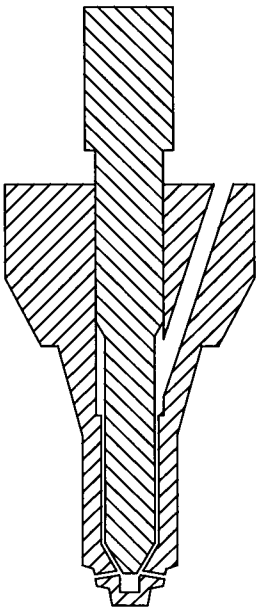

Figure 3.9 Cross-section of injector tip and needle (schematic).

Mach number at the nozzle, the Mach number within the injector will be low, and frictional effects in those areas have not been considered. The outlet of the nozzle being in the combustion chamber, Fig. 3.10 can be considered to represent one of the injector holes.

The nozzle exit plane velocity, density and temperature, can be estimated from the pressure ratio across the nozzle, assuming one-dimensional flow of a perfect gas in a constant-area duct with friction. The upstream and chamber temperature are taken as atmospheric temperature, which is justified by long residence time in long pipes. Assuming a fully developed flow, an average friction coefficient and a surface roughness e/D of 0.005, friction in the constant-area duct accounts for a reduction in mass flow rate of approximately 7.5% for choking cases. The flow is not fully developed in this short duct, so the friction is potentially higher than that predicted by the fully developed assumption. Friction effects are responsible for the common use of a discharge coefficient, and for a similar nozzle configuration, Naber *et al* [1994] report a discharge coefficient of 0.87.

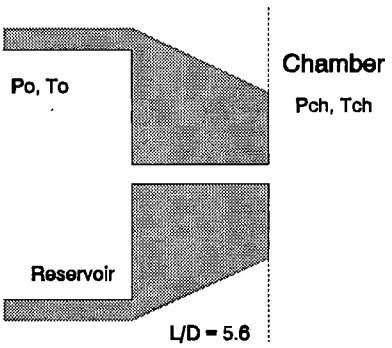

Figure 3.10 Physical representation for each nozzle.

Deviations from perfect gas law are significant for some of the cases considered. For example for the highest pressure ratio considered in the experiments, the pressure is 8.1 MPa

and the temperature 300 K, at which conditions the compressibility factor Z is 0.88 (as can be seen in Table 3.1), yielding a mass flow at the nozzle almost 10% higher than that predicted with the perfect gas law assumption. A methane equation of state was used to find conditions at the nozzle for cases of significant compressibility. The truncated virial equation of state of Kleinraum *et al* [1988] was extended to fit experimental data of Douslin *et al* [1964], providing an equation of state valid for temperatures between 273.15 and 400 K, and for pressures below 25 MPa. The equation fits both Douslin's data and Kleinraum's data within .05%, and is reported in Appendix C. The equation of state was also verified against methane state tables from Setzmann and Wagner [1991]. The equation of state was used to calculate the conditions at the nozzle in conjunction with one-dimensional conservation equations written for a control volume matching the duct section between the reservoir and the chamber. Isentropic acceleration was assumed between reservoir motionless gas at P_o and T_o and the conditions at the entrance of the duct. A summary of the solution can be found in Appendix D.

Table 3.1 shows the conditions obtained at the nozzle for the specified upstream conditions, and an indication of the effect of friction and compressibility on mass and momentum injection rate is indicated. For example, in the case of the highest injection pressure, consideration of real gas behavior led to a 7.6% increase in mass injection rate.

3.3.3 Scaling

Using the estimated boundary conditions of Table 3.1, the experimental results were non-dimensionalized. The length scale $d_{eq}=d_n(\rho_n/\rho_{ch})^{1/2}$ and the time scale d_{eq}/U_n were used to non-dimensionalize the data. The scaling can be seen on the left graph in Fig. 3.11. The three underexpanded cases are seen to collapse well to the same curve. The apparent

Case	P_o	ρ_o	Z_o	M_n	P_n	T_n	ρ_n	V_n	$\Delta\dot{m}$	$\Delta\dot{M}$	d_{eq}
	(MPa)	(kg/m^3)			(MPa)	(K)	(kg/m^3)	(m/s)	%	%	(mm)
1	8.088	59.31	0.877	1	4.006	252.9	34.93	394.1	7.6	1.7	0.70
2	6.001	42.65	0.904	1	2.995	254.4	24.99	400.3	5.7	1.2	0.59
3	3.726	25.52	0.939	1	1.864	256.2	14.85	407.9	3.3	0.6	0.46
4	2.285	15.28	0.962	.76	1.494	273.9	10.91	323.6	2.0	-0.2	0.39

Table 3.1 - Boundary conditions at the nozzle exit plane (subscript n) assuming real gas behavior and friction. P_{ch} is 1.494 MPa, T_o is 300 K. A surface relative roughness *e/D* of 0.005 was assumed. The diameter is 0.5 mm, and the *L/d* ratio is 5.6. $\Delta\dot{m}$ and $\Delta\dot{M}$ are the percentage difference in mass and momentum injection rate compared to estimates obtained using perfect gas law and friction.

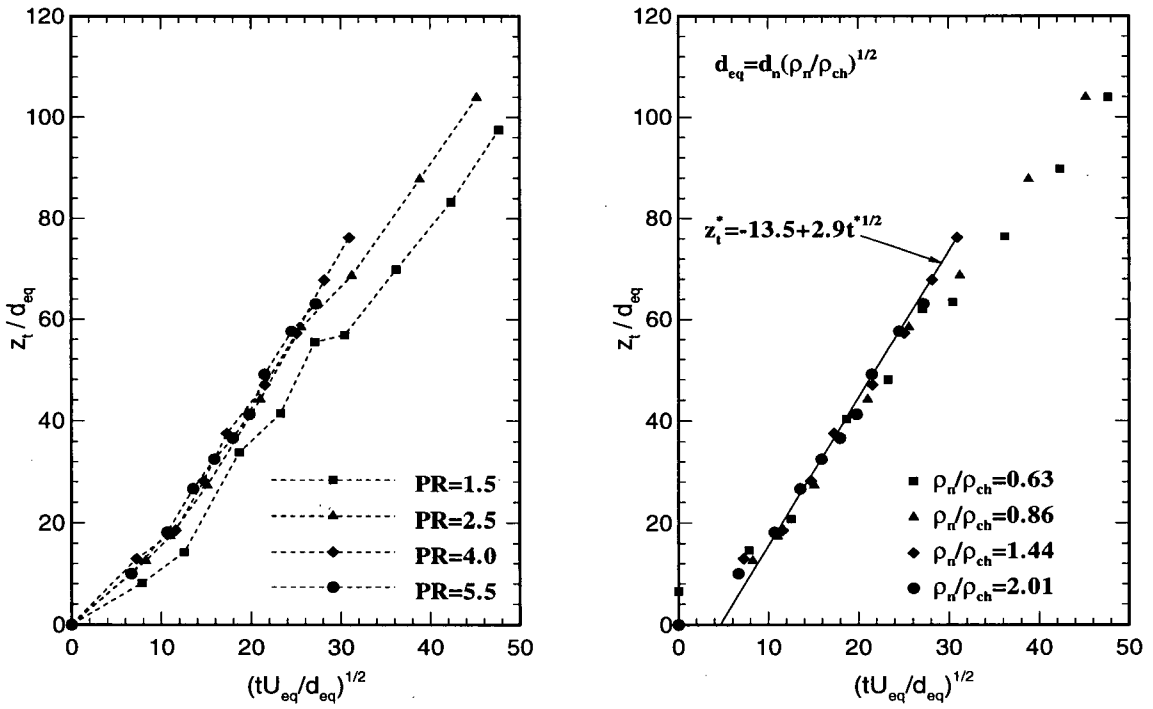

Figure 3.11 - Non-dimensional experimental data. Same conditions as in Fig. 3.8.

scattering at later time is due to wall effects which become significant as the vortex head velocity diminishes. The correctly expanded case does not appear to scale well with the underexpanded case. It appears however that the slope of the correctly expanded case is quite

close to that of the underexpanded cases in the 20 to 60 diameters range, but that the initial development rate is different. The scaling does not incorporate the length of the expansion region, as proposed in Section 2.2.4. However, its consideration did not significantly change the results. It appears from the data presented in Fig. 3.11 that there is a difference in injector response time as the pressure ratio is lowered below choking conditions. In the right-hand-side graph of Fig. 3.11, the lower pressure ratio case is corrected for this difference in initial development time.

The slope of the scaled data for equivalent diameters between 20 and 60 is 2.85, in good agreement with the value of 2.9 obtained for other transient jet penetration data in Chapter 2. The penetration can therefore be expressed as

$$\frac{z_t}{d_{eq}} = C_c + 2.9 \left(\frac{tU_n}{d_{eq}}\right)^{1/2} \qquad \textbf{(3.1)}$$

The value of C_c reflects both the time required for establishment of similarity and transient characteristics of the injector. For the present cases, C_c has a value of -13.4 for the underexpanded case. The value is -20.4 for the correctly expanded case, which further indicates that the injector has a different transient response at the lower pressure level.

3.3.4 Determination of Visible Mass Fraction

In order to compare numerical results and experimental results, it is of interest to evaluate the visible mass fraction in the schlieren photographs. Schlieren photography is sensitive to density gradients, such that the edge of a jet is visible due to the difference in density between the surrounding air and the gas within the jet. The gas in the jet is composed of a mixture of methane and air. An experiment was devised to determine the smallest mass fraction of methane in a methane/air mixture which would offer a visible edge

when injected in air.

Two 0.5 mm converging nozzles were installed at the closed end of a common pipe. The other end of the pipe was open to the surrounding air. One nozzle was fed compressed methane, the other compressed air. The respective flow rates could be calculated from the pressure ratio across each nozzle, so the mass fraction of the flowing mixture could be determined. Schlieren observation of the flowing mixture as it emerged from the common tube gave an indication of the strength of the mixture that could be perceived. The methane mass faction was reduced by reducing the methane pressure or by increasing the air pressure until the mixture became undistinguishable from the surrounding air on a photograph.

The jet edge remained visible on photographs for methane mass fractions down to about 2 to 4%. It should be noted that this result is specific to the schlieren configuration used in this project. A mass fraction of 3% was chosen as a representative sensitivity, and corresponds to a stoichiometric equivalence ratio of 0.5 for the direct oxidation of methane to carbon monoxide and water.

CHAPTER 4

MULTIDIMENSIONAL MODELLING OF TRANSIENT JETS

4.1 INTRODUCTION

Multidimensional simulations of transient gas injections are used in this thesis to examine various hypotheses and to answer some questions relevant to the use of natural gas in diesel engines. Before these questions can be investigated however, the capability of the numerical model used in this work to predict transient jets is assessed. In this chapter, the non-reactive flow is considered, while the ignition and combustion models are discussed in Chapters 6 and 7.

A first indication of the performance of the model is obtained by comparing the calculated penetration of an incompressible turbulent jet with the experimental data of Witze [1980]. Then the injection conditions of the flow visualization study are reproduced numerically, and the predicted underexpanded methane jet tip penetrations are compared with experimental results.

The KIVA-II code was used as a base code to solve the compressible equations of motion for a mixture of ideal gases. Developed in Los Alamos, the KIVA-II case is particularly suited to study engine-based problems. The code solves the compressible equations of motion for gas, includes the k-ε turbulence model, piston motion with associated compression, a basic chemical conversion model, an evaporative liquid spray model, and can readily handle various chamber geometries. A convenient input file allows one to change initial conditions in the chamber and injection conditions, as well as various flow parameters. Furthermore the code is organized such that modifications to various sub-models is facilitated. KIVA-II is described in Section 4.2.

The algorithm and modelled equations in KIVA-II have not been modified. KIVA-II does

not readily offer a means of injecting gaseous fuel, so that modifications were needed for that purpose. The required changes are principally related to the nozzle boundary conditions, and to the grid definition in the nozzle area. There are also important modifications to the chemical conversion sub-model discussed in Chapter 6.

As discussed in the introduction, multidimensional models can be used in a most valuable way. Once validated against some experimental data, their controllability and repeatability render them particularly useful in assessing the impact of parameter variation. They can be used in "numerical experiments" to test hypotheses. The development of a validated model also demands an analysis of the problem which improves its understanding. Multidimensional models are particularly useful in handling situations where there are interactions between various physical processes which are evolving in time and space. As such they provide the potential to identify unforeseen interactions.

Although they can well represent mass, momentum and energy conservation, the transport equations are modelled for turbulent flows, and are not general. As was discussed in Chapter 2, the k-ε turbulent model does not accurately represent steady-state jets. When turbulent combustion is considered, there are further approximations which render the simulation more approximate, as will be discussed in Chapter 6.

In the next section, the KIVA-II code is briefly presented. An incompressible air jet is then modelled and compared with experiments in the literature. Underexpanded methane jets are then simulated and compared with the flow visualization results of Chapter 3. A sensitivity study is also presented to assess some of the model considerations such as the grid size and computational accuracy.

4.2 THE KIVA-II NUMERICAL MODEL

KIVA-II solves the unsteady equations of motion for turbulent chemically reactive flows with sprays. As the equations are not modified, only a brief description of the modelled equations and of the algorithm follows, with the relevant equations reported in Appendix F and with complete details given in Amsden *et al* [1989]. The boundary conditions, the algorithm and modifications made in this work are discussed in Sections 4.2.2 to 4.2.4.

4.2.1 Gas Phase Solution

KIVA-II offers a solution for gas phase flows within a chamber and for the propagation of a liquid spray (liquid phase) within that chamber. Only the gas phase flow is discussed in this chapter. The gas phase solution is a finite-volume approximation to two- or three-dimensional compressible equations of motion. An arbitrary number of species, treated as a mixture of ideal gases, can be specified. The equations are typical Navier-Stokes equations for a mixture of gases. However as the reader may not be familiar with multi-species treatment, the equation of conservation of species is presented. In the following equations, the vector notation is employed:

$$\vec{v} = u(x,y,z,t)\,\vec{i} + v(x,y,z,t)\,\vec{j} + w(x,y,z,t)\,\vec{k} \tag{4.1}$$

$$\overrightarrow{\nabla} = \vec{i}\frac{\partial}{\partial x} + \vec{j}\frac{\partial}{\partial y} + \vec{k}\frac{\partial}{\partial z} \tag{4.2}$$

The continuity equation for species m is

$$\frac{\partial \rho_m}{\partial t} + \overrightarrow{\nabla}\cdot(\rho_m \vec{v}) = \overrightarrow{\nabla}\cdot[\rho D \overrightarrow{\nabla}(\frac{\rho_m}{\rho})] + \dot{\rho}_m^c + \dot{\rho}_{(m=1)}^s \tag{4.3}$$

where ρ_m is the density of species m, ρ the total mass density, and D a single diffusion coefficient. Fick's Law has been assumed for diffusion. The term $\dot{\rho}_m^c$ is the source of species

from chemical reactions. The term $\dot{\rho}_{(m=1)}^{s}$ represents the source of diesel fuel vapor from the evaporating spray (species m=1). When summing over all species, the total mass conservation is obtained as usual

$$\frac{\partial \rho}{\partial t} + \vec{\nabla} \cdot (\rho \vec{v}) = 0 \tag{4.4}$$

Similarly the energy equation has a source term for heat release from chemical reactions and for heat loss to the evaporative process of the spray. The transport coefficients used in KIVA-II are:

$$\mu = \mu_{air} + c_{\mu} \frac{k^2}{\varepsilon} \quad , \quad K = \frac{\mu C_p}{Pr} \quad , \quad D = \frac{\mu}{\rho Sc} \tag{4.5}$$

where K is the heat conductivity, and D the species diffusion coefficient. Values of the constant used in this thesis are reported in Appendix F. The perfect gas law for a mixture is used in KIVA-II as a state equation :

$$P = R_o T \sum_m (\rho_m / W_m) \tag{4.6}$$

where W_m is the molecular weight of species m. The internal energy I, the constant pressure specific heat C_p and the enthalpies h for species m are obtained from:

$$I(T) = \sum_m (\rho_m / \rho) I_m(T) \tag{4.7}$$

$$C_p(T) = \sum_m (\rho_m / \rho) C_{pm}(T) \tag{4.8}$$

$$h_m(T) = I_m(T) + R_o T / W_m \tag{4.9}$$

and the values of $h_m(T)$ and $C_{pm}(T)$ are taken from JANAF tables.

4.2.2 Wall Boundary Conditions

The wall boundary conditions are briefly described here, while the nozzle boundary conditions will be discussed Section 4.4.2. The turbulent law-of-the-wall implemented in KIVA-II is used to bridge the turbulence model with the wall. The law of the wall matches the tangential components to a logarithmic profile in the boundary layer. The details of the formulation can be found in Amsden *et al.* Both heat transfer and wall shear stress are handled by the law-of-the-wall. Either adiabatic or constant temperature wall can be specified. The constant-temperature wall condition was applied in the simulations, being more representative of engine conditions than the adiabatic option.

Some assumptions involved in the law of the wall function may be violated in engines. In particular for the modelling of transient jets, if the jet tip is propagating in contact with the wall, the assumption of quasi-steadiness leading to the derivation of the wall function would be violated in the vicinity of the vortex head. The wall function is properly evaluated when the grid point closest to the wall is within the turbulent boundary layer. This may be difficult to accomplish if a jet travels at high velocity near a wall, particularly in the vicinity of the nozzle. Therefore the possibility of inaccuracy is kept in mind in interpreting computational results in which these conditions occur.

4.2.3 Solution Algorithm

The basic equations are obtained by integrating differential terms over the control volumes corresponding to the cell volumes. Each computational time step is divided in two phases, a Lagrangian phase and a rezone phase. In the Lagrangian phase the vertices move with the flow, such that there is no convection across the cell faces. In the rezone phase, the flow is frozen, and the mesh is moved to the appropriate position, the convection terms being calculated during

that operation. The temporal difference solution is largely implicit, which permits one to adjust the time-step on accuracy conditions rather than stability conditions. All diffusion terms and pressure wave propagation terms are solved during the Lagrangian phase, using an algorithm similar to SIMPLE (see Amsden *et al* [1989] for details). Explicit differencing is used in the convection phase, with sub-cycling of the time-step if needed to satisfy the Courant stability condition. Finally, KIVA-II uses a quasi-second order upwind scheme for convection, which improves false diffusion tendencies.

4.2.4 Modifications of KIVA-II

KIVA-II does not readily have inputs for gaseous injections. Boundary conditions corresponding to the injector/chamber interface must therefore be implemented. At the injector/chamber interface, the velocity, temperature and density of the incoming gas must be set. In the current project, the computational domain did not extend within the nozzle area. Figure 4.1 shows the injector/chamber interface for a 2-D grid with downward injection originating from the center of the top wall, at the symmetry axis. The chamber in this case would have the shape of a cylinder (as that of Fig. 4.11), with the jet propagating along its axis. The velocity and temperature must be provided at the vertices within the nozzle/chamber interface (**a, b** and **c**). The density, internal energy, turbulent length scale and turbulent kinetic energy flux across the cell faces (**a-b**, **b-c**) in the interface region must also be provided. The temperature, velocity and density are inputs

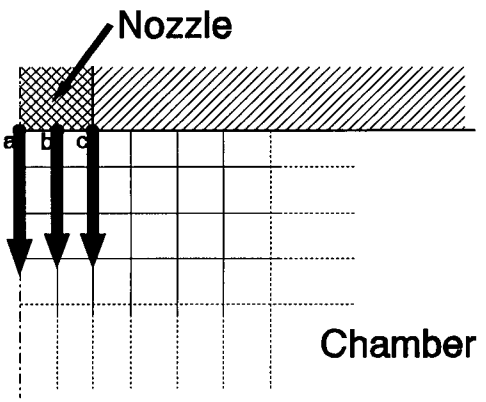

Figure 4.1 Injector/Nozzle interface in 2-D computational mesh.

to the solution and have been calculated as outlined in Section 3.3.2. The internal energy is obtained from the JANAF tables once the temperature has been calculated. The specific turbulent kinetic energy and the turbulent length scale influx must also be specified. In this thesis, unless otherwise specified, the specific turbulent kinetic energy influx was set at 10% of the nozzle flow specific kinetic energy, while the turbulent length scale was set at 50% of the nozzle diameter. These values were identified in the literature (see Gaillard [1984], MacInnes and Bracco [1990]), and the sensitivity of the results to this choice is assessed in Section 4.5.

4.3 TRANSIENT INCOMPRESSIBLE AIR JETS

To verify the proper implementation of boundary conditions in KIVA-II and to estimate its capability to reproduce transient jets, a computational case was compared with the experimental data of Witze [1980]. Witze took hot wire measurements on the centerline of a suddenly started air jet. For the case considered here, the nozzle was 1.2 mm in diameter and the nozzle velocity was 53 m/s. The jet is considered incompressible, such that the density of air at atmospheric pressure and temperature were used at the nozzle.

The nozzle conditions were reproduced in KIVA-II, and air was injected in a cylindrical chamber of radius 20 mm and length 100 mm. These dimensions were chosen to minimize wall effects over the time period considered. A mesh of 60 axial cells and 24 radial cells was used, with the size of cells expanding in both directions from the nozzle. The grid is similar to that depicted in Fig. 4.11. The injection took place at the center of the top wall, as in Fig. 4.1, the gas being injected downward. That geometry permitted an axisymmetric case to be performed. For this particular case, the penetration definition of Witze was used: the penetration time is obtained at one location when the axial velocity is 70% of the steady-state velocity at that location.

Figure 4.2 shows the results of the comparison between the experimental penetration data of Witze (reported in Kuo and Bracco [1982]) and those obtained with KIVA-II. At the

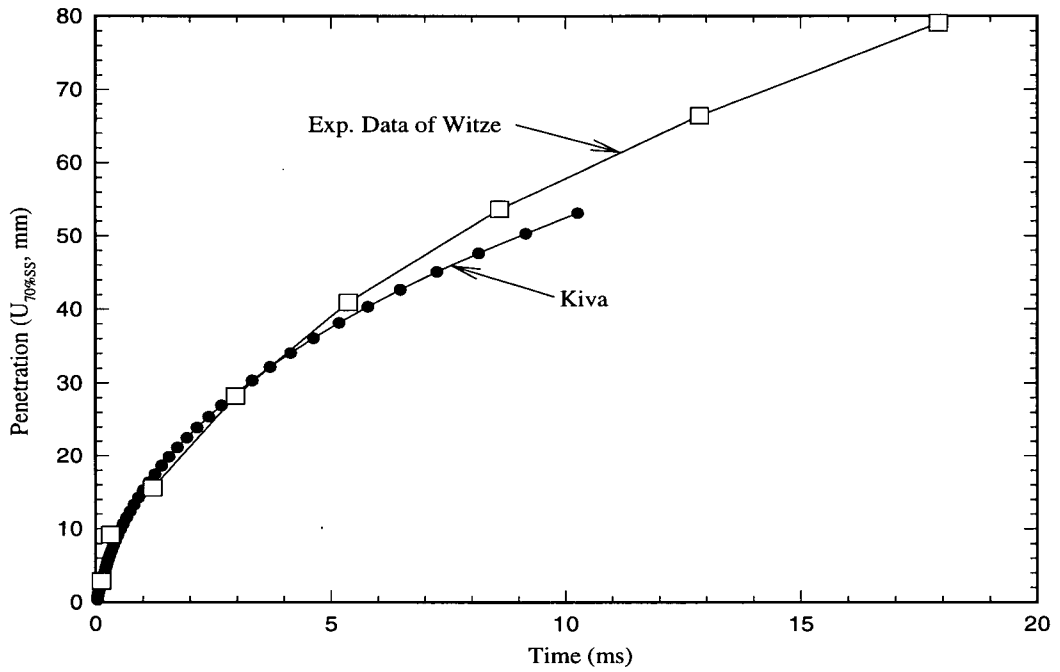

Figure 4.2 Comparison of predicted penetration rate with experimental data of Witze [1980]. Incompressible air jet into air, U_n=53 m/s, d_n=1.2 mm.

beginning both are in good agreement, but the simulated penetration lags behind the observed one at a later stage. The turbulence model and wall effects may be source of that discrepancy. As previously discussed, the k-ε turbulence model is known to cause a larger spreading rate in steady-jets, which should result in a smaller penetration for transient jets, as observed above. The difference in penetration at 10 ms is 9.3%, corresponding interestingly to the estimate made in Chapter 2. Better agreement is expected in the first 10 diameters, where the axial velocity remains constant. As the jet penetrates in the fixed volume chamber, there is some recirculation of the air which would result in an increase in mixing rate and a decrease in penetration rate. However, at a penetration of 40 mm, the jet width is roughly 11 mm, which represents only 27%

of the chamber width.

4.4 TRANSIENT UNDEREXPANDED METHANE JETS

In the following sections, the mesh, boundary conditions and treatment of underexpansion that have been used in reproducing experimental data are presented. The scaling of the numerical data is also presented.

4.4.1 Numerical Mesh

In the flow visualization experiments, there is some interaction between the jet and the top wall. To account for that interaction, three-dimensional computations were performed. The modelled chamber was round for ease of computations and had the same volume as that of the flow visualization square chamber. Figure 4.3 shows the three-dimensional mesh used in these comparisons.

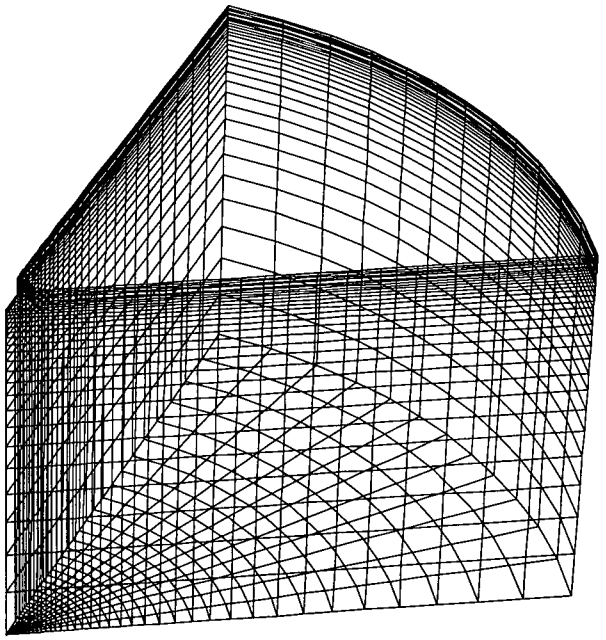

Figure 4.3 Three-dimensional mesh used in simulating flow visualization results.

The mesh is made of 30 axial cells, 32 radial cells and 12 azimuthal cells. The radius of the modelled chamber is 61.5 mm, and the length is 45 mm.

4.4.2 Boundary and Initial Conditions

The gas is injected radially from the side of the injector tip, seen in the grid as the notch in the upper central section. Figure 4.4 shows a cross-section of the nozzle area. The round nozzle is modelled as a square nozzle of equivalent area where flux terms and velocities are

specified. An axial velocity component was specified as well as a radial one to consider the 10° injection angle. Since the nozzle conditions are calculated from one-dimensional considerations, the specified nozzle flow velocity is the same at all grid points within the nozzle (square velocity profile). In the following computations, the nozzle is made of 1 axial cell and 2 azimuthal cells. Notes about the choice of grid density near the nozzle can be found in Section 4.5.

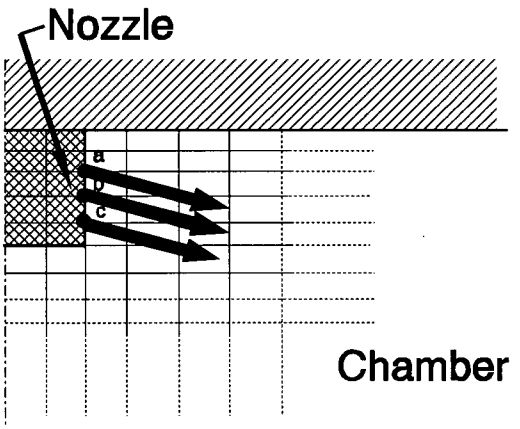

Figure 4.4 - Nozzle/chamber interface in computational mesh (3-D).

Initial conditions in the chamber were the following in the simulations: the air temperature is ambient temperature, the pressure was set at that recorded in the experiments, 1.5 MPa, and the initial turbulence levels in the chamber were assumed to be negligible, each injection being separated by several seconds.

The conditions at the nozzle have been determined in Section 3.3.2 and were used here in simulating the experimental work. The transient needle lift in the experiments was found to be 0.1 ms, and was modelled here as a half-sine wave shaped velocity ramping, from 0 to U_n in 0.1 ms. This reproduces the mass injection rate adequately, but initially underestimates the initial momentum injection rate.

4.4.3 Treatment of Underexpansion

The nozzle conditions calculated in Section 3.3.2 correspond to underexpanded conditions. KIVA-II solves compressible equations of motion, and can in principle handle the underexpansion. Since the expansion process outside the nozzle involves some shocks, it is

doubtful that the predicted flow field will be accurate, unless a very fine grid is used. It was decided in this work to use the notion of pseudo-diameter discussed in Section 2.2.4 to alleviate the fine grid requirement.

The pseudo-diameter was calculated using

$$d_{ps}=d_n\left(\frac{\rho_n}{\rho_{ps}}\right)^{1/2}\left(\frac{U_n}{U_{ps}}\right)^{1/2} \tag{4.10}$$

which is Eq. 2.13 without a discharge coefficient. It should be stressed that the pseudo-diameter correction is used strictly to remove the underexpansion constraints on the numerical simulation. It is not used as a correction for the density difference between methane and air caused by the different molecular weight and by the sonic flow, which is handled directly by KIVA-II.

Accordingly, the nozzle diameter d_{ps} is used instead of d_n in the computations, and the velocity, temperature and density corresponding to the pseudo-diameter are used instead of the actual underexpanded nozzle conditions. The pseudo-diameter velocity U_{ps} is calculated assuming that the perfect gas law prevails at the pseudo-diameter (although real gas conditions are considered at the nozzle):

$$U_{ps}=\sqrt{\gamma RT_{ps}}=\sqrt{\frac{2\gamma}{\gamma+1}RT_o} \tag{4.11}$$

The density ρ_{ps} is calculated as $P_{ch}/(R\,T_{ps})$ and T_{ps} is the temperature at Mach equal 1. Since the chamber pressure is used at the pseudo-diameter, correctly expanded conditions are provided at the nozzle boundary conditions.

Two test cases were calculated, the first one with the original nozzle conditions used directly (KIVA-II handled the underexpansion), and the second one with the pseudo-diameter correction. The pressure ratio in the test was 5. The predicted simulated penetration rates were

sensibly the same, the pseudo-diameter case predicting a 2.5% faster penetration rate. However, there was a 33% reduction in computation time when the pseudo-diameter correction was used, a definite advantage.

As the pressure ratio is increased, the underexpansion model results in a larger diameter being used in the simulation. The velocity at that equivalent diameter being the same for underexpanded cases, the grid size must be increased to accommodate the larger nozzle. In the following computations, the cells adjacent to the nozzle were kept at the same absolute size in all computations (not a fraction of the diameter). This was to ensure that remaining grid density effects are not dependent themselves on the pressure ratio (see discussion in Section 4.5).

4.4.4 Comparison with Experimental Data

Figure 4.5 shows a methane mass fraction contour for the pressure ratio of 2.5 at 1.07 ms compared to flow visualization results. In comparing the results, one must remember that the numerical solution produces an average flow, which must be compared with an instantaneous observation.

It is seen that there is good agreement on the penetration distance. In both observed and visualized jet, the bulge of the head vortex can be seen, the simulated one being further back. Clinging to the top wall is also visible in both cases. The simulated jet is thicker in the region between the nozzle and the head vortex, leading to an under-prediction of the penetration compared to the experimental case.

Figure 4.6 shows a comparison between the simulated and observed penetration rate for the pressure ratio of 2.5, with different mass fraction contour line choices. The penetration rate is well reproduced by the simulation. As can be seen the choice of the penetration definition from the 3% to 1% mass fraction contour line can change the simulated estimate by 8% for the

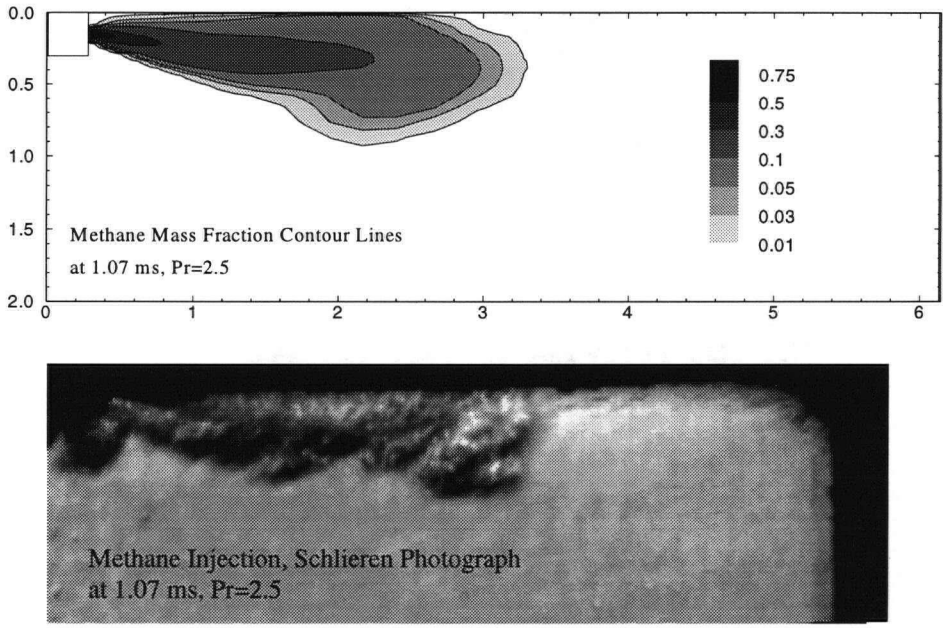

Figure 4.5 Comparison between numerical predictions and flow visualization results for a pressure ratio of 2.5.

presented 3-D case. The 3% mass fraction contour line has been chosen as a definition based on the experimental discussion of Section 3.2.4, recognizing that there is an uncertainty associated with that choice. On the right-hand-side graph, the theoretical curve of Eq. 2.24 is also shown.

Figure 4.7 shows overall results for the four pressure ratios considered. The penetration of the computed jet is obtained by measuring the contour lines, which are themselves interpolations of the data. Because of wall effects and grid size at the furthest distances, the computed penetration data point cannot be perfectly fitted by a curve. The order of penetration rate and of the pressure ratio dependency is well reproduced. The difference in penetration at the maximum time of each curve is as follow, starting from the pressure ratio of 5.5: -6.8%,

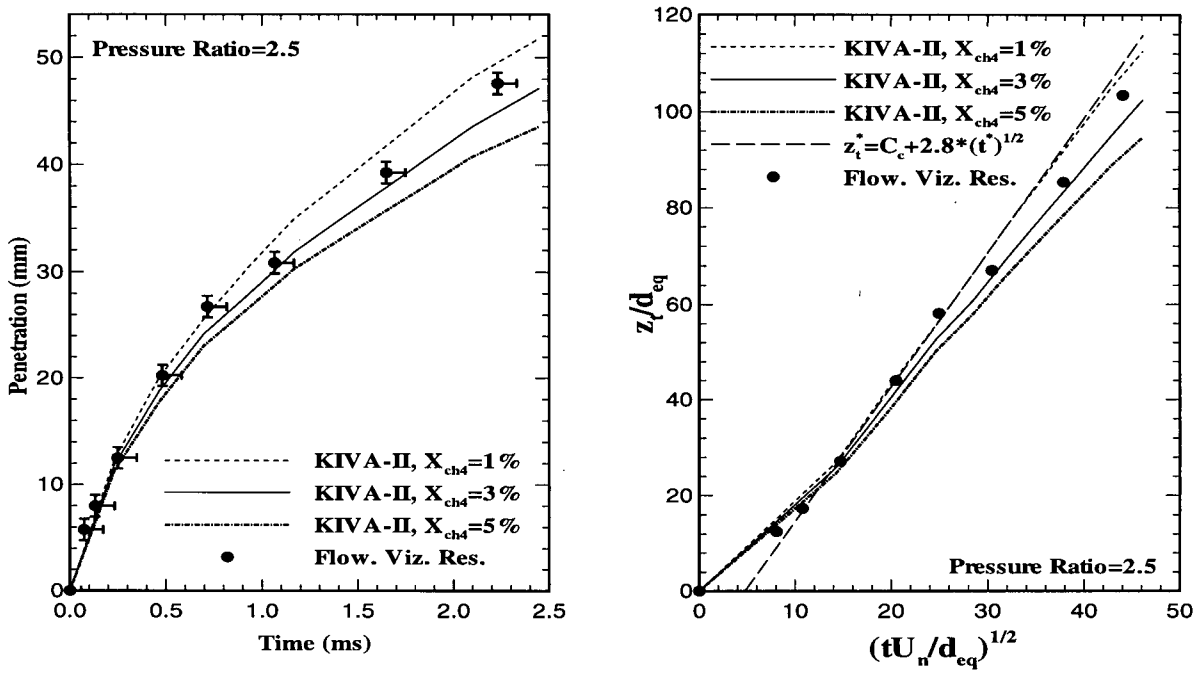

Figure 4.6 Comparison between KIVA-II predictions and experiments. Three-dimensional computations, pressure ratio of 2.5. The error bar on time represent a maximum error, while the error bar on penetration is a standard deviation.

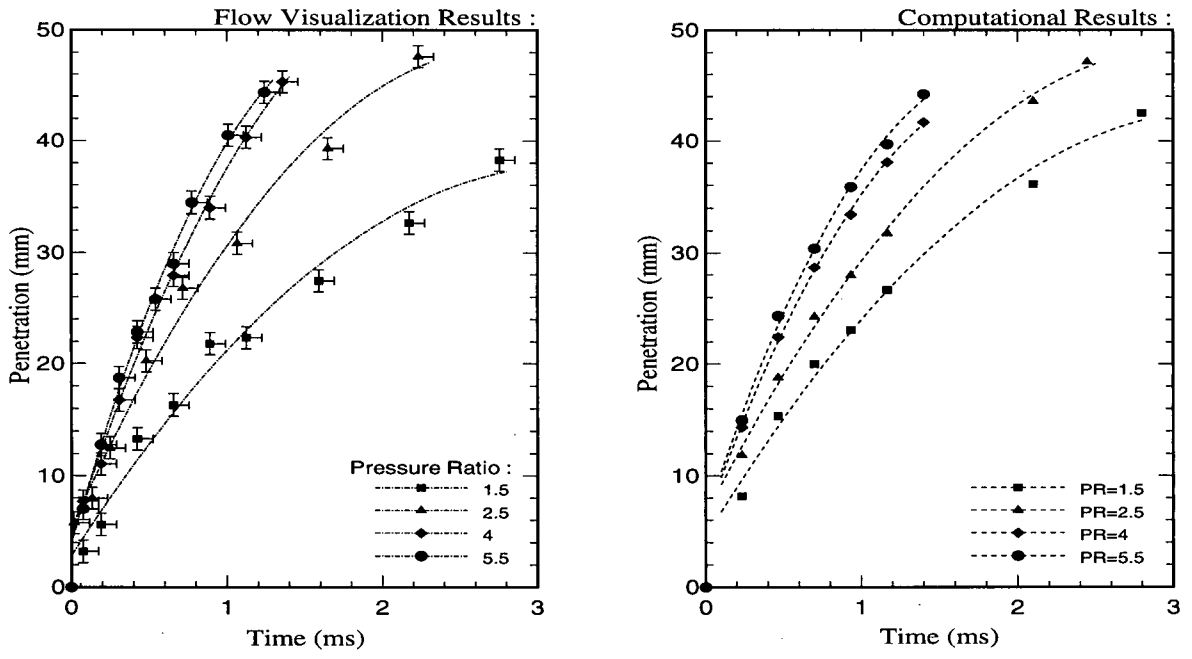

Figure 4.7 Comparison between predictions and experimental data for all pressure ratios.

-6.7%, -3.2% and 13.5%. The penetration is over-predicted considerably for the pressure ratio of 1.5. This case did not scale well in the experimental chapter, suggesting that the estimated boundary conditions are incompletely described. As mentioned in the previous chapter, the injector's transient response may well be dependent on the pressure ratio.

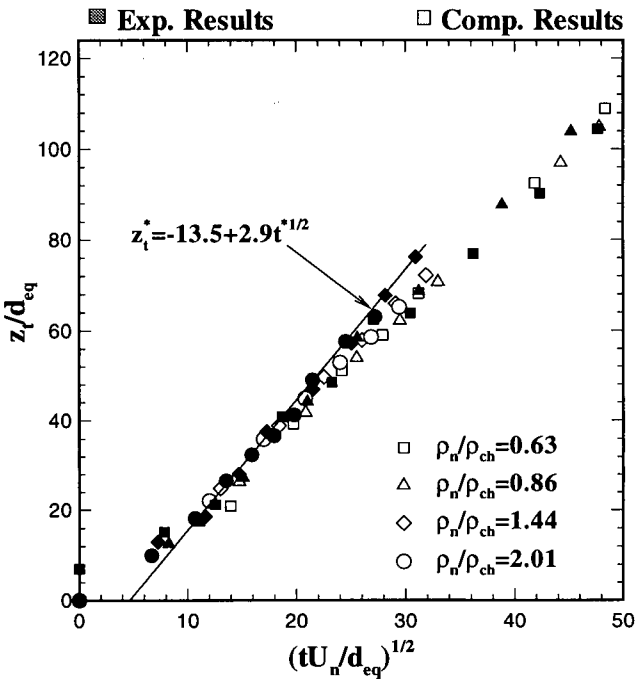

Figure 4.8 - Comparison between flow visualization results (filled symbols) and computations (open symbols).

In Fig. 4.8, the experimental and computed penetration data are compared on a non-dimensional graph. Computational and experimental results (those presented on the right graph of Fig. 3.11) are seen to collapse well on a same curve. The slope of the computed non-dimensional penetration rate is approximately 2.5 over the range of 20 to 60 equivalent diameters, while the slope of the experimental data is closer to 2.85. The agreement remains good at further distances; however the grid deteriorates at larger radial distances in these three-dimensional computations, as discussed in the next section, and the calculated penetrations are expected to be over-estimated by roughly 5%. Overall, the tip penetration calculation is under-predicted, in parallel to the observed trend in Section 4.3.

4.4.5 Scaling of Computational Results

Figure 4.8 also shows the predicted non-dimensional penetration of the four transient jets under consideration. As in Chapter 3, $d_{eq}=d_n(\rho_n/\rho_{ch})^{1/2}$. The four pressure ratio cases are seen

to collapse well, including the correctly expanded case (PR=1.5). Yet the corresponding experimental case did not scale well. This further suggests that there is a discrepancy between real nozzle conditions and estimated boundary conditions for this case. As mentioned above, the constant C_t corresponding to Eq. 2.24 is approximately 2.5 while the constant C_c is approximately -7.5 for the underexpanded cases and -1.1 for the correctly expanded case (the difference in C_c is probably due to the fact that the length of the expansion region was not considered).

4.5 SENSITIVITY STUDIES

4.5.1 Grid Density Effects

The injected gas velocity at the nozzle is in the order of 400 m/s and it is expected that grid density in the area near the nozzle will affect the mixing rate of the injected methane. The effect of grid density near the nozzle was investigated in an axisymmetric case, with the nozzle centrally located on the top wall of a cylindrical chamber, and in a three-dimensional chamber. An upstream pressure of 3 MPa and a chamber pressure of 2 MPa were chosen, yielding a pressure ratio of 1.5. The upstream gas temperature and the chamber temperature were set at 300 K. Based on one-dimensional isentropic flow approximation, and assuming perfect gas law, these conditions yield, at the nozzle, a velocity of 365 m/s, a temperature of 270 K and a density of 14.3 kg/m^3. A 0.38 mm diameter nozzle was considered, corresponding to a 0.403 mm equivalent diameter. The chamber was 80 mm in length and 24 mm in radius.

The parameters considered for the grid density study are illustrated in Fig. 4.9. N_{inj} is the number of cells where the gas injection boundary conditions are specified. For an axisymmetric case, there are automatically two cells within the diameter of the nozzle. dx_{min} is the size of the cell column adjacent to the nozzle area. dz_{min} is the size of the cells located just

below the top wall. Geometric expansions are used to size the cells radially from the nozzle and axially from the top wall. Table 4.1 indicates the cases performed. The parameters *nx* and *nz* are the number of cells radially and axially respectively. For each case, the downstream locations of the 0.5, 1 and 2 equivalence ratio contour lines on the axis of the chamber were obtained as a function of time from 0 to 2 ms. The grid and equivalence ratio contour lines for case 5 can be seen in Fig. 4.10.

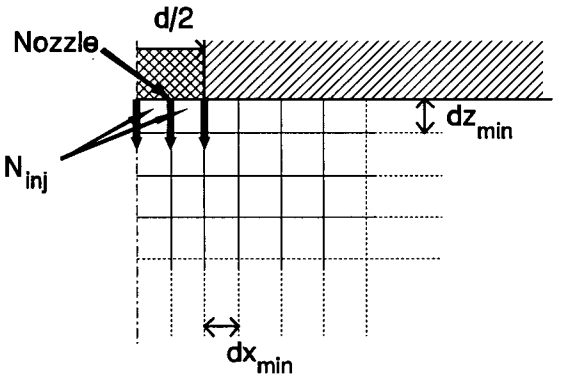

Figure 4.9 Grid density study parameters

Cases 3 and 3A permitted to verify that the number of axial planes did not affect significantly the location of the contour line observed.

Case #	N_{inj}	dx_{min}	dz_{min}	*nx*	*nz*	E.C.(z)
1	2	1 d	1 d	25	50	1.05
2	2	0.75 d	0.75 d	26	52	1.056
3	2	0.5 d	0.5 d	27	54	1.063
4	2	0.25 d	0.25 d	28	56	1.078
5	4	0.25 d	0.25 d	29	56	1.078
3A	2	0.5 d	0.5 d	27	59	1.056

Table 4.1 Cases performed in determining the effect of grid density in the nozzle area. The nozzle diameter *d* is equal to 0.38 mm, E.C.(z) is the grid axial expansion factor.

Cases 4 and 5 were computed to look at the effect of having more cells in the injector nozzle area. It was found however that the increase in cell number (effectively from 2 to 4) did not result in a significant difference in the jet penetration in these 2-D computations. The size of the cells adjacent to the nozzle was found to bear more consequences on the mixing characteristics. As Fig. 4.11 illustrates, changing the size of the cell adjacent to the nozzle from *1d* to *1/4d* changed the downstream axial location of the stoichiometric and rich contour line.

The magnitude of the change observed is not consistent with the magnitude of the change in expansion factor, such that the effect must be linked to the grid density near the nozzle. The high velocity gradient near the axis is artificially increased by too coarse a grid, which causes a faster lateral mixing, and slower penetration. The near-nozzle area is not affected as much as the downstream area, presumably because the velocity and concentration profiles are still influenced by the nozzle profiles. The difference between the cases is reduced as the grid gets finer, but even with a *d/4* nozzle size, there is still a grid dependency. The difference between the two finest grid cases is 4% for the equivalence ratio of 1. For the equivalence ratio of 0.5, there is little difference in the computed penetration as the cell size is decreased. This is explained by the fact that leaner conditions also correspond to jet regions which have smaller velocity gradients and are therefore not affected to the same extent by the minimum cell size used here. An equivalence ratio of 0.5 corresponds to a mass fraction of 3% for methane, such that penetration simulation based on a 3% definition would be independent of the grid size for near-nozzle cell sizes of approximately 1 diameter, or in this case 0.4 mm, and for grid expansion factor of less than 10%.

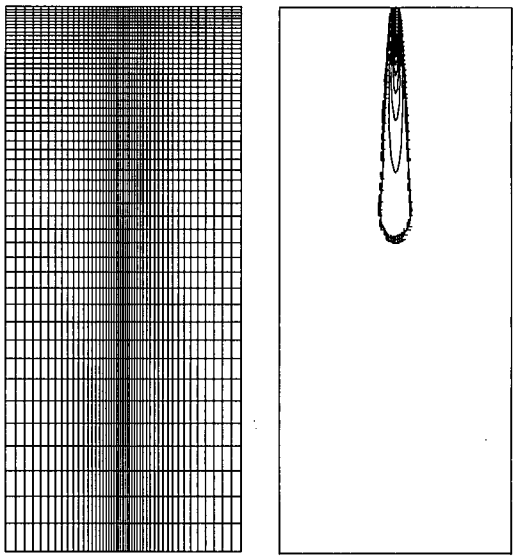

Figure 4.10 Grid and equivalence ratio contour lines for case 5. The increment of contour lines is 0.5, the lowest equivalence ratio being 0.5. The diameter D is 0.38 mm, the chamber is 80 mm long and has a radius of 24.1 mm.

For the cases considered, the velocity was 365 m/s. For higher pressure ratios, velocities can reach 450 m/s, for which grid dependency may be slightly more pronounced.

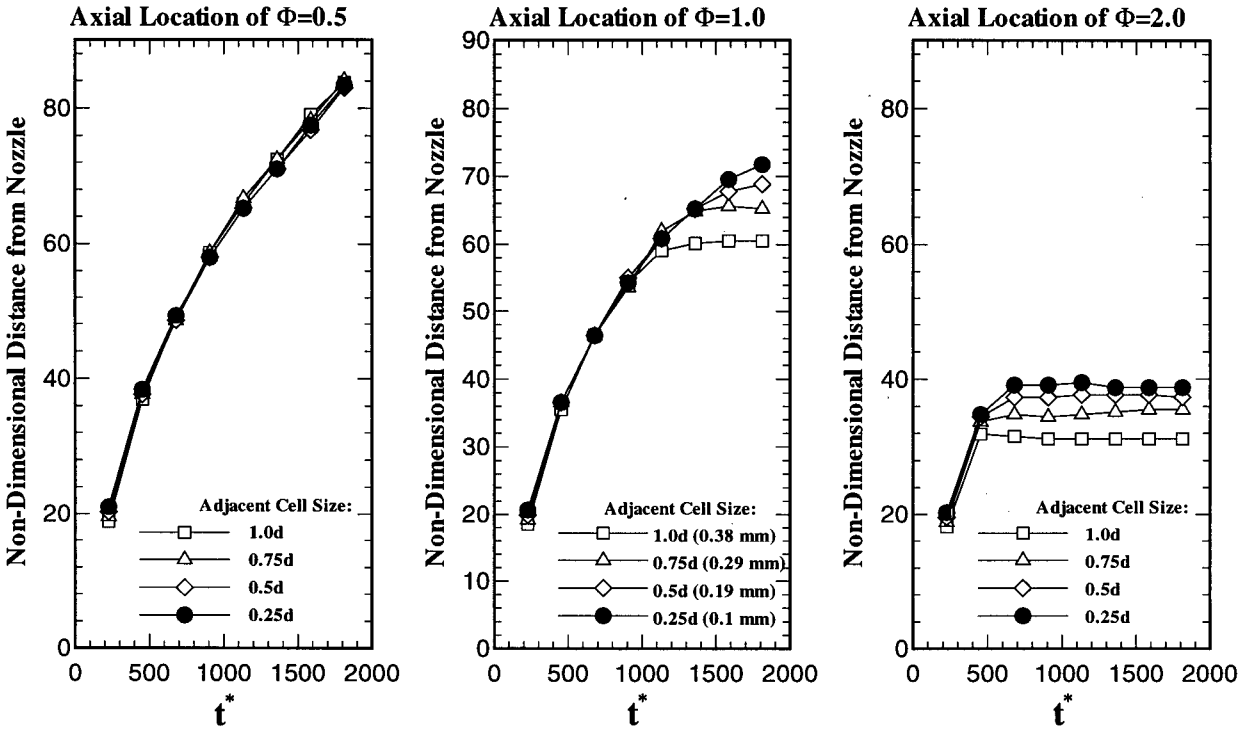

Figure 4.11 Effect of grid density near nozzle on the mixing of the jet. Φ is the equivalence ratio.

Smaller cell size corresponds to a smaller time step in KIVA-II because of the algorithm employed. At a *1/4d* cell size, the time step was prohibitively small and finer grids were never used. In most of the remaining study, grid sizes near the nozzle of *d/2* were employed, recognizing the faster mixing prediction incurring.

When three-dimensional cylindrical computations are performed, as those performed in last section, grid density in the azimuthal direction is more critical, the cell absolute width increasing rapidly with the radius, as seen in Fig. 4.3. For that reason, it was found to be preferable to place two cells in the nozzle area in the azimuthal directions for 3-D cases. Computations with a three-dimensional sector of 60 degrees with 32 radial cells, 12 azimuthal cells and 30 axial cells were performed and compared to two-dimensional computations. The

nozzle was lowered in the 3-D chamber to mid-chamber location to avoid wall effects. The cells adjacent to the nozzle were set to *3d/4* in the radial and axial direction and to *d/2* in the azimuthal direction. Also, there were two cells within the nozzle in the azimuthal direction. In that configuration, results were fairly close to those predicted in 2-D. This can be seen in Fig. 4.12 where the three-dimensional case is compared to 2-D cases 1 and 4. Because of the azimuthal cell expansion with the radius, there is eventually a larger prediction of the penetration by 5% compared to 2-D cases.

4.5.2 Other Sensitivity Studies

A number of sensitivity studies were also performed. The accuracy of the computations, controlled by the specified maximum value of the residuals, was increased by a factor of 10 over the recommended value with no significant effect. A change in the value of the influx of turbulent kinetic energy from 20% to 5% of the jet kinetic energy had no influence on the jet penetration, suggesting that near the nozzle, the shear-generated turbulence is the main source of turbulent kinetic energy. The turbulent Prandtl and Schmidt numbers were in all the above tests set to 0.9. For jets it is sometimes recommended to use values of 0.6. A case was performed with these new values. This change had little effect on the jet penetration. It did affect the distribution of mass fraction in the richer core of the jet,

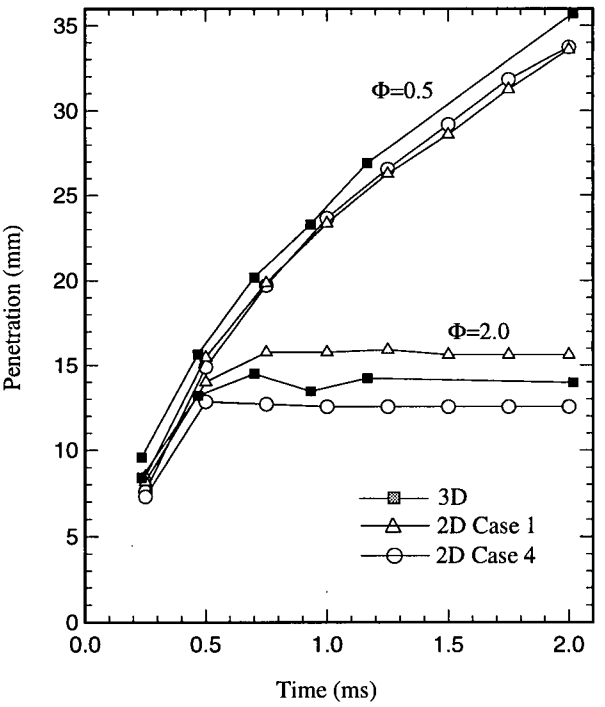

Figure 4.12 Comparison between 2-D and 3-D computations and effect of grid density on penetration.

reducing the amount of fuel in the rich zone at the expense of the leaner zone, but the changes were modest.

4.6 SUMMARY

The simulated penetration rate of an incompressible turbulent jet compared favorably well with the experimental data of Witze [1980], the predictions leading to an approximately 10% slower penetration rate. The slower penetration is believed to be caused by the reported inaccuracy of the k-ε model for jets. Predicted penetration rates for underexpanded methane jets compared also well with the experimental data obtained in Chapter 3. The predicted penetration rates collapsed on a single curve when scaled with the equivalent diameter proposed in Chapter 2, including the correctly expanded case. The penetration was underestimated by roughly 5% compared to the experimental data. Grid density studies indicated that the 3-D computations performed tend to over-estimate the penetration by 5%, which would bring the underestimate of simulated penetration rates to approximately 10%. The grid density studies also indicated that the penetration rate estimated in axisymmetric computations and based on a 3% mass fraction contour line were grid independent for near-nozzle grid size of 0.4 mm and for grid expansion factor of less than 10%, which was verified over a distance of 85 diameters.

CHAPTER 5

GASEOUS FUEL JETS PENETRATION AND MIXING

5.1 INTRODUCTION

In Chapters 2 and 3, it was shown that the penetration of free turbulent transient jets can be expressed as

$$\frac{z_t'}{d_n(\rho_n/\rho_{ch})^{1/2}} = C_t \left(\frac{U_n t}{d_n(\rho_n/\rho_{ch})^{1/2}}\right)^{1/2} \tag{5.1}$$

where C_t was evaluated to be approximately 2.9. This equation is valid for turbulent jets, incompressible or compressible, with constant momentum injection rate and issued from converging round nozzles. The validity of Eq. 5.1 extends for penetration distances greater than 20 d_{eq}, was verified up to 120 d_{eq}, and for times less than t_{inj} (injection duration). It was also suggested that the penetration of free turbulent jets depends on t_{inj} and on the specific turbulent kinetic energy k of the flow in the chamber, such that it could also be expressed more generally as:

$$\frac{z_t}{d_n\sqrt{\rho_n/\rho_{ch}}} = f\left[\frac{tU_n}{d_n\sqrt{\rho_n/\rho_{ch}}}, \frac{t}{t_{inj}}, \frac{\sqrt{k}}{U_n}\right] \tag{5.2}$$

for jets of Reynolds number greater than $3\text{x}10^4$, with no significant wall effects.

The first objective of this chapter is to examine the effects of injection and chamber conditions on the penetration of the gaseous fuel with the air in a chamber at typical engine conditions. The penetration rate dependencies of Eq. 5.1 (equivalent diameter and nozzle velocity) and of Eq. 5.2 (finite injection duration and turbulence levels) are considered in

Sections 5.1 and 5.2. The mixing rate of the injected fuel with the air in the chamber is then investigated in Section 5.3. In Section 5.4, the mixing rate of gas jets and of evaporating sprays is compared, while a summary and practical comments are presented in Section 5.5.

While comparing experimental results with numerical simulations in Chapter 4, the penetration rate was the object of the comparison. The mixing rate of the fuel with the air in the chamber is also important. The mixing rate controls the combustion rate, while the jet penetration rate influences where combustion predominantly takes place. Over-penetration of the jet causes an impingement on the piston or cylinder wall, a usually undesirable situation leading to flame quenching. As the flame is quenched, intermediate species may not oxidize completely, and emissions are affected. Also, under-penetration is undesirable as it reflects poor air utilization in the chamber. Too high a mixing rate would cause over-leaning of the methane, which may not burn completely.

For a single jet, as the angle of spread of turbulent jets is a constant, the mixing rate and the penetration rate are directly related. This is supported by the discussion in Section 2.3.3. For multiple jets, the penetration and the mixing can be well separated; the penetration rate of each jet can be reduced by using smaller holes, the mass injection rate being kept the same by using more holes. On the basis of numerical modelling, it was shown by Abraham, Magi, MacInnes and Bracco [1994] and Jennings and Jeske [1994] that using more smaller holes enhances the mixing of the injected gas with the surrounding air. This point is also discussed in Section 5.3.

While studying gaseous jets, Jennings and Jeske sought to find the maximum mixing rate between the injected fuel and the air in the chamber given a particular mass injection rate. Fastest mixing may be warranted if there are concerns that gaseous fuels may not mix as fast as diesel fuel sprays. However, numerical simulations performed in this work and presented in

Section 5.4 show that evaporating sprays and gaseous jets have much the same mixing rate given an equivalent nozzle momentum injection rate. Recognizing that jets and sprays mix with chamber air at a similar rate, the apparent incentive for the achievement of fastest mixing is not as obvious, and optimal mixing rate should be determined based upon the combustion characteristics.

Before starting Section 5.1, the analytical approach followed in this chapter is discussed. Numerical experiments were performed to study jet penetration and mixing. The use of the numerical experiments is appropriate, as the comparisons between experimental results and computational results performed in Chapters 3 and 4 indicated that the numerical model reproduced well the jet tip penetration experimental data and the dependencies upon injection and chamber conditions. The numerical experiments presented in this chapter simulate the injection of a single methane jet in a constant-volume chamber. The numerical experiments are intended to be general, but when examples are used to demonstrate a point, realistic temperatures and pressures are obtained from the DDC 6V-92 engine experimental data. The particular examples are discussed in Section 5.5. The considered conditions were determined as follows: at 10° BTDC (injection typically occurs in the 15° to 0° BTDC), typical pressure and temperature are 4 MPa and 800 K (medium load, 1200 RPM). The following assumption is made in the following tests: the diesel fuel has been injected and has burned, raising the average chamber temperature to 1200 K. This temperature is chosen somewhat arbitrarily as a desirable temperature for the autoignition of natural gas. The corresponding pressure level for a constant volume (the volume change is small near TDC) is approximately 6 MPa. Approximate turbulence levels were assumed to be 10% of the piston specific kinetic energy. At 10° BTDC, the piston speed is approximately 3.4 m/s (for 1200 RPM), and the specific kinetic energy is 5.8 m^2/s^2. The flow specific turbulent kinetic energy would be approximately 0.58 m^2/s^2. In the

following calculations the specific turbulent kinetic energy was set at 0.36 m^2/s^2, which correspond to a turbulent fluctuation of approximately 0.5 m/s. This is a turbulent fluctuation of the order of the ones experimentally measured in engines near TDC. The sensitivity of calculations to that choice will be assessed.

The numerical experiments were performed in an axisymmetric chamber of the type seen in Fig. 4.11. The mesh was made of 23 radial cells for a radius of 23 mm and 45 axial cells for a length of 62 mm. Table 5.1 summarizes the chamber conditions. The following injection pressures were used; 8, 10, 15 and 20 MPa. The conditions at the nozzle were calculated assuming real gas behavior and friction, following the method outlined in Section 3.2.2. The *L/d* of the modelled nozzle was that of the prototype injector used

Pressure (P_{ch})	6 MPa
Temperature (T_{ch})	1200 K
Turbulent Kinetic Energy (k)	$3.6e10^3$ cm^2/s^2
Wall Temperature	400 K
Cylinder Length	62 mm
Cylinder Radius	23 mm

Table 5.1 - Conditions used for computational studies of penetration and mixing rate.

P_o (MPa)	d_n (mm)	ρ_n (kg/m^3)	U_n (m/s)	ρ_{ch} (kg/m^3)	t_{inj} (ms)	$t_{inj}U_n/d_{eq}$	d_{eq} (mm)	$\dot{m}$ (kg/s)	M (kgm/s^2)
8	0.74	37.58	285.6	17.42	1.17	299.5	1.087	.0046	1.318
15	0.5	54.13	436.25	17.42	1.17	579.4	0.881	.0046	2.023
20	0.431	73.4	439.1	17.42	1.17	565.8	0.885	.0047	2.065
15	0.5	54.13	436.25	20.91	1.17	634.1	0.804	.0046	2.023
10	0.5	40.26	375.4	17.42	1.74	859.5	0.760	.0030	1.114
10	0.5	40.26	375.4	17.42	2.58	1274.4	0.760	.0030	1.114
10	0.67	40.26	375.4	17.42	0.97	357.3	1.019	.0053	2.00
15	0.433	54.13	436.25	17.42	1.17	579.4	0.763x 8	.0035 x8	1.517 x8
15	0.612	54.13	436.25	17.42	1.17	579.4	1.079x 4	.0069 x4	3.030 x4

Table 5.2 - Conditions used for numerical experiments. In all these cases P_{ch} = 6 MPa and T_o = 350K.

in the experiments. The nozzle conditions, the equivalent diameter and non-dimensional injection durations for the cases considered in this chapter are presented in Table 5.2.

5.2 NUMERICAL EXPERIMENTS - PENETRATION RATE

5.2.1 Long Injection Duration and Constant Specific Turbulent Kinetic Energy

Given an injection duration longer than the time span of interest and constant turbulence levels in the chamber, the dimensional analysis reduces to

$$\frac{z_t}{d_n\sqrt{\rho_n/\rho_{ch}}} = f\left[\frac{tU_n}{d_n\sqrt{\rho_n/\rho_{ch}}}\right] \qquad \textbf{(5.3)}$$

Equation 5.3 indicates that the penetration will be identical for cases with the same equivalent diameter $d_{eq}=d_n(\rho_n/\rho_{ch})^{1/2}$ and for a constant nozzle velocity (which is essentially the case when considering choked nozzles). In a first numerical experiment, ρ_{ch} and U_n were kept constant, while the diameter and nozzle density were changed keeping $d_n\rho_n^{1/2}$ constant. The first calculated case has an injection pressure of 20 MPa, yielding a nozzle density of 73.4 kg/m^3, with a nozzle of 0.433 mm. For the second case, the injection pressure was set at 15 MPa, yielding a nozzle density of 54.13 kg/m^3 with a nozzle of 0.5 mm.

The penetration rate and non-dimensional penetration rate are presented in Fig. 5.1. The actual penetration rate is seen to be essentially the same as expected. This is a result of considerable practical importance as will be discussed in Section 5.4.

In a second test, the chamber density was changed by reducing the temperature from 1200 K to 1000 K, corresponding to a density increase from 17.4 to 20.9 kg/m^3. The result of this test is also presented in Fig. 5.1. The actual penetration is reduced as the chamber density increases. The penetration still scales well with the equivalent diameter.

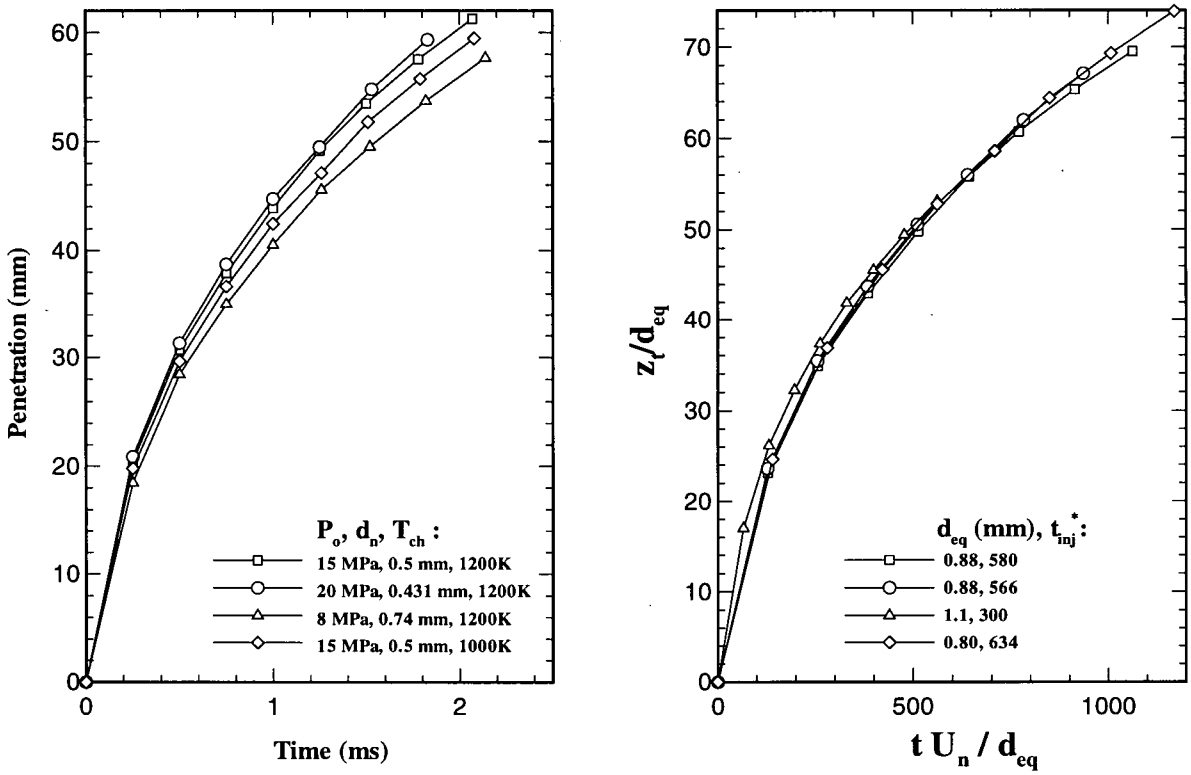

Figure 5.1 - Penetration and non-dimensional penetration for cases with constant t_{inj} and k ($t_{inj}^*=t_{inj}U_n/d_{eq}$)

In a third test, the choking condition at the nozzle was removed by lowering the injection pressure to 8 MPa, such that the nozzle velocity was lower than for the above cases. The injection duration was kept constant by increasing the nozzle diameter to 0.74 mm, such that the statement of Eq. 5.2 remains appropriate (the mass injection rate was the same as for the other cases presented). The results are also presented in Fig. 5.1, where it is seen that the actual penetration is lower than for the choking cases. As seen in Table 5.2, the momentum injection rate of that case is lower, explaining the lower penetration rate despite the same mass injection

rate. The penetration rate still scales well, as seen on the right-hand side graph[1].

In all the cases of Fig. 5.1, the injected mass is constant. This does not need to be so to satisfy the relationship of 5.2. Figure 5.2 shows the penetration rate for jets issued from nozzles of different diameters (0.43 and 0.61 mm). In both cases, the injection pressure is 15 MPa and

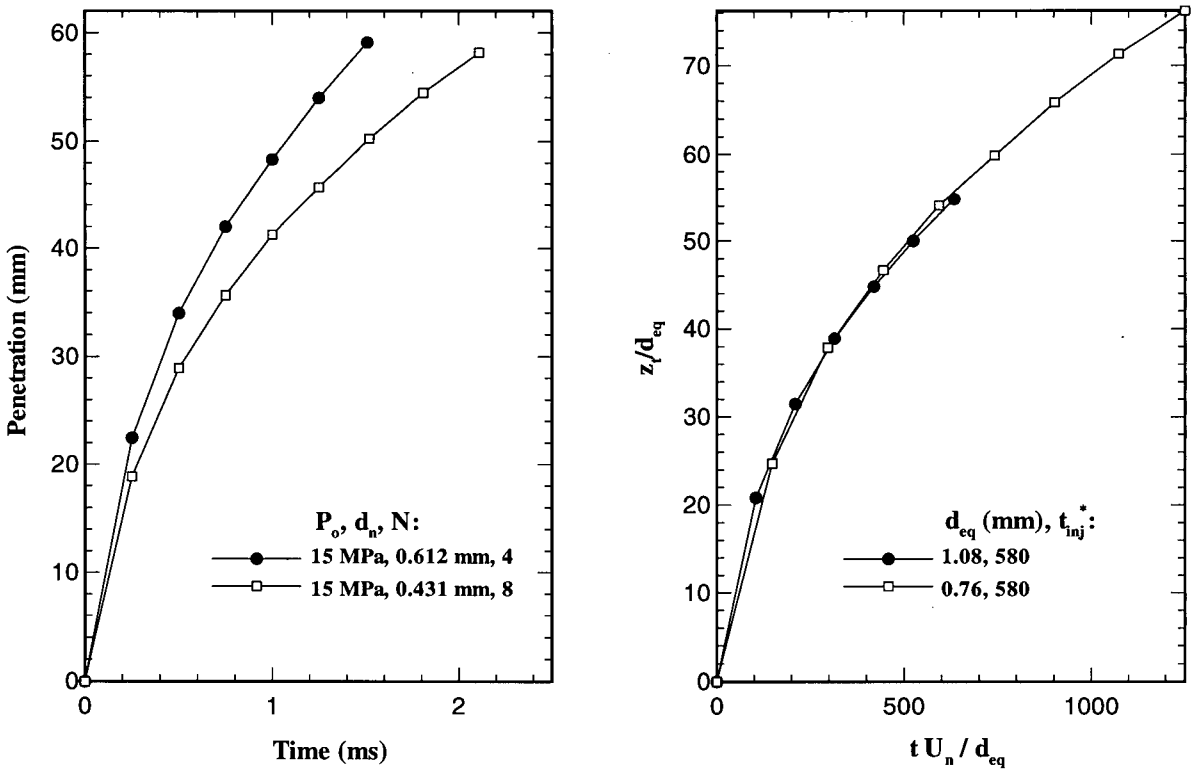

Figure 5.2 - Penetration rate for jets issued from nozzles of different diameters.

the injection duration is 1.17 ms. As the mass injection rate is different, the total injected mass is different. Figure 5.2 shows that the scaling is still appropriate.

[1] In the non-dimensional graph of Fig. 5.1, the correctly expanded case does not initially scale perfectly. Considering the barrel length of the underexpansion region (about 1 nozzle diameter) when comparing underexpanded and correctly expanded cases may help improving the scaling.

5.2.2 Short Injection Duration

The second parameter in Eq. 5.2 is the injection duration. In order to test separately its effect, one must keep the first and third parameters constant. One way to do this is to maintain the mass injection rate constant, and change only the mass to be injected, which requires a longer injection time. This situation is presented in Fig. 5.3 where an injection pressure of 10 MPa is used with a nozzle of 0.5 mm. In the first case the injection duration is 1.75 ms, while in the second it is 2.6 ms. It is seen that until 3 ms, there is no distinguishable difference in penetration rate (in fact computations had to be performed in a longer chamber for these cases because the wall was reached before 3 ms when using the 62 mm long chamber). The difference in penetration rate does appear after 3 ms. Apparently the quasi-steady-state jet stem keeps feeding

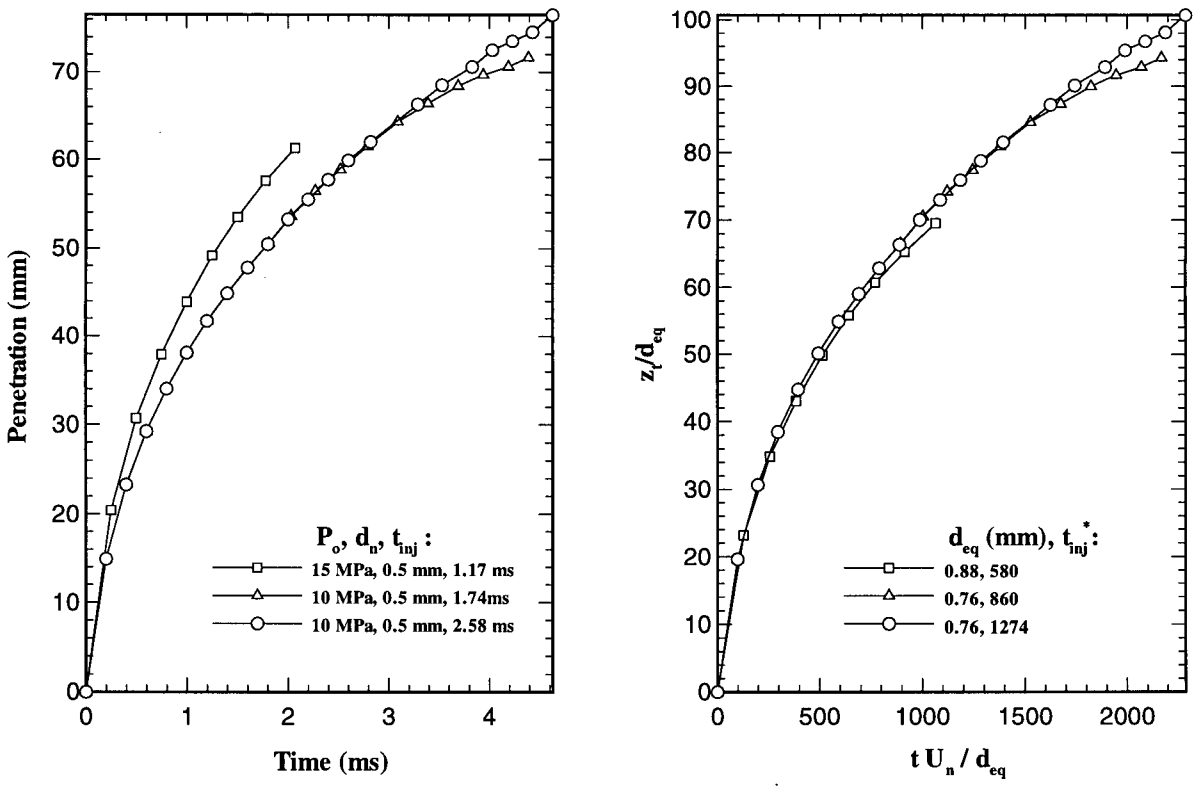

Figure 5.3 - Penetration and non-dimensional penetration for a variation in t_{inj}.

mass and momentum to the head vortex for some time after the EOI until its own momentum becomes less or equal to that of the head vortex.

It is also possible to vary t_{inj}, while keeping the first and third parameters of Eq. 5.2 constant, and keeping the injected mass constant. For a choked nozzle this is not possible unless the chamber density is changed; for a constant chamber density, this conditions would require that:

$$d_{n1}\ \rho_{n1}^{1/2} = d_{n2}\ \rho_{n2}^{1/2} \tag{5.4}$$

and to meet the same injected mass condition, the injection duration must satisfy

$$\frac{t_{inj1}}{t_{inj2}} = \frac{\rho_{n2} U_{n2} d_{n2}^2}{\rho_{n1} U_{n1} d_{n1}^2} = 1 \tag{5.5}$$

It is possible, however, to have a choked and an unchoked nozzle meeting that requirement. To keep the first parameter of Eq. 5.2 constant, for a constant ρ_{ch}, then:

$$\frac{U_{n1}}{U_{n2}} = \frac{d_{n1}\rho_{n1}^{1/2}}{d_{n2}\rho_{n2}^{1/2}} \tag{5.6}$$

and to satisfy constant injected mass:

$$\frac{t_{inj1}}{t_{inj2}} = \frac{\rho_{n2} U_{n2} d_{n2}^2}{\rho_{n1} U_{n1} d_{n1}^2} \tag{5.7}$$

Replacing 5.6 into 5.7 yields:

$$\frac{t_{inj1}}{t_{inj2}} = \left[\frac{d_{n2}\rho_{n2}^{1/2}}{d_{n1}\rho_{n1}^{1/2}}\right]^3 \tag{5.8}$$

Figure 5.3 shows this situation; a choked nozzle of 0.5 mm in diameter and operated at 15 MPa

for 1.17 ms satisfies the requirement of Eq. 5.8 when compared with an unchoked nozzle of 0.5 mm in diameter operated at 10 MPa for 1.74 ms. This second case leads to a slower jet penetration since the momentum at the nozzle is smaller. The result scales well up to a t_{inj}^* of 800, but there is a slight deviation later on. This deviation may be due to the difference in t_{inj} as one would expect, but it may be also due to wall effect as the jet comes in contact with the wall shortly after. Based on the two other cases presented, it appears that the effect of t_{inj} does not come into play until t/t_{inj} greater than approximately 2.

5.2.3 Chamber Turbulence

The third parameter of Eq. 5.2 is the chamber turbulence level. Jets create their own turbulence, but the turbulent fluctuations decrease in magnitude at the outskirts of the shear layer. There are certainly some radial positions where the turbulence levels in the chamber become of the same order of magnitude as those in the jet. Those radial locations would depend on the distance from the nozzle and on the actual turbulence level in the chamber, a higher turbulence level affecting regions closer to the jet centerline.

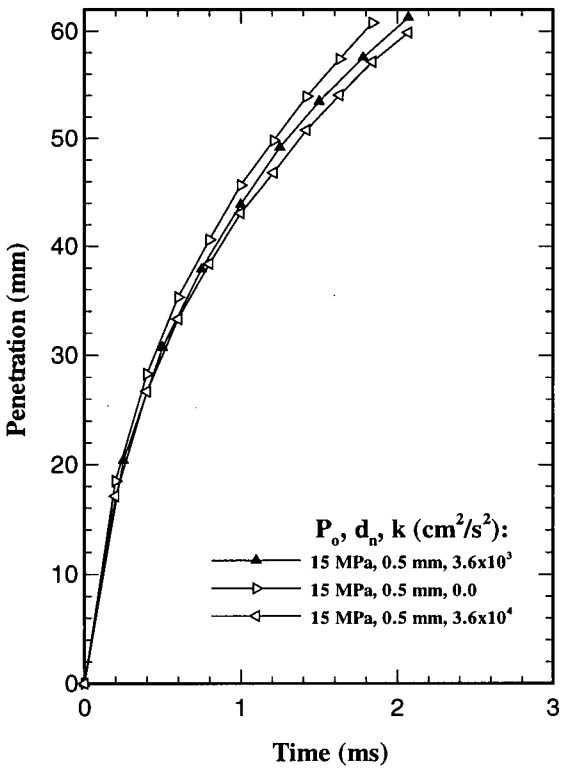

Figure 5.4 - Effect of chamber turbulent kinetic energy on jet penetration.

Figure 5.4 compares three cases, one with zero initial turbulence in the chamber, one with those suggested in Table 5.1 and representative of engine conditions, and one with ten

times higher turbulence levels. The nozzle velocity and equivalent diameter were 436 m/s and 0.88 mm. As may be seen, increasing the turbulence level by a factor of 10 led to a modest change in penetration rate of approximately 2.5%, based on a 3% mass fraction definition of penetration (one would expect a slightly larger effect on a penetration defined on a 1% mass fraction). Observation of the mass fraction distribution indicated that the reduction in penetration is accompanied by an increased jet spreading. For the case with turbulence levels typical of engines, the penetration is found to be approximately 4% lower than if the jet would propagate in a zero turbulence chamber.

5.3 NUMERICAL EXPERIMENTS - MIXING RATE

In Section 2.3.3, it was suggested, on the basis of the steady-state results of Ricou and Spalding [1961], that the mass entrainment rate of air into a transient gas jet could be expressed in terms of the same parameters as those used for the jet penetration; the nozzle momentum injection rate $\dot{M}_n$ and the chamber density ρ_{ch}. It was also suggested that the ratio of entrained mass to injected mass could be expressed in terms of the non-dimensional time. To verify that the mixing rate benefits from the same scaling laws, and also to observe the typical distribution of fuel in a transient jet, the mixing rate of the transient jets presented in Fig. 5.1 is now considered. In engines, it is of particular interest to consider the mixing in terms of equivalence ratio. Following Abraham *et al* [1994], the fraction of fuel within lean, flammable and rich zones was plotted as function of non-dimensional time tU_n/d_{eq}. The fraction of methane in the flammable zone is the total mass of methane in the chamber which exists within an equivalence ratio range between 0.5 and 2.0 divided by the total mass of fuel in chamber. For diesel engine combustion, burning may take place outside this specified "flammability" limit, but it is used here as a representative mixing characteristic.

The results of the scaling may be seen in Fig. 5.5. The mass fraction of fuel within rich and lean zones are also shown. As may be seen, all three mixture fractions scale well with the

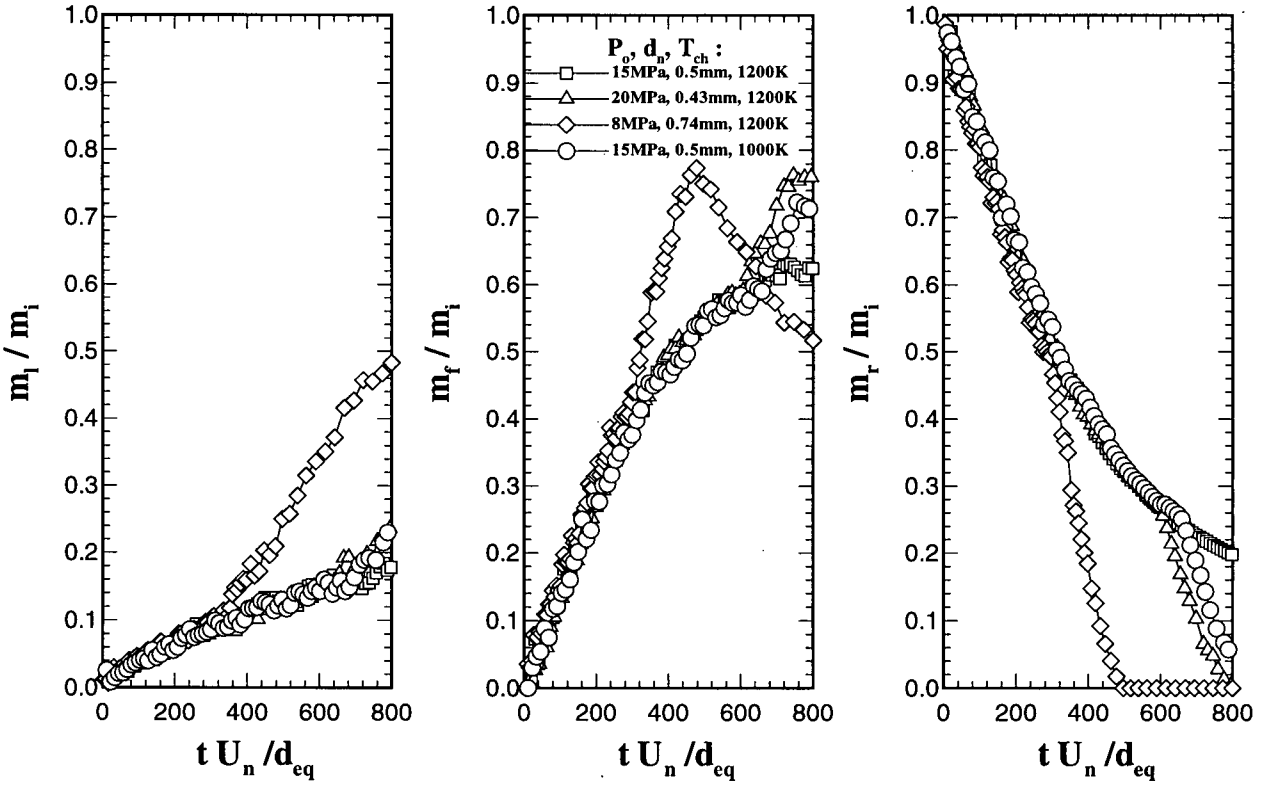

Figure 5.5 - Non-Dimensional mixing rate. m_l, m_f, m_r are the mass of methane in lean (Φ<0.5), flammable (0.5<Φ<2.0) and rich zones (Φ<2.0). m_i is the total injected mass.

equivalent diameter and nozzle velocity. The scaling is valid until the dimensionless end-of-injection (can be found in Table 5.2).

Abraham *et al* [1994] followed a dimensional argument to suggest that $d_{eq}=d_n(\rho_n/\rho_{ch})^{1/2}$ was the appropriate scale for transient jets, the same one found in this thesis on the basis of experimental work and dimensional analysis. They also proceeded to scale numerically obtained mixing rates for transient gas jets. As above, the amount of flammable methane-air mixture non-dimensionalized by the mass of injected fuel was plotted as a function of non-dimensional time

tU_n/d_{eq}. Numerical simulations for different nozzle diameters indicated that the non-dimensional amount of flammable mixture as a function of non-dimensional time was the same. When different density ratios were used, the non-dimensional amount of flammable mixture also collapsed reasonably well on the same curve. The results of Abraham *et al* provide support the findings in this work.

As mentioned in the introduction of this chapter, the mixing rate can be controlled by changing the number of nozzles. A question arises however as whether distributing the mass injection rate amongst a different number of nozzles has an impact on the mixing rate. In Chapter 2, it is suggested that the mass of air entrained in a jet issued from one nozzle of diameter d_n could be expressed as:

$$m_{ch} \propto \dot{M}_n^{3/4} \rho_{ch}^{1/4} t^{3/2} \qquad \textbf{(2.30)}$$

If the area of one nozzle is distributed amongst N nozzles of diameter d_s, according to $d_s^2 = d_n^2/N$ where N is the number of nozzles, then the total mass of air entrained is given by

$$m_{ch_N} \propto N \left(\frac{\pi}{4} d_s^2 \rho_n U_n^2\right)^{3/4} \rho_{ch}^{1/4} t^{3/2} \qquad \textbf{(2.30)}$$

The ratio of mass entrained in N jets to that entrained in one jet for the same mass injection rate is given by taking the ratio of Eq. 5.9 to Eq. 2.30, which yields

$$\frac{m_{ch_N}}{m_{ch_1}} = N^{1/4} \qquad \textbf{(5.10)}$$

Equation 5.10 indicates that distributing the mass injection rate amongst smaller nozzle increases the mixing according to $N^{1/4}$.

This situation is presented in Fig. 5.6, which shows the mixing rate for two cases, one with 8 holes of 0.43 mm and one with 4 holes of 0.612 mm (same total area). The ordinate is

the methane mass within the specified equivalence ratio zones (dimensional this time). For both cases, the injection pressure is 15 MPa and the total injected mass is 30 mg. Figure 5.6 shows that the formation rate of lean mixture is increased by using smaller holes, while the formation of rich mixture is decreased. The results show that over the range of interest, the formation rate of flammable fuel fraction is very similar for both cases, at least until the EOI (end of injection).

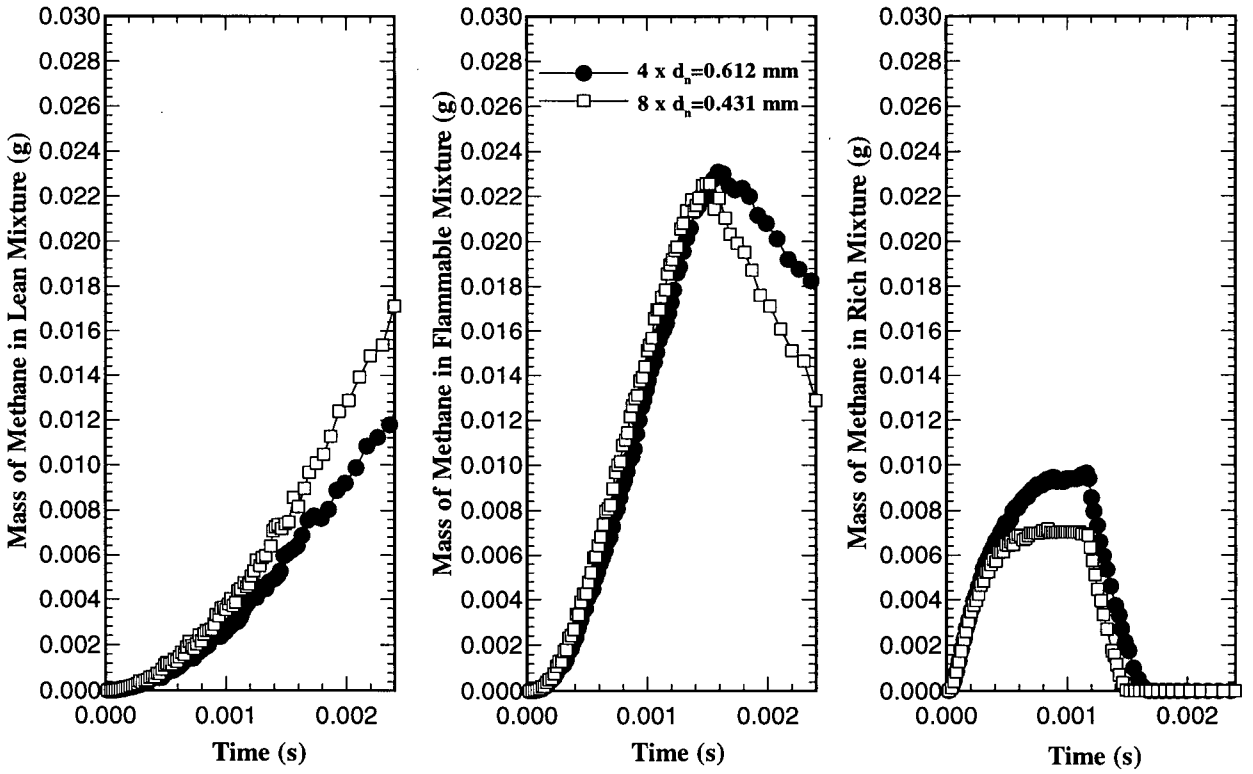

Figure 5.6 - Effect of using more, smaller holes on mixing rate. P_o=15 MPa, t_{inj} = 1.17 ms.

The result of Fig. 5.6 confirms that using more nozzles of smaller diameter increases the mixing between the fuel and the chamber air. The result can also be understood by considering that the total volume of rich cores is smaller for smaller nozzles than for larger ones (this can be easily demonstrated using the fact that the rich cores have a length proportional to the diameter, and then comparing the total core volume of N_1 holes with diameter d_1 with that of N_2 holes of diameter d_2, for the conditions that $N_1 d_1^2 = N_2 d_2^2$).

This result is also supported by the work of Jennings and Jeske [1994], who performed three-dimensional numerical simulations of gaseous jets for application in diesel engines. They numerically investigated the mixing rate of transient jets, defined as the mass of fuel with an equivalence ratio below 2, changing the number of holes while keeping the mass injection rate the same. Their numerical results also indicated that using more smaller holes was more effective at mixing the injected fuel, implying that lean mixtures were formed more rapidly. The authors also suggested that the smaller size of the rich core was the reason for that numerical observation.

The work of Jennings and Jeske also contains valuable practical information. For example the authors point out that above a certain number of holes, there is merging between jets, and the mixing advantage of smaller nozzles is lost. Based on separateness of equivalence contour lines of 0.5, their numerical results indicated that a maximum of 12 holes could be used. It is possible to arrive at this conclusion somewhat differently; turbulent jets have a spreading rate of approximately 25°, such that one can foresee a maximum of $360/25 \approx 14$ jets, assuming that the injector tip diameter is relatively small. They also found that smaller jets were more subject to top wall clinging than larger jets, which also reduces mixing by decreasing surface contact between the jets and the chamber air.

5.4 GASEOUS JETS VERSUS SPRAYS MIXING RATE

It is of interest to understand the differences between gaseous and diesel fuel liquid injections, since much is known about the conventional diesel combustion process. As discussed in Chapter 2, the angle of spread of sprays is affected by nozzle conditions, such that it is possible to obtain sprays that have a larger angle of spread than that of gaseous jets. Given equivalent momentum injection rate, a larger angle of spread should lead to a reduced

penetration, but the mixing rate may remain similar on the basis that the momentum drives the mixing. As an evaporative spray model is readily implemented in KIVA-II, a few cases were simulated to investigate this hypothesis.

The spray model consists of a Lagrangian treatment of spray particles superimposed on the gas flow. The computational spray particles represent droplets of identical velocity, size and temperature. A Monte-Carlo sampling technique is used such that a distribution of droplet size, velocity and temperature is considered. The particles exchange mass (evaporation), heat and momentum with the gas flow. Turbulence interaction, coalescence and aerodynamic breakup models are present and can be used.

The only modification brought to the spray model was to ensure that the mass and momentum injection rates were the same as those used for gaseous injections, including the initial transient velocity ramping. The comparison was performed in the same cylindrical chamber as the one used in the rest of the chapter. The boundary conditions were determined such that the mass and momentum injection rates were identical between sprays and gaseous jets. This required that the injection velocity be the same. To further ensure the similarity between sprays and gaseous jets, the cone angle of the sprays was set at 26°, which corresponds to that of the gaseous jet (based on the computed radial location where the velocity is 0.5% of the centerline velocity). The aerodynamic droplet break-up option of KIVA-II does not allow an angle of spread selection, consequently it was decided to inject small droplets without using the break-up option, retaining the capability of selecting the spray angle. Droplets of Sauter mean radius (*smr*) of 5 microns and 10 microns were considered. Turbulence interactions were considered, but coalescence of droplets was not. The conditions in the chamber (6 MPa, 1200 K) were the same for the sprays and for the gaseous injection case.

Figure 5.7 shows the mixing rate, defined once again in terms of equivalence ratio[2] for 3 different sprays and the gaseous injection. As can be seen, there is a not a great difference

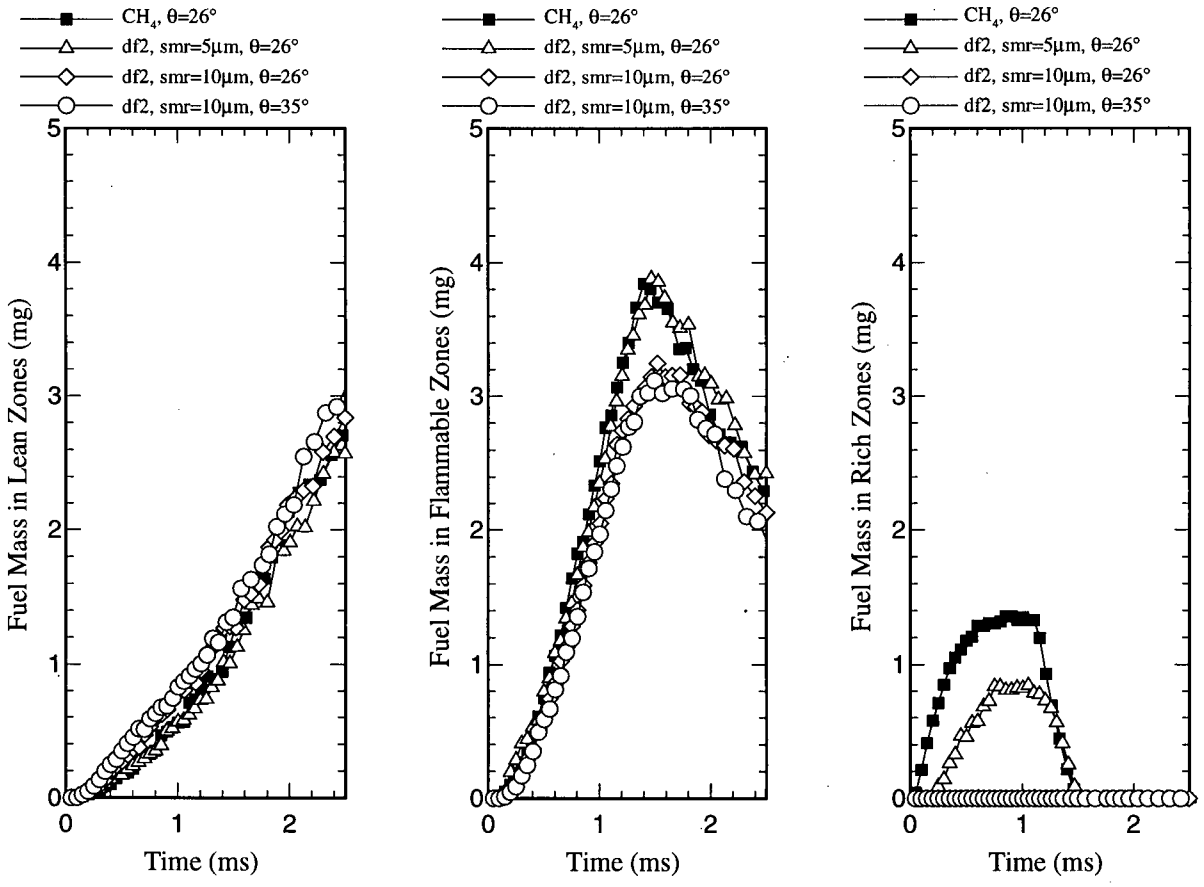

Figure 5.7 - Mixing rate for a gaseous jet and 3 different sprays, all with identical mass and momentum injection rate, and identical chamber conditions (T_{ch} = 1200 K, P_{ch} = 6 MPa).

between the mixing rate of sprays and that of jets. For the 10 μm droplets, the amount of rich and flammable mixture formation is slower, however the lean mixture formation rate remains essentially the same. This points to a significant difference between sprays and gaseous jets. In jets, there is automatically a rich core and a gradual leaning out towards the air side. In sprays, the droplets bring fuel far in the shear layer where they evaporate, such that there may

[2] The stoichiometric equivalence ratio corresponds to a mass fraction of approximately 6.3% for diesel fuel, and of 5.5% for methane, such that comparing mass fraction or equivalence ratio leads to similar results.

not be a rich vapor core. This is illustrated further in Fig. 5.8, where the gas jet is compared with two sprays, with droplets of *smr* equal to 5 and 10 μm, both with a cone angle of 26°. In

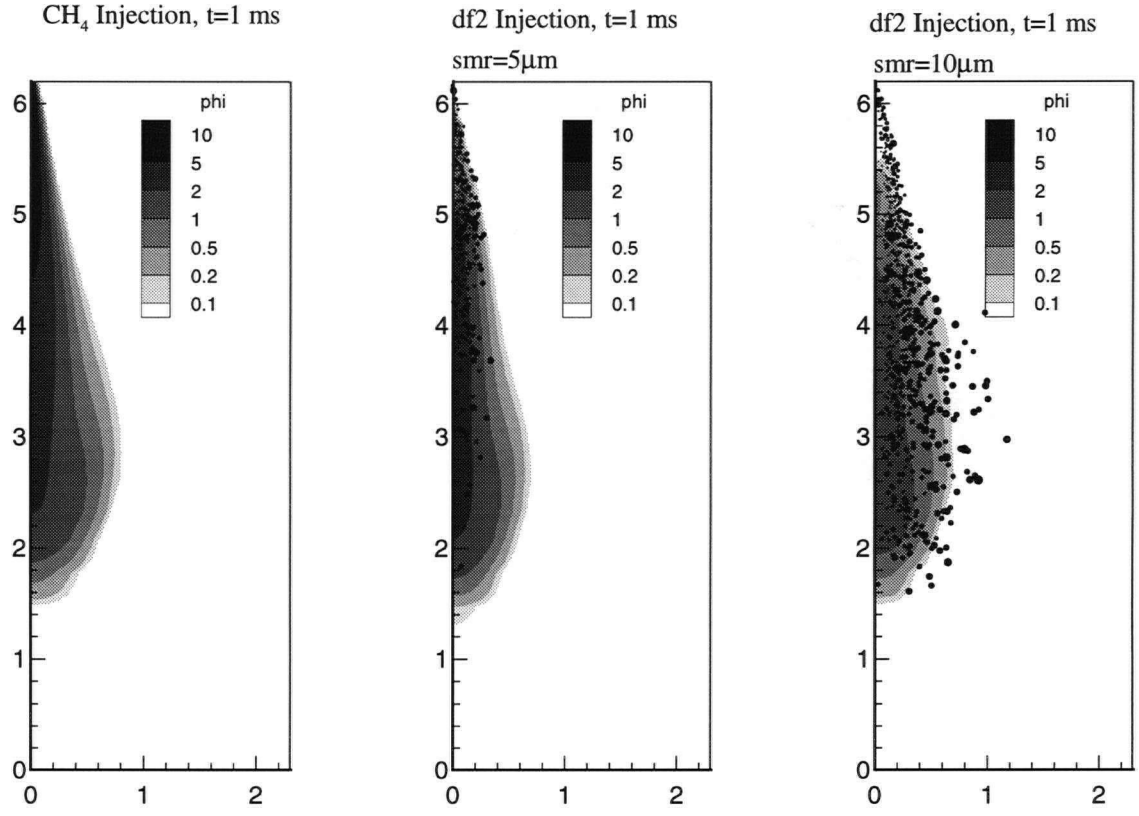

Figure 5.8 - Difference in equivalence ratio contours for a gaseous jet and sprays (cone angle for sprays is 26°).

these contour plots, as in Fig. 5.7, the droplets are not considered in the equivalence ratio calculation. It is particularly evident in the last case that there is a smaller rich area and that remaining droplets are brought to the lean area. This may be an advantage in combustion since droplets will bring fuel well into the oxidizer side of the reaction zone. It is also seen that for equal momentum and similar spreading rate, the penetration distance is roughly the same.

Figure 5.7 also shows the effect of increasing the cone angle of the spray from 26° to 35°[3]. As hypothesized, the mixing rate did not change significantly. Looking at the equivalence ratio contours, Fig. 5.9, reveals that the mixing took place closer to the nozzle, but that the penetration was slower.

As a final note, it should be mentioned that the similarity between the mixing rate of sprays and that of gaseous jets obtained in this work contrasts with one of the conclusions of Abraham *et al* [1994]. They conclude, following numerical simulations of both sprays and jets with equivalent mass and momentum injection rate, that sprays mix significantly faster than gaseous jets. In investigating the possible sources of discrepancies between their work and this work, it was found that the gaseous mixing rate reported by Abraham *et al* was abnormally low. This was shown by reproducing the conditions of their simulation with the current validated model. The compared mixing rates can be seen in Appendix G.

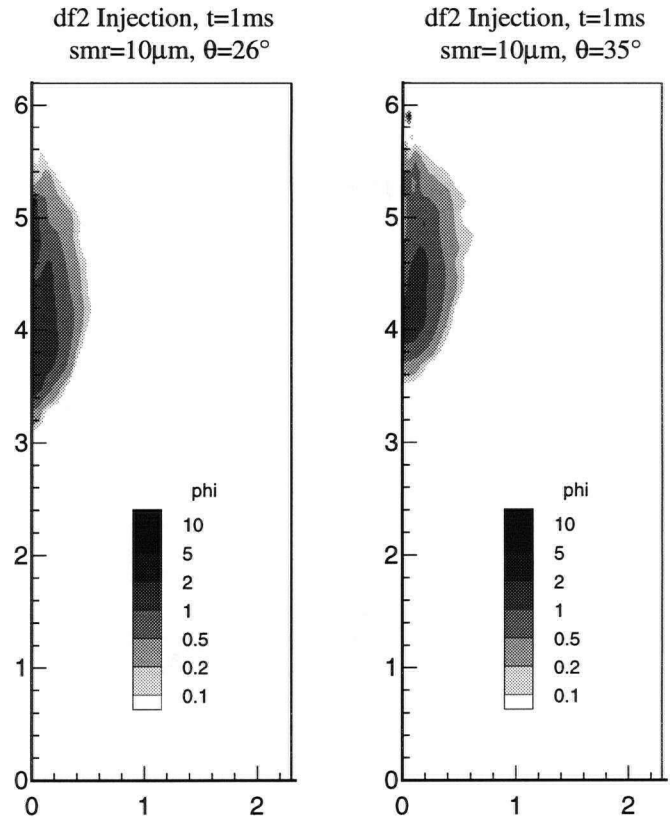

Figure 5.9 - Equivalence ratio contour lines for sprays with angle of 26°and 35° at 1 ms after BOI.

[3] The selection of a spray angle of 35° is not intended to represent a practical condition, only to investigate the effect of angle change. The two-dimensional spray investigated in Abraham *et al* [1994] also has, apparently (based on velocity field), such an angle.

5.5 SUMMARY AND PRACTICAL CONSIDERATIONS

5.5.1 Summary

The work presented in this chapter shows that the numerical predictions of jet tip penetration, in a chamber with typical diesel engine conditions, could be well scaled with the equivalent diameter d_{eq} and the time scale d_{eq}/U_n. The numerical model was used to investigate the mixing rate of transient gaseous jets, which was also found to collapse on a universal curve when plotted as a function of non-dimensional time (for times up to t_{inj}). The effect of injection duration was also investigated and it was found that the penetration remains much the same for times up to 2 t_{inj}. A large change in specific turbulent kinetic energy was found to only mildly affect the jet penetration as defined in terms of the 3% mass fraction contour line. The mixing rate of gaseous jets was compared to that of sprays in Section 5.4. It was found that, for sprays with droplets of 5 and 10 μm (*smr*) injected in a chamber at 1200 K, the mixing rates of gaseous jets and sprays were much the same for equivalent nozzle momentum and mass injection rate. Furthermore, when the cone angle of the sprays and spreading angle of the gaseous jet were roughly equal, the penetration was also similar. When the spray cone angle was increased, the penetration of the fuel vapor was found to be reduced, but the mixing rate remained much the same.

5.5.2 Gaseous Fuel Jets for Diesel Engine Fueling

With the above findings, it is possible to investigate a few practical questions regarding transient gaseous jets for compression-ignition engine fueling. In particular, what should be the size and number of holes and what should be the injection pressure. Here the intent is not to answer these questions, since they are engine dependent and since combustion needs to ultimately be taken into account; however, there are a few guidelines that can be readily established. First

the questions of injection pressure and nozzle diameter are discussed. Comments on the number of nozzles for gaseous fueling are discussed in Section 5.5.2.2.

5.5.2.1 Injection Pressure and Nozzle Diameter

Figure 5.1 shows an important fact; one can in principle replace a small nozzle operated at high injection pressure by a larger nozzle operated at a lower injection pressure. This is particularly important in this project, as the gaseous fuel must be compressed from a tank with low fuel content and low fuel pressure to the desired injection pressure. As the compression is an energy expenditure, lower injection pressures are better. For choked nozzles, it is possible to duplicate both the mass injection rate and the momentum injection rate. If the choking condition is removed, then one can either duplicate the momentum injection rate or the mass injection rate.

In practice, there are some constraints on the choice of hole size diameter and on the choice of injection pressure. If it is desired to maintain a choked nozzle, which is an advantage from the point of view of injection control, then the injection pressure must be set at roughly twice the maximum engine pressure. Furthermore the combined area of all holes must represent a minimum area in the injector; this provides a maximum diameter given a certain number of holes.

The penetration rate is controlled by the nozzle momentum injection rate, which is governed by injection pressure and nozzle diameter. Prevention of over-penetration is a constraint on the choice of injection pressure and nozzle diameter. One way to determine the maximum desirable momentum injection rate is direct engine testing, which may reveal for example higher unburned fuel fraction in the exhaust as the momentum injection rate is increased. Another approximation is to set a target time for the jet penetration based on engine size and

ignition delay. For example, the arrival time of the jet tip at the closest wall (cylinder wall or piston) should be shorter than the ignition delay. For the engine under consideration, the distance between the injector nozzle and the bowl of the piston at TDC is approximately 45 mm. In Fig. 5.1, for an injection pressure of 15 MPa and a nozzle of 0.5 mm, that distance is reached in just over 1 ms. If the ignition delay is of that order, than the jet would impinge on the wall before burning, which is not desirable. When engines of different bore sizes are considered, the penetration rate can be readily estimated from Eq. 3.1, rewritten here

$$\frac{z_t}{d_{eq}} = C_c + C_t\left(\frac{tU_n}{d_{eq}}\right)^{1/2} \qquad \textbf{(5.11)}$$

where the constant C_t is approximately 2.9 from the experimental data of Fig. 3.11 and the literature data, and where the constant C_c depends on the injector's transient response (in this work, C_c was approximately -20 for correctly expanded cases, and -13 for the underexpanded cases). For the reported experimental data of Chapter 3, the linear dependency holds from a non-dimensional time t^* greater than 150, or for distances greater than 20 z_t/d_{eq}.

Another possibility for the determination of the injection rate is to duplicate the penetration rate of the diesel fuel sprays for the engine considered. This assumes that the diesel fuel spray penetration has been optimized for best air utilization in the chamber without over-penetrating, and requires knowledge of the sprays penetration rate. As an example, this argument is followed below for the engine under consideration.

As shown in Section 5.4, sprays which have a cone angle similar to the angle of spread of gaseous jets would penetrate at a similar rate for a given momentum injection rate. In Chepakovich [1993], diesel sprays issued from the diesel injector for the 6V-92 were visualized and have a cone angle of approximately 22° (non-evaporating). The angle of spread of the gaseous jets in the numerical experiments of this chapter is roughly 26°, but, based on the

comparison between experimental and numerical work in Chapter 4, it is overestimated by approximately 10%, so that the angle of spread of gaseous jets is expected to be approximately 23°. Assuming, for the engine under consideration, that the angle of spread is similar between gaseous jets and sprays, then to reproduce penetration rate one must reproduce the nozzle momentum injection rate. This argument is supported by the results of Fig. 5.8. Now when diesel fuel is substituted by natural gas, the equivalent momentum at the nozzle leads to

$$d_n = d_{df} \left(\frac{\rho_{df} U_{df}^2}{\rho_n U_n^2}\right)^{1/2} \tag{5.12}$$

where the subscript *df* refers to diesel fuel. For diesel fuel, the density is approximately 780 kg/m^3. For the engine under consideration, there are 9 nozzles 0.14 mm in diameter per cylinder. The velocity can be evaluated by correlating the injection duration with the fuel consumption for various load levels. This provides an average velocity over the injection event of 330 m/s. For natural gas, the nozzle density and velocity depend on the choice of injection pressure. The estimate of nozzle diameter for various injection pressures, assuming P_{ch} = 6 MPa and T_o=350 K is given in Table 5.3. In that table, only the injection pressures of 15 and 20 MPa would satisfy a choked nozzle criterion at all times, while the 12 MPa injection pressure case would

P_{inj} [MPa]	ρ_n [kg/m^3]	U_n [m/s]	d_n - max. [mm]
8	37.6	285.6	0.74
10	40.6	375.4	0.54
12	45	430	0.45
15	54.13	436	0.40
20	73.4	439	0.35

Table 5.3 - Maximum hole diameter for gas nozzles to approximate diesel momentum injection rate (based on 6V-92 DDC engine figures).

satisfy it over a wide range of operating conditions.

As a final note on establishing nozzle diameter and injection pressure, it is interesting to consider the consequences of their determination based on mass injection rate rather than momentum injection rate. If one aims to duplicate the mass injection rate per nozzle, the following situation arises:

$$\frac{\dot{M}_n}{\dot{M}_{df}} = \frac{\rho_n U_n^2 \, d_n^2}{\rho_{df} U_{df}^2 \, d_{df}^2} = \frac{U_n}{U_{df}} \qquad \textbf{(5.13)}$$

which indicates that the gas injection momentum rate could be higher than that of diesel fuel given a U_n greater than U_{df}. For the example above, the momentum injection rate would be 33% greater than for the diesel operation (440/330). It should be restated that these estimates are approximate, are based on the assumption that one wants to reproduce the diesel fuel sprays penetration rate, and therefore may be considered as initial estimates.

5.5.2.2 Mixing Rate

Figure 5.5 and the discussion that accompanied it indicated that the mixing rate of a jet issued from one nozzle is controlled not by the mass injection rate but by the momentum injection rate at that nozzle. To further illustrate this point, one more example is presented. Three cases are presented in Fig. 5.10 and serve to illustrate two situations. The first situation considers the injection of 5 mg of methane for cases with equal mass injection rate, but different momentum injection rate (P_o=15 MPa, d_n=0.5 mm leading to U_n=436 m/s, and P_o=8 MPa, d_n=0.74 mm leading to U_n=285 m/s). The mixing rate of the 15 MPa injection case is faster, as the nozzle momentum injection rate is faster. The second situation considers cases with different mass injection rate but with equal momentum injection rate (P_o=15 MPa, d_n=0.5 mm and P_o=10

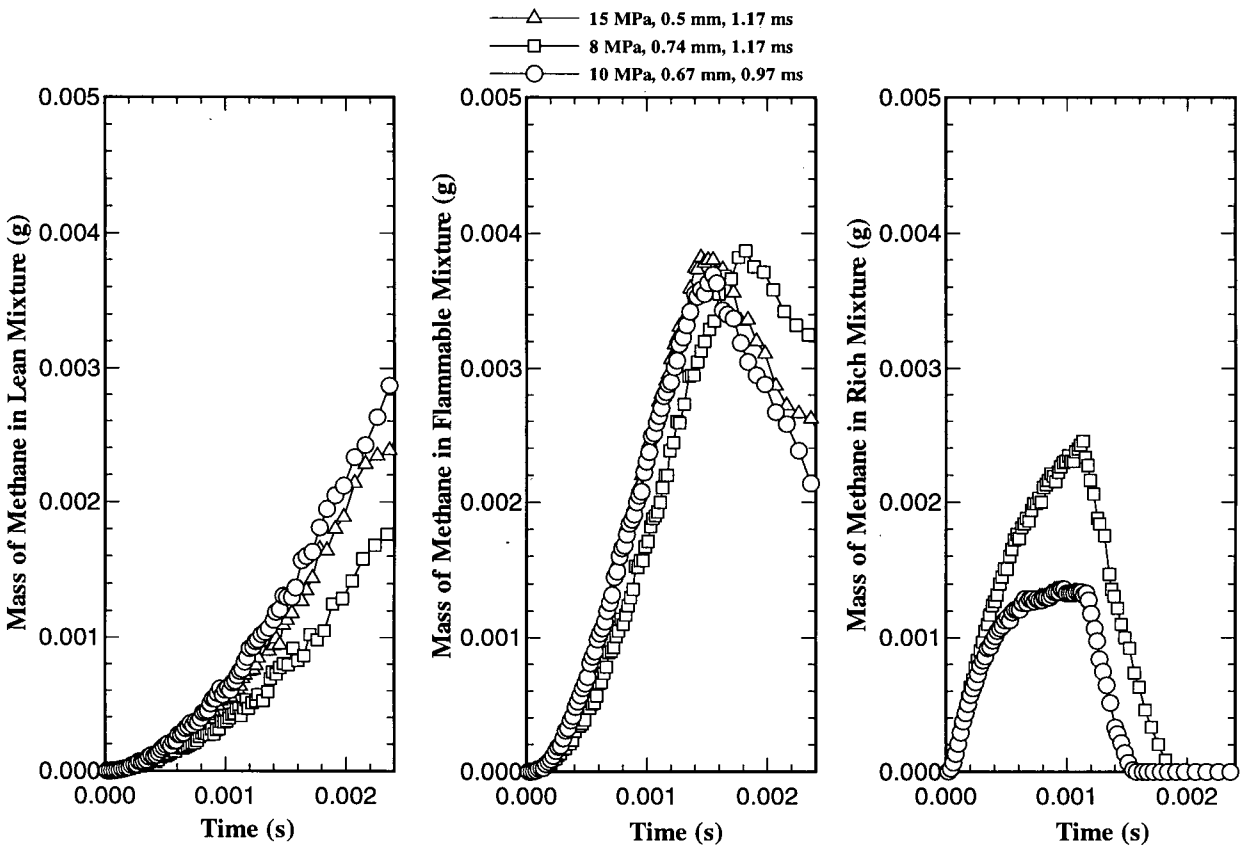

Figure 5.10 - Mixing rate for cases with equal momentum injection rate and for cases with equal mass injection rate.

MPa, d_n=0.67 mm leading to U_n=375 m/s). Clearly the mixing rate is almost identical despite the difference in mass injection rate and injection duration. Of course one also obtains the same mixing rate if both mass and momentum injection rates are reproduced (which requires the same nozzle velocity), as reported in Fig. 5.5. Figure 5.10 shows that the momentum injection rate controls the mixing rate. (The penetration rate is also the same for the two cases with equal momentum but different for the cases with constant mass injection rate).

When multi-holes are considered, the mixing rate is slightly improved, as discussed in Section 5.3. The mixing rate remains however more dependent on the momentum injection rate (power 3/4) than on the number of holes (power 1/4), and as an approximation the total mixing rate in the chamber is dictated by the total momentum injection rate.

Following the approach discussed in the previous section, it is assumed, as a first estimate, that one wants to duplicate the combustion rate of the conventional diesel fuel engine. This would ensure for example that the maximum pressure would not be exceeded and that the combustion rate optimized on the basis of best performance and emissions is maintained. Recognizing that there will be some differences in emission formation with the use of natural gas, the combustion rate should be re-optimized when natural gas is used as a fuel.

To duplicate the combustion rate, one would need to essentially duplicate the chemical heat-release rate. The heat release rate depends on the burning rate and energy content of the fuel. The burning rate, after the ignition, is mainly controlled by the turbulent mixing rate of fuel and air and, as such, the chemical kinetic characteristics of the fuels are of lesser importance following ignition. For diesel fuel and high-methane content natural gas, the difference in LHV is of the order of 5 to 10%, so that duplicating the mixing rate on a mass basis would be a good approximation. As discussed above, to duplicate the mixing rate one must duplicate the momentum injection rate.

Based on the assumption that the broad features of the original diesel engine operation are to be reproduced, the following comments can be made regarding the choices in number of holes for gaseous fuel injection. Since the gaseous momentum injection rate of each nozzle is at most that of the diesel spray nozzle (Section 5.5.2.1), and since the total momentum injection rate is to be duplicated, it follows that the number of holes for gaseous operation should be equal or greater than the number of holes of the diesel injector. Fewer holes would require a higher nozzle momentum rate to provide the same mixing rate which could lead to over-penetration (fewer holes could be operated at the maximum momentum injection rate for a longer time but then the overall mixing rate would also be slower). More holes could be used, with nozzle momentum injection rate lower than the determined maximum rate. This would result in smaller

penetration rates than that of sprays in the original engine (see Fig. 5.2 which shows that using more smaller nozzles while keeping the overall injection rate constant also changes the extent of penetration rate). More holes operated at the maximum momentum injection rate and operated for a shorter time could also be used, but would lead to an overall faster mixing rate.

The presented analysis is simplified, and some aspects of the system need further consideration. In particular, in the proposed system, the natural gas does not replace all the diesel fuel, since pilot diesel fuel is used to assist ignition. The optimal or minimum level of pilot diesel fuel is not known at this stage, but operation so far has been done with some 20% pilot fuel at medium load. This does not change the momentum injection requirement for each nozzle but invites further consideration of the number of holes. Also, since there may be a longer delay incurred by the need to ignite two different fuels, one may well need to increase the combustion rate when using natural gas.

CHAPTER 6

MULTIDIMENSIONAL MODELLING OF IGNITION AND COMBUSTION OF METHANE TURBULENT JETS

6.1 INTRODUCTION

The dependency of the penetration rate of transient methane jets upon injection and chamber conditions was established in the previous chapters, and it was shown that multi-dimensional modelling could well reproduce the experimentally observed penetration rate and the dependance upon injection and chamber conditions. Part of the objectives of this thesis is to also verify the impact of ignition and combustion on the findings of Chapters 2 to 5, and to establish the effects of injection pressure, nozzle diameter and chamber conditions on the ignition and combustion of methane in a diesel environment. The multidimensional model was accordingly extended to investigate the ignition and combustion of transient underexpanded methane jets. A combustion sub-model was incorporated in the multidimensional code presented in Chapter 4 which is capable of capturing the main features of methane combustion in diesel engines. The objective of this chapter is to establish a suitable methane combustion model. Since the usage of detailed kinetic schemes within the current multidimensional model would lead to prohibitively long computational times, simple oxidation schemes are sought. First, combustion modelling work discussed in the literature is reviewed in Sections 6.2 to 6.4. The suggested combustion model is presented in Section 6.5, while its behavior and sensitivities are assessed in Section 6.6. The ignition and combustion of transient underexpanded methane jets in a diesel-like environment

are investigated in Chapter 7.

The combustion of the fuel in a diesel engine progresses in space and time through various regimes characterized by the type of mixture (premixed or non-premixed) and by time scales associated with the turbulent mixing and the chemical kinetics of the mixture. Typically, three phases are encountered over a diesel combustion cycle: ignition, premixed-phase burning and mixing-limited burning.

In diesel engines, there is a delay in the order of 1 ms between the beginning of fuel injection and the ignition, which manifests itself by a sudden increase in pressure rise in the chamber. This ignition delay is the sum of physical delays - the need to atomize and evaporate the liquid fuel - and of the chemical delay. For a given mixture strength and temperature, it takes a finite time to reach a state where the heat generation causes a rapid acceleration of the reaction rate. In gaseous injection systems, the delay is expected to be mainly a chemical delay, although there may also be a short mixing delay. That this delay is short can be appreciated by realizing that the velocity is high in the nozzle area while the length scale is small due to the small nozzle diameter.

In this chapter, the ignition of methane is treated as an autoignition problem. It is acknowledged that in the proposed conversion system, the pilot diesel fuel spray promotes the methane jet ignition. As will be discussed in Chapter 7, the pilot fuel combustion helps the methane ignition by raising the chamber pressure and temperature and by providing pockets of hot combustion products. In the case of temperature increase, the autoignition treatment is warranted. Autoignition is also suited to represent the thermal effect of hot combustion product entrainment, particularly considering that the combustion products may be cooled by mixing with chamber air prior to being entrained in the gas jet. A simple autoignition scheme would not however reproduce the chemical effect of radical entrainment on the ignition of the methane jet.

It should also be mentioned that pilot fuel combustion is not the only approach to assist the auto-ignition of natural gas. High-compression ratio engines and glow plugs locally warming the methane/air mixture could also be used, in which case the autoignition scheme would be appropriate.

During the ignition delay, some of the incoming fuel mixes with the air in the chamber, generating a premixed blend of varying equivalence ratio. This premixed fuel is consumed during the premixed phase with a high heat-release rate. At some time, the fuel within premixed regions in the chamber is consumed, and the subsequent reaction rate becomes dependent on how fast the fuel and oxidizer mix together. This is the mixing-limited phase, and a diffusion type flame is established with a reaction zone locating itself near the stoichiometric point of the mixing layer between the oxidizer and the fuel. A schematic of the three phases can be seen in Fig. 6.1.

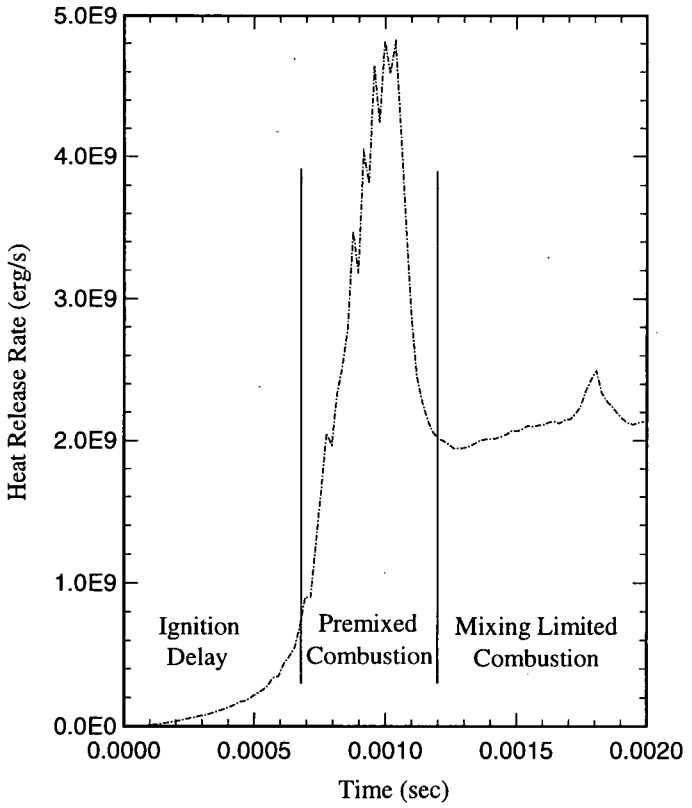

Figure 6.1 - Three combustion phases typical in diesel engines (KIVA-II Simulations).

The ignition phase is characterized by chemical time scales longer than turbulent mixing time scales, and is therefore dependent on the chemical kinetic properties of the fuel, which themselves are functions of the temperature and pressure in the chamber. Following ignition, the

temperature rises and the chemical time scales become, at some times and places, smaller than the mixing time scales. The turbulent mixing time typically governs the combustion during the premixed and mixing-limited phases in diesel engines. During the mixing-limited phase, the combustion rate becomes a mixing rate problem and can be approximated as independent of the fuel chemical kinetic properties.

To represent the combustion history with a multidimensional code, the model must include a kinetic scheme appropriate for the ignition phase, and a turbulent combustion model capable of representing the combustion rate in both the premixed and the mixing limited phase. There may be a need for a transition between these two sub-models as the ignition kinetic scheme is expected to have a limited range of applicability. In the next section the ignition of methane and its modelling are discussed. Reduced methane oxidation schemes applicable to temperatures higher than those prevailing at ignition and which may serve as a transition between the ignition and mixing-limited combustion are discussed in Section 6.3. Section 6.4 reviews the problem of turbulent combustion.

6.2 AUTOIGNITION OF METHANE

6.2.1 Experimental Investigations

Autoignition of methane in a diesel environment has been studied by Fraser, Siebers and Edwards [1991] and in a refined apparatus by Naber *et al* [1994]. The later work is an extension to the work of Fraser *et al*, with similar experiments performed in an upgraded apparatus, and is discussed here. In these experiments, natural gas or methane is injected at high velocity in a cylindrical chamber. The temperature of the air in the chamber is controlled by burning a premixed air and fuel blend whose products are similar in composition to air. The walls of the chamber are kept at a fixed temperature of 450 K. Ignition of the gaseous jet was identified with

optical techniques and by recording the pressure rise in the chamber.

Figure 6.2 presents the experimental results of Naber *et al* for pure methane. The most significant result is that to obtain an acceptable delay of 1 to 2 ms with a conventional natural gas blend, the temperature must be greater than 1120 K. By comparison, the peak temperature in diesel engines before ignition maybe between 750-900 K; thus illustrating the need for ignition assist.

The results in Fig. 6.2 exhibit three features. i) The ignition delay is proportional to $P^{-0.94}$, P being the pressure in the chamber. Numerical computations based on a detailed kinetic scheme

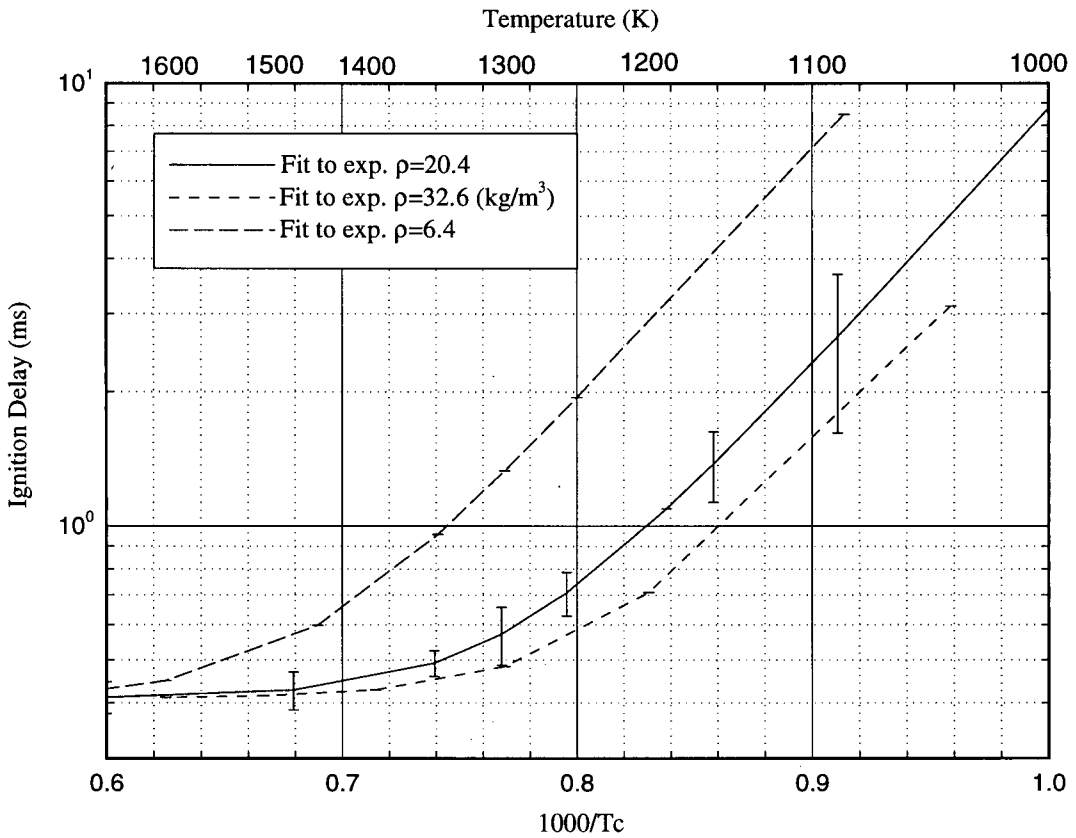

Figure 6.2 - Fit to the experimental data of Naber *et al* [1994] for the autoignition of methane in a simulated diesel environment.

in the same paper lead to a pressure dependency of $P^{-0.76}$. ii) The tailing off of the curve at high

temperature is not a kinetic effect. A fixed pressure rise of 14 kPa above the pressure decay fit was used as the ignition delay definition. To raise this chamber by 14 kPa requires the consumption of a minimum amount of fuel (~0.33mg), and to inject 0.33 mg of fuel takes about 0.4 ms, which explains the tailing off of the curve at high temperatures. iii) At lower temperatures, where injection is not limiting the pressure rise, the ignition delay is a linear function of the inverse of the temperature; this indicates that ignition is mainly a kinetic phenomenon and that an Arrhenius relationship can be used to model it.

Naber *et al* proposed a correlation, a fit to their data, between the ignition delay and the temperature and pressure in the chamber. The intent of this correlation is to provide an estimate of ignition delay given a pressure and initial temperature in the chamber. The correlation is not suitable to use as an ignition model within a multidimensional model, in which a delay or a rate function of local equivalence ratio is required. The data of Naber *et al* do represent a valuable set of experimental conditions which will be used to confirm the proposed model (Section 6.5.1).

Unlike the experiments described above, the composition, pressure and temperature can be considered uniform in shock-tube determination of autoignition. Reports in Tsuboi and Wagner [1974] and Lifshitz, Scheller, Burcat and Skinner [1971] indicate that the ignition delay can be well correlated with an Arrhenius relationship. These correlations provide dependency on pressure and temperature, as well as on mixture strength. Tsuboi and Wagner conducted a large amount of experiments with variable densities, variable mixture fraction, variable temperature and variable dilution factor. The range encompassed is the following : temperatures between 1200 and 2100 K, equivalence ratios between 0.2 and 2.0, and total densities between $2x10^{-5}$ and $2x10^{-3}$ mol/cm^3, which correspond to pressures between 3 and 300 atm at 1800 K. They obtained the following autoignition correlation, where the ignition delay is in seconds and the concentrations in mol/cm^3:

$$\tau_i = 4 \cdot 10^{-15} [CH_4]^{0.32} [O_2]^{-1.02} [Ar]^{0.0} \cdot e^{\left(\frac{222 kJ/mole}{RT}\right)} \quad \textbf{(6.1)}$$

which was found to be valid for fuel/oxidizer dilution in Argon above 1%. The group of Lifshitz *et al* have performed a similar experimental study and found an analogous correlation for temperatures between 1500 and 2150 K, equivalence ratios between 0.5 and 2, and pressures between 2 and 10 atm:

$$\tau_i = 3.62 \cdot 10^{-14} [CH_4]^{0.33} [O_2]^{-1.03} [Ar]^{0.0} e^{\left(\frac{195 kJ/mole}{RT}\right)} \quad \textbf{(6.2)}$$

These results suggest that a single oxidation step with a reaction rate incorporating an apparent activation energy and the proper empirical species exponents could predict the autoignition with some accuracy under various pressures and equivalence ratios. In both cases the ignition was found to exhibit a pressure dependency of approximately $P^{-0.7}$. According to Eqs. 6.1 and 6.2, the equivalence ratio dependency is of the order of unity (a richer mixture takes longer to ignite).

6.2.2 Modelling

It is generally recognized that autoignition in diesel engines remains largely a chemical kinetic problem, despite the turbulent levels typical of engines. This is supported by the experimental data of Naber *et al* presented in Fig. 6.2, where the delay is well correlated by an Arrhenius relationship at the lower temperatures (in these experiments, turbulence levels typical of diesel engines were produced using a small fan inside the chamber). This can also be justified by realizing that the ignition phase is characterized by long chemical times compared to mixing times (small Damkholer numbers). The ignition delay can be taken as a chemical time scale (~1 ms), while a mixing time scale can be estimated as l/u' where l is a turbulent length scale

typically taken as a fraction of the nozzle diameter (~0.1 mm) and u' is a fluctuating velocity. The value of the fluctuating velocity can be obtained as a fraction of the main flow kinetic energy, which may yield values between 1 m/s far from the jet nozzle to 10 m/s in the vicinity of the nozzle. This indicates that chemical time scales may be 10 to a 100 times larger than the mixing time scales prior to ignition. Consequently, a kinetic treatment of ignition is warranted. This does not mean that turbulence has no influence on ignition in diesel engines, but only that the reaction rate can be computed based on the average properties at a given point.

Detailed kinetic schemes for the oxidation of methane can be used for prediction of autoignition. Modern methane oxidation schemes now have more than 100 reactions and species. The most severe limitations of the detailed schemes for engine simulation, at this time, is a much too long computing time when such schemes are integrated within multidimensional fluid flow models. Consequently, their utilization is limited to problems where details of the flow can be simplified.

Detailed oxidation mechanisms may be used in homogeneous cases to stress particular features of the ignition process. In particular, it was hoped that reported autoignition studies using detailed mechanism would confirm or refute the accuracy of an Arrhenius relationship between temperature and ignition delay.

Glassman [1987] reports that there is a low and a high temperature mechanism for methane oxidation, and one would think that the low-temperature mechanism is the one of interest for autoignition problems. However, Glassman reports that the boundary between the low and high temperature scheme is 1000 K. Since at these low temperatures the ignition delay of methane is too long to be considered of interest in engines, the high temperature oxidation

mechanism would be of interest here[1].

Coffee *et al* [1983] used a detailed scheme (that of Dixon-Lewis, 14 species, 34 reactions) and found that there was a definite change in the slope of the Arrhenius plot for heat release at 1000 K. Westbrook computed ignition delays based on a detailed mechanism of methane oxidation (in Naber *et al* [1994]). The results of ignition delays for different temperature do not show sign of change at 1000 K (nor did the experimental data, but the scattering is large). The results display a linear relationship between the logarithm of the ignition delay and the reciprocal temperature. The detailed scheme (156 reactions) used by Mulholland, Sarofim and Beer [1992] does not either have such a change at 1000 K. Apparently most recent detailed models still predict an Arrhenius relationship for the ignition of methane. This suggests that over the temperatures of interest, a constant single-step activation energy could be used for a wide temperature range (800 - 2000 K).

Contrasting with this view is the study provided by Zhou and Karim [1994], who used their own methane oxidation mechanism (148 elementary reactions) to study the ignition of stoichiometric methane and air mixtures at atmospheric pressures. Contrary to other simulations, the relationship between the ignition delay and the reciprocal of the temperature is not linear, with apparently lower activation energy at lower temperature. The scheme of Mulholland *et al* mentioned above also showed a slight curvature, but with higher activation energy at low temperature. Apparently there is still considerable uncertainty in using detailed mechanisms, partly because reaction rates of many sub-species are not well known.

Among the models that can be realistically incorporated in multidimensional codes, are

---

[1] Glassman reports that the cut-off at 1000 K occurs because the oxidation of the methyl radical to form formaldehyde and hydroxyl, which represents the main chain propagating step, does not occur significantly above 1000 K. Instead the methyl radicals react with oxygen to form methoxy radicals, an endothermic reaction which slows down the oxidation process, explaining the slower burning characteristics of methane.

reduced schemes, such as the one proposed by Mulholland *et al.* The scheme contains 13 species and 10 reactions, but has been validated only for stoichiometric mixtures at atmospheric pressure, whereas ignition occurs at high pressure and tends to take place in lean mixtures in diesel engines.

The Shell ignition model (Halstead, Kirsch and Quinn [1977]) is a generalized scheme based on up to 8 generalized reactions that has been developed to reproduce ignition features in premixed charge such as cool flames and negative temperature exponent of the reaction rates. Single-step mechanisms cannot reproduce such features. However, methane does not exhibit these phenomena and it appears unnecessary at this stage to utilize the Shell model for compression ignition of methane.

Following the practice in diesel engine modelling, an autoignition correlation can be used to predict the ignition. Abraham and Bracco [1993] have simulated autoignition of diesel fuel in diesel engines by modelling the rate of formation of a species representative of radical formation. The rate of formation of that species is

$$RR = 1/\tau \tag{6.3}$$

where τ is a delay of the form:

$$\tau = A \left(\frac{P}{P_{ref}}\right)^{B} e^{D(1+C|1-\Phi|)/T} \tag{6.4}$$

where P and P_{ref} are the pressure and a reference pressure respectively, and Φ the equivalence ratio. Presumably a correlation for methane could be obtained by matching the experimental data of Naber *et al* or shock-tube autoignition data.

6.3 REDUCED OXIDATION MECHANISMS FOR METHANE

Once ignition has occurred in a particular region of the jet, the temperature and concentration of combustion products increase, given that the rate of species formation and of heat release are greater than the local heat and mass diffusion. The ignition mechanism may not be applicable under these conditions, and the reaction rate may not yet be limited by turbulence. Most published multidimensional engine simulations, either of premixed charge or of compression ignition, only consider an ignition phase and a turbulence-limited control of the subsequent combustion. Because of the wide inhomogeneity in temperature and equivalence ratio present in diesel engines, it may be that at least a simplified kinetic scheme with reasonable flame propagation capability is warranted. Furthermore, a simplified but realistic kinetic scheme may permit the determination of a more accurate chemical time scale, which can be compared to the turbulent-mixing time scale.

Westbrook and Dryer [1981] have performed the most comprehensive work on the usage of reduced kinetic schemes for hydrocarbon oxidation. Experimental laminar flame speeds for various hydrocarbon fuels were reproduced with either a single-step or a two-step oxidation mechanism. The dependency of the laminar flame speed on pressure and equivalence ratio is introduced through empirical species reaction order. For methane, the following one-step reaction rate was used for complete oxidation of CH_4 to CO_2 and H_2O[2]:

$$RR\ [mol/cm^3/s] = 1.3\times10^9\ [CH_4]^{-0.3}\ [O_2]^{1.3}\ e^{\frac{-202kJ/mol}{RT}} \qquad \textbf{(6.5)}$$

In this case, the flame speed pressure dependency is given by $P^{-0.5}$. It is interesting to note the

[2] For methane, Westbrook and Dryer proposed 2 schemes, the second one having an activation energy of 125.6 kJ/mol and a accordingly different pre-exponential constant. Here the activation of 202 kJ/mol is chosen as it is found to be more representative of the activation energy observed for ignition delays data.

presence of a negative exponent on methane, in parallel to the shock tube ignition correlations discussed above (Eqs. 6.1 and 6.2).

The adiabatic flame temperature is better reproduced when a two-step oxidation mechanism is considered:

$$CH_4 + \tfrac{3}{2}O_2 \rightarrow CO + 2H_2O$$
$$CO + \tfrac{1}{2}O_2 \rightarrow CO_2 \qquad \textbf{(6.6)}$$

For methane dissociation, the rate is given by:

$$RR\ [mol/cm^3/s] = 2.8\times10^9\ [CH_4]^{-0.3}\ [O_2]^{1.3}\ e^{\frac{-202kJ/mol}{RT}} \qquad \textbf{(6.7)}$$

while for the CO oxidation the rate is:

$$RR_f = 3.98\times10^{14}\ [CO]^1\ [H_2O]^{0.5}\ [O_2]^{0.25} e^{\frac{-167.5kJ/mol}{RT}} \qquad \textbf{(6.8)}$$

A reverse reaction for the CO oxidation was also proposed in order to reproduce the proper $[CO]/[CO_2]$ equilibrium in steady-state flames.

Coffee, Kotlar and Miller [1983] report that the above scheme reproduces fairly well the temperature profile in the flame but not the heat release profile. They attempted to improve the heat release profile predicted by a single-step mechanism, still aiming to reproduce experimental flame speeds under various conditions. They found that a single-step mechanism could reproduce well the flame heat release and temperature profiles, but that the pre-exponential factor and the activation energy had to be changed with the equivalence ratio. Contrary to Westbrook and Dryer, they have not changed the species exponent and have kept the reaction order (3rd order for methane) of the direct oxidation mechanism. The proposed reaction scheme (Coffee *et al* [1983]) has been validated only at atmospheric pressure, and in its current form has the wrong

pressure dependency such that it cannot be applied directly for the problem under consideration.

Coffee [1985] commented, in a subsequent publication, on the mechanism of Westbrook and Dryer and found that the results were different when more accurate diffusion mechanisms were considered. He found that he had to reduce the pre-exponential factor proposed by Westbrook and Dryer by a factor of 2.7 to account for the roughly 3 times larger transport coefficient used by these authors. This requirement for a change in pre-exponential factor indicates that flame speed simulations depend not only on kinetics, but on the quality of the transport model, such that the kinetics obtained from such simulations must be considered carefully.

6.4 TURBULENT COMBUSTION

Combustion in diesel engines, in both the premixed and mixing-limited burning phase, is influenced by turbulence. Turbulence increases the mixing of fuel, air and hot combustion products. A simple approach to predict the reaction rate of a turbulent reactive flow is to use the average properties of the flow to calculate a mean reaction rate. The reaction rate in this case is obtained using one of the available kinetic models. This approach is defendable when chemical reaction time scales are much longer than the mixing time scales, such that the temperature and species concentration tend to become relatively uniform over the time scale associated with the chemical kinetics. This may be the situation prevailing at ignition in diesel engines.

However, as chemical reaction time scales decrease, the usage of average quantities becomes inaccurate. The inaccuracy arises as the reaction rate has a non-linear dependency on temperature and species concentration. When fluctuations are important, the actual reaction rate may differ significantly from that obtained when using the averaged quantities. This is

demonstrated in most combustion textbooks (e.g. Glassman [1987], Liñán and Williams [1993]), where it is shown that the inclusion of temperature fluctuations of the order of 10% in an Arrhenius reaction rate leads to mean reaction rates differing by 25% from the reaction rate obtained from the mean temperature. For these circumstances where the turbulent time scales influence the chemical reaction while the kinetics still affects the combustion rate, a model must be used to take fluctuations into account when computing a mean reaction rate.

The usage of probability density functions (*pdf*) to describe the turbulent fluctuations of flow properties addresses this situation. Given the shape of these *pdf*, the average and the statistical distribution can be used to provide a more accurate mean reaction rate. *Pdf* models become complicated for problems like diesel engine combustion, as a single *pdf* shape cannot be expected to be accurate over the heterogeneous flow field, and where several species are present.

The flamelet model is based on the concept that reactions occur in thin laminar flame fronts. The surface density of flame sheets is altered by turbulence, affecting therefore the combustion rate. A conservation equation for the flame front densities can be written and solved with the flow. This method is attractive because the concept is meaningful. There is some empiricism in modelling the transport equation for the flame surface densities.

When the chemical time scales τ_k are short compared to turbulent time scales τ_t, the reaction rate is limited by how fast the species involved in the combustion mix on the molecular level. Under the assumption that τ_k is much less than τ_t, a simplification arises as it is possible to assume that the chemical reaction rate is infinite and that the reaction proceeds at the rate of mixing. This is the basis of the eddy-dissipation model presented by Magnussen and Hjertager [1977]. The simplicity and meaningful concept of Magnussen's model contributed to making of the eddy-dissipation model a preferred combustion model for engine modelling.

If one uses a kinetic relationship and considers the average properties in a regime where τ_k is much less than τ_t, the reaction rate would proceed as though the fuel and oxidizer were indeed in a mixed state. If the flow could be resolved to the smallest length and time scales, the usage of the kinetic rate would be appropriate. When averaging techniques are used, as they are in KIVA-II, then one must consider the mixing time constraint of turbulence. Somewhat pursuing the idea of Spalding [1971], Magnussen and Hjertager [1977] suggested that the mixing at the molecular level proceeds at the rate of dissipation of the smallest eddies. As the smallest eddies dissipate, the reactants and hot products mix at the molecular level, and combustion is assumed to occur instantaneously. A time scale for the dissipation of the eddies can be obtained from k/ε where k is the turbulent kinetic energy of the flow and ε its dissipation[3]. Magnussen *et al* further suggested that the amount of mixture formed through eddy dissipation is proportional to the limiting mean concentration, which is formulated as:

$$RR = A\ \bar{C}_{\min}(\varepsilon/k) \tag{6.9}$$

where $\bar{C}_{min}$ is the mean concentration of the species that limits the rate. The combustion rate can be limited by either the amount of fuel, the amount of oxidizer or the amount of hot combustion products available to provide the heat necessary to the reactions:

$$\bar{C}_{\min} = \min[\bar{C}_f\ ,\ \frac{\bar{C}_o}{s}\ ,\ B\frac{\bar{C}_{cp}}{1+s}] \tag{6.10}$$

where the subscript *f*, *o* and *cp* refer to fuel, oxidizer and combustion products respectively, and *s* is the stoichiometric oxygen requirement. The model assumes that the instantaneous concentration is related to the average concentrations, and is applicable to both premixed and

[3] Strictly the time scale provided by k/ε is that of the dissipation of kinetic energy from the mean flow, which could be conceptualized as the dissipation of energy containing eddies. To satisfy equilibrium between turbulence production and dissipation, the time scale for the dissipation of small eddies must be of the same order as that of the larger eddies.

mixing-limited flames. In premixed flames, the eddies containing combustion products must dissipate to mix with the fuel-air mixture. In diffusion flames, fuel and oxidizer must mix with each other and with combustion products. A and B are constants, and for gas diffusion flames were found to best match experimental values when equal to 4 and 0.5 respectively. The model reproduced well premixed flame results with the same constants. However, when turbulent premixed mixing-limited flames were simulated, A and B needed to be multiplied by 8. The authors attributed that difference to the ill-predicted turbulence levels in the case of the premixed diffusion flame.

Gosman and Harvey [1982] suggested that in engines the ignition phase be simulated using a kinetic oxidation rate, while the latest stage of combustion be modelled using the Magnussen model (since it does not consider kinetic rate). The cut-off was to be determined by comparing the turbulent time scale and the kinetic time scale. They used the model to simulate a direct injection diesel engine and found that using A=20 and B=2.5 provided realistic heat release rate.

Abraham, Bracco and Reitz [1985] formulated the eddy-dissipation turbulent combustion model as follows:

$$\dot{\rho}_i = (\rho_i - \rho_i^*)/\tau_c \qquad \textbf{(6.11)}$$

where τ_c is a conversion time, and ρ_i^* is the thermodynamic equilibrium value of the partial density of species i. The conversion time was given by the longer of the laminar and the turbulent time scales: $\tau_c = \tau_l + \tau_t$. In their case, the laminar conversion time was obtained by a correlation providing the right laminar burning speed. The turbulent conversion time is expressed as:

$$\tau_t = C_{m2}\,\frac{k}{\varepsilon}\,[1-e^{\frac{-(t-t_s)}{\tau_d}}] \quad if \quad \frac{C_{m3}(Y_P-Y_{PS})}{C_{m2}(1+s)(Y_F-Y_F^*)} \geq 1 \tag{6.12}$$

$$\tau_t = C_{m3}\,\frac{k}{\varepsilon}\,(1+s)\,(\frac{Y_F-Y_F^*}{Y_P-Y_{PS}})\,[1-e^{\frac{-(t-t_s)}{\tau_d}}] \quad if \quad \frac{C_{m3}(Y_P-Y_{PS})}{C_{m2}(1+s)(Y_F-Y_F^*)} < 1 \tag{6.13}$$

where $s = (Y_{O2}-Y_{O2}^*)\,/\,(Y_F-Y_F^*)$. Y denotes the mass fraction and the subscript P, F and PS refer to the product, the fuel and the products at spark time. The star denotes equilibrium values. The introduced delay coefficient is necessary for spark-ignition, and sets the initial value of the conversion time to the laminar one until the flame has travelled a distance of 2 or 3 times the scale of turbulent eddies. The model, assuming zero equilibrium products and after the ignition delay, becomes identical to the original Magnussen model, except for the use of an ignition time delay. The constant C_{m2} and C_{m3} proposed by Abraham *et al* [1985] are 0.055 and .092, which corresponds in the Magnussen original formulation to A=18.2 and B=1.745. For a variety of loads and speeds, their model reproduced the pressure history within 8% of the measured ones.

Kuo and Reitz [1989] applied the combustion model of Abraham, Bracco and Reitz [1985] in KIVA to a different engine configuration (pancake and pent-roof) but still to a premixed charge engine. The turbulent combustion model was bypassed during ignition. Once again the computed pressures were found to be within 10% of the measured pressures in most cases, except in the cases of very retarded spark timing (for which case the laminar ignition phase may be ill-modelled). A sensitivity study revealed that uncertainties in gas temperature, in turbulence intensity or in length scales existing prior to combustion could have been the cause of the observed discrepancies.

Kuo and Reitz [1992] tested in a subsequent paper the eddy-dissipation model of Magnussen for premixed-charge engine and for direct-injection two-stroke engines in a

subsequent paper, considering the delivery ratio. They used a correlation to modify the reaction rate for the presence of residual gases. For cases with no or little residual gases, the computed and experimental pressure history over one cycle were within 10%, with better agreement for the premixed case. Agreement was equally good in the premixed charge case for engine speeds of 800 and 1600 RPM, which is of some reassurance since the turbulent level changes with engine speed.

In retrospect, the eddy-dissipation combustion model of Magnussen has provided better trends than strictly kinetic models had in the past for both premixed charge engine and diesel engines. It appears that a set of constants with values $16 < A < 20$ and $1.7 < B < 2.5$ have been most frequently reported for engine multidimensional simulation. No systematic comparison with experiments over a wide range of equivalence ratio, speed, load and temperature could however be found. The model cannot be easily tested systematically for engine application because of the other sources of errors involved in engine modelling. In particular, the wall heat transfer, the turbulence levels and the spray attributes all prevent decisive conclusions on the accuracy of the Magnussen model. The modelling of the ignition is also a potential source of difficulty. If the duration of the kinetic phase is over-predicted, than a slower turbulent controlled reaction rate is required to compensate.

6.5 COMBUSTION MODEL

In this section, the combustion model used in this work is presented. Following injection, the gaseous fuel mixes with hot air in the chamber, or with hot gases generated by the combustion of pilot diesel fuel, and ignites after a chemical delay. The prediction of this delay is of interest as it influences the amount of mixing taking place prior to combustion. A reasonable autoignition model is therefore required. Following ignition, the premixed fuel burns

at a rate limited by either chemical kinetics or by turbulent mixing. In this work a high-temperature kinetic scheme was used to treat premixed combustion following ignition, as long as the mixing time scale is longer than the kinetic time scale. Once the existing premixed fuel and air have burned, the reaction rate will depend on the mixing rate of fuel and air, which can generally be controlled by chemical kinetics or by turbulent mixing, although it is expected to be turbulence controlled.

6.5.1 Methane Ignition

In this work, the shock-tube experimental data of Tsuboi and Wagner [1974] and of Lifshitz *et al* [1971] were used to derive an ignition scheme. Because in the shock tube experiments, sufficiently far from the walls, the pressure, temperature and concentrations can be considered homogeneous, the ignition delay correlations (Eqs. 6.1 and 6.2) can be transformed into single-step kinetic expressions. To ensure the appropriateness of the proposed scheme, the results were compared to the experimental data of Naber *et al* (Section 6.6.1).

Because of the homogeneous conditions, the heat diffusion from the ignition sites is negligible. It may also be assumed that, because of the degree of dilution, the heat release is small, and that the kinetic energy of the gas after ignition is negligible. The heat release rate Q per kilogram of mixture can be expressed by:

$$\rho_{mix}\frac{\delta Q}{dt} = \frac{d(\rho_{CH_4})}{dt}(-LHV)$$

$$\rho_{mix} C_v \frac{dT}{dt} = \frac{d[CH_4]}{dt} W_{CH_4}(-LHV) \qquad \textbf{(6.14)}$$

where ρ_{mix} is the density of the mixture and C_v the constant volume specific heat. The rate of change of methane concentration is the reaction rate RR_{ign}, and a time scale is obtained by

rearrangement:

$$dt = \frac{C_v\, dT\, \rho_{mix}}{RR_{ign}\, W_{CH_4}\, (-LHV)} = \left(\frac{C_v}{-LHV}\right)\frac{1}{RR_{ign}}\frac{dT}{T}\frac{P}{R_{mix}\, W_{CH_4}} \qquad \textbf{(6.15)}$$

in which the perfect gas law has been used. Now assuming that the reaction rate is roughly constant until the explosion regime occurs, one can define a delay for achievement of ignition:

$$\tau_i = \left(\frac{C_v}{-LHV}\right)\left(\frac{\Delta T}{T}\right)_{\tau_i}\left(\frac{1}{RR_{ign}}\right)\left(\frac{P}{R_{mix}\, W_{CH_4}}\right) \qquad \textbf{(6.16)}$$

and re-arranging for the reaction rate:

$$RR_{ign} = \left(\frac{C_v}{-LHV}\right)\left(\frac{\Delta T}{T}\right)_{\tau_i}\left(\frac{P}{R_{mix}\, W_{CH_4}}\right)\left(\frac{1}{\tau_i}\right) \qquad \textbf{(6.17)}$$

such that if one has a correlation for τ_i as a function of species concentration and of an activation energy, the reaction rate can be obtained given a rate of temperature increase at ignition. Using C_v for nitrogen at 1200 K (0.74 kJ/kg/K), the gas constant for nitrogen (.290 kJ/kg/K), a *LHV* of -50010 kJ/kg and a W_{ch4} of 16.043 g/mol for methane, and correcting to obtain a RR_{ign} in mol/cm^3/s, one gets:

$$RR_{ign} = 3.19x10^{-12}\, P\, \left(\frac{\Delta T}{T}\right)_{\tau_i}\frac{1}{\tau_i} \qquad \textbf{(6.18)}$$

and then replacing Eq. 6.1 for the ignition correlation:

$$RR_{ign} = 7.975x10^{2}\, P\, \left(\frac{\Delta T}{T}\right)_{\tau_i}[CH_4]^{-0.32}[O_2]^{1.02}\, e^{\frac{-222kJ/mol}{RT}} \qquad \textbf{(6.19)}$$

where the rate is given in mol/cm^3/s if the pressure is given in Pa and the species concentration in mol/cm^3. The temperature rate of change can be taken as a constant at ignition, but will

depend on the definition of the ignition delay. If radical species are observed the rate of temperature will be smaller than if a measurable pressure change occur. As an initial approximation, $\Delta T/T$ is taken as 1%, leading to a pre-exponential of approximately 10. The reaction rate is then given by:

$$RR_{ign} = A\ P\ [CH_4]^{-0.32}[O_2]^{1.02}\ e^{\frac{-222kJ/mol}{RT}} \qquad \textbf{(6.20)}$$

where A is of the order of 10.

In the above results, the correlation of Tsuboi and Wagner was used (Eq. 6.1), but the correlation of Lifshitz *et al* would also lead to the same form of reaction rate, with a different pre-exponential constant and a different activation energy. As mentioned earlier, this delay is proportional to $P^{-0.7}$. This mechanism can readily be implemented in KIVA-II, with a slight modification for the pressure term. During ignition, it is assumed that methane and oxygen are readily converted to carbon dioxide and water. The presence of the pressure in the rate Eq. 6.20 is somewhat unusual, but it could be converted to a more conventional form by approximating the pressure by:

$$P = \rho_{mix} R_{mix} T \approx [N_2]\bar{R}T \qquad \textbf{(6.21)}$$

which leads to the following ignition scheme when replaced in the rate of Eq. 6.20:

$$RR_{ign} = A\ [CH_4]^{-0.32}[O_2]^{1.02}\ [N_2]^{1.0}\ T\ e^{\frac{-222kJ/mol}{RT}} \qquad \textbf{(6.22)}$$

and the pre-exponential constant A is now of the order of $1x10^5$.

6.5.2 High-Temperature Kinetic Oxidation

Following ignition, the methane that has premixed with the air during the ignition delay

burns. Depending on the species concentration and on the temperature, the rate of combustion will be regulated by kinetics or by turbulent mixing. One simple method is to apply the ignition conversion rate until the turbulence-limited combustion is established. However, the ignition scheme cannot be expected to yield reliable results once the ignition has taken place. A high-temperature kinetic scheme was consequently incorporated in the combustion model. This scheme would be representative of the one used to treat flame propagation problems. The transition between the ignition scheme and the high-temperature oxidation scheme is discussed in Section 6.5.3.

Independently of the combustion regime, the heat-release rate depends on the oxidation mechanism chosen. In the kinetically-controlled combustion, the conversion mechanism dictates also the reaction rate. A simple yet effective chemical scheme is sought. The scheme must predict reasonably well the reaction rate and the heat release following ignition for various pressures and equivalence ratios. During ignition, the chosen scheme produces directly small amounts of CO_2 and H_2O. The simplest model is to retain this direct conversion of methane to carbon dioxide and water; however, the inclusion of sequential oxidation reactions of methane to CO and then to CO_2 leads to a more accurate flame temperature (Westbrook and Dryer) and does not cause a major increase in computational times. Other sub-species resulting from the equilibrium and reactions of the H_2O-H_2-CO system were not considered in this work.

The one-step and two-step mechanisms of Westbrook and Dryer are readily applicable (Eqs. 6.7 and 6.8). There are concerns that the pre-exponential factor may not be adequate for KIVA-II in which a relatively crude species molecular diffusion mechanism is utilized. In KIVA-II a single diffusion coefficient is used for species, and at 1000 K and 5 MPa, and the original diffusion coefficient is 3 to 4 times lower than that used by Westbrook and Dryer for the main species. One-dimensional laminar flame propagation through a stoichiometric methane-

air mixture was performed with KIVA-II using Eq. 6.5. The simulation indicated that in fact a pre-exponential constant of $8x10^9$, rather than $1.3x10^9$, led to better flame speed prediction. This pre-exponential constant (the former) was also used by Coffee *et al* [1983] who also had lower diffusion coefficients than Westbrook and Dryer.

The usage of the two-step mechanism of Westbrook and Dryer provides us with an approximate variation of the reaction rate with species concentration and temperature. There are indications in the literature (Coffee *et al* [1983], Sloanne and Ronney [1992]) that the mechanism of Westbrook and Dryer does not represent well the heat release as a function of temperature. According to computations performed in Sloanne and Ronney, the scheme tends to over-predict the heat release at temperatures above 1700 K, while under-predicting it at lower temperatures. For flames propagating through a mixture already at some elevated temperature, the reaction rate and therefore the heat release rate can be expected to be over-predicted. The scheme will therefore be used with caution, and the sensitivity to the kinetic scheme will be verified.

6.5.3 Transition Between Ignition and High-Temperature Schemes

A criterion for the transition between the ignition regime and this high-temperature kinetic scheme must also be established. It is helpful to conceptualize the transition as the start of propagation of a flame from the ignition site. In SI engines the ignition occurs in a given location and a time delay or a particular location can be set. Because the time and location of the autoignition is not known *a priori* in CI engines, defining a time delay is not as appropriate as it is in SI engines. Typically, researchers studying CI engine problems have set a temperature or a rate of reaction in a particular cell at which the transition occurs.

In principle, a cell is in a flame propagation mode when the heat and species transferred to it are sufficient to bring that cell in a fast kinetic mode compared to the ignition mode. The

best criterion may be the temperature gradient across a cell. If the gradient is typical of that of a turbulent flame, a flame propagation scheme can be applied. However, finding the gradient is not computationally attractive as it is not known *a priori* what is the orientation of the reaction zone. For all intents and purposes, a high gradient corresponds to a higher cell temperature. One potential criterion is to use a transition temperature at which the reaction rate is, arbitrarily, 10% of the reaction rate for a methane-air stoichiometric mixture at typical engine pressures. This would yield a transition temperature of approximately 1700 K. Because there is some arbitrariness in the choice of the transition point, the sensitivity to that choice will be investigated.

The transition criterion may not be so critical, as the ignition scheme and the high-temperature scheme do not differ so much. The main difference between the two schemes is their pressure dependency. The ignition scheme leads to an ignition delay proportional to $P^{-0.7}$, while the high-temperature scheme of Westbrook and Dryer would lead to an ignition delay independent of pressure. For a stoichiometric mixture of methane at a temperature and pressure of 4 MPa and 1000 K, the Westbrook and Dryer scheme with a pre-exponential constant of 8×10^9 leads to a 50% higher reaction rate than the ignition scheme. The transition does not consequently need to accommodate orders of magnitude difference in reaction rates and the transition can be made smooth between ignition and flame mode. Since it is not known if the turbulent-limited or the chemical kinetic limited combustion will prevail immediately after ignition, it is convenient to take an average between ignition reaction rate and higher temperature reaction rate over a transition temperature range ΔT above the transition criterion temperature T_{lb} of 1700 K discussed above. Initially a temperature range of 100 K was chosen. Then if RR_{ign} and RR_{hts} are the reaction rates for ignition and high-temperature schemes, then the kinetic

reaction rate RR_k can be expressed as:

$$RR_k = \frac{(T_c - T_{lb})}{\Delta T} RR_{hts} + \frac{(T_{lb} + \Delta T - T_c)}{\Delta T} RR_{ign} \tag{6.23}$$

where T_c is the local (cell) temperature.

6.5.4 Eddy-Dissipation Turbulent Combustion

The eddy-dissipation model of Magnussen is considered here as a mean of investigating methane turbulent combustion in a direct-injection engine. The model proposed follows closely those applied by previous researchers. The rate of change of partial density of a species in KIVA-II is expressed by:

$$\dot{\rho}_m = W_m \sum_r (b_{mr} - a_{mr})\ RR_r \tag{6.24}$$

where W_m is the molecular weight of species m, b and a are stoichiometric coefficients to ensure mass conservation, and RR_r is the reaction rate of reaction r. The reaction rate is expressed as

$$RR_r = min\ [RR_{rk}, RR_{rt}] \tag{6.25}$$

where the subscript k and t refer to kinetic and turbulent. The choice of the minimum rate is not an abrupt choice, as the mixture must progress from ignition or high-temperature kinetic schemes to eddy-dissipation combustion. The kinetic reaction rate as written in KIVA-II is used, and is prescribed by:

$$RR_{rk} = k_{fr} \prod_m \left(\frac{\rho_m}{W_m}\right)^{a'_{mr}} - k_{br} \prod_m \left(\frac{\rho_m}{W_m}\right)^{b'_{mr}} \tag{6.26}$$

where the reaction order can be empirical. The progression constants are specified by an Arrhenius rate:

$$k_{fr} = A_{fr} T^{\xi_{fr}} e^{-\frac{E_{fr}}{RT}} \tag{6.27}$$

$$k_{br} = A_{br} T^{\xi_{br}} e^{-\frac{E_{br}}{RT}} \tag{6.28}$$

The pre-exponential constant A and the activation energy E_a depend on the choice of the kinetic scheme, and in this thesis are those of the ignition scheme or of the high-temperature kinetic scheme discussed in Sections 6.5.1 and 6.5.2. The turbulent reaction rate is given by

$$RR_{rt} = A_{mag} \bar{C}_{\min} \frac{\varepsilon}{k} \tag{6.29}$$

where $\bar{C}_{min}$ denotes the limiting mean concentration:

$$\bar{C}_{\min} = \min[\bar{C}_f , \frac{\bar{C}_{O_2}}{s} , B_{mag} \frac{\bar{C}_{CP}}{(1+s)}] \tag{6.30}$$

A_{mag} and B_{mag} are constants, and s is the stoichiometric coefficient. Based on the literature, constants A_{mag} and B_{mag} are initially chosen to be 18 and 2.

The turbulent reaction rate presented (Eq. 6.29) does not include a delay to allow ignition to take place. This delay may be required, and will be discussed in Section 6.6. It must be noted that the mean conditions are used to evaluate the chemical reaction rate, which does not provide an accurate rate. Since the model has been used in the literature with that idea, the mean chemical rate is maintained in this model.

6.6 TESTING OF COMBUSTION MODEL

6.6.1 Ignition Sub-Model

The experimental environment of the ignition studies of Naber *et al* was reproduced

computational. The experimental chamber was cylindrical with the injection occurring radially from the cylindrical wall. In order to perform faster axisymmetric calculation, a cylindrical chamber of the same volume was defined with injection taking place axially on the top wall. The length of the modelled chamber was chosen to be the same as the diameter of the experimental chamber, 120 mm. This ensured that wall effects due to impingement of the jet on the far wall would be considered. The radius of the modelled chamber was chosen to yield equivalent volume, such that the pressure rise would be the same. The radius was 27.8 mm, large enough that jet would not come in contact with the side wall, and was divided in 25 cells, expanding from the nozzle to the outside diameter. Fifty cells divided the chamber in the axial direction, with again a grid expansion used from the nozzle. The cell adjacent to the nozzle was set at 1 diameter.

The nozzle diameter corrected by an experimentally determined discharge coefficient (d_o=0.25 mm, C_D=0.87, d_n=0.233 mm) and the injection pressure (20.7 MPa) and temperature (450 K) used in the experiment were used to compute boundary conditions using the same technique as that described in Chapter 4. For chamber pressures yielding choked flow at the nozzle, the nozzle velocity, temperature and density were calculated to be : 517 m/s, 392 K and 52.3 kg/m^3. Simulating the experiments, the injection duration was set at 11.5 ms. It was determined experimentally that it took 0.33 ms to inject 0.33 mg and that the injection rate was roughly 1.25 mg/ms when the needle is fully opened. The calculated injection conditions provide an injection rate of 1.21 mg/ms, a 3% difference. A sinusoidal velocity ramping was used to simulate the needle opening, and to match the 0.33 mg injection in 0.33 ms, the opening delay was set at 0.136 ms. The wall temperature was also set to 450 K, the controlled wall temperature of the experiments. The chamber pressure was calculated from the density and temperature prevailing for each cases. Because of heat transfer to the wall, the pressure decays between the

beginning of injection and the ignition. Following the principle used in the experiments, the ignition delay was defined as the point when the pressure is 14kPa above a fit to the pressure decay. The pressure decay was calculated in KIVA-II for each condition without ignition and a fit to that decay was used in the ignition simulations.

As the researchers burned a mixture of fuel and air to attain the pressure and temperature of interest, the gas composition at ignition is not exactly that of air. The obtained composition (6% O_2 and 3.6% CO_2) was used as initial conditions in the simulations. The turbulence level in the chamber was set following the observations of the authors. A small fan ensures that the mixture is uniform and maintains a turbulence level similar to that in engines. LDV measurements indicated that a representative rms velocity was 0.7 m/s. The initial turbulence level was therefore set at 7350 $(cm/s)^2$ ($k=3/2\ u'^2$). The flux of specific turbulent kinetic energy at the nozzle was assumed to be 5% of the nozzle flow time-averaged specific kinetic energy, while the length scale influx was set at 20% of the nozzle diameter. These values are not critical however, as the jet establishes its own turbulence. The initial time step was set at 0.1 μs, and its growth was limited such that the rise in internal energy at each time step was no more than 10%.

Initial computations were preformed with only the ignition model, and without subsequent combustion models. Although the Tsuboi and Wagner data extended over a larger range, it was found that the activation energy of the correlation of Lifshitz *et al* gave better results. The pre-exponential constant was determined to match the experimental results of Naber *et al* at 1200 K for a density of 20.4 kg/m^3. The single-step ignition mechanism was then

$$RR_{ign} = 33\ P\ [O_2]^{1.03}\ [CH_4]^{-0.33} e^{\left(\frac{-194.67 kJ/mol}{RT}\right)} \quad [mol/cm^3/s] \qquad \textbf{(6.31)}$$

Figure 6.3 illustrates the simulated ignition results compared to those of Naber *et al* using the

mechanism of Eq. 6.31.

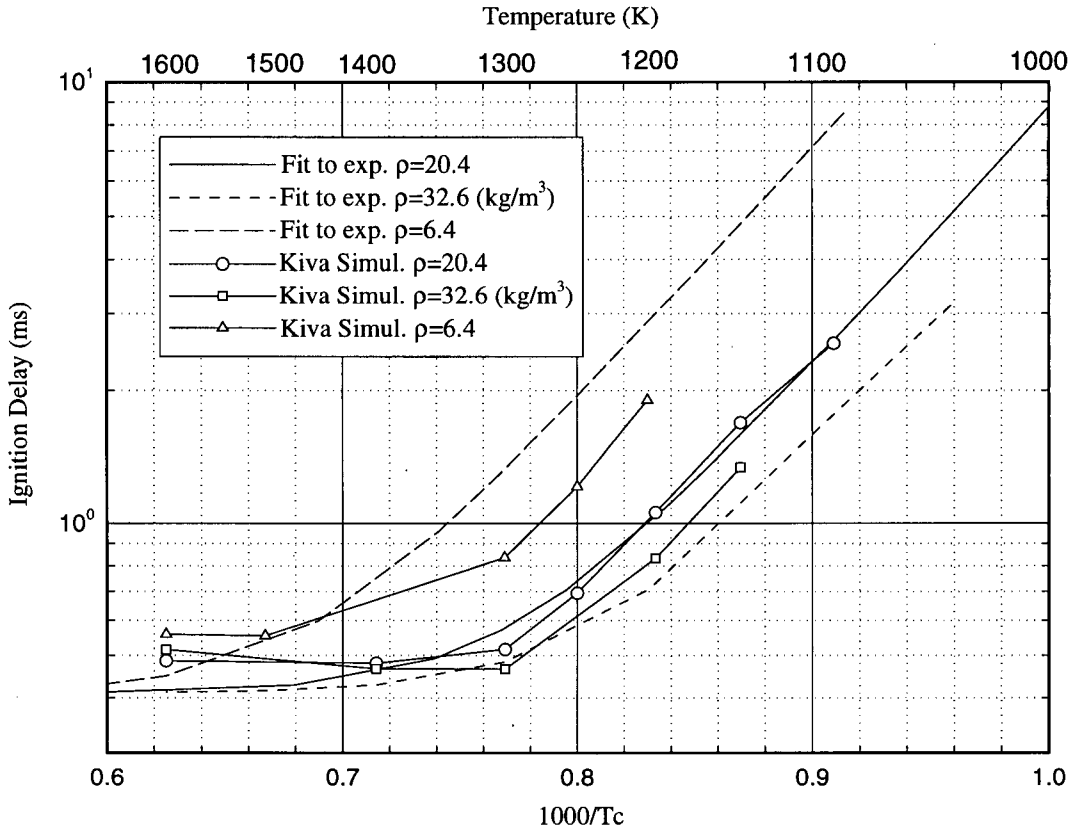

Figure 6.3 - Comparison between experimental ignition delays of Naber *et al* [1994] and simulation performed with KIVA with the single-step of Eq. 6.31.

The pressure dependency of -0.7 of the ignition scheme explains the difference seen at densities of 6.4 and 32.6 kg/m^3 between the simulations and the experimental results whose pressure dependency is -0.95. The shape of the ignition curve compares favorably over the temperature range. The ignition delay was found to be moderately dependent on initial turbulence levels. Simulations were performed with 10 times more turbulence and with essentially no turbulence for a chamber temperature of 1200 K. In the first case of no turbulence, the ignition delay was longer by 1.5%. When 10 times more turbulence was used, there was a reduction of 2.5% of the ignition delay. Limiting the internal energy growth by 1% instead of 10% did not change significantly the ignition delay.

6.6.2 Full Methane Oxidation Model

The complete methane oxidation model of methane - ignition, high-temperature kinetic and turbulent-limited - was used to predict combustion rate in a cylindrical chamber at high pressure and temperature. The cylindrical chamber was the same as that used in Chapter 5, except for the total length which is increased in some cases to remove wall impingement effects. The cylindrical constant volume chamber is convenient for testing and study of the implications of injection rate on combustion of methane jets. In all the test simulations, the injection rate was constant.

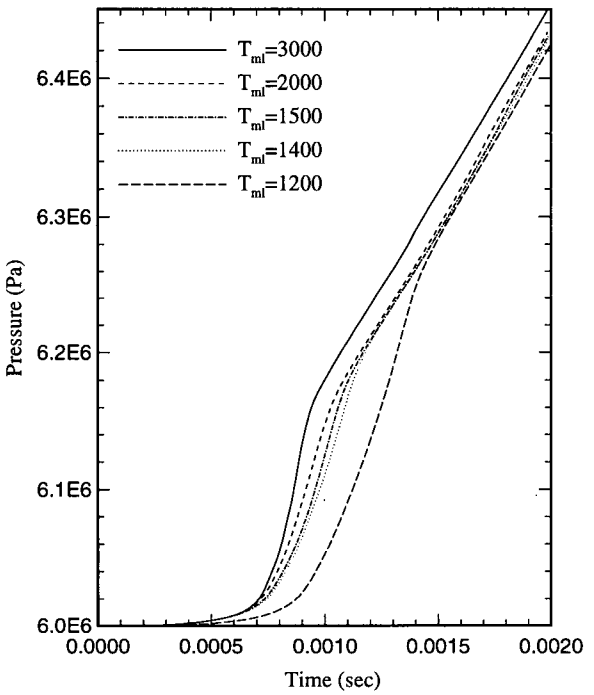

Figure 6.4 - Pressure rise caused by the combustion of a methane jet in a constant volume chamber. T_{ml} : temperature at which the turbulent-limited model is allowed to be active. T_{ch} =1250 K.

Figure 6.4 shows the pressure trace following ignition and combustion of the injected methane. For this case and all cases presented in this section, the injection pressure and temperature were 15 MPa and 350 K, the holes were 0.5 mm in diameter, and the injection was continuous. The air in the chamber was at 1250 K and at 6 MPa. The chamber was 90 mm in length, 23 mm in radius, and its walls were kept at 400 K. The turbulence level was set at 5.66×10^3 cm^2/s^2 unless otherwise specified. For the case illustrated in Fig. 6.4, T_{ml} is the temperature above which the eddy-dissipation combustion model (Eq. 6.29) is allowed to be effective. The eddy-dissipation model constants A_{mag} and B_{mag} were 18 and 2, respectively. The ignition model is the one tested in the above section.

When T_{ml} is equal to 3000 K, only the ignition mechanism is active (over the whole temperature range). With that scheme alone, the three combustion phases are visible on Fig. 6.4; the ignition delay, followed by a rapid combustion of the methane that has mixed with the air during the delay, and a mixing-limited phase. Although no eddy-dissipation turbulence-limited combustion is included for the case with T_{ml} equal to 3000 K, the rate of combustion is still limited by how fast a methane-air mixture becomes available. As T_{ml} is lowered, the rate of increase of pressure is slower following ignition. The reason for the slower rate is that some of the combustion during that phase is turbulence-limited and proceeds at a slower rate. There is relatively little difference in using T_{ml} of 2000, 1500 or 1400. This can be explained because during the premixed burning phase a significant fraction of the combustion occurs with a chemical kinetic rate (in this case controlled by the ignition scheme). However, when the minimum temperature is dropped to 1200 K, the ignition is significantly delayed, such that the ignition is longer than what we expect from the ignition model. The reason for that sudden change can be seen in Fig. 6.5, where a typical methane radial concentration profile is seen along with the corresponding reaction rates. Cold jet temperatures, concentrations and specific turbulent kinetic energy and dissipation profiles have been used to compute these rates.

As the ignition rate is dependent on $[CH_4]^{-0.3}$, the rate increases with decreasing methane concentration. On the other hand the eddy-dissipation rate is proportional to $[CH_4]$, such that the rate decreases rapidly on the outskirts of the jet. As may be seen, there is a radial location where the eddy-dissipation rate (RR_t) becomes smaller than the ignition rate (RR_k). The ignition starts in the outskirts of the jet, where the kinetic rate is high because of the high temperature and of the low fuel concentration. When the eddy-dissipation rate is allowed to proceed at all temperatures, it inhibits the ignition in its initial development.

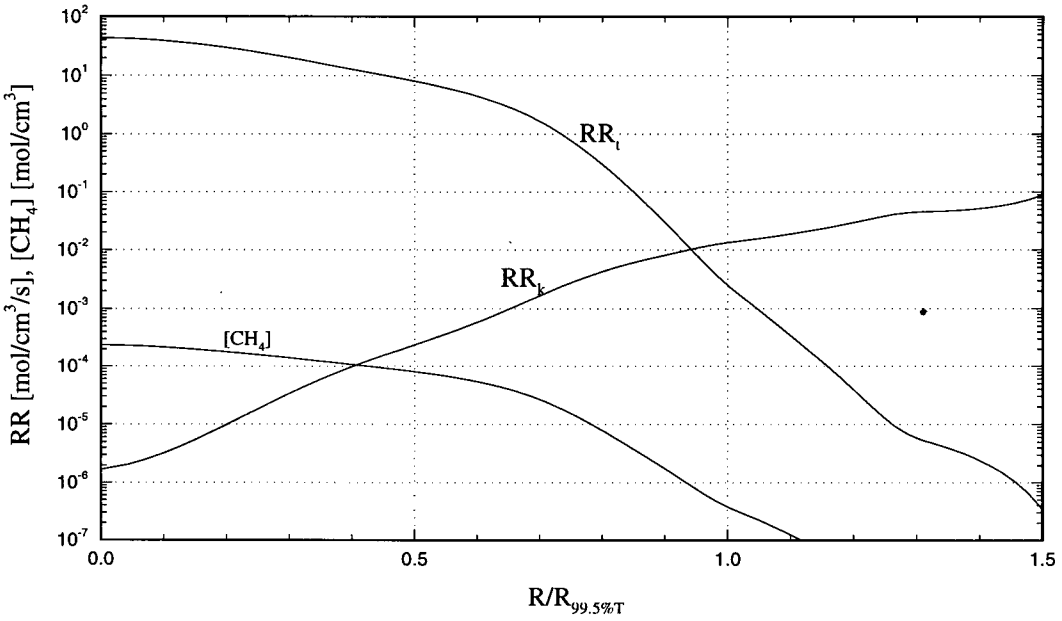

Figure 6.5 - Kinetic and turbulent-limited reaction rates and methane concentration profiles in the normal plane of a transient jets. The abscissa is the radial position divided by the location at which T is 99.5% of the chamber temperature.

The presence of the negative exponent on the methane concentration in the kinetic reaction rate raises questions about its validity at low concentrations. Tsuboi and Wagner studied ignition cases with very low reactant concentration, and found that their correlation remained valid for concentrations of methane down to $5x10^{-8}$ mol/cm^3. This result was also obtained however for equivalence ratios above 0.2, whereas in the present situation the equivalence ratio is well below, of the order of 0.01. Consequently there is some uncertainty regarding the kinetic model validity at the rate intersection point in Fig. 6.5. Although the eddy-dissipation model has been usually bypassed at ignition conditions in the literature, no indications were found that it ceases to be valid at low concentrations. It may be challenged during ignition for the following reason: the model is based on the physical understanding that combustion occurs as the small eddies dissipate their contents. It is assumed that the amount of dissipation is proportional to the mean concentration of the limiting species. At small concentrations, the mean concentration and

the concentration fluctuations may be of the same order, and the assumed linear relationship between the mean and fluctuating concentration may cease to be valid.

The ignition process is usually accepted as being a kinetic-controlled problem, and therefore the above problem is circumvented by allowing the kinetic to dominate during ignition. A number of possibilities exists. The first one is to introduce a time delay to the simulation such that the eddy-dissipation model is active only after a certain time. This option is not preferred here because in a diesel engine, one does not know *a priori* when the gas will ignite. Other possibilities rejoin the discussion about the transition between ignition and higher temperature kinetics. A minimum temperature or a minimum level of combustion products concentration can be used to determine whether or not a given cell is already ignited. The physical interpretation of the eddy-dissipation model would suggest that it can be applied relatively soon after ignition, as the propagation of the reaction zone may depend on the turbulent diffusion of hot combustion products. Figure 6.4 indicates that the ignition delay predictions remain good with a minimum transition temperature as low as 1400 K. A combustion product mass fraction level is however preferred, as the bulk temperature in the chamber rises due to compression. It was found that using a minimum of 1.8% product mass fraction for the eddy-dissipation model to be active produced the same results as the 1400 K minimum temperature in a constant volume chamber. Therefore, the eddy-dissipation model was allowed to be the limiting combustion rate when the combustion

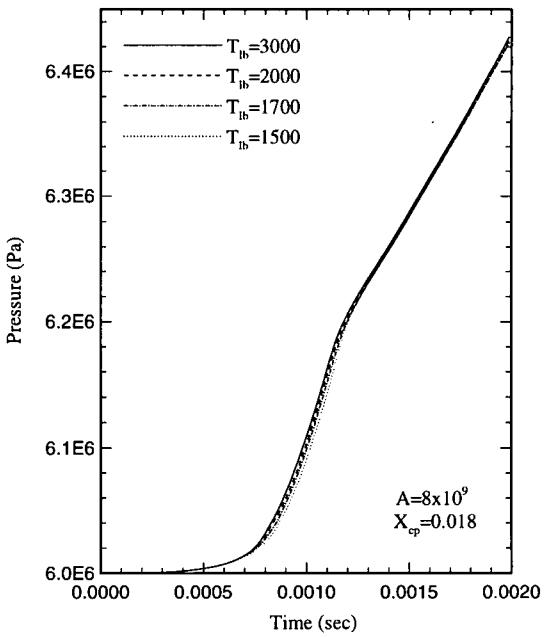

Figure 6.6 - Effect of changing the transition temperature from ignition to high temperature kinetic.

products mass fraction in a cell were above 1.8%.

The effect of allowing a high-temperature kinetic to be active and of changing the transition point at which it becomes active is presented in Fig. 6.6. In these cases the single-step reaction of Eq. 6.5 is used with a pre-exponential constant of $8x10^9$ and the eddy-dissipation model is allowed to proceed when X_{cp} is greater than 1.8%. There is a slight reduction in initial pressure rise during the premixed burning phase as the transition temperature is lowered, which is due to the slightly higher rate predicted by the higher temperature scheme at the pressure of 6 MPa.

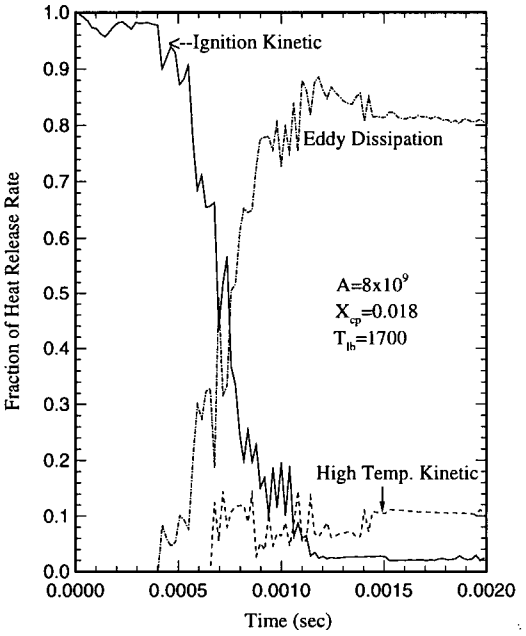

Figure 6.7 - Fraction of heat release rate occurring in ignition, high temperature kinetic and mixing-limited oxidation mode.

The effect is however modest, the main reason being that, for the cases considered, the amount of combustion occurring with the high temperature scheme is small. This is illustrated in Fig. 6.7, where the fraction of total heat-release rate occurring during ignition, high-temperature kinetic and eddy-dissipation controlled mode is presented. In the phase between the ignition phase and the mixing-limited phase, the heat released through kinetic oxidation at high temperature does not go above 20%. Figure 6.7 also shows that during the mixing-limited burning phase (t > 1 ms), a small amount of kinetically-controlled combustion proceeds along with the turbulent-limited combustion.

There is some uncertainty in the pre-exponential constant of the high-temperature kinetic scheme. Figure 6.8 shows the effect of reducing that constant by half. For the case with T_{lb} is equal to 1700 K, reducing the constant by half had little effect, reducing the premixed burning

phase rate slightly. With the reduced pre-exponential factor, the model was a bit more sensitive to the choice of the transition temperature T_{lb}. As may be seen in Fig. 6.8, using T_{lb} equal to 1500 K reduced the premixed-burning phase combustion rate more significantly.

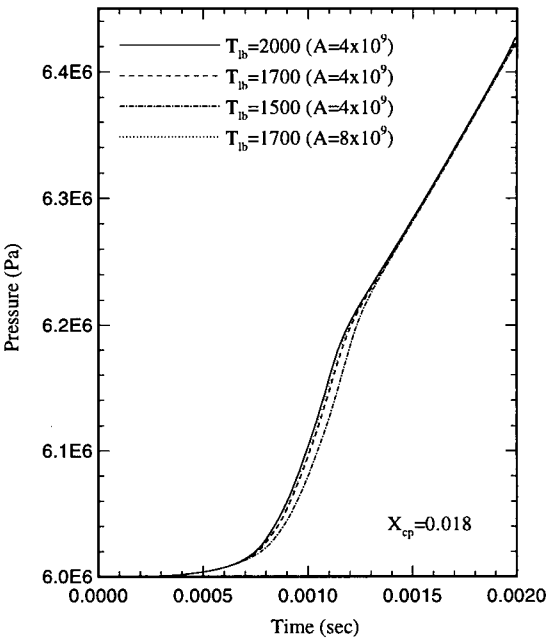

Figure 6.8 - Effects of changing the pre-exponential constant of the high-temperature scheme.

Changing the value of the eddy-dissipation model constant A_{mag} by 25% in either direction does not affect significantly the results, as can be seen in Fig. 6.9. The reason for the lack of significant effect is that the rate is controlled by how fast the fuel and oxidizer mix, which is more dependent in this case on the rate of injection than on the eddy-dissipation model constant.

In the above cases of Figs. 6.6 to 6.9, the limiting concentration of combustion products on the mixing-limited rate was active, but was found not to occur in the studied cases.

The dependency of the combustion rate on the initial specific turbulent kinetic energy field was assessed by computing two cases with respectively 10 times more and 10 times less specific turbulent kinetic energy. These cases are presented in Fig. 6.10. Increasing the specific turbulent kinetic energy readily reduced the ignition delay, indicating that the turbulence generated more ready-to-ignite mixture. It did not significantly increase the remainder of the combustion event, suggesting that the injection rate becomes the controlling factor. Decreasing the specific turbulent kinetic energy had little effect on the combustion rate.

With respect to some computational sensitivities, increasing the number of cells radially from 23 to 28 did not change the combustion rate. Finally, lowering the maximum amount of

heat released per cell from 1% of the cell internal energy to 0.25% did not change the combustion rate appreciably.

6.7 SUMMARY OF COMBUSTION MODEL

An autoignition model which reproduces well the experimental data of Naber *et al* was implemented in KIVA-II. A subsequent combustion model which includes a high-temperature kinetic scheme and a turbulent-limited combustion model was also implemented and tested. It was found that the choice of model parameters did not greatly affect the combustion rate, particularly in the mixing-limited phase, which is largely dependent on the mixing rate associated with the momentum injection rate. The combustion model is now summarized.

The oxidation of methane during the ignition phase is modelled as:

$$CH_4 + 2O_2 \rightarrow CO_2 + 2H_2O \qquad (\mathbf{R_{ign}})$$

while during the remainder of the combustion event it is modelled as:

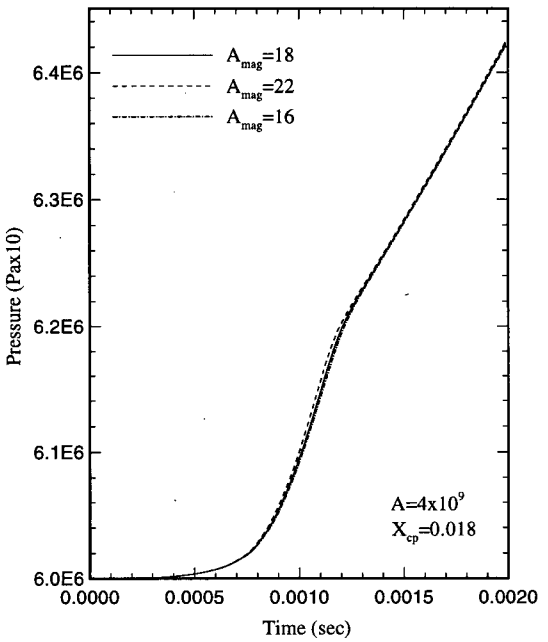

Figure 6.9 - Effect of varying the eddy-dissipation model constant A_{mag}.

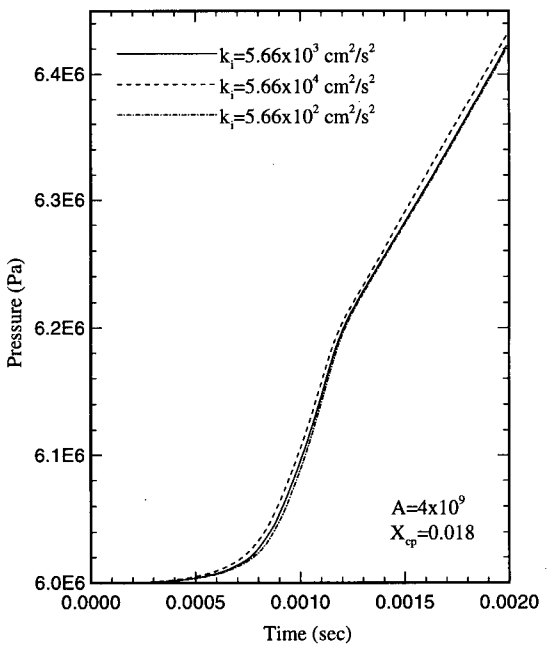

Figure 6.10 - Effect of initial turbulent kinetic energy on combustion rate.

$$CH_4 + \frac{3}{2}O_2 \rightarrow CO + 2H_2O \qquad (\mathbf{R_{hts}1})$$

$$CO + \frac{1}{2}O_2 \rightarrow CO_2 \qquad (\mathbf{R_{hts}2})$$

The reaction rate is provided by

$$\begin{aligned} RR &= RR_k \quad \text{if } X_{cp}<0.018 \\ RR &= \min[RR_k, RR_t] \quad \text{if } X_{cp}>0.018 \end{aligned} \qquad \mathbf{(6.25)}$$

where X_{cp} is the mass fraction of combustion products. The kinetic rate is provided by

$$RR_k = \frac{(T_c - T_{lb})}{\Delta T} RR_{hts} + \frac{(T_{lb} + \Delta T - T_c)}{\Delta T} RR_{ign} \qquad \mathbf{(6.23)}$$

where RR_{ign} is

$$RR_{ign}\ [mol/cm^3/s] = 33\ P\ [O_2]^{1.03}\ [CH_4]^{-0.33} e^{\left(\frac{-194.67 kJ/mol}{RT}\right)} \qquad \mathbf{(6.31)}$$

and RR_{hts} is

$$RR_{hts}\ [mol/cm^3/s] = 8.6\times10^9\ [CH_4]^{-0.3}\ [O_2]^{1.3}\ e^{\frac{-202 kJ/mol}{RT}} \qquad \mathbf{(6.7)}$$

for reaction ($R_{hts}1$). The pre-exponential of Westbrook and Dryer for $RR_{hts}1$ was increased by a factor of 3, following the discussion of Section 6.5.2. For the CO oxidation the rate is:

$$RR_f = 3.98\times10^{14}\ [CO]^1\ [H_2O]^{0.5}\ [O_2]^{0.25} e^{\frac{-167.5 kJ/mol}{RT}} \qquad \mathbf{(6.8)}$$

The turbulent-limited rate is

$$RR_{rt} = A_{mag}\,\bar{C}_{\min}\,\frac{\varepsilon}{k} \tag{6.29}$$

where $\bar{C}_{min}$ denotes the limiting mean concentration:

$$\bar{C}_{\min} = \min[\bar{C}_f\,,\ \frac{\bar{C}_{O_2}}{s}\,,\ B_{mag}\frac{\bar{C}_{CP}}{(1+s)}] \tag{6.30}$$

and A_{mag} and B_{mag} are taken as 18 and 2 respectively.

CHAPTER 7

METHANE JETS IGNITION AND COMBUSTION

7.1 INTRODUCTION

The dependency of the jet mixing and penetration rate on the injection conditions were established in Chapter 5 for cold jets. In this chapter, igniting transient methane jets are considered. Three main objectives are sought: i) verify whether the cold jet scaling remains valid for igniting jets and, if so, under which conditions, ii) establish the effects of ignition delay and of injection rate on the combustion, and iii) investigate the ignition of transient methane jets through pilot fuel combustion.

Multidimensional modelling, using the combustion model described and tested in Chapter 6, is applied in this chapter to investigate these questions. All considered cases have been simplified to the study of a single methane jet injected in a cylindrical chamber, as in Chapter 5, which permitted an axisymmetric treatment. The jets considered are underexpanded methane jets of finite injection duration, unless otherwise specified. Furthermore the igniting jets studied in this chapter are considered to be non-buoyant[1].

As for cold jets, the penetration rate of the flame is of particular interest, since over-penetration could cause flame quenching on contact with the combustion chamber walls or with the piston surface. The penetration must be redefined for igniting jets, and in this thesis the axial

---

[1] The Froude number, defined as follows (from Ricou and Spalding):

$$\frac{(C_pT)_{ch}}{-LHV+C_p(T_o-T_{ch})}\,\frac{u_n^2}{gd_{eq}}$$

can be estimated for a diffusion flame under typical conditions in diesel engines and is of the order of $5x10^5$.

location of the maximum heat release rate contour line is chosen.

In verifying the appropriateness of the cold jet scaling for flames, it is expected that the result will depend on the ignition delay. If, for example, the ignition delay is very long, then the gaseous jet will mix with the air in the chamber and a premixed combustion which bears little resemblance to the transient jet will take place. Because of this dependency on ignition delay, the cases of early ignition and of late ignition are considered separately. Early ignition is obtained by injecting methane in a chamber preheated to 1500 K. The ignition delay at this temperature is approximately 0.1 ms, and a diffusion flame is rapidly formed, with little or no premixed burning, as will be discussed in Section 7.3.

Late-ignition cases, between 0.5 and 1 ms, are obtained by using lower initial chamber temperatures. In order to maintain the penetration rate of the transient jets, the chamber density of all studied cases was kept constant by adjusting the chamber pressure when changing the initial chamber temperature. Late-ignition cases are considered in Section 7.3, where the impact of ignition delay on scaling is discussed, and where the effects of injection rate on ignition and combustion are investigated.

Finally, transient methane jet ignition through pilot fuel combustion is studied in Section 7.4. A simplified representation of the complex problem is presented and computational experiments are used to show the effects of spray and gaseous jet interaction, of injection delay between the pilot fuel and the gas jet, and of gaseous injection rate, on the combustion of methane in a diesel environment.

7.2 EARLY IGNITION - TRANSIENT DIFFUSION FLAME

When the ignition occurs nearly instantaneously, a transient diffusion flame is formed. The study of early-ignited transient diffusion flame is warranted, since an external source of

ignition is required to ignite the natural gas in compression-ignition engines (unless very high-compression engines would be considered). In particular, the use of pilot fuel combustion as a source of ignition can potentially cause an early ignition of the methane jet.

In the first section, the similitude and differences between a transient flame and a non-igniting jet are outlined. Then the scaling of cold jets is applied to various diffusion flames, and its adequacy verified. The features of finite-duration transient diffusion flames are presented in Section 7.2.3, followed by a brief comment on the achievements of quasi-steady flames in diesel engines.

7.2.1 Comparison of Non-Igniting and Igniting Jets

Figure 7.1 shows the global structure of a diffusion flame issued from a round nozzle in stagnant air. The profiles were produced by the numerical simulation, with the model described in Chapter 6. Plotted on the left-hand-side are contours of heat release, indicative of the location of the reaction zone. The reaction zone extends to a certain length below the nozzle, and may or may not correspond to the luminous flame length (in some flames, soot particles are oxidized outside the main fuel reaction zone, giving a yellow luminosity). The right-hand-side shows various time-averaged profiles across a normal plane of the flame. On the inside of the flame, there are fuel and combustion products that have diffused from the reaction zone. The temperature is high, because of heat diffusion from the reaction zone (temperature would be lower closer to the nozzle). At the reaction zone, both fuel and oxidizer disappear. On the outside of the flame, one finds oxidizer and diffused combustion products.

Figure 7.2 shows the corresponding profiles for the non-igniting jet (same chamber and injection conditions at same time after BOI). The main differences between the igniting case of Fig. 7.1 and this non-igniting case are as follow: i) the species distribution is different, which is

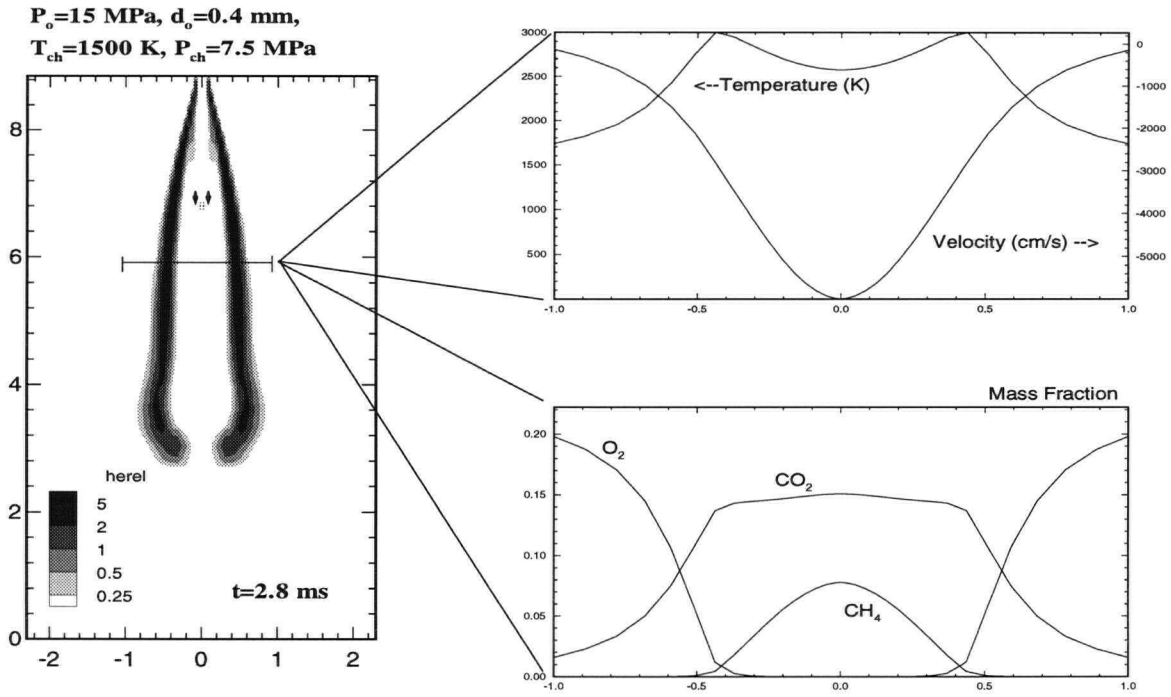

Figure 7.1 - Diffusion flame structure. Left : heat release contours [ergs]. (KIVA Computations).

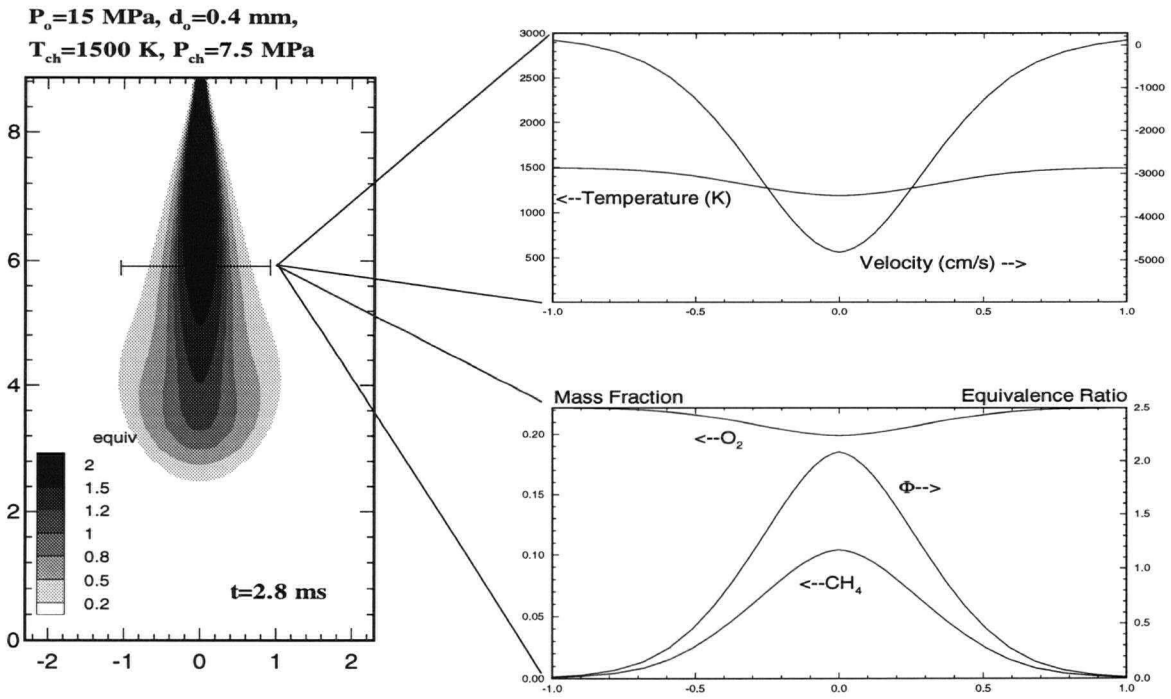

Figure 7.2 - Non-Igniting jet with same conditions as Figure 7.1 - left : equivalence ratio contours.

of course caused by combustion, ii) the temperature profile which is higher for the igniting case, iii) the velocity profile which is wider for the igniting case. These two last points are related as the higher temperature of the burned gases leads to a higher specific volume, causing the lateral expansion observed.

The most striking similitude between the igniting jet and the cold jet is the seemingly identical location of the flame (maximum centerline reaction rate) and of the unity equivalence ratio of the cold jet. This is an important result as it shows that the penetration rate of the cold jet describes as well the penetration of the flame. The identified scaling for non-igniting jets should therefore be valid for transient diffusion flames.

Since the penetration of the unity equivalence ratio and of the maximum axial heat release rate are the same, the increase in specific volume causes a lateral expansion of the jet, which may be approximated as $\rho_b(r_f)^2=\rho_{ch}(r_j)^2$ where ρ_b is the density of the burned gases, and where r_f and r_j are the width of the flame and of the jet, respectively, at any normal planes to the jet axis. The gases densities can be expressed in terms of the burned gases and chamber temperatures at the chamber pressure, such that as an approximation $r_f=r_j(T_f/T_b)^{1/2}$.

7.2.2 Transient Flame Scaling

Figure 7.3 shows the penetration rate of a cold jet and of that of three different transient diffusion flames. In the case of the non-igniting jet, the axial locus of the unity equivalence ratio is plotted as a function of time. In the case of the flame, the axial location of the maximum reaction rate is plotted. The first flame is one with conditions identical to those of the cold jet (which is not allowed to ignite). As seen on the left-hand graph, the penetration rates are nearly identical. For the two other flames, the nozzle diameter or the injection pressure was increased. The left-hand side graph of Fig. 7.3 shows that an increase in nozzle momentum corresponds to

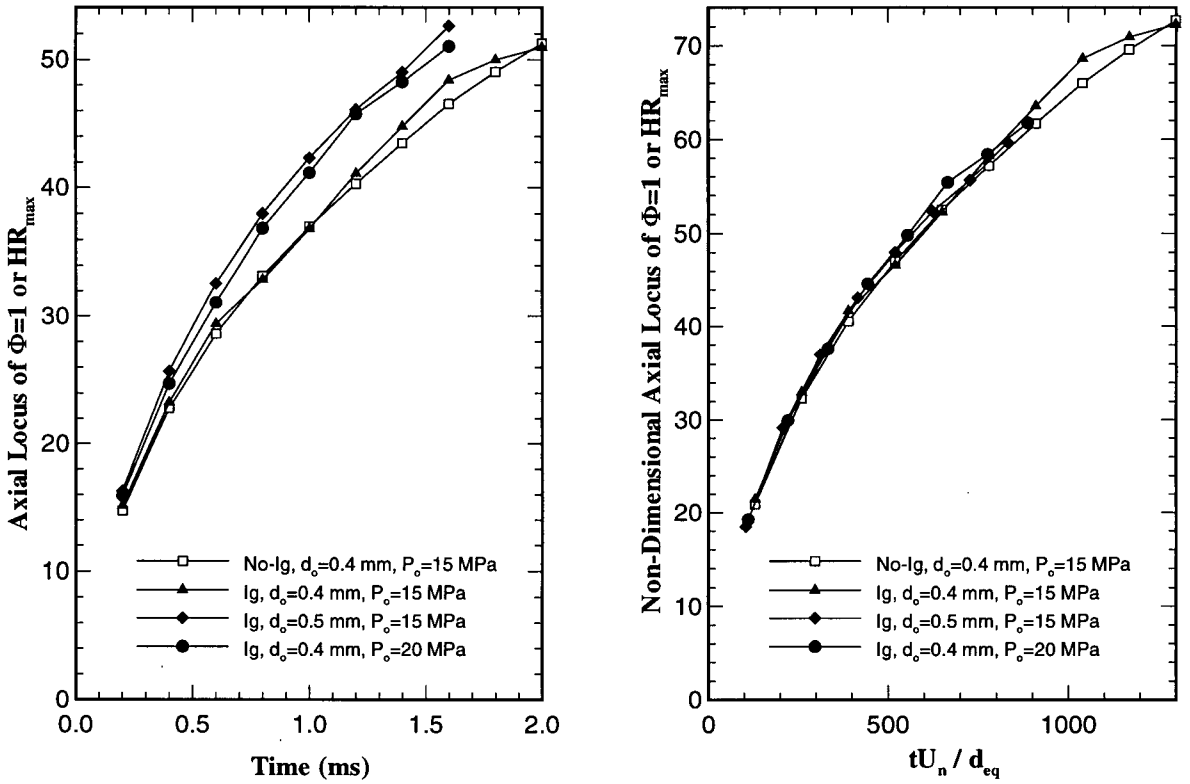

Figure 7.3 - Dimensional and non-dimensional location of the reaction zone and of the stoichiometric contour line for the cold jet. The injection duration were respectively 1.25 ms, 1.25 ms, 0.8 ms and 0.94 ms.

an increase in flame penetration rate. The right-hand side graph of Fig. 7.3 shows that using the same scaling as for the cold jets, the penetration rate of flames also scales well.

According to the above results, and to Figs. 7.1 and 7.2, the flame penetration is much the same as the cold jet penetration, while the width of the flame is larger than the width of the cold jet. The penetration of the flame remains dependent on the nozzle momentum and on the chamber density, the same dependency as that of the cold jet. This is supported by the experimental work of Ricou and Spalding [1961] who found that the mass entrainment rate of propane diffusion flames was still well represented by the mass entrainment rate correlation for the non-igniting jet.

7.2.3 Transient Flame Description

The diffusion flame of Fig. 7.1 corresponds to continuous injection. The combustion following the end of injection is now discussed, along with a brief description of an early ignited transient jet.

In the following examples, a methane jet issued from a nozzle with d_{eq} equal to 0.71 mm (0.4 mm nozzle operated at 15 MPa) is injected in a chamber at 7.5 MPa, 1500 K. The injection duration was 1.25 ms, and 3.3 mg of methane were injected. The high temperature was chosen to provide almost immediate ignition.

Figures 7.4 and 7.5 illustrate that the methane mass fraction contour zones at various times after the BOI. In Fig. 7.4, the jet is computationally prevented from igniting, while in Fig. 7.5 ignition takes place. The methane mass fraction contours are narrower for the igniting case, corresponding to the combustion of methane at the jet sides. After the EOI, the free vortex head keeps propagating in the chamber and is rapidly burning as it mixes with chamber air. It is readily observed from these contours that the propagation of the burning jet within the chamber is much the same as that of the non-igniting jet.

Figure 7.6 shows the chemical heat-release rate profiles, indicating the location of the reaction zone. The axial location of the reaction zone is the one plotted in Fig. 7.3 against the changing location of the unity equivalence ratio contour line of the cold jet.

The temperature profiles may be seen in Fig. 7.7. The lateral expansion of the jet discussed above is evident. Again the penetration of the forefront of the jet is seen to be essentially the same as the forefront penetration of the cold jet.

Finally, Fig. 7.8 shows the combustion mode taking place in the reaction zone. In the computations, an index between 0 and 4 was given to each cell, depending on the limiting reaction rate. An index of 0 means little or no reaction rate, 1 means that the ignition scheme

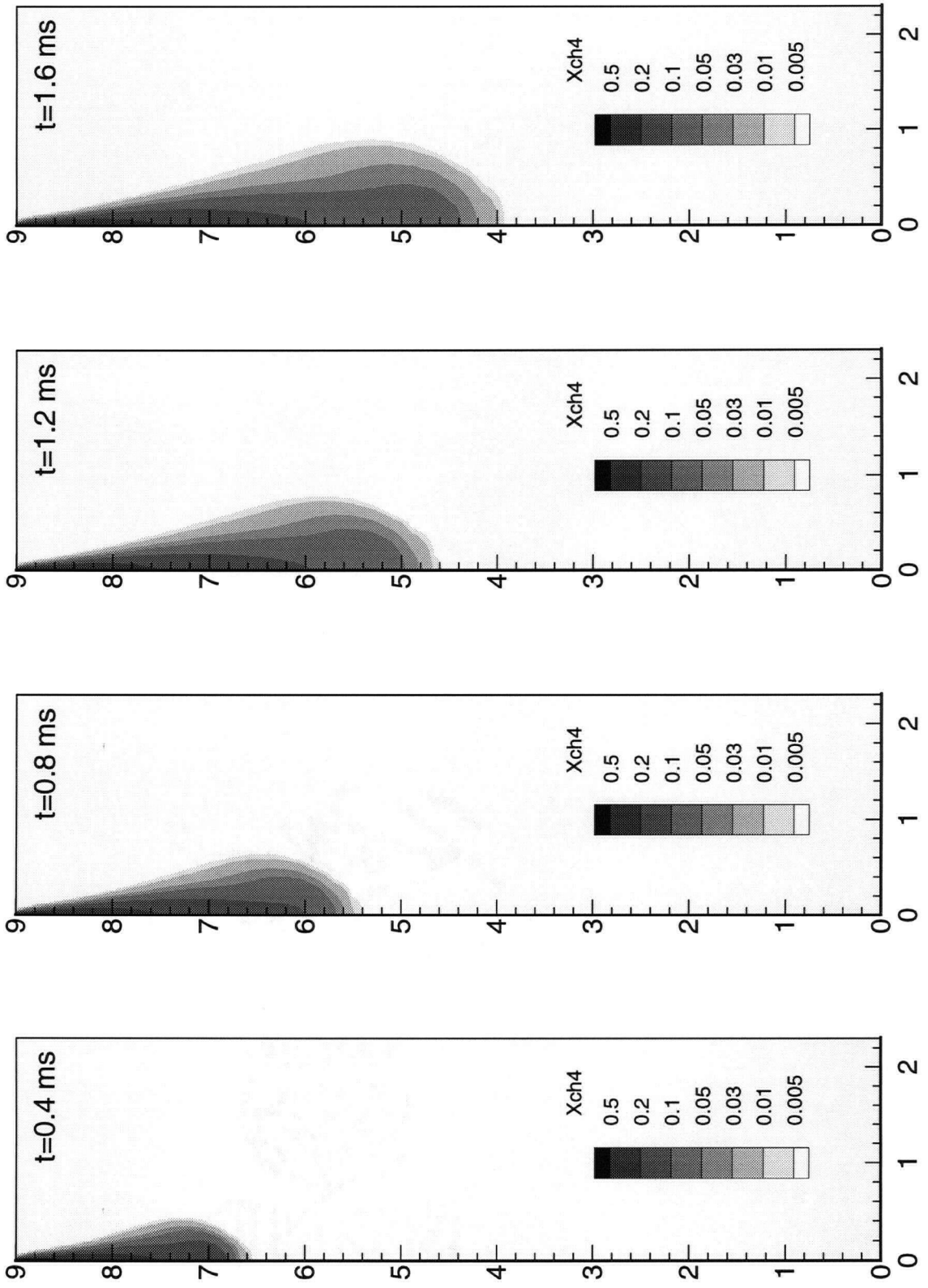

Figure 7.4 - CH_4 mass fraction contours - non-igniting case P_o=15 MPa, d_n=0.4 mm, T_{ch}=1500 K, P_{ch}=7.5 MPa

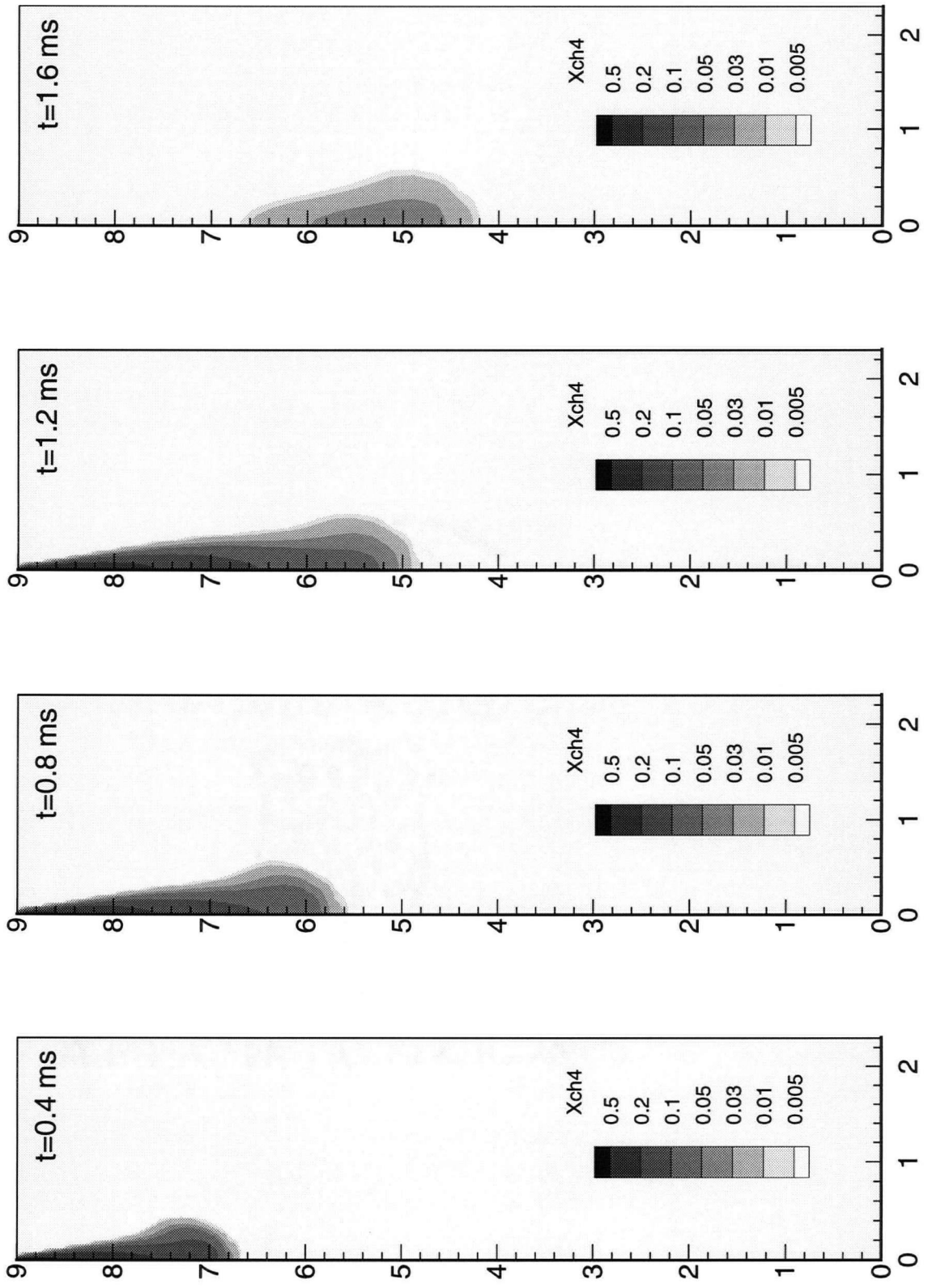

Figure 7.5 - CH_4 mass fraction contours - early-ignition case P_o=15 MPa, d_n=0.4 mm, T_{ch}=1500 K, P_{ch}=7.5 MPa

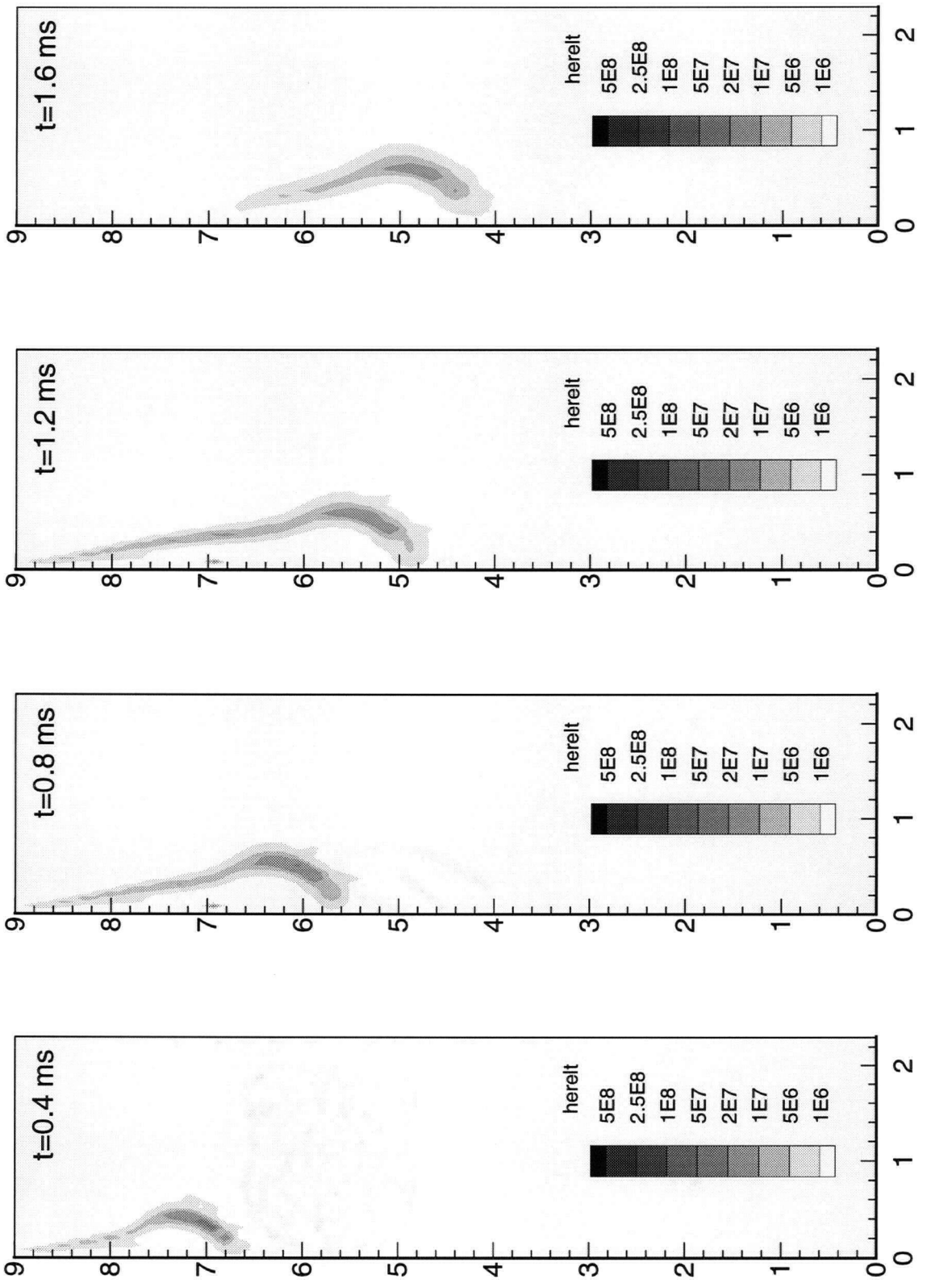

Figure 7.6 - Heat release rate contours - early-ignition case P_o=15 MPa, d_n=0.4 mm, T_{ch}=1500 K, P_{ch}=7.5 MPa

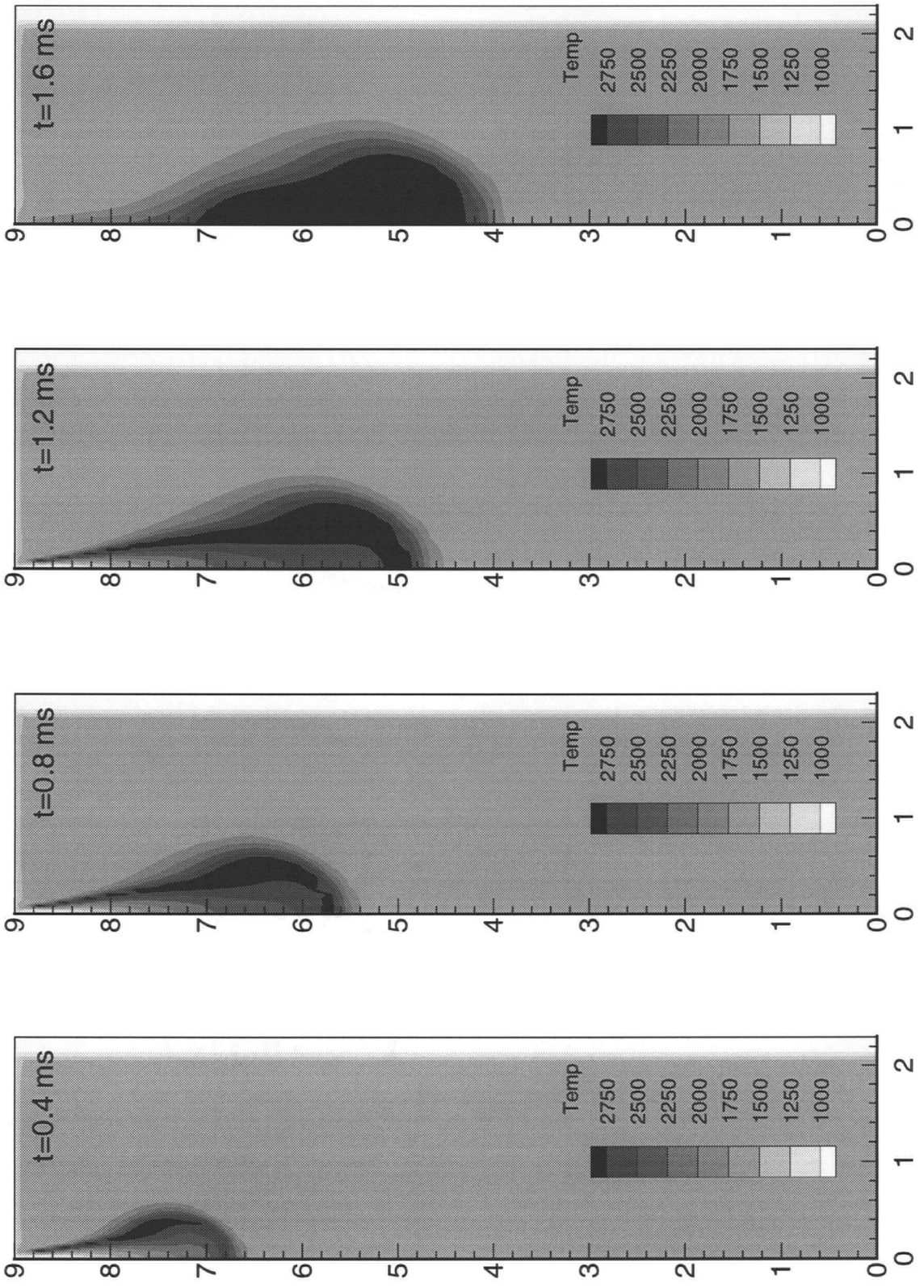

Figure 7.7 - Temperature contours - early-ignition case P_o=15 MPa, d_n=0.4 mm, T_{ch}=1500 K, P_{ch}=7.5 MPa

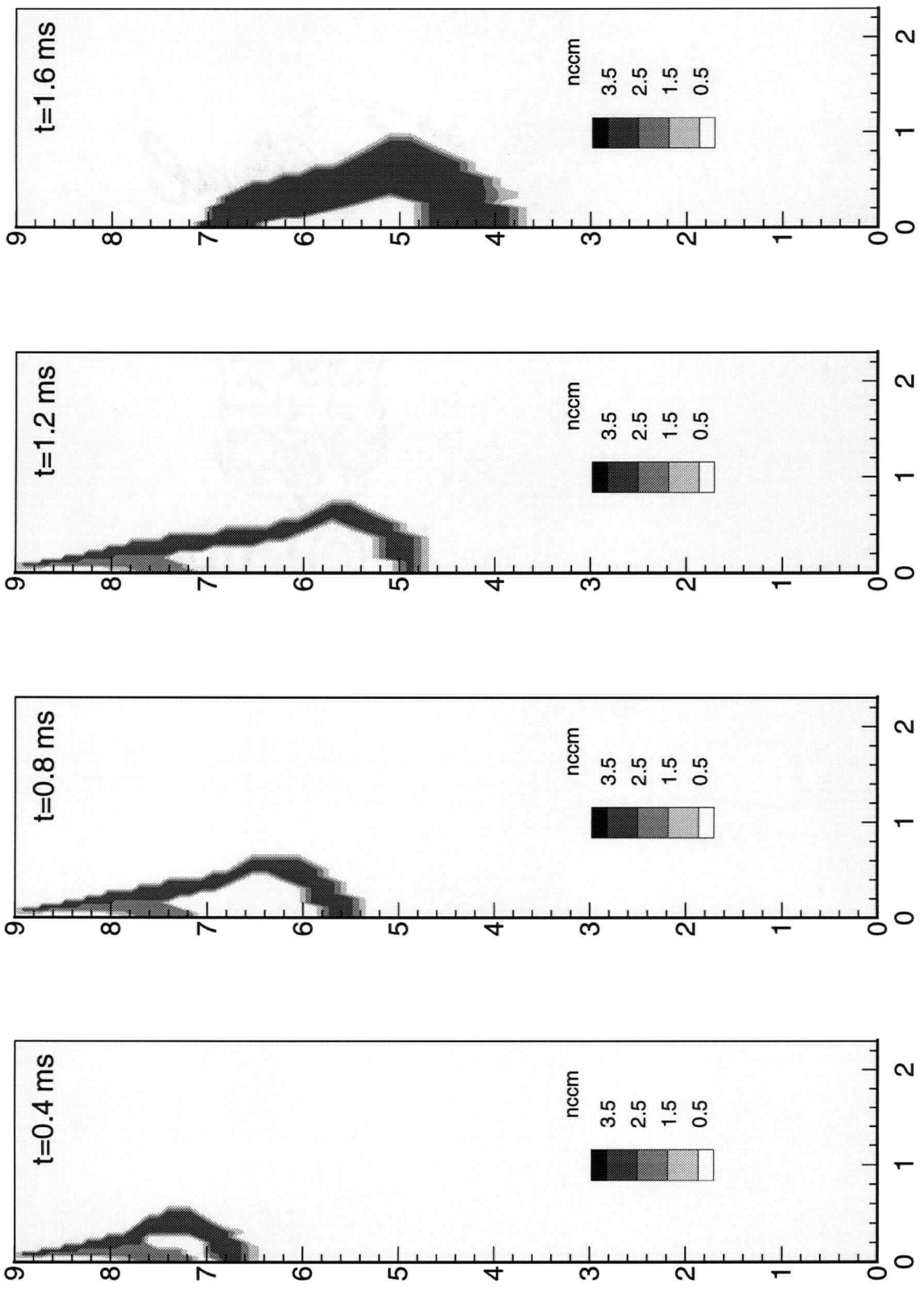

Figure 7.8 - Combustion mode contours - early-ignition case P_o=15 MPa, d_n=0.4 mm, T_{ch}=1500 K, P_{ch}=7.5 MPa (1:ignition, 2:high T kinetic, 3:mixing-limited)

is used, 2 that the high-temperature kinetic scheme is used, and 3 that the eddy-dissipation model is used. An index of 4 would indicate a turbulent combustion limited by the concentration of combustion products, instead of that of fuel and oxidizer. Figure 7.8 shows that in the main reaction zone the combustion is mixing-limited, while some kinetically-limited combustion takes place on either sides of that reaction zone. In the presented flames, the fuel and oxidizer concentrations always limited the mixing-limited rate.

7.2.4 Quasi-Steady Diffusion Flame

The diffusion flames discussed above are developing, but given a sufficiently long time, a quasi-steady diffusion flame would be established. The term quasi-steady is employed recognizing that a truly steady-state flame would not occur in the changing environment of a diesel engine. It may be of interest to estimate the length of the flame and the time required for the establishment of a steady-flame.

The above results indicate that the cold jet provides a good estimate of the reaction zone location based on the axial location of the stoichiometric point. Using the knowledge of steady-state jets, one can write, similarly to Eq. 2.9 :

$$\chi_m = \frac{k_c}{z/d_{eq}} \tag{7.1}$$

where χ_m is the centerline mass concentration of nozzle fluid, and k_c is a constant equal to approximately 4.55 (Birch *et al* [1984]). Replacing z by z_f, the axial flame length, where χ_m is equal to $\chi_{\Phi=1}$:

$$z_f = \frac{k_c d_{eq}}{\chi_{\phi=1}} \tag{7.2}$$

The mass concentration for stoichiometric methane is 0.055, such that an approximate turbulent

methane diffusion flame length can be obtained from $z_f \approx 83\ d_{eq}$.

The result that the turbulent flame length is only dependent on the nozzle diameter (and not on nozzle velocity) is well supported in the literature. The most cited source is the classical result of Hawthorne *et al* [1948] who showed experimentally that above a certain Reynolds number, the ratio of the flame length to nozzle diameter of turbulent flames remains constant.

As a further test, an igniting jet was computed until it reached steady-state with the numerical model. The reaction zone was found to be at approximately 85 d_{eq} from the nozzle, in good agreement with the above estimate.

To reach a non-dimensional distance of 85, it takes a non-dimensional time tU_n/d_{eq} of approximately 1000 (Eq. 3.1). Considering that U_n is approximately 400 m/s (choked nozzle) and that the equivalent diameter under considerations here are of the order of 0.8 mm (Table 5.2), then it would take of the order of 2 ms for the flame to establish itself. This is in most cases an upper limit since in most of the engine operating range the injection duration is less than 2 ms. Consequently, it is expected that quasi-steady flames are not usually established under the present conditions.

7.3 LATER IGNITION - MIXED COMBUSTION MODE

If the jet ignites at a later time, some premixing occurs between the fuel and the oxidizer. As a consequence, the flame has a different history, and the global heat release rate in the chamber is affected. In Section 7.3.1, a methane jet igniting at approximately 1 ms is compared with the transient diffusion flame of Figs. 7.4 to 7.7. In Section 7.3.2 and 7.3.3, the effect of ignition delay and of injection rate on the combustion of methane jets is discussed. In the present discussion, a formal ignition delay definition is not necessary. However, for clarification, it may

be taken as the intersection of the tangent to the pressure rise curve and the time axis.

7.3.1 Comparison with Transient Diffusion Flames

An ignition delay of approximately 1 ms is obtained for an initial chamber temperature of 1200 K. An initial chamber pressure of 6 MPa is set, yielding the same chamber density as the case illustrated in Figs. 7.4 to 7.7.

Figure 7.9 shows the methane-mass-fraction contour zones. The jet appears initially unaffected by chemical reactions, but the narrowing of the mass fraction profile after 1 ms indicates that some oxidation has taken place. This is best seen in the heat-release contour plots of Fig. 7.10. There is initially little activity going on, but zones of higher reactivity appear at the back of the vortex head after 1 ms. The total volume of the reaction zone at this time is correspondingly greater than for the early-ignition case. Figure 7.11 shows the corresponding temperature profile, and differs spatially from the previous case in that the zone of high temperature, and therefore the lateral expansion, is localized around the initial ignition sites. Finally, the reaction mechanism is presented in Fig. 7.12, where it appears that most of the combustion is still mixing-limited, but restricted by the presence of oxidizer.

In Section 7.2.2, the diffusion flame scaled well with the non-igniting jet as seen in Fig. 7.3. For the later ignition cases, such as the one illustrated in Figs. 7.9 to 7.12, it is more difficult to show the same scaling. The center of the reaction zone no longer corresponds to the stoichiometric point of the non-igniting jet, but is rather located on the lean side of the mixing layer (at the jet axis). Since mixing takes place before ignition, the reaction zone also tends to be broader.

Nevertheless, when comparing Figs. 7.9 to 7.11 with Fig. 7.4, it is clear that transient flames still follow closely cold jets penetration rate.

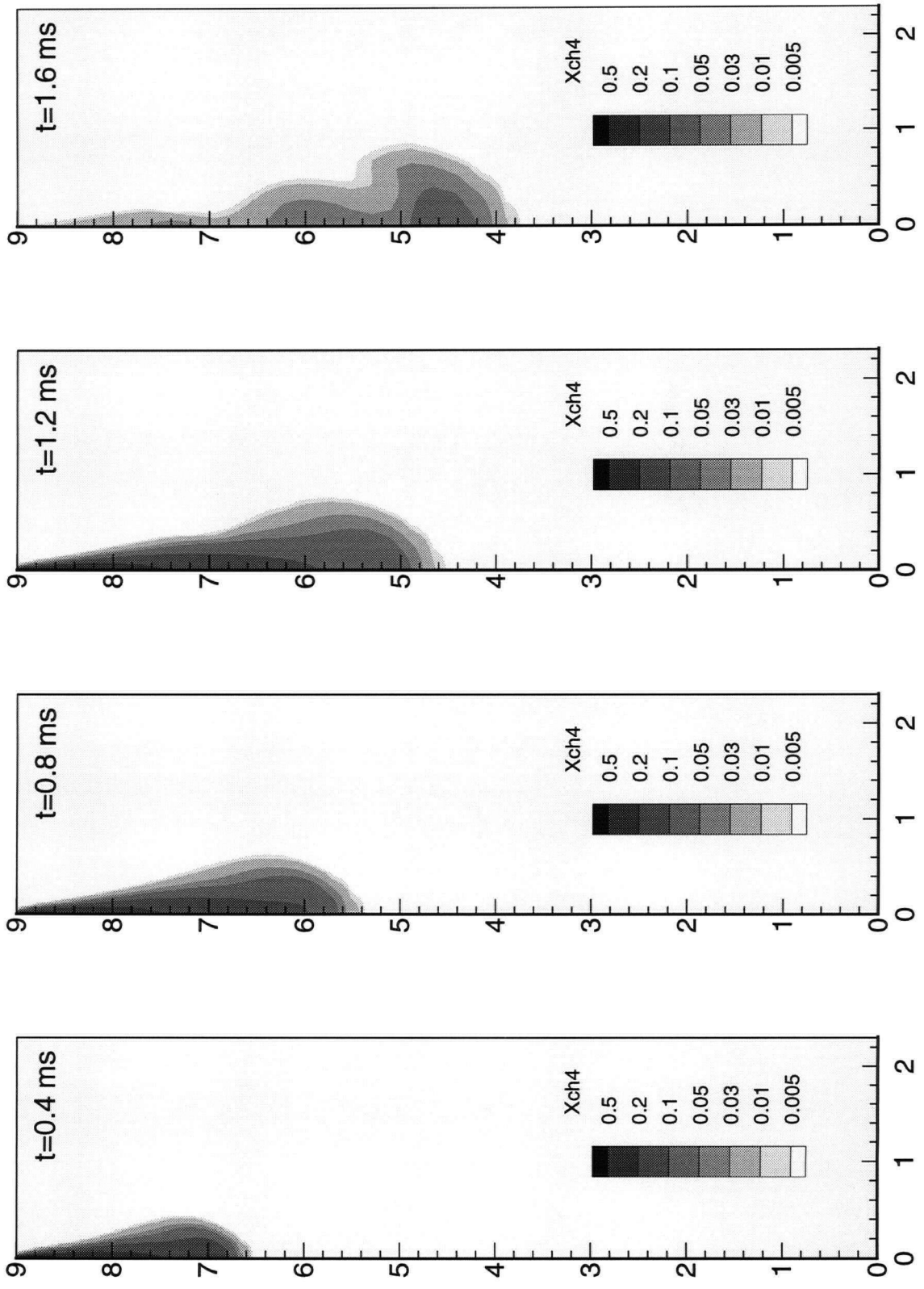

Figure 7.9 - CH_4 mass fraction contours - ignition at 1 ms. P_o=15 MPa, d_n=0.4 mm, T_{ch}=1200 K, P_{ch}=6.0 MPa

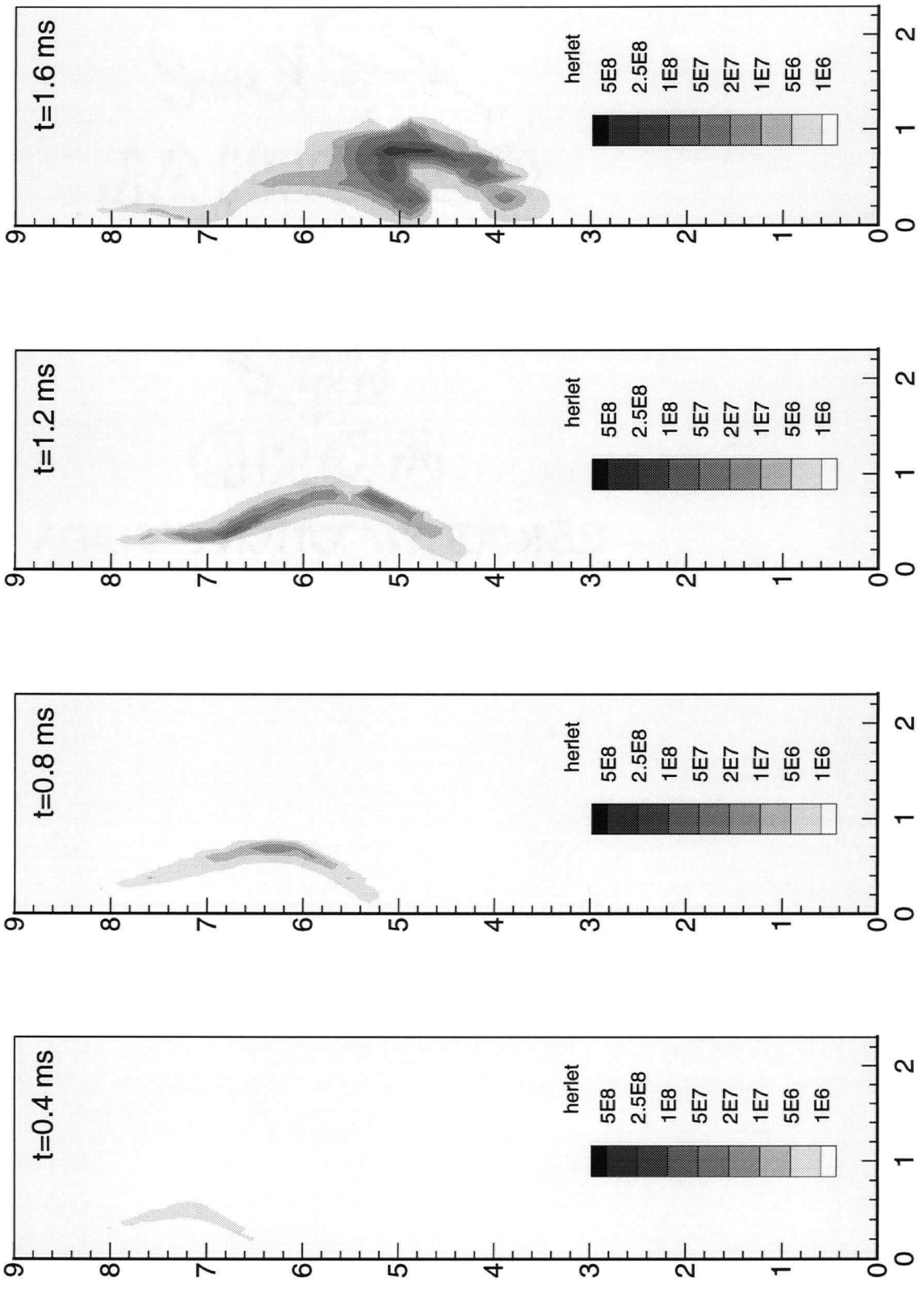

Figure 7.10 - Heat release rate contours - ignition at 1 ms P_o=15 MPa, d_n=0.4 mm, T_{ch}=1200 K, P_{ch}=6.0 MPa

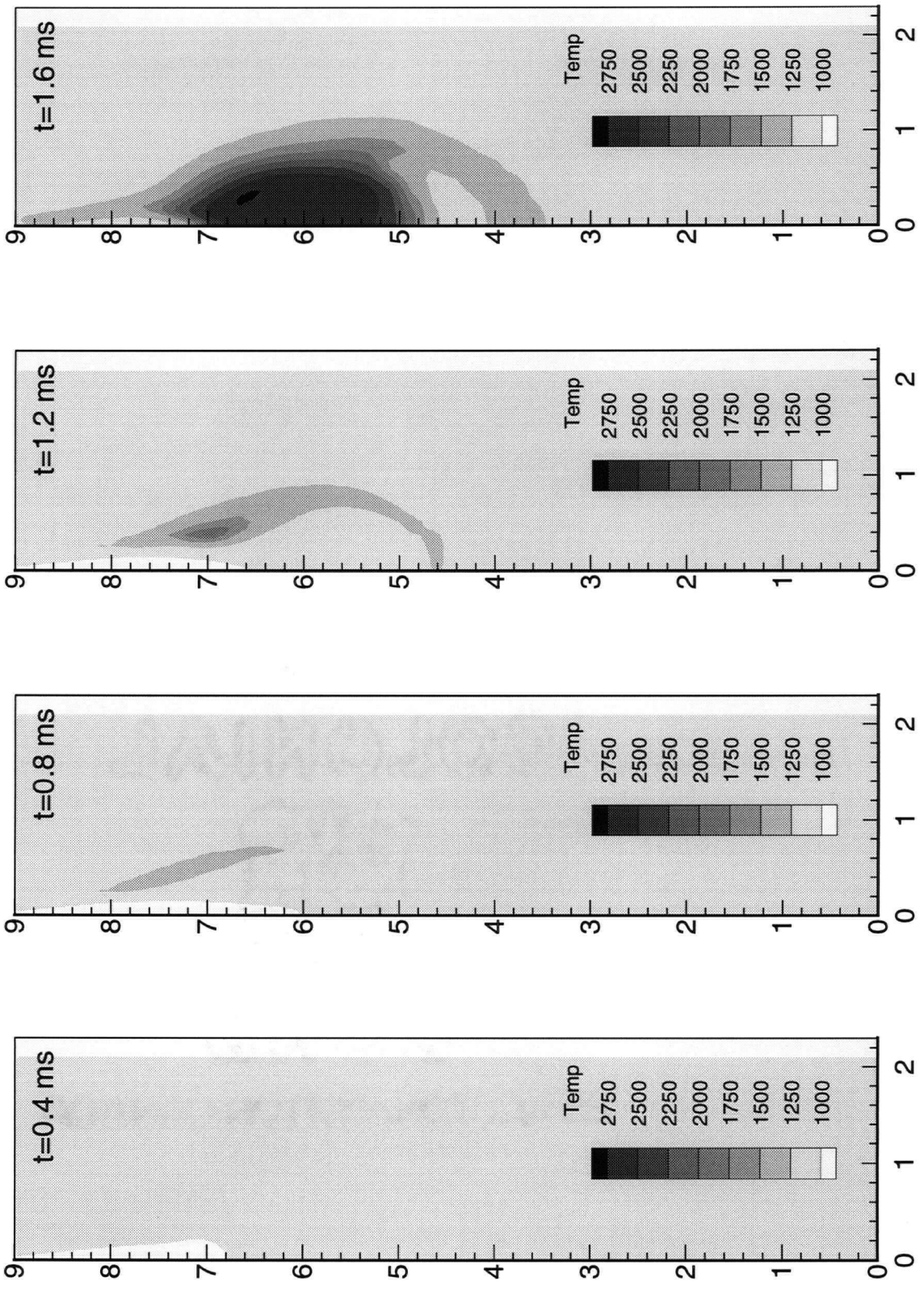

Figure 7.11 - Temperature contours - ignition at 1 ms P_o=15 MPa, d_n=0.4 mm, T_{ch}=1200 K, P_{ch}=6.0 MPa

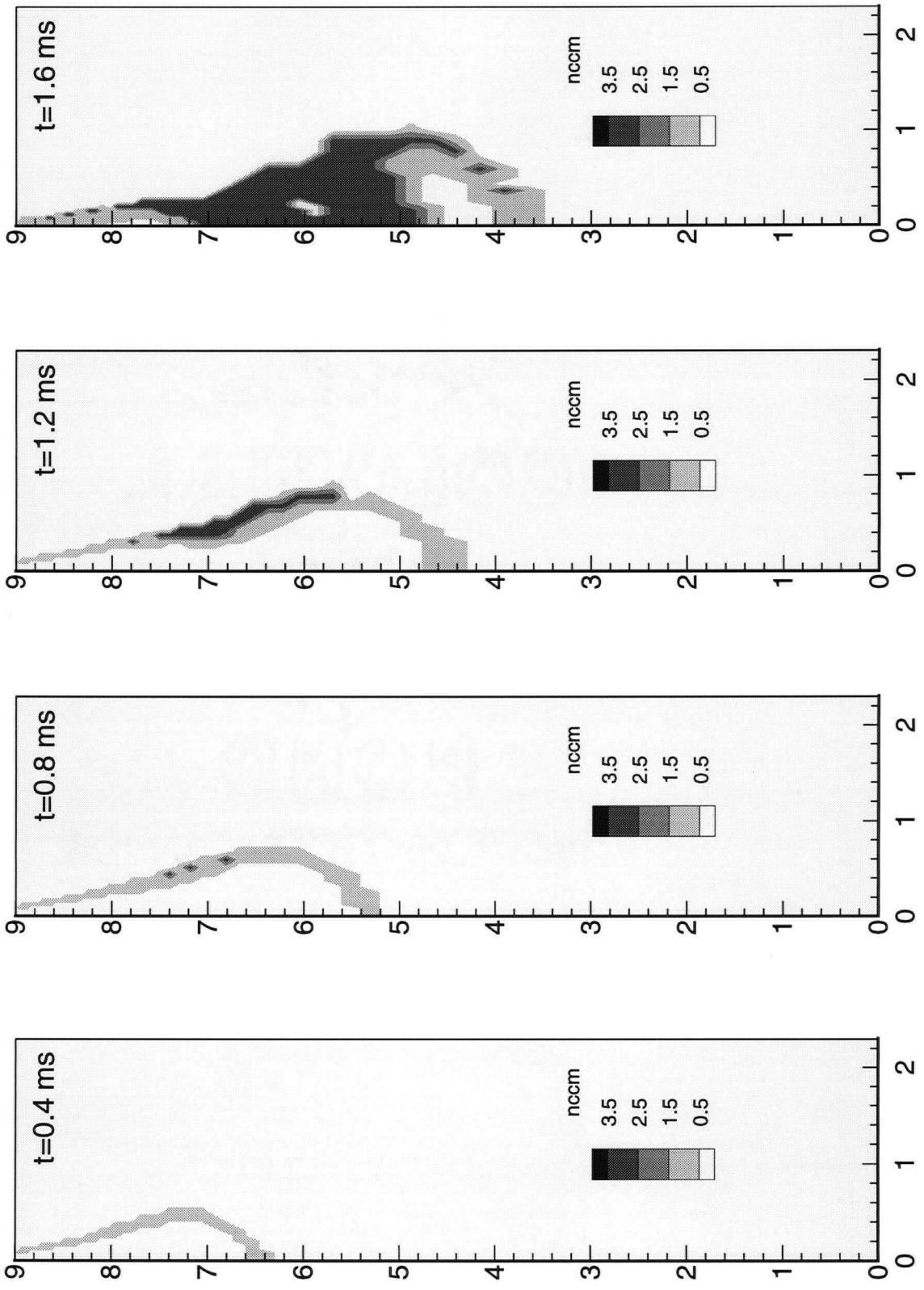

Figure 7.12 - Combustion mode contours - ignition at 1 ms P_o=15 MPa, d_n=0.4 mm, T_{ch}=1200 K, P_{ch}=6.0 MPa (1:ignition, 2:high T kinetic, 3:mixing-limited)

7.3.2 Ignition Delay

The effect of ignition delay on the combustion can be seen by looking at the heat-release rate for various cases. Figure 7.13 shows the normalized pressure rise and the heat release rate as a function of time for ignition delays of 0.1, 0.45 and 1.1 ms. For all cases the injection rate and the chamber density is the same, but the temperature is changed. The total mass injected is

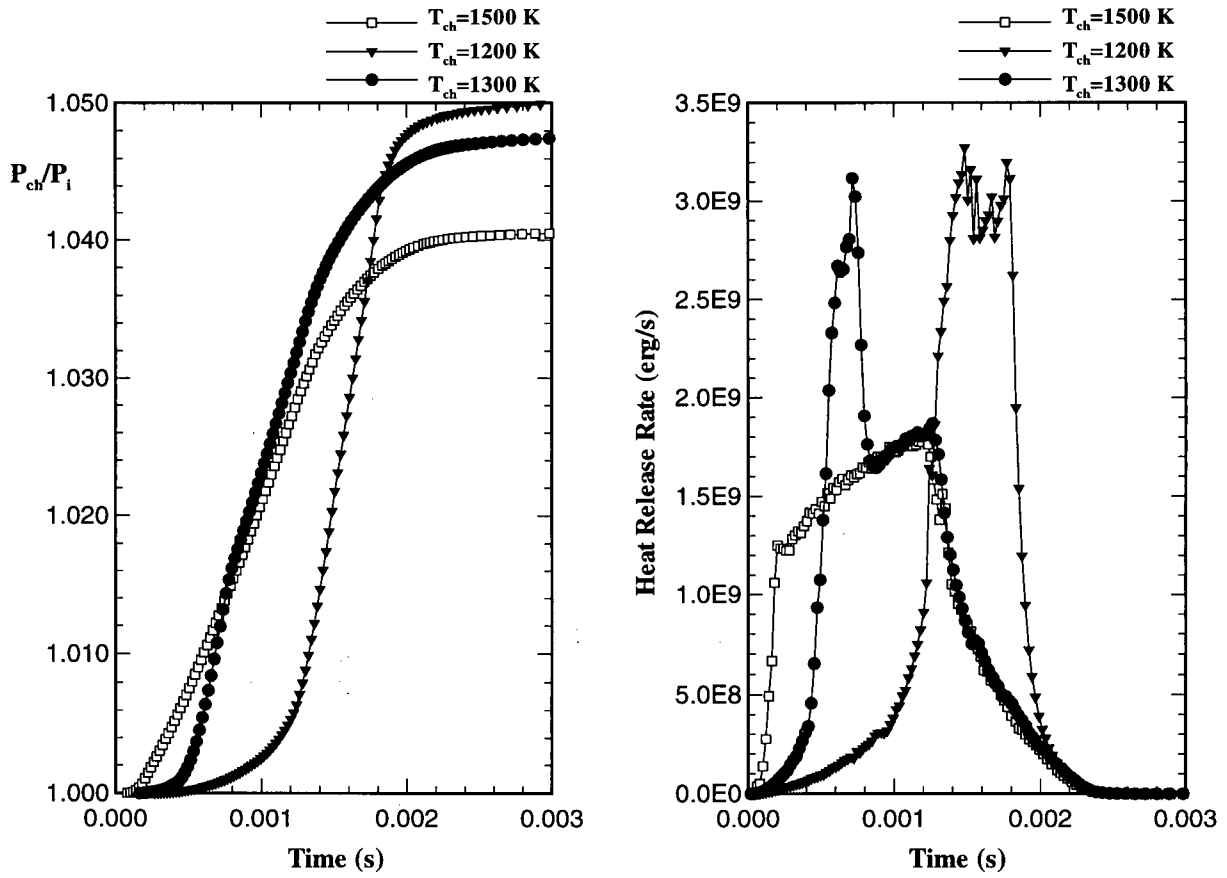

Figure 7.13 - Normalized pressure and heat-release rate for various ignition delays (d_n=0.4 mm, P_o=15 MPa, ρ_{ch}=17.5 kg/m^3, t_{inj}=1.25 ms).

also the same. However, because the heat transfer to the wall is larger for cases with higher initial temperature, the pressure level does not rise to the same level.

The heat release rate shows the different combustion modes. In the case of early ignition, the heat is released in a steady fashion following a very short delay. For the 1 ms ignition delay

case, there is a high heat-release rate peak following the ignition delay. For this case, there is practically no diffusion type burning. Rather there is a rapid combustion of the premixed gases. The intermediate case was calculated with a chamber temperature T_{ch} of 1300 K, for which case the ignition delay is approximately 0.45 ms. A premixed burning phase peak and a mixing-limited diffusion burning phase can be seen.

Figure 7.14 shows the maximum temperature in the chamber and the carbon monoxide as a function of time over the combustion event. The peak temperature may be considered as

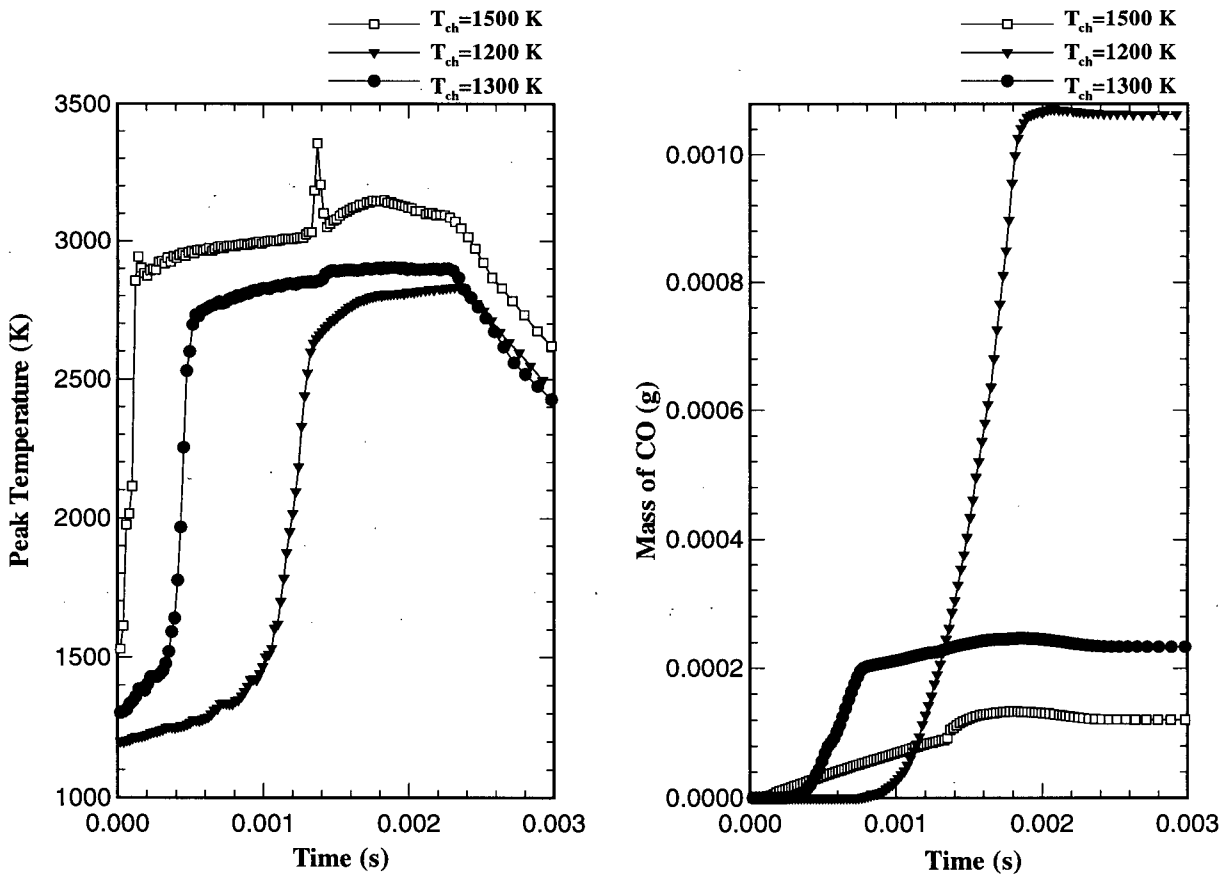

Figure 7.14 - Peak temperatures and carbon monoxide mass fraction (same conditions as Fig. 7.13).

an indication of NO_x formation potential. In the presented cases the temperature is different, but the timing is discussed here. An obvious consequence of earlier ignition is a sooner rise in

temperature, which tends to favor nitrogen oxides formation. The CO formation shows a surprising trend. For late ignition, there is a marked increase in CO formation. The combustion of the premixed fuel-air blend following a long ignition delay is oxygen starved (rich), because oxygen has the time to diffuse to the jet center, but not in enough quantity to result in an overall stoichiometric mixture. At low load, the CO formed in the combustion chamber can typically be oxidized while mixing with the excess air following combustion. At high loads, however, this situation could lead to high CO emissions, which are typically accompanied in diesel engines by high smoke emissions.

7.3.3 Injection Rate

Figure 7.13 shows that the ignition delay controls to some extent the type of combustion taking place. The injection rate also affects the combustion mode by governing the amount of premixed combustion taking place prior to the ignition delay. This is illustrated in Figs. 7.15 and 7.16 where cases with different injection pressures are considered.

High injection rates provide more mixing prior to ignition, and also lead to some rich combustion. Lower injection rates reduce the amount of premixed combustion. The injection rate does not affect the ignition delay significantly, and therefore the peak temperature occurs simultaneously. For a higher injection rate, the reaction zone will be larger (because the jet has penetrated further) and one would expect a higher NO_x formation potential.

7.4 IGNITION BY PILOT FUEL COMBUSTION

In the previous sections, the minimum initial chamber temperature considered was 1200 K. However, the end-of-compression temperature is closer to 800 K in a medium-size diesel engine with a compression ratio of 17:1. At 800 K, the ignition of the natural gas jets would

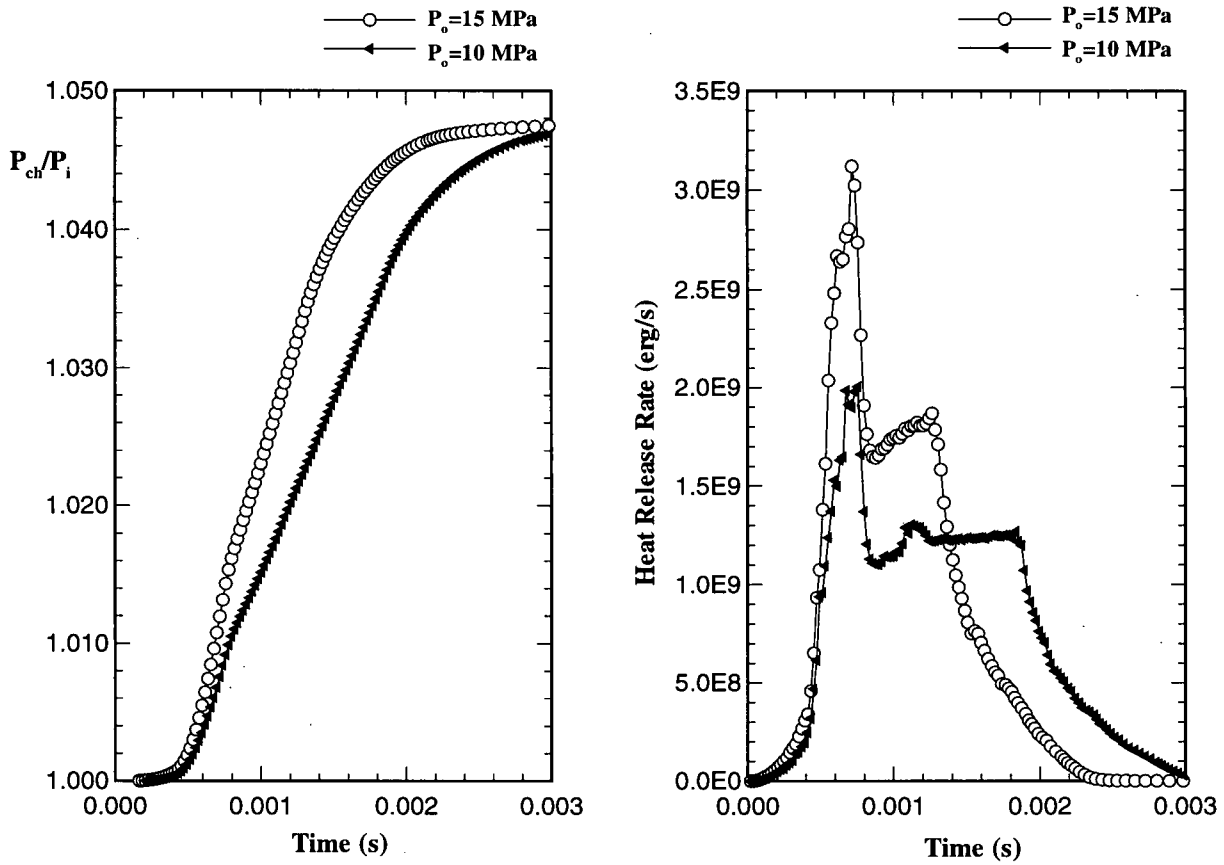

Figure 7.15 - Pressure rise and heat-release for different injection rates (d_n=0.4mm, T_{ch}=1300K, P_{ch}=6.5 MPa, 3.3 mg, were injected in both cases).

take up to 30 ms. As mentioned in the introduction, the combustion of pilot diesel fuel is used in the current research and development effort as a means to ignite the natural gas jets.

There are two main mechanisms by which the pilot fuel combustion can cause the ignition of the gaseous jets. The first one is by raising the pressure and temperature of the chamber air charge as a result of the pilot combustion, while there is no direct interaction between the pilot fuel jets and the gaseous jets. Although this may be contributing to the gaseous jets ignition to some extent, it cannot, under normal operation, raise the air temperature to 1200 K. For example, if the pre-combustion temperature and pressure of an operating diesel engine are approximated to be 800 K and 4 MPa, and if the peak pressure is 7 MPa, then the end-gas temperature may rise to 950 K, assuming an isentropic compression of the chamber air (although

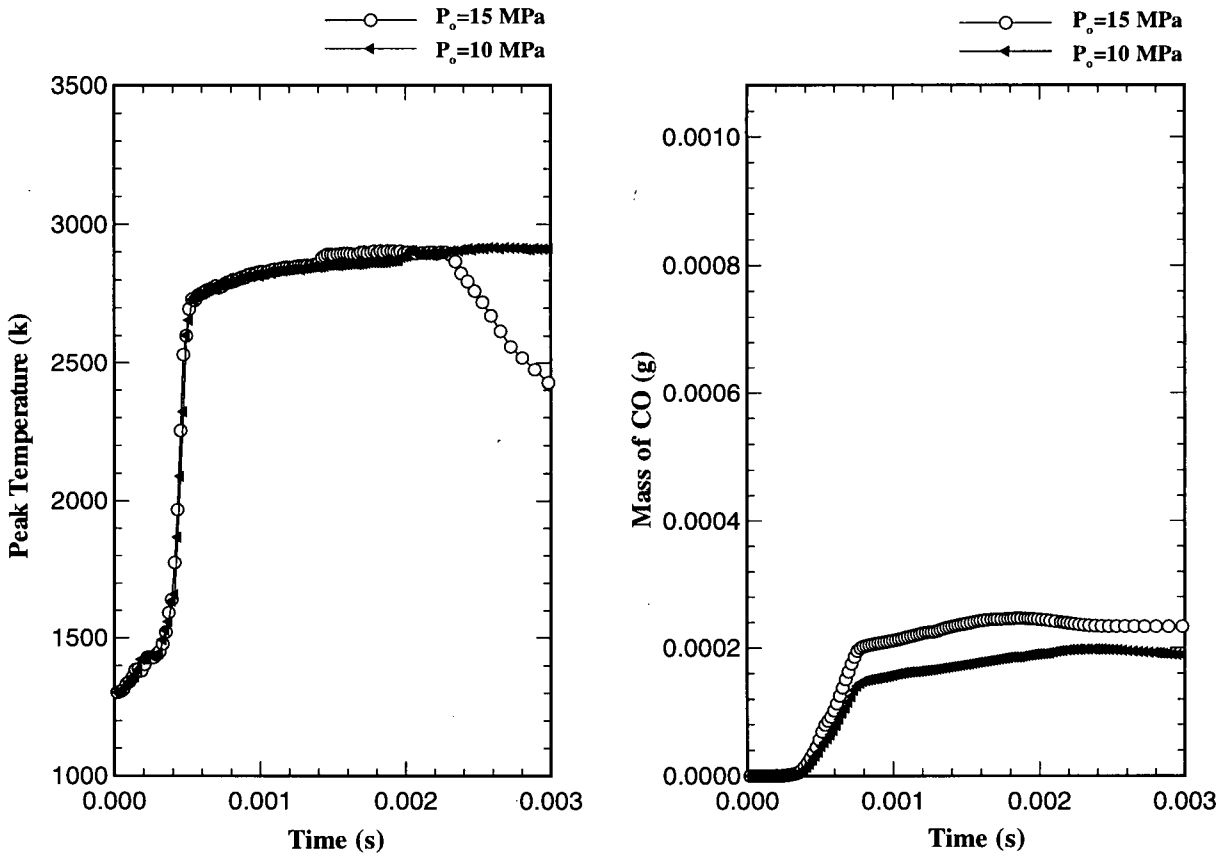

Figure 7.16 - Average temperature and CO formation for different injection rates (same conditions as Figure 7.15).

the average temperature would be above 1200 K). At that temperature, the ignition delay is still unacceptably high, being still in the order of 10 ms.

The second mechanism is through a direct interaction between the pilot fuel jets and the gaseous jets. The nature of this interaction would be the entrainment in the gas jet of hot combustion products, raising, at least locally, the temperature of the gas/air mixture in the jet (hot combustion products would also contain radicals, but their effect is not considered here).

The intent of this section is to investigate the effects of the interaction extent between the pilot flame and the gaseous jets. Furthermore, it has been suggested that an injection delay be used between the pilot fuel BOI and that of the gas jet. The consequence of this delay, and that of injection rate once that delay is fixed, are also investigated numerically.

In the first sub-section, the numerical experiments are described. In Sections 7.4.2 to 7.4.4, the effect of interaction extent, of injection delay and of injection rate are observed. The significance of the observed results are discussed in Section 7.5.

7.4.1 Interaction between Pilot Fuel Sprays and Gaseous Jets

In the following numerical experiments, a spray of liquid diesel fuel is injected in a constant volume chamber initially at 800 K and 4 MPa. The spray evaporates and ignites following a short delay (0.45 ms). The spray is oriented such that there is some interaction with a gas jet injected at the same time or later. In order to retain the axisymmetric treatment, a conical sheet of diesel fuel was injected at an angle from the methane jet axis. The spray, its vapor and the location of the methane jet shortly after the ignition of the diesel fuel can be seen in Fig. 7.17.

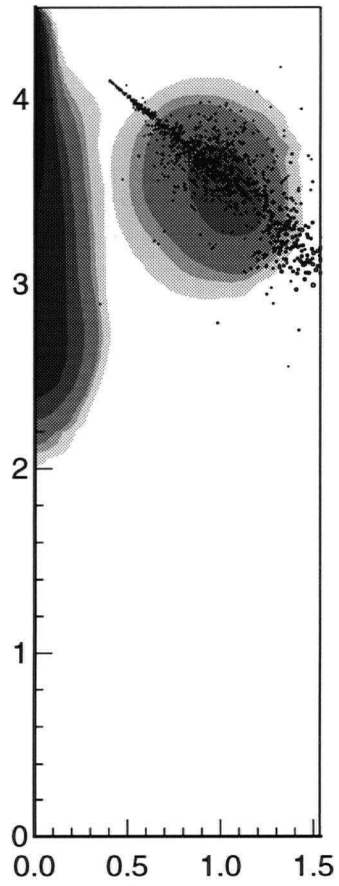

Figure 7.17 - Diesel fuel spray, diesel fuel vapor and methane jet in pilot fuel ignition studies.

The injection location of the diesel fuel was offset from the center of the chamber and from the top wall, because it was found that the combustion products otherwise migrated too quickly towards the center of the chamber. This rapid migration takes place in conical sheets because the entrainment of air within the cone

formed by the sheet acts as a pump.

The extent of interaction between the burned pilot fuel and the gaseous jet, or, in other words, the amount of combustion products entrainment in the gas jet can be effectively controlled by changing the injection angle of the spray sheet (angle between the jet axis and the spray axis). The proposed arrangement is therefore a satisfactory one for the general study of methane jet ignition through entrainment of combustion products. However, the proposed arrangement (central gas jet surrounded by a conical spray) differs from the situation that would prevail in an engine in a number of points. The conical sheet does not penetrate as much as a discrete spray, and offers a continuous surface of interaction with the gas jet, whereas a single spray offers a smaller area of contact. The results of the numerical experiments must be interpreted accordingly with these differences.

In order to represent as well the compression-heating of the pilot fuel combustion, the ratio of diesel fuel mass injected to combustion chamber volume was chosen to be representative of that used in engine testing. This ratio is approximately 1 mg/ 10 cm^3, and in the computations, 3.3 mg of diesel fuel were injected in a 33 cm^3 chamber.

The emphasis of this section is on the ignition and combustion of the gaseous jet through entrainment of combustion products, and the details of the spray are consequently of importance inasmuch as they affect the amount and distribution of combustion products. As stated

Table 7.1 - Pilot fuel spray attributes.

Droplets Sauter mean radius :	5 μm
Droplets injection velocity :	200 m/s
Spray cone angle :	5°
Spray injection duration :	0.4 ms
Mass injected (diesel):	3.3 mg
reaction rate : $RR = A\,[C_{12}H_{26}]^{1.5}\,[O_2]^{0.25}\,e^{-Ea/RT}$	
$A = 2x10^{11}$	
E_a= 125 kJ/mol	
(rate constants taken from Westbrook and Dryer [1981] for dodecane, *A* was reduced by half to provide an ignition delay of approximately 0.5 ms)	

earlier, this is controlled to some extent by controlling the spray injection angle. The spray attributes used in the numerical experiments are given in Table 7.1. The combustion model presented in Chapter 6 remains the same, except for the inclusion of a new reaction rate for diesel fuel and for the change to the stoichiometric coefficient s of the eddy-dissipation rate (Eq. 6.30) which must be generalized for either fuel. The diesel fuel oxidation was modelled as:

$$C_{12}H_{26} + 37/2\ O_2 \rightarrow 12CO_2 + 13H_2O \qquad \textbf{(7.3)}$$

The reaction rate is provided in Table 7.1.

7.4.2 Entrainment of Combustion Products

The entrainment of hot combustion products in the gaseous jet can be seen in Fig. 7.22, where temperature contour plots are presented. The pocket of hot products at 0.6 ms is the result of pilot fuel combustion. Some of the products are drawn into the centrally injected gaseous jet. For the case illustrated the spray angle is 50°. Figure 7.18 shows the pressure rise rate and the heat-release rate in the chamber for spray injection angles of 30°, 50° and 70°. A larger angle signifies less entrainment of combustion products. For the case illustrated, there is a delay of 0.25 ms between the injection of diesel fuel (at t=0) and the injection of methane.

The graph shows the pressure rise due to diesel fuel combustion, and then a subsequent rise for the combustion of methane. The heat release graph shows a large peak associated mainly with the combustion of diesel fuel, and a mixing-limited phase associated with the combustion of methane.

Increasing the interaction between the spray and the gaseous jet reduced the ignition delay of methane and increased its initial combustion rate. This can be seen in Fig. 7.19, which shows the methane mass burned fraction corresponding to Fig. 7.18. Presumably, the increased

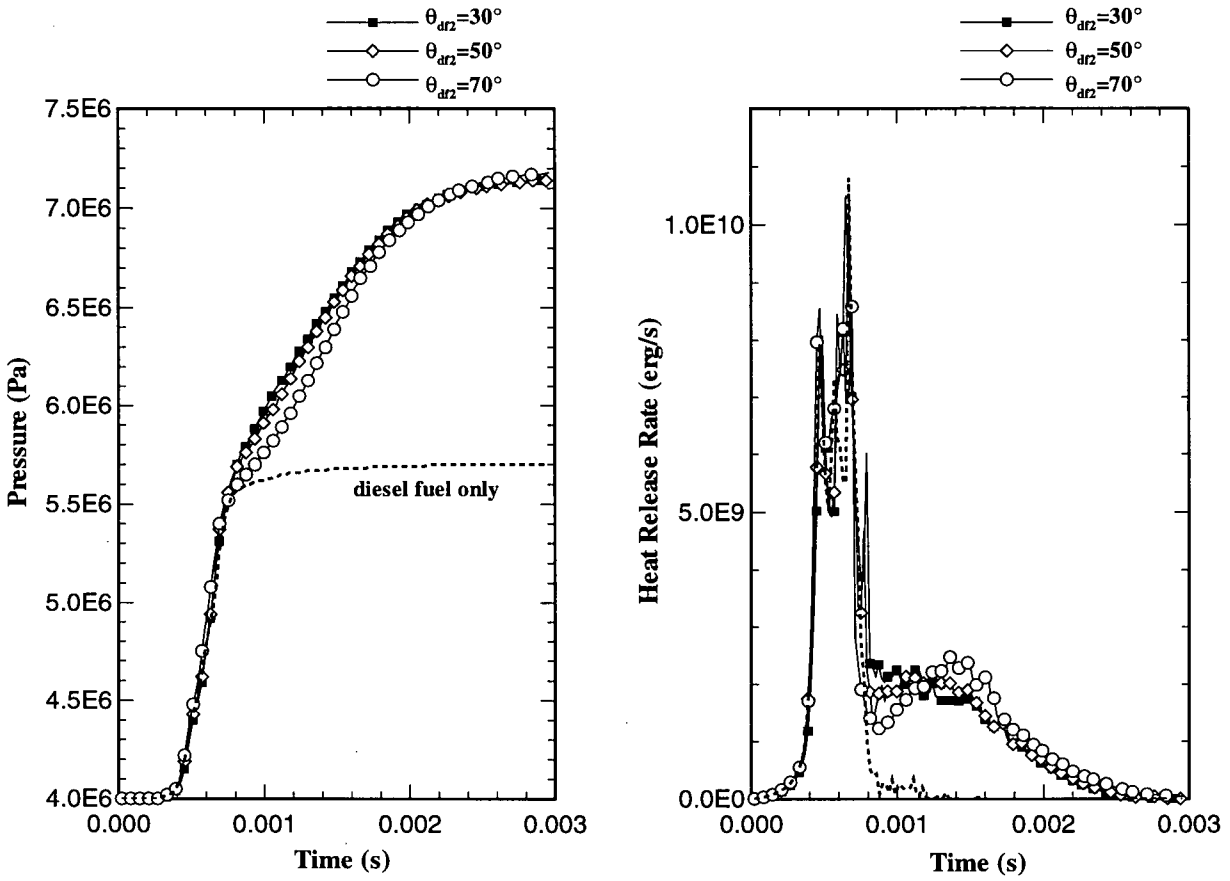

Figure 7.18 - Pressure rise and heat-release rate for pilot diesel and methane combustion. θ_{df2} is the spray injection angle. (P_o=15 MPa, d_n=0.4 mm, Δt=0.25 ms, t_{inj}=1.22 ms).

interaction has two effects; the first is to bring hot combustion products sooner within the gas jet, favoring early ignition, while the second is to entrain more combustion products, increasing the initial combustion rate of the gaseous jet.

7.4.3 Injection Delay

When pilot diesel fuel jets are used to cause the ignition of the gaseous jets, it is possible to introduce an injection delay between the injection of diesel fuel and that of the gaseous fuel. Presumably, injecting the natural gas after the pilot diesel fuel has ignited increases its chances of igniting early by interacting sooner with combustion products.

Figure 7.20 shows the methane mass burned fraction for no injection delay and for

injection delays of 0.25 and 0.5 ms. The diesel fuel ignition is occurring at approximately 0.45 ms. The methane is seen to ignite at much the same time, indicating that the diesel fuel combustion controls the ignition of the methane jet.

One consequence of the injection delay is that the overall combustion event is longer for a given injection rate. As the fuel is injected later, it may be necessary to increase the injection rate to be able to inject the required amount of fuel within a reasonable time near TDC.

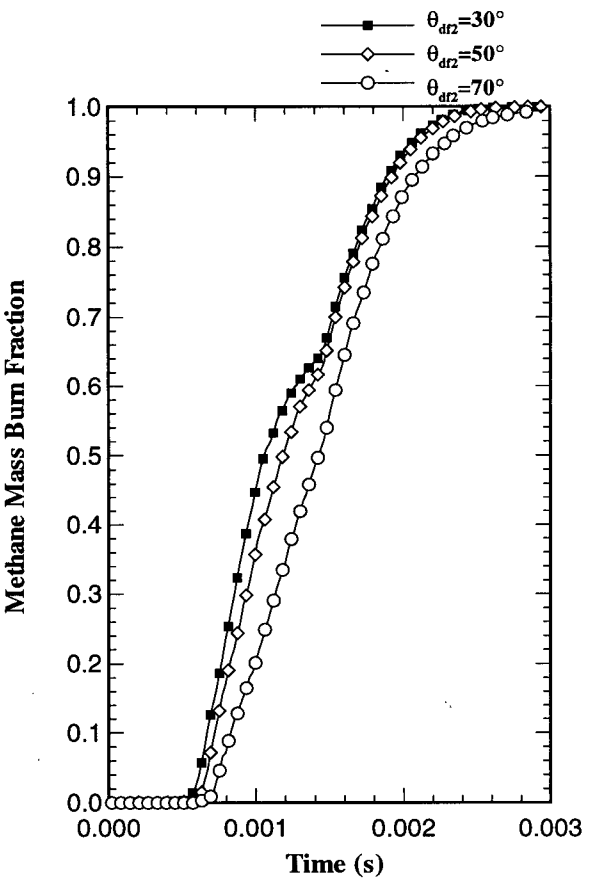

Figure 7.19 - Methane mass burned fraction for case of Fig. 7.18.

Figure 7.24 shows the formation rate of carbon monoxide for injection delays of 0 and 0.5 ms. It may be seen that there is more carbon monoxide formed when there is no delay. This is analogous to the effect of ignition delay on the combustion of autoigniting jets, discussed in Section 7.3.2. A short injection delay corresponds to a long autoignition delay; more premixing takes place, and a richer combustion proceeds.

It may also be seen in Fig. 7.20 that the combustion of methane is incomplete for the case of zero injection delay. The flame progression presented in Figs. 7.21 and 7.22 helps explain the reason for this incomplete combustion. The entrainment of combustion products is recognizable at 0.8 ms on the temperature contours. But at the same time the head of the jet is already far into the chamber. For the illustrated configuration, the high temperature zone lags behind the

head of the jet, and some of the methane reaches the wall before burning. As the injection delay is increased, the gas jet is not as far into the chamber at the pilot fuel ignition time, and this situation is avoided. It should be mentioned that this observation is somewhat dependent on the configuration presented here. If the interaction takes place further downstream, as may be expected for discrete jets, the entrainment of combustion products may more easily be distributed within the gaseous jet.

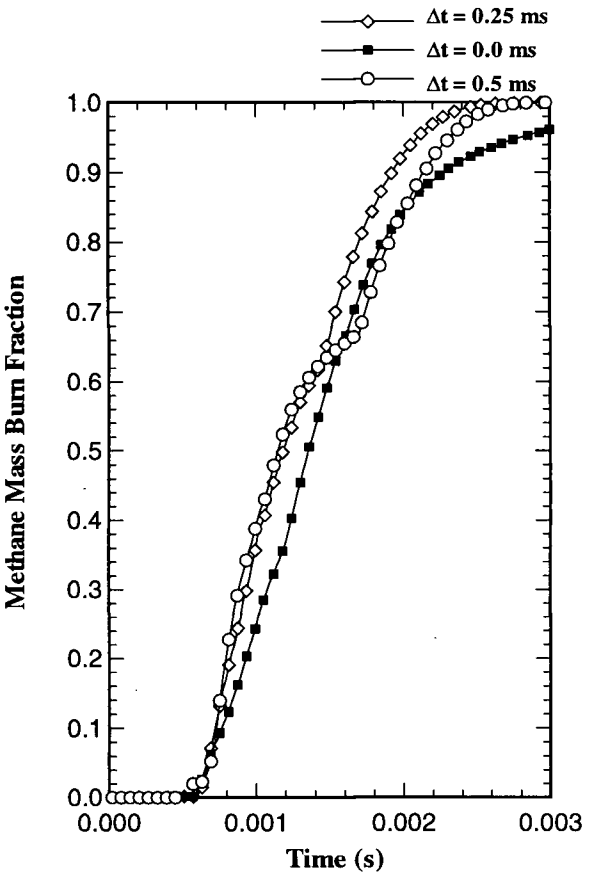

Figure 7.20 - Methane mass burned fraction for different injection delay Δt. θ_{df2}=50°. Other conditions same as in Fig. 7.18.

In Figs. 7.19 and 7.20, the mass burned fraction is seen to change slope at the time corresponding to the end of injection. Prior to the end of injection, the reaction zone grows with time, such that the combustion rate also increases. This growth stop at the end of injection.

7.4.4 Injection Rate

Figure 7.23 shows the effect of changing the injection rate on the ignition and combustion of a methane jet ignited by pilot fuel combustion. In all cases a mass of 3.3 mg of methane was injected, adjusting the injection duration accordingly. The pressure rise and heat-release rate are shown. The injection delay in these cases was 0.25 ms. As may be seen, the principal effect of the injection rate is to change the combustion rate, with little effect on ignition delay.

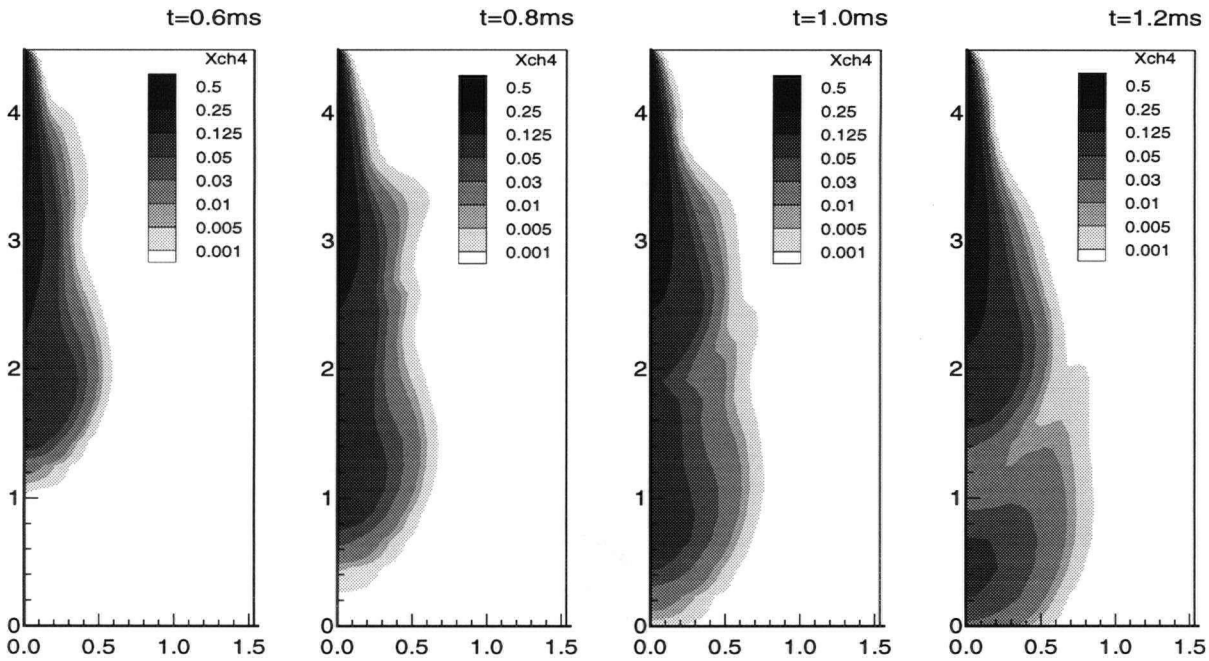

Figure 7.21 - Methane mass fraction contours. Ignition of methane jet through diesel fuel combustion. Δt = 0 ms. Same conditions as in Fig. 7.20.

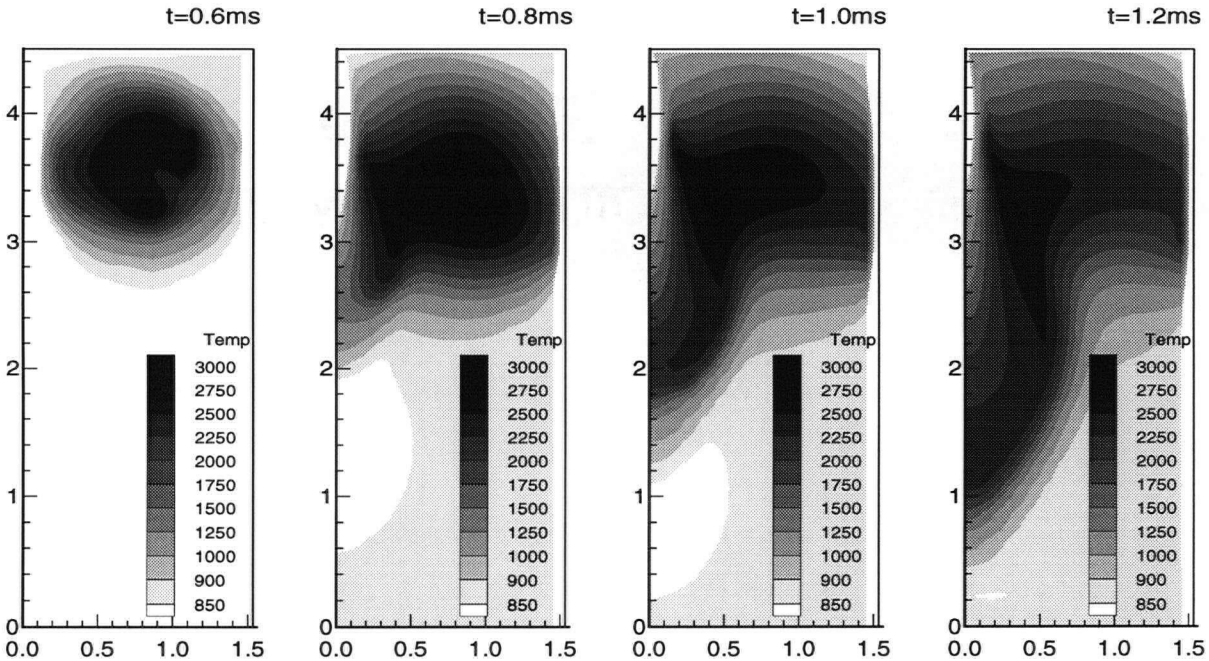

Figure 7.22 - Temperature contours. Same conditions as Fig. 7.21.

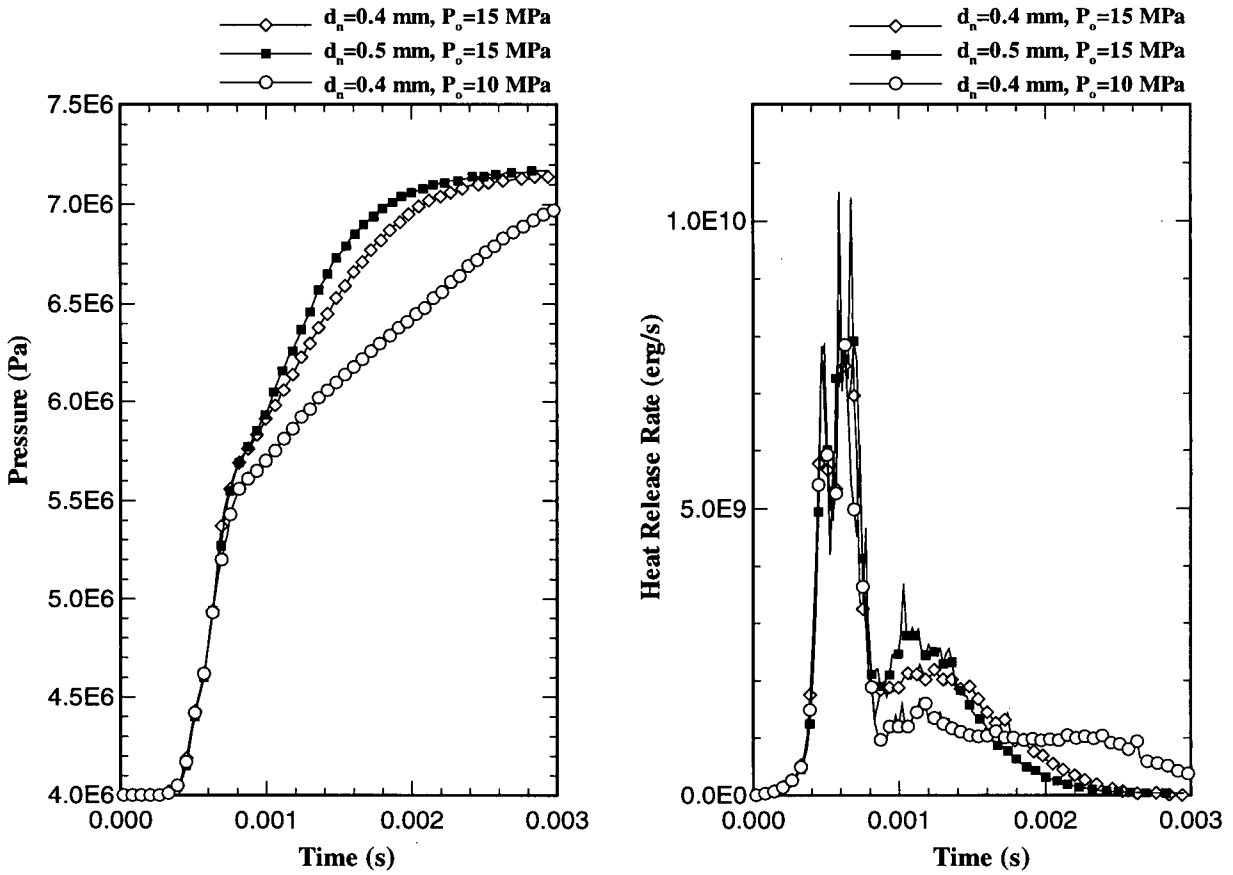

Figure 7.23 - Effect of changing the injection rate on the combustion of methane ignited by pilot combustion. (P_{ch}=4 MPa, T_{ch}=800 K, Δt=0.25 ms)

However, as can be seen in Fig. 7.24, the injection rate also increases the amount of premixed combustion. As for the autoignition cases, increasing the injection rate increases the mixing prior to the jet ignition, and leads to the formation of more CO.

7.5 SUMMARY AND DISCUSSION

Early-ignited transient flames were found to penetrate at the same rate as cold jets, when the axial location of the maximum reaction rate in the flames was compared to the axial location of the unity equivalence ratio in the cold jets. Flames issued from nozzles of different diameters and operated at different injection pressures scaled well with the equivalent diameter, indicating that the cold jet scaling laws are valid for the penetration of flames. In all cases, flames were

found to be wider than the cold jets, due to the expansion of the burned gases.

Flames in which a large amount of premixing occurs prior to ignition were observed, from numerical simulations, to also follow closely the penetration of cold jets, but a criterion could not be found to formally compare those flames with cold jets.

When pilot-ignited jets are considered, numerical simulations indicated that increasing the interaction between sprays and gaseous jets is beneficial. An increased interaction leads to earlier entrainment of combustion products, causing earlier methane jet ignition, and to a larger amount of entrained combustion products, thus increasing the burning rate of the methane jet.

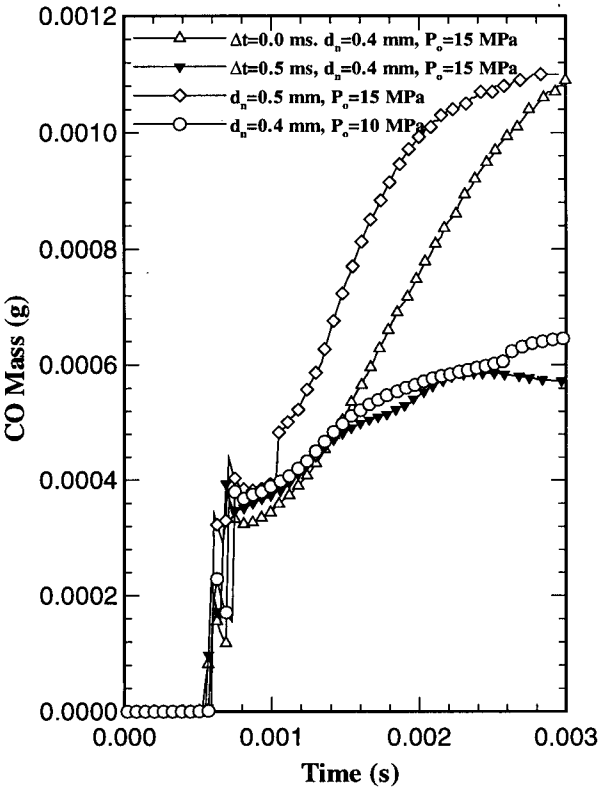

Figure 7.24 - Effect of injection delay and injection rate on the formation of carbon monoxide. (P_{ch}=4 MPa, T_{ch}=800 K)

In practice, there are many options to increase the interaction between sprays and jets, for example by orienting and locating the respective fuel nozzles on the injector tip. Increasing the number of nozzles would also increase the interaction between fuel sprays and jets. However, the diesel fuel spray should be left free to ignite in air before interacting with the gaseous jets. Engine testing with combined diesel fuel sprays and natural gas was found to result in very long ignition delays (Hodgins *et al* [1992]).

For both the autoignited and the pilot-ignited jets, changes in injection rate were found to change the combustion rate and to change the relative amount of premixed to mixing-limited

combustion. Higher injection rates lead to more mixing taking place before ignition, which resulted in rich premixed combustion. This rich combustion occurs because not enough air reaches the center of the jet prior to ignition, and was observed by higher carbon monoxide formation. The injection rate was not found to significantly affect the ignition delay.

Longer ignition delays, given a fixed injection rate, also lead to more mixing between the fuel and the air prior to combustion. A long ignition delay can be thought of as a long autoignition delay or as a short delay between the injection of the pilot fuel and that of the natural gas jet.

Injecting the gas a short time after the injection of the pilot fuel was found to be beneficial for the studied configuration, as it ensured the ignition and combustion of the whole methane jet. Injection delays of the order of the pilot fuel ignition delay were considered. With such delays, it was found that the injected methane jet ignited almost instantaneously, as the early-ignited flames discussed in Section 7.3.

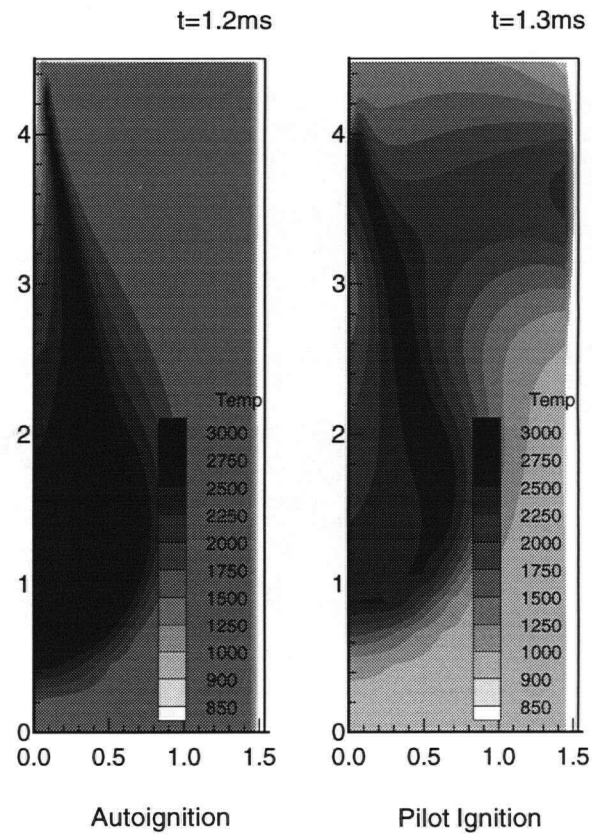

Figure 7.25 - Comparison between the temperature contours of autoignited jet (T_{ch}=1500 K) and of the pilot-ignited jet.

Given a suitable injection delay, pilot-ignited methane flames may therefore penetrate like the early-ignited diffusion flames of Section 7.3, which were themselves following the penetration of cold jets. Unfortunately, the presence of the conical sheet pilot jet changes to some extent the entrainment rate of air in the chamber, and the smaller chamber tends

to enhance the effects of confinement. Consequently, it is harder to demonstrate this last suggestion. In Fig. 7.25, a pilot-ignited methane jet is compared to a autoignited (early-ignition) methane jet. It may be seen that the pilot-ignited jet has penetrated less in the chamber and is broader than the autoignited jet. Still the penetration distances are similar.

CHAPTER 8

CONCLUSIONS

Transient turbulent underexpanded jets are formed when natural gas is directly injected in a diesel engine. Following ignition, the gas combustion rate is controlled by the mixing of the jets with the chamber air. The penetration rate of the jets is a measure of mixing, and controls the location of the reacting zones within the combustion chamber.

The first objective of this work was to establish the dependency of the penetration and mixing rate of transient gaseous fuel jets upon the injection and chamber conditions. A simple yet comprehensive description of transient turbulent compressible jets, representative of the jets formed by natural gas injection in diesel engines, was established. This description is presented in Section 8.1, with other conclusions regarding cold (non-igniting) jets. The second objective aimed to verify that cold transient jet scaling was applicable to igniting jets. The third objective was to determine the effect of injection and chamber conditions on the ignition and combustion of transient methane jets. Finally, a fourth objective was to investigate the interaction between pilot fuel sprays and gaseous jets, and the consequences of injection delay and injection rate on the ignition and combustion of pilot-ignited gaseous jets. Igniting jets, either through autoignition or pilot-ignition, were found to penetrate at much the same rate as cold jets, but an appropriate penetration criterion could only be well established for diffusion flames with little or no premixed burning. The second, third and fourth objectives pertained to igniting jets, and the corresponding conclusions are presented in Section 8.2. These conclusions are followed by a discussion of their implications for diesel engine fueling, and by suggestions for future work.

8.1 NON-IGNITING TRANSIENT TURBULENT COMPRESSIBLE JETS.

I) Equivalent Diameter for Steady-State Jets

▹ The equivalent diameter $d_{eq}=d_n\ (\rho_n/\rho_{ch})^{1/2}$, where d_n is the nozzle diameter, ρ_n the density at the nozzle exit and ρ_{ch} the chamber density, is an appropriate length scale for turbulent jets issued from round nozzles.

The equivalent diameter as stated above is appropriate for round jets with nozzle Reynolds number greater than $3x10^4$, and for jets that are incompressible, compressible, underexpanded, of different molecular weights and of different temperatures. Support for an equivalent diameter based on ρ_g/ρ_{ch}, the ratio of injected gas density to chamber gas density taken at the same pressure, was known, the main contribution of this work being to show, based on experimental data available, that underexpanded jets could also be included by using the density ρ_n at the nozzle instead of ρ_g.

II) Transient Jet Penetration

▹ For a turbulent jet issued from a round nozzle, the jet tip penetration can be expressed as

$$z_t' = 3.1\ \left(\frac{\dot{M}_n}{\rho_{ch}}\right)^{1/4} t^{1/2} \qquad \textbf{(8.1)}$$

where z_t' is the distance from the virtual origin of the jet, $\dot{M}_n$ is the momentum injection rate at the nozzle, and t the time from the beginning of the injection. Equation 8.1 is equivalent to and derived from the following equation which shows the length and time scales employed

$$\frac{z_t'}{d_{eq}} = 2.9\ \left(\frac{tU_n}{d_{eq}}\right)^{1/2}, \qquad d_{eq} = d_n\left(\frac{\rho_n}{\rho_{ch}}\right)^{1/2} \qquad \textbf{(8.2)}$$

where U_n is the nozzle exit velocity.

These relationships were found to be applicable at 15 to 20 equivalent diameters from the nozzle, depending on the opening delay of the injector and on the nozzle exit velocity profile. Equations 8.1 and 8.2 are valid relationships for all jets specified in the first conclusion. The validity was verified for distances up to 120 d_{eq}, and for times shorter than the injection duration. The main support for this conclusion is the scaling of experimentally determined penetration rate data for compressible jets. Another support for this conclusion is the observation that integral models, which simulate transient jets as quasi-steady jets feeding a vortex head, perform well when compared with experiments. This supports the argument that the length scale for steady-state jets can be extended to transient jets. Also, dimensional analysis indicates that the variables in Eq. 8.2 can completely describe the transient jet.

III) Validity of Multidimensional Model

▹ A two-dimensional prediction of a transient incompressible jet penetration was compared with the experimental data of Witze [1980]. The prediction was found to under-estimate the penetration rate by 10%. Three-dimensional predictions of underexpanded methane jets were found to under-estimate the penetration rate by approximately 10% when compared to the experimentally determined penetration rates obtained in this work.

The reported inaccuracy of the k-ε turbulence model (used in this work) in treating steady-state jets is a potential explanation for the penetration under-estimates. In the case of the underexpanded jets, other uncertainties are the choice of a comparison mass fraction criterion between the observed jets and the computations, and the accurate determination of the boundary conditions. Grid sensitivity studies for near-sonic jets indicated that using a grid size of the order

of 0.4 mm in the nozzle area led to grid independent penetration predictions, based on a 0.5 equivalence ratio contour line definition. In the center of the jet where gradients are steeper, grid independence was not quite achieved. Even with a near-nozzle grid size of the order of 0.1 mm, the equivalence ratio contour line of 2 was still slightly affected by grid size.

IV) Mixing Rate of Transient Jets

The mixing rate was defined as the rate of formation of lean, flammable and rich mixtures within the chamber. The non-dimensional mixing rate was defined as the mass of methane within the specified equivalence ratio range (0.5 to 2 for flammable mixtures) divided by the total mass of methane injected.

▹ Numerical modelling indicated that the equivalent diameter of Eq. 8.2 and the time scale provided by d_{eq}/U_n are appropriate scales for the mixing rate between the injected gas and the chamber air. Numerical predictions of mixing rate for jets issued from nozzles operated at different injection pressures and of different diameters scaled well when the time scale normalized the time and the mass injected normalized the methane mass mixed within specified fractions.

The above conclusion was found to be valid until the end of injection. It was also suggested that the jet mixing rate, defined as the mass of air entrained within the jet as a function of time, is proportional to $\dot{M}_n^{3/4}\rho_{ch}^{1/4}t^{3/2}$. Consequently, the mixing rate is reproduced for different cases when this product is constant. Distributing the mass injection rate amongst more holes of smaller diameter was found to improve mixing slightly. The above conclusion, and the ones that follow, were obtained by calculating the injection of methane along the axis of a constant-volume cylindrical chamber, where typical diesel engine conditions prevailed. This simplification allowed an axisymmetric treatment of the problem, and unequivocal interpretation of the results.

V) Injection Duration

▹ When finite duration injections are taking place, the penetration of the jet following the end of injection is eventually altered. It was found however that the jet penetration following the end of injection remains essentially the same for up to 2 times t_{inj}, the injection duration.

VI) Chamber Turbulence Levels

▹ Computational results showed that turbulence levels representative of engine conditions promoted jet lateral spreading and reduced the penetration rate by 4% compared to the penetration occurring in a zero turbulence chamber. This result was obtained by observation of the 3% methane mass fraction contour line, which corresponds approximately to an equivalence ratio of 0.5. Increasing the chamber turbulence levels by a factor of 10 compared to typical engine levels caused a further decrease in penetration rate of 2.5%.

These results suggest that the flammable mixture formation of the transient methane jets under consideration is not strongly affected by engine turbulence levels.

VII) Comparison of Gaseous Jets and Sprays

▹ Numerical simulations predicted an essentially equal rate of formation of flammable mixture when considering a gas jet and a spray with identical nozzle momentum injection rate, and penetrating in a chamber at the same density. Furthermore the penetration was much the same when the cone angle of the spray was set at a similar angle to that of the gaseous jet spreading rate.

These numerical results were obtained by considering droplets of Sauter mean radius of

5 and 10 μm injected in a chamber at 1200 K. When the spray angle was increased, the mixing rate stayed essentially the same, at the expense of the penetration rate. In the above case, the spray angle was imposed in the computations. In practice, the spray angle depends on the density ratio and on the length-to-diameter ratio of the nozzle. Because of this nozzle dependency, the penetration of spray cannot be scaled as simply as gaseous jets, which can be considered independent from the nozzle in the fully developed region.

Conclusions *I)* to *VII)* provide an understanding of gaseous injection in diesel engines. Regarding the gaseous injection design parameters, much can be understood by considering Eq. 8.1 alone. The penetration and mixing of one jet are increased by increasing the nozzle momentum injection rate, which depends on the size of the nozzle, the nozzle density and the nozzle velocity. The nozzle velocity and density are increased by an increase in injection pressure, until the choking condition is met. Further increase in injection pressure raises the nozzle density only (under the perfect gas law assumption). For the calculation of the nozzle conditions, the knowledge of the pressure ratio across the nozzle and of the upstream temperature are required. The chamber density also appears in Eq. 8.1; the penetration is decreased and the mixing increased by an increasing chamber density.

8.2 IGNITING TRANSIENT JETS

At typical end-of-compression temperatures, the autoignition of methane is prohibitively long, and consequently another source of ignition must be provided. In the natural gas fueling system discussed in Section 1.1 of the thesis, pilot diesel fuel sprays are used as a source of ignition. The mechanism by which the pilot fuel sprays cause the ignition of the gaseous jets is by entrainment of hot combustion products within the gas jets. Since the extent of interaction

between the pilot fuel sprays and the gaseous jets is not known *a priori*, a kinetic scheme capable of reproducing the temperature dependency of methane ignition was implemented in the numerical model. The ignition of the gaseous jet through pilot fuel combustion was also considered.

VIII) Methane Autoignition

▹ A single-step methane autoignition model was derived from shock-tube experiments found in the literature and was implemented in the multidimensional model. The model was used to simulate the autoignition of transient gaseous methane jets available in Naber *et al* [1994], and reproduces well the temperature dependency of the experimental autoignition delays. However, the proposed ignition scheme has a pressure dependency of $P^{-0.7}$, while the experimental data of Naber *et al* have a pressure dependency of $P^{-0.95}$.

The ignition kinetic scheme was tested against experimental data of underexpanded jets (injection pressure of 20.7 MPa) in a chamber at densities of 6.4, 20.4 and 32.6 kg/m^3, and at temperatures between 1100 and 1600 K. The scheme pre-exponential constant was adjusted to best fit the 20.4 kg/m^3 data.

IX) Similarity between Diffusion Flames (early-ignited) and Cold Jets

▹ Jets that almost immediately ignite as they enter the combustion chamber become transient diffusion flames. The simulated penetration of the maximum axial reaction rate of those flames was found to be the same as the penetration of the unity equivalence ratio contour line of cold jets injected under the same conditions. Furthermore, the penetration of flames generated from nozzles of different diameters and operated at different injection pressures was found to scale well with d_{eq} and U_n. The width of the flame, based on the

velocity profile for example, was found to be larger than that of the cold jet.

This result shows that the scaling laws established for the penetration of cold jets remain valid for the penetration of diffusion flames. The lateral expansion of the jet is caused by the low density of the burned gas. It should be emphasized that early-ignited flames burn almost entirely in a mixing-limited combustion mode. To simulate diffusion flames, a turbulent combustion model of the eddy-dissipation type was implemented in the multidimensional model. The implemented model is closely related to similar models found in the literature. The dependency of the combustion rate on the model constant was verified, and it was found that in the mixing-limited combustion phase, the rate was determined by the mixing rate of fuel and air and was only slightly affected by the choice of model constant. Early-ignition was obtained by injecting methane in a chamber at a temperature of 1500 K.

X) Late Ignition

▹ For jets that ignite at a later stage (around 1 ms), an appropriate criterion upon which to compare cold jets and flames could not be found. As a result of the premixing taking place before ignition, the reaction zone is broader and tends to locate itself on the lean side of the jet. It is observed, however, that the predicted penetration of late-igniting jets is much the same as that of the cold jets.

▹ An increase in momentum injection rate favors ignition by providing more ready-to-ignite mixture, but the changes in ignition delay are modest.

When considering autoignition, the chamber temperature becomes an important parameter, as it controls the ignition delay. As this delay is increased, the amount of premixed combustion increases, while less mixing-limited combustion occurs. The nozzle momentum injection rate affects the mixing rate and, therefore, the relative amount of premixed and mixing-limited

combustion occurring following ignition. A higher nozzle momentum injection rate also led to a faster combustion rate. While comparing with jets issued in chambers at different temperatures (different ignition delays), the pressure was adjusted to retain the same chamber gas density.

XI) Consequence of Premixed and Diffusion Combustion

▹ Simulations showed that for ignition delays of 1 ms, some oxygen reaches the center of the jet prior to ignition. The amount of oxygen is, however, less than that required for stoichiometric combustion and, consequently, a rich combustion proceeds.

▹ The rich combustion does not take place when ignition occurs early. High temperatures are however occurring sooner in the combustion process.

The oxidation of methane was modelled as a two-step mechanism, with an initial oxidation of methane to CO and a subsequent oxidation of CO_2. The occurrence of rich combustion for jets burning predominantly in a premixed fashion was indicated by a higher rate of formation of CO than for the diffusion flame. Also, the combustion was found to be predominantly turbulent-limited during that premixed phase, but limited by the concentration of oxygen. Since high temperatures occur sooner for short ignition delays, nitrogen oxides would have more time to form; however their formation was not modelled in this work.

XII) Gaseous Jet Ignition through Pilot Fuel Combustion

Two-dimensional simulations of a gaseous jet ignited by a pilot diesel fuel jet were performed. A conical sheet spray was injected at an angle from the gaseous jet axis. Changing the axis of the spray sheet changed the amount of interaction between the burning pilot fuel and the injected gas. The chamber in these simulations was 800 K, at which temperature methane does not ignite within the time span of interest.

▹ Simulations of transient gaseous jets ignited through the combustion of pilot diesel fuel showed that increasing the interaction between the diesel fuel sprays and the gas jet led to a decrease in ignition delay (of the gaseous jet) and to an increase in initial burning rate.

▹ Providing an injection delay between the pilot fuel and the gaseous fuel jet ensured the ignition and combustion of the entire jet. For injection delays shorter than the combustion duration of the pilot fuel, ignition of the gas jet took place at the same time despite the considered change in injection delay.

The reduction in methane ignition delay accompanying the increased interaction is due to an earlier entrainment of combustion products within the gas jet. The observed increase in initial combustion rate is due to a larger amount of entrained combustion products. The second stated conclusion can be better understood considering that if the gas jet has penetrated too far into the chamber at the time of pilot ignition and combustion, the forefront of the jet may not come into contact with combustion products and may not burn, a situation that was predicted in this work. Also, decreasing the injection delay leads to more premixed combustion taking place prior to combustion, as in the case of late ignition. This indicates a parallel situation between the injection delay of pilot-ignited flames and the ignition delay of autoignited flames. In the configuration studied, when an injection delay of the order of the pilot ignition delay was chosen, the injected methane jet became rapidly a diffusion flame, without premixed combustion, as in the case of early-ignited flames in the autoignition discussion. Since early-ignited flames were found to penetrate at the same rate as cold jets, then pilot-ignited jets that ignite almost immediately as they enter the chamber, following a suitable injection delay, should also penetrate at the same rate as cold jets. However, the chamber air motion was significantly affected by the presence of the conical pilot fuel spray, and this similitude could not be formally verified. Visual

observation does reveal however that the penetration is much the same.

8.3 DIRECT-INJECTION OF NATURAL GAS IN DIESEL ENGINES

The dependency of the injection rate and of the mixing rate on the injection pressure, nozzle diameter and chamber conditions was discussed at the end of Section 8.1, on the basis of Eq. 8.1. The are further practical design considerations that follow from the work done in this thesis (c.f. Sections 5.5.2 and 7.4):

- In an ideal case, a smaller nozzle operated at high injection pressure can be replaced by a larger nozzle operated at a lower injection pressure. This is significant as the injection pressure requires on-board compression of the gas. (In practice there is however a trade-off; to maintain a choked nozzle, which is desirable from a control point of view, the total area of the holes must be smaller than the ports inside the injector.)

- The momentum injection rate must be reproduced if one wants to reproduce the mixing rate.

- High nozzle momentum may favor mixing and high heat release rate, but it also favors high penetration rate and can cause over-mixing. Over-penetration with wall impingement is not desirable due to potential quenching of the reactions. Over-penetration sets a limit on the momentum injection rate of each hole. Over-mixing can occur if too much lean mixture is formed prior to ignition of the gas jet.

- When substituting natural gas for diesel fuel, one may want to ensure that the penetration rate of the gaseous fuel does not exceed the penetration rate of the diesel fuel. It may be difficult to know this penetration rate, but it may be evaluated on the basis of various correlations. Assuming that the diesel injector produces sprays with a spreading angle reasonably close to that of the gaseous fuel, then the penetration rate conditions

requires an equivalency of the momentum at each nozzle.

- When substituting natural gas for diesel fuel, a first estimate of injection parameters can be obtained by duplicating the total momentum injection rate of the diesel fuel operation. This may lead to different conditions than trying to match the mass injection rate as the liquid fuel and gaseous fuel velocities at the nozzle are likely to differ.

- Under the assumptions stated in the two above considerations, it can be stated that when injecting natural gas rather than diesel fuel, a number of nozzles equal or greater than that of the diesel injector can be used.

- Choosing an injector tip configuration that favors some interactions between the pilot fuel jets and the gaseous jets is advantageous (the diesel fuel jets should however be left free to ignite in an oxygen environment). Using more nozzles is a way to increase jet interaction.

- Injecting the gaseous fuel a short time after the pilot diesel fuel injection minimizes the risk of over-leaning of the gaseous jet prior to ignition. A suitable injection delay may be the ignition delay of the diesel fuel.

8.4 SUGGESTIONS FOR FUTURE WORK

More results of practical importance could be learned by performing three-dimensional studies. In particular the effect of injection angle and piston motion on the jet mixing and combustion would be of interest. Three-dimensional calculations would be better suited to investigating the pilot fuel ignition of gaseous jets. In particular the effect of injection angle and relative position of the pilot diesel fuel sprays relative to the gaseous jets could be studied.

Combustion modelling would be nicely augmented by the addition of an appropriate nitrogen oxide scheme.

On the experimental side, it would be of interest to repeat the experiments with an injection angle such that the contact with the wall be reduced. The results would remove some uncertainty about the wall effects and extend the distance range over which the scaling can be applied.

Finally, it would be of interest to obtain some engine results following the implementation of some of the design suggestions. New injector tips with more smaller holes have been designed, are being manufactured and will be tested in the engine.

REFERENCES

Abraham J., Bracco F.V., Reitz R.D., "Comparison of Computed and Measured Premixed Charge Engine Combustion", Combustion and Flame, Vol. 60, pp. 309-322, 1985

Abraham J., Bracco F.V., "Simple Modeling of Autoignition in Diesel Engines for 3-D Computations", SAE Paper # 932656, 1993

Abraham, J., Magi, V., MacInnes, J., Bracco, F.V., "Gas versus Spray Injection: Which Mixes Faster?", SAE Paper #940895, 1994

Abramovich, G.N., The Theory of Turbulent Jets, M. I. T. Press, 1963

Abramovich, S., Solan, A., "The Initial Development of a Submerged Laminar Round Jet", Journal of Fluid Mechanics, Vol. 59, pp. 791-801, 1973

Amsden, A.A., O'Rourke, P.J., Butler, T.D., "KIVA-II: A Computer Program for Chemically Reactive Flows with Sprays", Los Alamos report LA-11560-MS, 1989

Batchelor, G.K. An Introduction to Fluid Dynamics, Cambridge Press, 1967

Birch, A. D., Brown, D. R., Dodson, M. G., Thomas, J. R., "The Turbulent Concentration Field of a Methane Jet", Journal of Fluid Mechanics, Vol. 88, pp. 431-449, 1978

Birch, A. D., Brown, D. R., Dodson, M. G., Swaffield, F., "The Structure and Concentration Decay of High Pressure Jets of Natural Gas", Combustion Science and Technology, Vol. 36, pp. 249-261, 1984

Chepakovich, A., "Visualization of Transient Single- and Two-Phase Jets Created by Diesel Engine Injectors", M.A.Sc. Thesis, The University of British Columbia, 1993

Coffee T.P., Kotlar A.J., Miller M.S., "The Overall Reaction Concept in Premixed, Laminar, Steady-State Flames. I. Stochiometries", Combustion and Flame, Vol. 54, pp. 155-169, 1983

Coffee T.P., "On Simplified Reaction Mechanisms by Oxidation of Hydrocarbon Fuels in Flames by C.K. Westbrook and F.T.Dryer", Combust. Sci. and Tech., Vol. 43, pp. 333-339, 1985

Doulsin, R.D., Harrison, R.H., Moore, R.T., McCullough, J.P., P-V-T relations for methane, J. Chem. and Eng. Data, Vol. 9, No. 3, pp. 358, 1964

Ewan, B. C. R., Moodie, K., "Structure and Velocity Measurements in Underexpanded Jets", Combustion Science and Technology, Vol. 45, pp. 275-288, 1986

Fraser R.A., Siebers D.L., Edwards C.F., "Autoignition of Methane and Natural Gas in a Simulated Diesel Environment", SAE Paper #910227, 1991

Gaillard, P., "Multidimensional Numerical Study of the Mixing of an Unsteady Gaseous Fuel Jet with Air in Free and Confined Situations", SAE Paper #840225, 1984

Glassman I,. Combustion, 2nd ed., Academic Press, 1987

Gosman A.D., Harvey P.S., "Computer Analysis of Fuel-Air Mixing and Combustion in an Axisymmetric D.I. Diesel", SAE Paper #820036, 1982

Grasso F., Bracco F.V., "Evaluation of a Mixing-Controlled Model for Engine Combustion", Combust. Sci. and Tech., Vol. 28, pp. 185-210, 1982

Halstead, M.P., Kirsch, L.J., Quinn, C.P., "The Autoignition of Hydrocarbon Fuels at High Temperatures and Pressures - Fitting of a Mathematical Model", Combustion and Flame, Vol. 20, pp. 45-60, 1977

Hanjalic K., Laundner B.E., "Sensitizing the Dissipation Equation to Irrotational Strains", Transaction of the ASME, Vol. 102, pp. 34, 1980

Hawthorne, W.R., Weddell, D.S., Hottel, H.C., "Mixing and Combustion in Turbulent Gas Jets", 3rd Symposium on Combustion, Flame and Explosion Phenomena, 1948

Heywood, J. B., Internal Combustion Engine Fundamentals, McGraw-Hill Book Company, 1988

Hodgins, K.B., Gunawan, H., Hill, P.G., "Intensifier-Injector for Natural Gas Fueling of Diesel Engines", SAE paper #921553, 1992

Jennings, M.J., Jeske, F.R., "Analysis of the Injection Process in Direct Injected Natural Gas Engines: Part 1 - Study of Unconfined and In-Cylinder Plume Behavior", Journal of Engineering for Gas Turbines and Power, Vol. 116, pp.799, 1994

Kleinraum, R., Duschek, W., Wagner, W., Jaeschke, M., "Measurement and correlation of the (pressure, density, temperature) relation of methane in the temperature range from 273.15 K to 323.15 K at pressures up to 8 MPa", J. Chem. Thermodynamics, Vol.20, pp. 621-631, 1988

Kuo, T. W., Bracco, F. V., "On the Scaling of Transient Laminar, Turbulent, and Spray Jets", Society of Automotive Engineers, SAE Paper #820038, 1982.

Kuo T.W., Reitz R.D., "Computation of Premixed-Charge Combustion in Pancake and Pent-Roof Engines", SAE Paper #890670, 1989

Kuo T.W., Reitz R.D., "Three-Dimensional Computations of Combustion in Premixed-Charge and Direct-Injected Two-Stroke Engines", SAE Paper #920425, 1992

Lifshitz A., Scheller K., Burcat A., Skinner G.B., "Shock-Tube Investigation in Methane-Oxygen-Argon Mixtures", Combustion and Flame, Vol. 16, pp. 311-321, 1971

Liñán, A., Williams, F.A., Fundamental Aspects of Combustion, Oxford University Press, 1993

MacInnes, J.M., Bracco, F.V., "Computation of the Spray from an Air-Assisted Fuel Injector", SAE Paper #902079, 1990

Malin M.R., "Modelling the Effects of Lateral Divergence on Radially Spreading Jets", Computers and Fulids, Vol. 17, No. 3, pp. 453-465, 1989

Magnussen B.F., Hjertager B.H., " On Mathematical Modeling of Turbulent Combustion with Special Emphasis on Soot Formation and Combustion", 16th Symposium on Combustion, The Combustion Institute, 1977

Miyake, M., Biwa, T., Endoh, Y., Shimotsu, M., Murakami, S., Komoda, T., "The Development of High-Output, Highly Efficient Gas Burning Diesel Engines", CIMAC Paper D11.2, 1983

Mullholland, J.A., Sarofim, A.F., Beer, M.,"On the Derivation of Global Ignition Kinetics from a Detailed Mechanism for Simple Hydrocarbon Oxidation", Combust. Sci. and Tech., Vol. 87, pp. 139-156, 1992.

Naber J.D., Siebers D.L., Caton J.A., Westbrook C.K., Di Julio S.S., "Natural Gas Autoignition Under Diesel Conditions: Experiments and Chemical Kinetic Modeling", SAE Paper #942034, 1994

Ouellette, P., Hill, P.G., "Visualization of Natural Gas Injection for a Compression Ignition Engine", SAE Paper #921555, 1992

Richards, J.M., "Puff Motions in Unstratified surroundings", Journal of Fluid Mechanics, Vol.21, Part 1, pp.97-106, 1965

Ricou, F.P., Spalding, D.B., "Measurements of entrainment by axisymmetrical turbulent jets", Journal of Fluid Mechanics, Vol. 11, pp. 21-32, 1961

Setzmann, U. and Wagner, W., "A New Equation of State and Tables of Thermodynamic Properties for Methane Covering the Range from the Melting Line to 625 K at Pressures up to 1000 MPa", J. Phys. Chem. Ref. Data, Vol. 20, No. 6, 1991

Sloane T.M., Ronney P.D., "A Comparison of Ignition Phenomena Modelled with Detailed and Simplified Kinetics", Combust. Sci. and Tech., Vol. 88, pp. 1-13, 1992

Solomon, A.S., "Plasma-Jet Ignition of Fuel Sprays in a Rapid Compression Machine", SAE Paper #880205, 1988

Spalding D.B., "Mixing and Chemical Reaction in Steady Confined Turbulent Flames", 13th Symposium on Combustion, The Combustion Institue, 1971

Tao, Y., Hodgins, K.B., Hill, P.G., "NO_x Emissions from a Diesel Engine Fueled with Natural Gas", ASME, Petroleum Division (Pub), PDV 57, pp. 35-42, 1994

Tsuboi T., Wagner H.G., "Homogeneous Thermal Oxidation of Methane in Reflected Shock Waves", 15th International Symposium on Combustion, The Combustion Institute, 1974

Turner, J.S., "The "starting plume" in neutral surroundings", Journal of Fluid Mechanics, Vol. 13, pp. 356-368, 1962

Van Dyke, M., An Album of Fluid Motion, Parabolic Press, Stanford, California, 1988

Witze, P., "The Impulsively Started Incompressible Turbulent Jet", SAND80-8617, pp. 3-15, 1980

Westbrook C.K., Dryer F.L., "Simplified Reaction Mechanisms for the Oxidation of Hydrocarbon Fuels in Flames", Combustion Science and Technology, Vol. 27, pp. 31-43, 1981

Wygnanski, I. and Fiedler, H., "Some measurements in the self-preserving jet", Journal of Fluid Mechanics, Vol. 38, Part 3, pp. 577-612, 1969

Zhou G., Karim G.A., "A Comprehehsive Kinetic Model for the Oxidation of Methane", PD_Vol. 57, Emerging Energy Technology, ASME, 1994

APPENDIX A

Detroit-Diesel Corporation 6V-92 TA Diesel Engine Specifications

Basic Engine :	2-cycle-Vee
Number of Cylinders :	6
Control :	DDEC II
Bore and Stroke :	123 x 127 mm (4.84 x 5.0 in)
Displacement :	9.05 litres (552 cu in)
Compression Ratio :	17.0 to 1
Gross Power Output :	224 kW (300 BHP) @2100 RPM
Gross Rated BMEP :	9.2 bar @ 1200 RPM
Rated Peak Torque :	1322 N°m (975 lb°ft) @ 1200 RPM
Inlet Port Closure :	55° ABDC

APPENDIX B

Dimensional Analysis for Transient Trubulent Free Jets

Assuming that i) there is one nozzle, ii) that the Reynolds number is large enough, iii) that the chamber is large, then the following parameters can be considered for the penetration of the jet issued from a round nozzle (conditions in nozzle not considered):

$$z_t = f(P_n,\ T_n,\ d_n,\ U_n,\ P_{ch},\ T_{ch},\ t,\ t_{inj},\ k) \tag{B.1}$$

Using an equation of state for nozzle and chamber conditions, the densities can be obtained from pressure and temperature:

$$z_t = f(\rho_n,\ d_n,\ U_n,\ \rho_{ch},\ t,\ t_{inj},\ k) \tag{B.2}$$

There are 8 significant variables and 3 primary groups, such that 5 dimensionless groups can be obtained. The following groups are proposed:

$$\frac{z_t}{d_n} = f\left(\frac{\rho_n}{\rho_{ch}},\ \frac{tU_n}{d_n},\ \frac{t}{t_{inj}},\ \frac{\sqrt{k}}{U_n}\right) \tag{B.3}$$

Which can be rearranged as

$$\frac{z_t}{d_n\left(\frac{\rho_n}{\rho_{ch}}\right)^{1/2}} = f\left(\frac{tU_n}{d_n\left(\frac{\rho_n}{\rho_{ch}}\right)^{1/2}},\ \frac{t}{t_{inj}},\ \frac{\sqrt{k}}{U_n}\right) \tag{B.4}$$

APPENDIX C

Methane Equation of State

The virial equation of state for methane of Kleiraum *et al* [1988], valid for temperatures between 273.15 and 323.15 K and pressures below 8 MPa, was extended to fit the experimental data of Douslin *et al* [1964] for pressures up to 25 MPa. The equation of state is

$$Z = \frac{Pv}{RT} = 1 + A(T)\rho + B(T)\rho^2 + C(T)\rho^3 + D(T)\rho^4 + E(T)\rho^5 \qquad \textbf{(C.1)}$$

and the functions are:

$A(T)=A_1\tau^{a_1}+A_2\tau^{a_2}$ $\quad A_1=0.00376136 \quad a_1=0.25$

$\quad A_2=-0.00708823 \quad a_2=1.25$

$B(T)=B_1\tau^{b_1}$ $\quad B_1=0.0000103301 \quad b_1=1$

$C(T)=C_o+C_1\tau^{c_1}$ $\quad C_o=-1.19057\times10^{-8} \quad C_1=8.69027\times10^{-9} \quad c_1=-2$

$D(T)=D_o+D_1\tau^{d_1}$ $\quad D_o=-6.39867\times10^{-11} \quad D_1=1.06645\times10^{-10} \quad d_1=3$

$E(T)=E_o+E_1\tau^{e_1}$ $\quad E_o= 4.92006\times10^{-13} \quad E_1=-5.65524\times10^{-13} \quad e_1=3$

where τ is 273.15/T. The equation of state fits experimental data within 0.05% for temperatures between 273.15 and 400 K, and for pressures below 25 MPa. The equation of state was integrated to obtain an Helmholtz function as $P=-(\partial\psi/\partial v)_T$. Isentropic conditions were calculated using the identity $s=-(\partial\psi/\partial T)_\rho$.

APPENDIX D

Nozzle Condition Estimates

Referring to Figure 3.10, and assigning the subsrcipt 1 to the duct entrance and 2 to the duct exit to the chamber, the mass and momentum conservation equations were written:

$$\rho_1 V_1 = \rho_2 V_2 \tag{D.1}$$

$$(P_1 - P_2) - 4\tau_w \frac{L}{D} = \rho V (V_2 - V_1) \tag{D.2}$$

where the wall friction is given by

$$\tau_w = f \frac{\rho V^2}{2} \tag{D.3}$$

An average velocity and friction factor were considered over the pipe length in calculating the wall friction. Using these assumptions and the equation of state, the exit conditions were calculated in the following manner:

- T_2 is guessed,
- ρ_2 is obtained such that M_2 is equal to 1 (choked flows) or $P_2 = P_{ch}$,
- T_1 is guessed,
- ρ_1 is calculated to satisfy mass conservation,
- T_1 is adjusted to satisfy momentum conservation,
- s_1 is compared to s_o,
- finally, T_2 is adjusted until $s_1 = s_o$.

The state relationship and the isentropic requirements were calculated based on the methane equation of state and on the Helmholtz function derived from it.

APPENDIX E

Data Points

In all experiments, the temperature can be taken as 298 K. The diameter of the nozzle was 0.5 mm. The error on the penetration z_t is typically of the order of 1 mm due predominantly to randomness of the jet. The error on time is the shutter speed of 0.1 ms, and an additional random variation of 0.05 ms on the BOI.

P_o [MPa]	P_{ch} [MPa]	PR	Time [ms]	z_t [mm]
2.285	1.494	1.529	0.00	0
			0.08	3.2
			0.19	5.6
			0.42	13.3
			0.66	16.3
			0.89	21.8
			1.12	22.3
			1.59	27.5
			2.17	32.7
			2.76	38.3
3.725	1.494	2.493	0.00	0.0
			0.08	5.8
			0.13	8.0
			0.25	12.5
			0.48	20.2
			0.72	26.8
			1.07	31.5
			1.65	40.2
			2.23	47.6

P_o [MPa]	P_{ch} [MPa]	PR	Time [ms]	z_t [mm]
6	1.494	4.016	0.00	0.0
			0.07	7.7
			0.19	11.1
			0.31	16.7
			0.42	22.3
			0.66	27.9
			0.89	34.0
			1.12	40.3
			1.36	45.3
8.088	1.494	5.414	0	0
			0.08	7.0
			0.19	12.8
			0.31	18.7
			0.42	22.8
			0.54	25.8
			0.66	29.0
			0.77	34.5
			1.01	40.5
			1.24	44.4

APPENDIX F

KIVA-II Equations of Fluid Motion

In the following equations, the vector notation is employed:

$$\vec{v} = u(x,y,z,t)\vec{i} + v(x,y,z,t)\vec{j} + w(x,y,z,t)\vec{k} \tag{F.1}$$

$$\nabla = \vec{i}\frac{\partial}{\partial x} + \vec{j}\frac{\partial}{\partial y} + \vec{k}\frac{\partial}{\partial z} \tag{F.2}$$

The continuity equation for species m is

$$\frac{\partial \rho_m}{\partial t} + \nabla\cdot(\rho_m \vec{v}) = \nabla\cdot[\rho D \nabla(\frac{\rho_m}{\rho})] + \dot{\rho}_m^c + \dot{\rho}_{m=1}^s \tag{F.3}$$

where ρ_m is the density of species m, ρ the total mass density, and D a single diffusion coefficient. Fick's Law has been assumed for diffusion. The $\dot{\rho}_m^c$ is the species source term from chemical reactions, while $\dot{\rho}_{m=1}^s$ is a source term from the evaporating spray. Summing over all species, the total mass conservation is

$$\frac{\partial \rho}{\partial t} + \nabla\cdot(\rho \vec{v}) = 0 \tag{F.4}$$

The momentum equation:

$$\frac{\partial(\rho \vec{v})}{\partial t} + \nabla\cdot(\rho \vec{v}\vec{v}) = -\nabla p + \nabla\cdot\vec{\tau} + \rho\vec{g} - \nabla(2/3\rho k) \tag{F.5}$$

where the stress tensor is

$$\vec{\tau} = \mu\ [\nabla\vec{v} + (\nabla\vec{v})^T] - \frac{2}{3}\mu(\nabla\cdot\vec{v})I \tag{F.6}$$

The energy equation is:

$$\frac{\partial(\rho I)}{\partial t} + \nabla\cdot(\rho \vec{v} I) = -p\nabla\cdot\vec{v} - \nabla\cdot J + \dot{Q}^c + \dot{Q}^s + \rho\varepsilon \tag{F.7}$$

where I is the internal energy, $\dot{Q}^c$ is the heat release from chemical reactions and $\dot{Q}^s$ the heat loss to the evaporation of the spray. The heat flux vector J is:

$$J = -K\nabla T - \rho D\sum_m h_m \nabla(\frac{\rho_m}{\rho}) \qquad \textbf{(F.8)}$$

In the above energy equation the viscous heat generation term has been omitted since it is negligible for turbulent flows (the term is present for laminar cases in Amsden *et al* [1989]). The $\rho\varepsilon$ term is the heat generated as a result of turbulent dissipation. The above equations are averaged over the flow, and turbulent transport properties are used to model the effects of turbulence. The transport coefficients are:

$$\mu = \mu_{air} + c_\mu \frac{k^2}{\varepsilon} \qquad \textbf{(F.9)}$$

$$K = \frac{\mu C_p}{Pr} \qquad \textbf{(F.10)}$$

$$D = \frac{\mu}{\rho S_c} \qquad \textbf{(F.11)}$$

and the constant values are given in Table F.1 below. The specific turbulent kinetic energy k is defined as

$$k = \frac{1}{3}\overline{(u'^2+v'^2+w'^2)} \qquad \textbf{(F.12)}$$

where the primes indicate fluctuating components, and ε is the dissipation rate of k. Transport equations are written for k and ε :

$$\frac{\partial(\rho k)}{\partial t} + \nabla\cdot(\rho\vec{v}k) = \tau:\nabla\vec{v} + \nabla\cdot[(\frac{\mu}{Pr_k})\nabla k] - \rho\varepsilon - \frac{2}{3}\rho k\nabla\cdot\vec{v} \qquad \textbf{(F.13)}$$

$$\frac{\partial(\rho\varepsilon)}{\partial t} + \nabla\cdot(\rho\vec{v}\varepsilon) = \frac{\varepsilon}{k}[c_{\varepsilon_1}\tau:\nabla\vec{v} - c_{\varepsilon_2}\rho\varepsilon] + \nabla\cdot[(\frac{\mu}{Pr_\varepsilon})\nabla\varepsilon] - (\frac{2}{3}c_{\varepsilon_1} - c_{\varepsilon_3})\rho\varepsilon\nabla\cdot\vec{v} \qquad \textbf{(F.14)}$$

which are the standard k-ε equation with added terms to take into consideration the effect of velocity dilatation on turbulence which occur because of compression and expansion in the engine. The operator **:** is the complete contraption :

$$\tau:(\nabla\vec{v}) = \nabla\cdot(\vec{\tau}\cdot\vec{v}) - \vec{v}\cdot(\nabla\cdot\vec{\tau}) \qquad \textbf{(F.15)}$$

The perfect gas law for a mixture is used in Kiva-II as a state equation :

$$p = R_o T \sum_m (\rho_m / W_m) \qquad \textbf{(F.16)}$$

Table F.1

$C_\mu = 0.09$	$Pr_k = 1.0$
$C_{\varepsilon 1} = 1.44$	$Pr_\varepsilon = 1.3$
$C_{\varepsilon 2} = 1.92$	$Pr = 0.9$
$C_{\varepsilon 3} = -1.0$	$Sc = 0.9$

where W_m is the molecular weight of species m. The internal energy I, the constant pressure specific heat and the enthalpies for species m are:

$$I(T) = \sum_m (\rho_m/\rho)\, I_m(T) \qquad \textbf{(F.17)}$$

$$C_p(T) = \sum_m (\rho_m/\rho)\, C_{pm}(T) \qquad \textbf{(F.18)}$$

$$h_m(T) = I_m(T) + R_o T/W_m \qquad \textbf{(F.19)}$$

and the values of $h_m(T)$ and $C_{pm}(T)$ are taken from the JANAF tables. The rate of formation of species form chemical kinetics is presented in Chapter 6.

APPENDIX G

Mixing Rate of Abraham *et al [1994]*

It was initially thought that the difference in mixing rate between sprays and gaseous jets reported by Abraham *et al* was due to their modelling of a spray with a larger angle of spread. However, as shown in Section 5.4, this does not change the mixing rate significantly. Although the spray characteristics differ between the study of Abraham *et al* and this study, the main source of discrepancy is the mixing rate of the gaseous jet. To investigate that difference, the boundary and chamber conditions used by Abraham *et al* were utilized in the current model and the mixing rate was calculated. The boundary conditions used in Abraham *et al* do not provide a correctly expanded jet. They use a velocity of 300 m/s and a density of 56.8 kg/m^3, and a chamber pressure of 6 MPa and 750K. For the jet to be correctly expanded at that velocity, the stagnation temperature should be around 224 K. Using a temperature of 300 K will lead to an underexpanded jet, but with a sub-sonic velocity. Figure G.1 shows the mixing rate obtained with the current model when the boundary conditions used by Abraham *et al* and a temperature of 300 K are considered. In this case, following Abraham *et al*, the methane is injected in a cylindrical chamber. Figure G.1 is contrasted with Fig. G.2, the mixing rate obtained by Abraham *et al*. Using a temperature of 224 K did not change considerably the results. As may be seen, the current model predicts a much faster mixing than the one reported. It is suspected that the calculation of the mass fraction is erroneous, as the penetration rate reported in Abraham *et al* is very similar to the one obtained in this thesis.

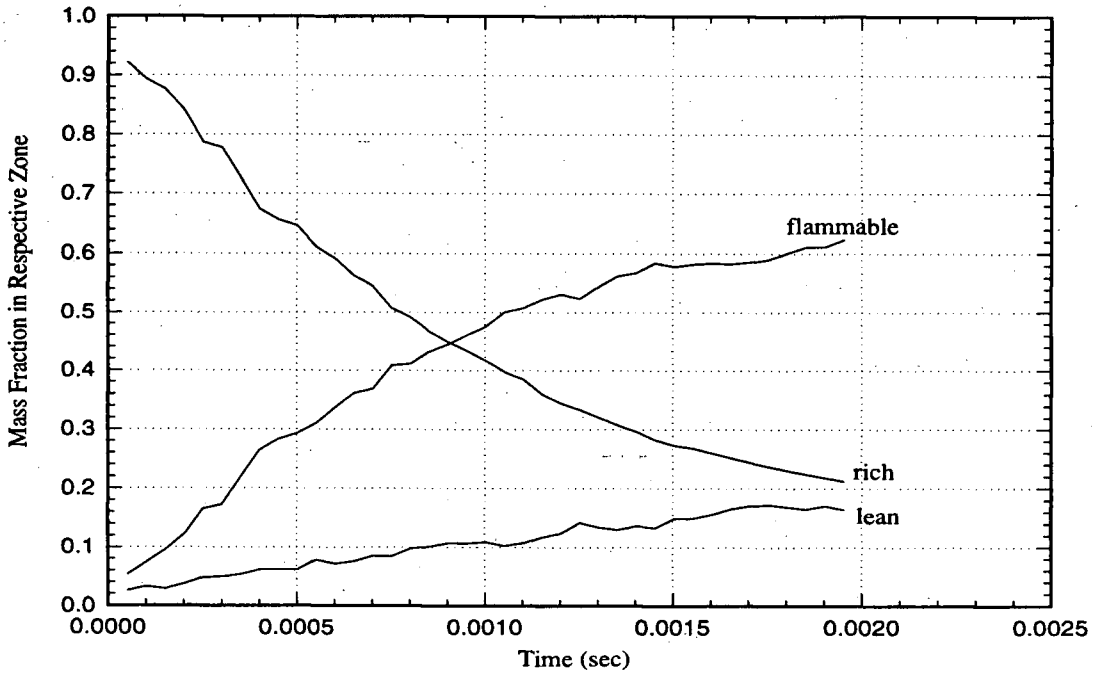

Figure G.1 - Mixing rate of methane injected in a cylindrical chamber using Abraham *et al* [1994] boundary conditions.

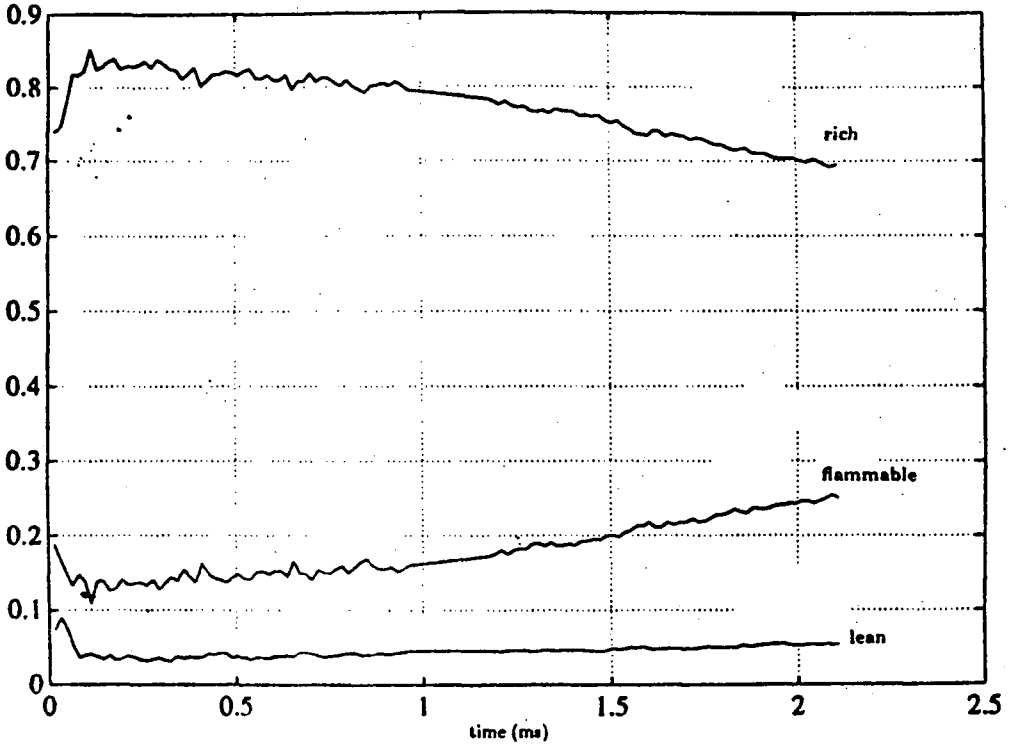

Figure G.2 - Mixing rate reported by Abraham *et al* [1994].